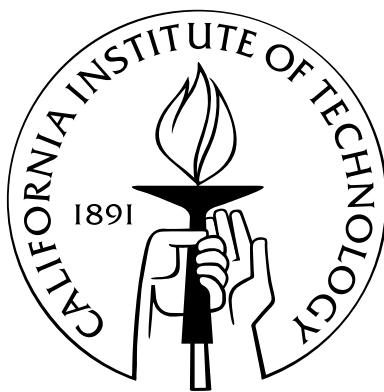


# Rheological Measurements in Liquid-Solid Flows

Thesis by  
Erin Koos

In Partial Fulfillment of the Requirements  
for the Degree of  
Doctor of Philosophy



California Institute of Technology  
Pasadena, California

2009

(Defended March 19, 2009)

© 2009

Erin Koos

All Rights Reserved

# Acknowledgements

When I look back at my time here at Caltech, I know it would not have been possible without the help I received along the way.

First, I would like to thank Professor Melany Hunt, my advisor, for her guidance and support. From my first day in her lab to these very last days, her door has always been open to answer questions, give encouragement, and offer an understanding ear. Melany gave me the support I needed when nothing seemed to work allowing me to eventually succeed. I would also like to express the gratitude I have for the help and motivation I received from Professor Christopher Brennen. On everything from the practical to the theoretical, he would always have time to help with my questions – each meeting ending with the ever present “press on.”

I also extend my thanks to Prof. John F. Brady, Prof. Joseph E. Shepherd, and Prof. Roberto Zenit for serving on my committee and reviewing my dissertation. I appreciate their time and comments. Each red mark was a chance to make the finished product that much better.

I also owe a debt of gratitude to Dr. Jim Cory. Jim designed and had constructed the apparatus used for these experiments. It has undergone a few small redesigns since, but the bulk of the experiment is still his work. I would also like to express my thanks to Esperanza Linares for helping me with some of my measurements; I wish you luck in your future experiments. Angel Ruiz-Angulo served as my mentor and made me feel welcome not to mention supplying me with many samples of apple cake as he perfected his recipe. To the other members of the Granular Flows Group, both past and present, thank you.

Just about every week, I’d be in Cheryl Geer’s office asking her to help schedule time with my advisors, arrange travel, and serve as my informal guide for the administrative requirements as I tried to graduate. I also owe a debt of gratitude to John Van Deusen. John helped me get parts unstuck, lubricated and back to functioning properly. When I

needed to redesign components, I'd usually end up in John's office asking him if the idea was feasible (or advisable). I would also like to thank Candace Rypisi and Felicia Hunt as directors of the Women's Center for providing a welcome home, weekly lunches and an always sympathetic ear. Many thanks are also extended to the many other members of the Caltech community without whom, my experiences as both a student and researcher would have been hindered.

Without my friends here at Caltech and elsewhere, my life would be much diminished. Adam Mills was always available when I needed a soft shoulder or to escape for a weekend. Maybe one day, I'll be able to answer my own "should I" questions. I will always remember tramping through the woods with Anna Folinsky. In summer and winter, you put up with my slow pace (and occasional blisters). I would certainly have been less active and seen much less of California were it not for you. Dr. Jennifer Stockdill, creative genius, my kitchen is always open for you; invite yourself over any time. Dr. Deepak Kumar, thank you for all of your help and the many relaxing meals I was able to share with you. You need to take me up flying when you finish your pilot's license. Jenny Roizen, you are one of the kindest people I know: from my very first day on campus, you have been there whenever I needed a hug or to go out and have fun.

Most of all, I would like to extend my deepest gratitude to my parents. Their unabating, unconditional support was always appreciated. I would not be here now if it wasn't for you both. My thesis is dedicated to you.

# Abstract

This thesis presents experimental measurements of the shear stresses of a fluid-particulate flow at high Reynolds numbers as a function of the volume fraction of solids. From the shear stress measurements an effective viscosity, where the fluid-particulate flow is treated as a single fluid, is determined. This viscosity varies from the fluid viscosity when no solids are present to several orders of magnitude greater than fluid viscosity when the particles near their maximum packing state. It is the primary goal of this thesis to determine how the effective viscosity varies with the volume fraction of solids.

A variety of particle sizes, shapes, and densities were obtained through the use of polystyrene, nylon, polyester, styrene acrylonitrile, and glass particles, used in configurations where the fluid density was matched and where the particles were non-neutrally buoyant. The particle sizes and shapes ranged from 3 mm round glass beads to 6.4 mm nylon to polystyrene elliptical cylinders. To properly characterize the effect of volume fraction on the effective viscosity, the random loose- and random close-packed volume fractions were experimentally determined using a counter-top container that mimicked the *in situ* (concentric cylinder Couette flow rheometer) conditions. These volume fractions depend on the shape of the particles and their size relative to the container.

The effective viscosity for neutrally buoyant particles increases exponentially with volume fraction at fractions less than the random loose-packing. Between the random loose- and random close-packed states, the effective viscosity increases more rapidly with volume fraction and asymptotes to very large values at the close-packed volume fraction. The effective viscosity does not depend on the size or shape of particles beyond the influence these parameters have on the random packing volume fractions.

For non-neutrally buoyant particles, the difference in particle buoyancy requires an additional correction. The volume fraction at the time of the force measurement was recorded for several different ratios of particle-to-fluid density. This volume fraction increases with

the shear rate of the Couette flow and decreases with the Archimedes number in a way that when plotted against the Reynolds number over the Archimedes number, these curves collapse onto one master curve. When the local volume fraction is used, the effective viscosity for non-neutrally buoyant particles shows the same dependence on volume fraction as the neutrally buoyant cases.

Particle velocities were also measured for both neutrally buoyant and non-neutrally buoyant particles. These particle velocities near the stationary inner wall show evidence for a small region near the walls with few particles. This particle depletion layer was measured directly using the velocity data and indirectly using the difference between the measured effective viscosities for the smooth- and rough-wall configurations. The slip in the smooth wall experiments can significantly affect the measured viscosity, but this deficiency can be corrected using the thickness of the depletion layer to find the actual value for the effective viscosity.

# Contents

<b>Acknowledgements</b>	<b>iii</b>
<b>Abstract</b>	<b>v</b>
<b>List of Figures</b>	<b>xi</b>
<b>List of Tables</b>	<b>xvii</b>
<b>Nomenclature</b>	<b>xix</b>
<b>1 Introduction</b>	<b>1</b>
1.1 Flow regimes . . . . .	2
1.1.1 Continuum assumptions . . . . .	3
1.1.2 Secondary flows . . . . .	4
1.1.3 Diffusion and Brownian motion . . . . .	6
1.1.4 Phase diagrams . . . . .	8
1.1.5 Particle interactions . . . . .	9
1.2 Previous experiments . . . . .	11
1.2.1 Secondary flows . . . . .	13
1.2.2 Non-neutrally buoyant particles . . . . .	16
1.3 Thesis outline . . . . .	18
<b>2 Packing</b>	<b>21</b>
2.1 Implications for the effective viscosity . . . . .	22
2.1.1 Random loose-packing and the dilatancy onset . . . . .	22
2.1.2 Random close-packing and jamming . . . . .	23
2.2 Determination of random packing volume fractions . . . . .	24

2.2.1	Random close-packing . . . . .	24
2.2.2	Random loose-packing . . . . .	25
2.2.3	Containers . . . . .	27
2.2.4	Packing of non-spherical particles . . . . .	28
2.2.5	Nearly spherical particles . . . . .	30
2.3	Experimental data . . . . .	32
2.3.1	Current particles . . . . .	32
2.3.2	Previously reported experiments . . . . .	33
2.4	Summary . . . . .	35
<b>3</b>	<b>Apparatus and Experimental Procedure</b>	<b>37</b>
3.1	Rotating cylinder rheometer . . . . .	38
3.2	Experimental measurements . . . . .	40
3.2.1	Particle velocity and volume fraction measurements . . . . .	40
3.2.2	Shear stress . . . . .	46
3.2.3	Pure fluid calibration . . . . .	51
3.3	Particle characterization . . . . .	53
3.3.1	Glass . . . . .	53
3.3.2	Nylon . . . . .	54
3.3.3	Polyester . . . . .	56
3.3.4	Polystyrene . . . . .	58
3.3.5	Styrene acrylonitrile . . . . .	60
3.4	Summary . . . . .	62
<b>4</b>	<b>Neutrally buoyant particles</b>	<b>63</b>
4.1	Theory . . . . .	63
4.2	Experiments . . . . .	64
4.2.1	Polystyrene . . . . .	66
4.2.2	Nylon particles . . . . .	70
4.2.3	Styrene Acrylonitrile . . . . .	72
4.3	Summary . . . . .	75



<b>5</b>	<b>Non-neutrally buoyant particles</b>	<b>79</b>
5.1	Theory . . . . .	79
5.2	Experiments . . . . .	80
5.2.1	Polystyrene . . . . .	81
5.2.1.1	Particle velocity . . . . .	81
5.2.1.2	Volume fraction . . . . .	85
5.2.1.3	Effective viscosity . . . . .	89
5.2.1.4	Coefficient of friction . . . . .	94
5.2.2	Glass . . . . .	96
5.2.3	Polyester . . . . .	97
5.3	Summary of experimental data . . . . .	101
5.4	Experimental fits . . . . .	103
5.4.1	Dilute curve fits . . . . .	103
5.4.2	Continuous contact curve fits . . . . .	105
<b>6</b>	<b>Slip layer and the influence of surface roughness</b>	<b>107</b>
6.1	Theory . . . . .	107
6.1.1	Apparent viscosity . . . . .	112
6.1.2	Particle velocity . . . . .	114
6.2	Experiments with polystyrene . . . . .	114
6.2.1	Actual viscosity measurements . . . . .	116
6.2.2	Particle velocity . . . . .	122
6.2.3	Smooth and rough wall boundary conditions . . . . .	124
6.3	Corrections for smooth walls . . . . .	126
6.4	Summary . . . . .	127
<b>7</b>	<b>Summary and conclusions</b>	<b>129</b>
7.1	Neutrally buoyant particles . . . . .	129
7.1.1	Reynolds number . . . . .	130
7.1.2	Volume fraction of solids . . . . .	131
7.2	Non-neutrally buoyant particles . . . . .	132
7.3	Surface roughness . . . . .	133
7.4	Topics for future investigation . . . . .	134

<b>A</b>	<b>MATLAB source code</b>	<b>137</b>
A.1	Peak finding algorithm ( <code>fpeak.m</code> and <code>getPeak.m</code> ) . . . . .	137
A.2	Cross-correlation for the entire signal ( <code>correl_full.m</code> ) . . . . .	140
A.3	Cross-correlation for individual peaks ( <code>correl.m</code> ) . . . . .	142
<b>B</b>	<b>Drawings</b>	<b>147</b>
	<b>Bibliography</b>	<b>197</b>

# List of Figures

1.1	Critical Reynolds number for the onset of Couette-Taylor flow . . . . .	5
1.2	Increase in torque for inner and outer rotating Couette flows . . . . .	5
1.3	Critical Reynolds number for the onset of turbulence in pipe flow with particles	7
1.4	Phase diagram for non-Brownian fluid-particulate flows . . . . .	8
1.5	Experimental apparatus used in Bagnold (1954, 1956) . . . . .	12
1.6	Reynolds number-volume fraction phase diagram of previous experiments .	15
1.7	Experimental apparatus used in Savage and McKeown (1983) . . . . .	15
1.8	Experimental apparatus used in Acrivos et al. (1994); Hanes and Inman (1985); Prasad and Kytömaa (1995) . . . . .	17
2.1	Dilatancy of particles . . . . .	22
2.2	Hexagonally close-packed spheres . . . . .	24
2.3	Images of random packing in a confined container . . . . .	27
2.4	Oscillation of the volume fraction near a wall . . . . .	28
2.5	Influence of finite containers on the volume fraction of round particles . . . .	29
2.6	Approximations for close- and close-packing for nearly spherical particles . .	31
3.1	Coaxial rotating cylinder, Couette flow device . . . . .	38
3.2	Typical response curve for the MTI KD-300 photonic sensors used with a MTI 0623H optical probe . . . . .	41
3.3	Schematic of the optical probe configuration to measure particle counts and velocities . . . . .	42
3.4	Bode magnitude plot for the combined lowpass and bandstop filter . . . . .	43
3.5	Filtered and unfiltered voltage data . . . . .	44

3.6	Filtered and normalized voltage signal from two probes located in the lower observation port . . . . .	45
3.7	Converted voltage signal used for the cross-correlation of the full voltage signals for two adjacent optical probes . . . . .	46
3.8	Normalized cross-correlation amplitude showing the likely particle velocities	47
3.9	Histogram of particle velocities found using the <code>correl.m</code> function . . . . .	48
3.10	Post peak displacement as a function of normalized voltage for the MTI optical displacement sensors . . . . .	49
3.11	Spring stiffness for three different springs . . . . .	50
3.12	Pure fluid calibration . . . . .	52
3.13	The glass spheres used in the rheological experiments . . . . .	54
3.14	Histogram of glass particle sizes . . . . .	55
3.15	The nylon spheres used in the rheological experiments . . . . .	55
3.16	Histogram of nylon particle sizes . . . . .	56
3.17	The polyester scalene ellipsoids used in the rheological experiments . . . . .	57
3.18	Histogram of polyester particle sizes . . . . .	58
3.19	The polystyrene elliptical cylinders used in the rheological experiments . . .	59
3.20	Histogram of polystyrene particle sizes . . . . .	59
3.21	The SAN scalene ellipsoids used in the rheological experiments . . . . .	61
3.22	Histogram of SAN particle sizes . . . . .	61
4.1	Shear stress measurements for suspensions of polystyrene particles in aqueous glycerine . . . . .	66
4.2	Ratio of measured-to-pure fluid torques for suspensions of polystyrene particles in aqueous glycerine . . . . .	67
4.3	Effective viscosity ratio for neutrally buoyant polystyrene particles in aqueous glycerine solutions . . . . .	68
4.4	Deviation from the mean effective viscosity ratio . . . . .	69
4.5	Shear stress measurements for suspensions of nylon particles in aqueous glycerine . . . . .	70
4.6	Ratio of measured-to-pure fluid torques for suspensions of nylon particles in aqueous glycerine . . . . .	71

4.7	Effective viscosity ratio for neutrally buoyant nylon particles in aqueous glycerine solutions . . . . .	72
4.8	Shear stress measurements for neutrally buoyant SAN particles in aqueous glycerine . . . . .	73
4.9	Ratio of measured-to-pure fluid torques for suspensions of SAN particles in aqueous glycerine . . . . .	74
4.10	Effective viscosity ratio for neutrally buoyant SAN particles in aqueous glycerine solutions . . . . .	75
4.11	Effective viscosity for neutrally buoyant particles in aqueous glycerine . . . .	76
4.12	Effective viscosity for neutrally buoyant particles in aqueous glycerine . . . .	77
5.1	Graph of the particle velocity obtained from optical probes mounted on the stationary inner cylinder . . . . .	82
5.2	Graph of the normalized particle velocity obtained from optical probes . . . .	83
5.3	Histogram of velocity fluctuations . . . . .	84
5.4	Standard deviation in particle velocity normalized by the mean value . . . .	85
5.5	Graph of the particle counts obtained from optical probes mounted on the stationary inner cylinder . . . . .	86
5.6	Volume fraction across the floating cylinder for various aqueous glycerine solutions . . . . .	87
5.7	Volume fraction across the floating cylinder as a function of the Reynolds number divided by the Archimedes number . . . . .	89
5.8	Shear stress measurements of polystyrene particles in varying concentrations of aqueous glycerine . . . . .	90
5.9	Ratio of measured-to-pure fluid torques of polystyrene particles in varying concentrations of aqueous glycerine . . . . .	92
5.10	Effective viscosity ratio as a function of the density of the interstitial fluid normalized by the particle density . . . . .	93
5.11	Effective viscosity ratio for both neutrally buoyant and non-neutrally buoyant experiments of polystyrene in aqueous glycerine solutions . . . . .	94
5.12	Coefficient of friction versus gap Reynolds number . . . . .	95

5.13	Coefficient of friction versus the gap Reynolds number divided by the Archimedes number . . . . .	96
5.14	Shear stress measurements for non-neutrally buoyant glass particles in aqueous glycerine . . . . .	97
5.15	Ratio of measured-to-pure fluid torque for non-neutrally buoyant glass particles in aqueous glycerine . . . . .	98
5.16	Shear stress measurements for non-neutrally buoyant polyester particles in aqueous glycerine . . . . .	99
5.17	Ratio of measured-to-pure fluid torques for non-neutrally buoyant polyester particles in aqueous glycerine . . . . .	100
5.18	Effective viscosity ratio for neutrally buoyant polyester particles in aqueous glycerine solutions . . . . .	101
5.19	Effective viscosity for all particles . . . . .	102
5.20	Effective viscosity for all particles compared with other experimental data . .	103
5.21	Theoretical curve fits for dilute particle concentrations . . . . .	104
5.22	Curve fits using experimentally determined fitting parameters . . . . .	106
6.1	Types of slip occurring near a smooth wall . . . . .	108
6.2	Typical depletion layer thicknesses . . . . .	109
6.3	Ratio of the apparent viscosity to the actual bulk viscosity for several depletion layer thicknesses . . . . .	113
6.4	Photograph of typical surface roughness . . . . .	115
6.5	Shear stress measurements for suspensions of polystyrene particles in aqueous glycerine with rough cylinder walls . . . . .	117
6.6	Ratio of measured torque to pure fluid torques for suspensions of polystyrene particles in aqueous glycerine with rough cylinder walls . . . . .	118
6.7	Effective viscosity ratio for neutrally buoyant polystyrene particles in aqueous glycerine solutions with rough cylinder walls . . . . .	120
6.8	Depletion layer thicknesses calculated from apparent and actual viscosity measurements . . . . .	121
6.9	Particle velocities and apparent viscosities as used to find the depletion gap thickness . . . . .	122

6.10	Depletion layer thickness calculated from the velocity measurements shown as a function of the Reynolds number . . . . .	123
6.11	Depletion layer thickness calculated from velocity measurements . . . . .	124
6.12	Particle velocity near the stationary wall for smooth and rough walls . . . . .	125
6.13	Smooth wall data corrected for the presence of particle depletion layers . . . .	127
7.1	Phase diagram for fluid-particulate flows showing delimitations in the vol- ume fraction and Reynolds number . . . . .	131





# List of Tables

1.1	Previous experiments on non-Brownian shear flows . . . . .	14
2.1	Random close-packing volume fraction . . . . .	25
2.2	Random loose-packing volume fraction . . . . .	26
2.3	Random packing volume fractions for current particles . . . . .	32
2.4	Previous experiments of non-Brownian shear flows . . . . .	33
3.1	Dimensions and properties of the rotating cylinder rheometer . . . . .	39
3.2	Properties for experiments . . . . .	53
B.1	Drawings . . . . .	147



# Nomenclature

## Greek Characters

$\beta$	Volume quality
$\dot{\gamma}$	Shear rate of the interstitial fluid
$\delta$	Perturbation in the diameter of a nearly spherical particle
$\mu$	Viscosity of the interstitial fluid
$\mu'$	Effective viscosity for the fluid-solid mixture
$\rho_f$	Density of the interstitial fluid
$\rho_p$	Particle density
$\tau$	Shear stress for the fluid-solid mixture, usually as measured on the inner, floating cylinder
$\phi$	Volume fraction of solids
$\phi_c$	Volume fraction of solids at random close-packing
$\phi_l$	Volume fraction of solids at random loose-packing
$\Omega$	Angular velocity of outer rotating cylinder

## Latin Characters

$A_p$	Surface area of an individual particle
$Ar$	Archimedes number, $Ar = gd^3 \rho_f   \rho_p - \rho_f   / \mu^2$
$b$	Annular gap width, $b = r_o - r_i = 3.15 \text{ cm (1.24 in)}$

$Ba$	Bagnold number, $Ba = \lambda^{\frac{1}{2}} \rho_p d^2 \dot{\gamma} / \mu$
$C_f$	Coefficient of friction, $C_f = 4\tau / (\rho_f \dot{\gamma} b^2)$
$C_i$	Displacement fit coefficients
$D$	Spring displacement
$d$	Particle diameter
$d_{large}$	Largest measured particle diameter
$d_{small}$	Smallest measured particle diameter
$E$	Voltage measured from the optical displacement probes
$g$	Gravitational acceleration, $g = 9.81 \text{ m/s}^2$
$H$	Height of the floating cylinder, $H = 11.22 \text{ cm (4.42 in)}$
$h$	Height of the annulus, $h = 36.98 \text{ cm (14.56 in)}$
$k$	Boltzmann constant
$L$	Average particle separation
$l$	Particle length for cylindrical particles
$M$	Torque generally or as measured on the inner, floating cylinder
$M_{fluid}$	Torque calculated using the fluid viscosity
$n$	Number of particles per unit time
$p$	Pressure for the fluid-solid mixture
$Pe$	Péclet number, $Pe = 3\pi\mu d^3 \dot{\gamma} / 4kT$
$r$	Radial coordinate
$Re$	Reynolds number, $Re = \rho_f \dot{\gamma} d^2 / \mu$
$Re'_b$	Effective gap Reynolds number, $Re'_b = \rho \dot{\gamma} b^2 / \mu'$

$Re_b$	Gap Reynolds number, $Re_b = \rho_f \dot{\gamma} b^2 / \mu$
$r_i$	Radius of the inner drum, $r_i = 15.89$ cm (6.26 in)
$r_o$	Radius of the outer drum, $r_o = 19.05$ cm (7.50 in)
$St$	Stokes number, $St = \rho_p \dot{\gamma} d^2 / (9\mu)$
$\mathbf{T}$	Effective stress tensor for the fluid-solid mixture
$T$	Temperature
$u$	Particle velocity
$V$	Velocity of the outer, rotating cylinder
$V_p$	Volume of an individual particle
$v_{slip}$	Slip velocity, $v_{slip} = V - u$

# Chapter 1

## Introduction

Fluid-solid flows are observed in a variety of fields ranging from mining operations to the erosion of the Martian landscape. Particulate flows help polish and cut metals in manufacturing practices, but are also associated with the rapid deterioration of industrial components. The mechanics of particulate flows cause dune formation and determine the damage caused by a landslide. These are just a few examples of the vast range of fluid-solid material flows of interest to engineers and scientists.

The rheology of granular flows was first studied by Bagnold (1954, 1956). In this groundbreaking work, Bagnold investigated the effect of particulates on the pressure and shear forces in a coaxial rheometer. Bagnold concluded that there was a transition – characterized by the ratio of the inertial stress to the viscous stress, now called the Bagnold number – from the “macro-viscous region” where the shear stress and the pressure grow linearly with shear rate, to the fast “grain-inertia region” where shear stress and pressure grow quadratically with the shear rate. Later analysis by Hunt et al. (2002) found that Bagnold’s experiments were marred by the presence of secondary vortices and the boundary layer on the top and bottom annular end caps. Additional work by Chen and Ling (1996) found that the higher volume fractions tested by Bagnold ( $\phi = 0.606$  and  $\phi = 0.623$ ) were inconsistent with the lower volume fractions due to particle slip against the cylinder walls.

This thesis is part of an effort to establish a base of rheological data for fluid-solid flows. In the following section (section 1.1), fluid-particulate flows is described in more detail, highlighting the specific assumptions and parameters, which characterize these flows. Following that explanation, a portion of the previous experiments conducted on these flows is highlighted in section 1.2.

## 1.1 Flow regimes

In general, fluid-solid flows are associated with the movement of particles through an interstitial fluid where the viscous effects of the fluid, the inertia of the fluid and particles, and the collisions between particles all contribute to the mechanics. In addition to these mechanisms, additional forces associated with many particles in the fluid (e.g. lift, drag, added mass) may also significantly change the mechanics of the flow.

To investigate the nature of these fluid particulate flows, particles with diameter  $d$  and density  $\rho_p$  are placed in a Couette flow device consisting of two concentric cylinders (with shear rate  $\dot{\gamma}$  and gap width  $b$ ) filled with a Newtonian fluid with viscosity  $\mu$  and density  $\rho_f$ . This fluid-solid flow can be characterized by an effective stress tensor  $\mathbf{T}$  composed of shear stress  $\tau$  and pressure  $p$ . To simplify the form of the stress tensor, it is hypothesized that the fluid-solid mixture is also Newtonian, thus

$$\tau = \mu' \dot{\gamma}, \quad (1.1)$$

where  $\mu'$  is the effective viscosity of the fluid-solid mixture. This effective viscosity depends on the properties of the fluid, the properties of the solid, the fluid shear rate, the gap width, the volume fraction of solids  $\phi$ , and thermal energy  $kT$ :

$$\mu' = f(\mu, \rho_f, \rho_p, d, g, \dot{\gamma}, b, \phi, kT). \quad (1.2)$$

Reducing this dependance to non-dimensional parameters,

$$\frac{\mu'}{\mu} = f\left(\phi, \text{Re}, \text{Pe}, \text{Ar}, \frac{\rho_p}{\rho_f}, \frac{d}{b}\right), \quad (1.3)$$

where the Reynolds number, the ratio of fluid inertial force to the fluid viscous force, is defined by

$$\text{Re} = \frac{\rho_f \dot{\gamma} d^2}{\mu}, \quad (1.4)$$

for a Couette flow. The Reynolds number is an indicator for the onset of turbulence and the existence of secondary flows. The Peclet number, the ratio of particle advection to thermal diffusion, is defined by

$$\text{Pe} = \frac{3\pi\mu d^3 \dot{\gamma}}{4kT}. \quad (1.5)$$

The Archimedes number

$$\text{Ar} = \frac{gd^3 \rho_f |\rho_p - \rho_f|}{\mu^2}, \quad (1.6)$$

describes the ratio of gravitational forces to viscous forces. The remaining non-dimensional parameters are  $\rho_p/\rho_f$ , the ratio of the particle-to-fluid density, and  $d/b$ , the ratio of the particle diameter to the gap width.

The equation for the effective viscosity, equation (1.3), can be simplified by employing a few key assumptions. In the following subsections, several of these assumptions are discussed in more detail.

### 1.1.1 Continuum assumptions

Inherent in the examination of bulk fluid properties is the assumption that the flow is a continuum: enough particle-particle and particle-wall collisions occur during a measurement so that their effect is averaged. Furthermore, it is argued that the results are not affected by the presence of the cylinder walls. For the continuum assumption to hold, limits must be placed on the volume fraction of particles  $\phi$  and on the ratio of gap width to particle diameter,  $b/d$ . The volume fraction must be large enough so that, over the time of the experiments, a sufficient number of particle collisions occur. In the present experiment, the volume fraction of solids was larger than 0.05, for which the continuum assumption should hold.

Appropriate limits on the ratio of gap width to particle diameter are more difficult to determine. The slip of particles against the cylinder walls causes a lower effective shear rate within the bulk of the fluid-particulate mixture. A general rule for experiments with suspensions of particles in a fluid is that the gap width must be at least 10 times the particle diameter (Barnes 1995). In the current experiments, the ratio  $b/d$  is often close to this limit of 10 (e.g. 9.5 for the polystyrene particles). The nature of slip on the outer walls and its influence on shear stress measurements are discussed in chapter 6.

The presence of the outer walls can also change the maximum obtainable volume fractions; particles tend to arrange themselves in an ordered, lower volume fraction pattern near the container walls. If the container is small, the total volume consumed by this ordered arrangement can significantly affect the total volume fraction. To compensate for this source of error, the random packing of particles is measured in box with a gap equal



to the gap between the concentric cylinders. (The height and width of the box are much greater than the gap and should not change the volume fraction). See section 2.2 for a detailed discussion of this behavior.

### 1.1.2 Secondary flows

The radial inertia due to a rotating flow can induce a radial velocity in the fluids and particles. At low Reynolds numbers, the viscosity can suppress this radial velocity, but as the Reynolds number increases, Taylor vortices develop. As with single component flows, secondary flows and turbulence can develop in fluid-particulate flows. In a concentric cylinder Couette flow where the outer rotates and the inner cylinder is held stationary, secondary flows are present in the form of Taylor vortices and the boundary layer flows near the end caps. These secondary flows increase the shear stress on the cylinder walls and, without correction, can yield a higher effective viscosity than without these effects.

The growth of Taylor vortices depends on the geometry of the annular gap as well as the rotational velocity of both the inner and outer cylinders. Even in the case of a granular flow, where the fluid effects are negligible, Taylor-like vortices develop at a slightly lower Reynolds number than in the fluid case (Conway et al. 2004). The vortices develop at a much lower Reynolds number for a Couette flow with the inner cylinder rotates than for a flow where the inner cylinder is fixed and the outer cylinder rotates. The data obtained by Taylor (1936a,b), shown in Figure 1.1, shows this trend very clearly. As the gap width  $b$  is increased relative to the inner cylinder radius  $r_i$ , the critical Reynolds number for the onset of Taylor-Couette vortices decreases for inner rotating Couette flows and increases for outer rotating Couette flows. The presence of Taylor-Couette vortices can greatly increase the observed torque in a nonlinear manner, as shown in Figure 1.2. Even small errors in the Reynolds number can lead to large changes in the pure fluid torque. The effective viscosity of the fluid-particulate mixture is calculated relative to pure fluid viscosity through the normalization of the measured to pure fluid torque. Through this normalization, small uncertainties in the Reynolds number can create significant errors in the normalized effective viscosity measurement. Due to this possible error, care is taken to avoid Taylor-Couette flows in the present experiment.

Secondary flows are also present near the end caps at the top and bottom of the an-

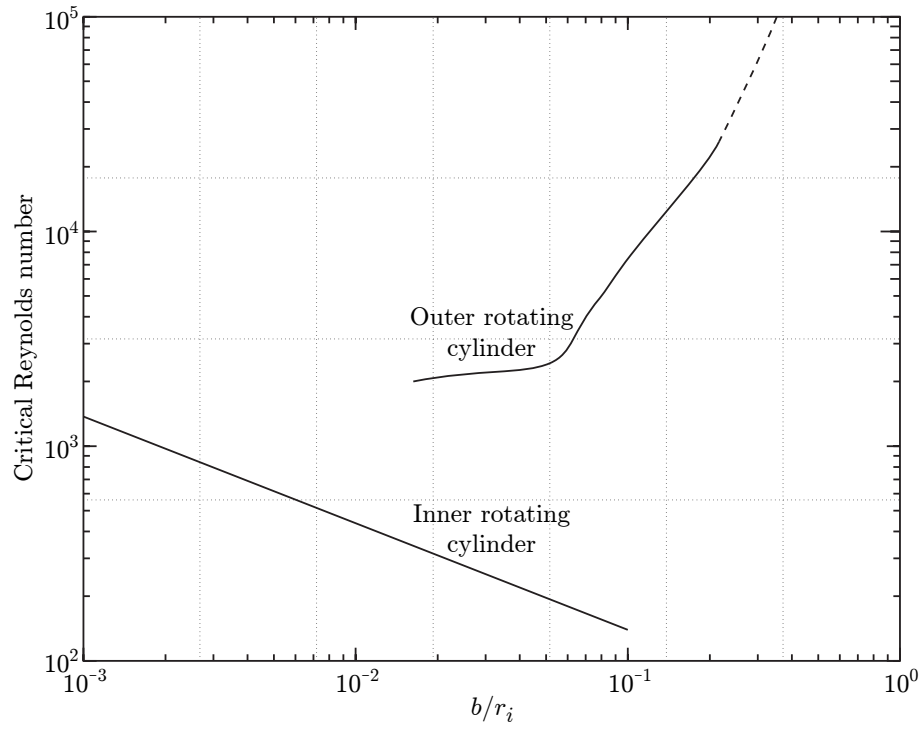


Figure 1.1. Critical Reynolds number for the onset of Couette-Taylor flow for both inner and outer rotating cylinders as a function of the ratio of gap width to inner radius. (Taylor 1936a).

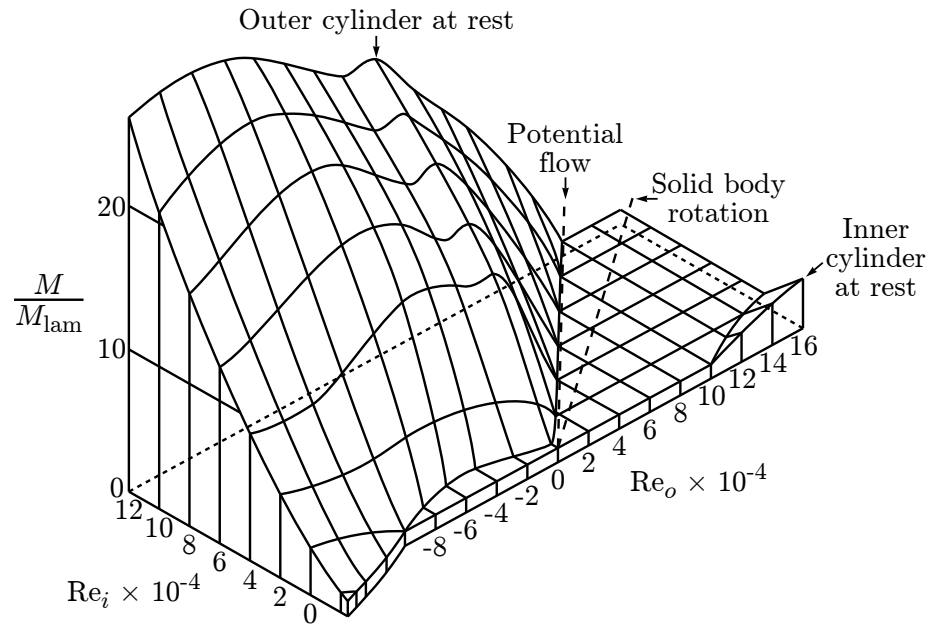


Figure 1.2. Increase in torque for inner and outer rotating Couette flows for  $b/r_i = 0.176$  (Coles 1965).

nulus. The inertial opposition to the centripetal acceleration is balanced by a pressure gradient in the center of the flow. An axial gradient exists near the end caps due to the non-slip condition, which disrupts the pressure gradient. This resultant force near the end caps drives a radial flow close to the boundary (Czarny et al. 2003). When the end caps are fixed, these boundary layers are termed Bödewadt flows, or termed Ekman boundary layers when the end caps and flow are rotating at different angular velocities (Lingwood 1997). As the rate of rotation increases, the boundary layers decrease in size but increase in strength, inducing counterrotating recirculation cells. These cells grow with the increasing Reynolds number until they eventually meet at the midplane. The boundary layer and its accompanying recirculation cell has an increasing influence on the torque measurements.

The influence of particles on the development or strength of secondary flows is another source of uncertainty. Experimental results summarized in Gore and Crowe (1991) show that turbulence is strengthened by small particles and attenuated by large particles. This attenuation is due in part to particle-fluid and particle-particle-fluid coupling, the magnitude of which is influenced by the volume fraction of particles (Elghobashi 1994). These two effects are summarized in the data from Matas et al. (2003), which looks at the critical Reynolds number for the onset of turbulence in horizontal pipe flow (Figure 1.3). A similar influence of the volume fraction is expected for the initiation of Taylor vortices or on boundary layer flows. The effect of particles on secondary flows is difficult to estimate, making comparisons between single phase experiments at the same Reynolds number problematic. The added complexity caused by these secondary flows should be avoided.

### **1.1.3 Diffusion and Brownian motion**

The diffusion of particles in a fluid is governed by advection, particle interactions, and thermal diffusion. Advection – diffusion caused by a fluid velocity gradient – depends on how quickly the Couette flow is being sheared; diffusion due to particle interactions is a function of the volume fraction of particles in the fluid; thermal diffusion is a function of the fluid temperature. Diffusion always occurs, but the dominant type of diffusion may change.

Thermal diffusion is caused by Brownian motion: the random movement of particles suspended in a fluid due to colliding, thermally excited atoms and molecules. As the tem-

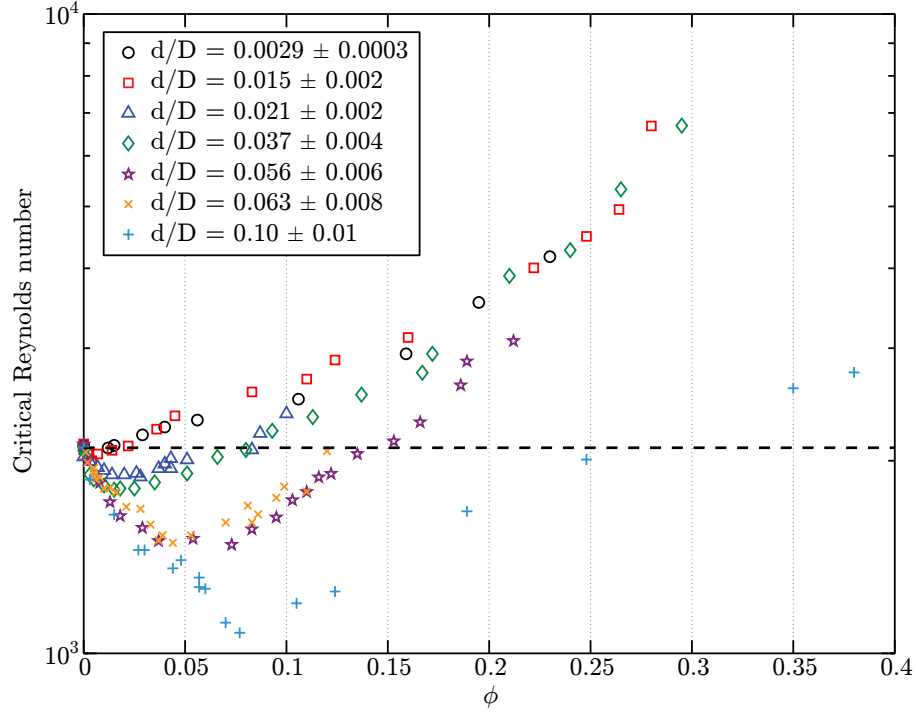


Figure 1.3. Critical Reynolds number for the onset of turbulence in pipe flow as a function of the volume fraction of solids  $\phi$  and the ratio of particle diameter to pipe diameter  $d/D$ . Turbulence is delayed for smaller particles and high volume fractions (Matas et al. 2003).

perature increases and as the particle diameter decreases, the Brownian motion of particles becomes more pronounced. At room temperature, particles with diameters smaller than 100  $\mu\text{m}$  show clear Brownian motion while particles with diameters greater than 1 mm do not. The ratio of advection to thermal diffusion is termed the Peclet number (equation (1.5)). For processes with Peclet numbers that are very large ( $Pe \rightarrow \infty$ ), the system is not subjected to Brownian diffusion. Generally, systems with  $Pe \gtrsim 10^3$  are considered non-Brownian (Stickel and Powell 2005). In all of the experiments considered in this thesis, the particle sizes are large enough and the fluid is moving sufficiently quickly that the flows are considered non-Brownian. Then, the effective viscosity depends only on the other non-dimensional parameters,  $\frac{\mu'}{\mu} = f\left(\phi, Re, Ar, \frac{\rho_p}{\rho_f}, \frac{d}{b}\right)$ .

The presence of diffusion based on particle interactions can also influence the effective viscosity of the flow. As the volume fraction increases, particle-particle collisions become increasingly frequent and exhibit a dominant behavior in the dynamics of the flow. Above a critical volume fraction  $\phi_{\text{crit}}$ , collisional diffusion dominates over advection. The exact criterion of the transition between a region of continuous particle interactions and non-

collisional flows is currently unclear and one of the goals of this thesis is to determine this transition. A further discussion of the transition toward the continuous contact regime can be found in chapter 2.

#### 1.1.4 Phase diagrams

Since Bagnold (1954, 1956) first explored fluid particulate flow in his concentric Couette experiment, other researchers have looked at different aspects of these flows. Generally, these experiments can be placed in several categories. The most basic differentiation of these categories is shown in Figure 1.4(a), which shows the phase diagram of volume fraction and of Archimedes number relative to the Reynolds number. The continuous contact

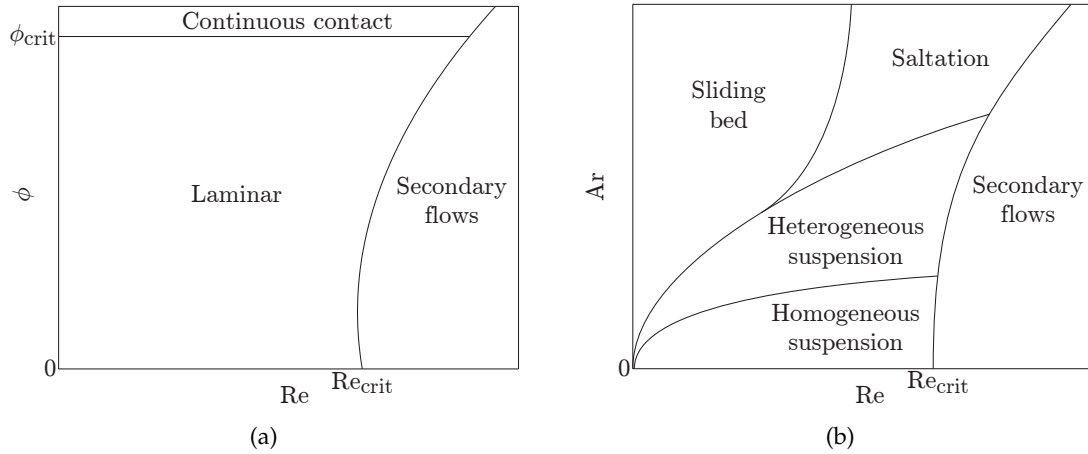


Figure 1.4. Phase diagram for non-Brownian fluid-particulate flows. As a function of the Reynolds number, the influence of (a) volume fraction and (b) Archimedes number are shown on the behavior of the flow. These figures are based on the work of Coussot and Ancey (1999) and King (2001).

regime comprises flows where the particles are always in contact and collisional diffusion dominates over advection. Above a critical Reynolds number, secondary flows are present. These secondary flows greatly complicate the flow behavior and can contribute to a higher observed torque. Since the particles can alter these secondary flows, comparisons between single phase and particle laden cases are complicated. This regime is avoided in this thesis. The third region comprises laminar flow without secondary flows where advection dominates.

Variations in the Archimedes number, as seen in Figure 1.4(b), can also be significant to

the behavior of the fluid-particulate flow. As the density difference between the particles and fluid is increased, the Archimedes number increases and a higher Reynolds number is required to fluidize the bed (Bi and Fan 1992; King 2001). Particle mixtures undergoing saltation or in a heterogeneous suspension show variations in the local volume fraction in the axial direction. A variation in the effective viscosity, due to this volume fraction gradient, can complicate the dynamics of the flow. In the present experiments, when the particle density and fluid density were not matched (chapter 5), the volume fraction was measured locally. Thus, if the particles are not in a homogeneous mixture, the effective viscosity can be correlated directly with the local volume fraction.

In addition to the phase diagram for variations in the volume fraction and Archimedes number, variations in Peclet number can also be considered. For low Peclet numbers, the flow is Brownian and thermal diffusion dominates. As the Peclet numbers for the experiments discussed in the following chapters are all much larger than unity, any rheological effects in this region are small and are neglected.

### 1.1.5 Particle interactions

Individual interactions between two colliding particles can vary dramatically based on the relative inertia of the particles and the elasticity of the particles. Particle collisional behavior is characterized by the Stokes number, which describes the ratio of particle inertia to fluid viscous forces,

$$St = \frac{\rho_p u_{rel} d}{9\mu} \quad (1.7)$$

(Joseph and Hunt 2004; Joseph et al. 2001). For shear flows, the relative velocity between two adjacent particles is approximately equal to the shear rate times the distance between the two particle centers. This separation between two adjacent particles is close to particle diameter. The Stokes number for this flow is related to the Reynolds number by

$$St = \frac{\rho_p \dot{\gamma} d^2}{9\mu} \quad (1.8)$$

$$= \frac{1}{9} \frac{\rho_p}{\rho_f} Re. \quad (1.9)$$

For collisions against a wall, solid, rigid particles showed no rebound for a Stokes num-

ber less than about 10 (Joseph and Hunt 2004; Joseph et al. 2001). For collisions between two particles, a Stokes number based on the relative velocities between the two particles is chosen. As shown in Yang (2006); Yang and Hunt (2006), for small Stokes numbers ( $St \lesssim 2$ ), the slow particle began to move as the fast particle approached and there was no clear collision. For slightly larger Stokes numbers ( $St \approx 3 - 9$ ), there was a clear collision, but no rebound: the two particles travel as a single composite particle following the collision. At larger Stokes numbers, there was a clear rebound between the two particles. For oblique collisions, the normal collisional interaction proceeds just as described above, but the ratio of incident to rebound angle vary with Stokes number.

The collision of a particle with either a wall or a second particle is associated with energy dissipation due to the inelasticity of the contacts. This energy dissipation is described by the coefficient of restitution: the ratio of the rebound velocity  $v_r$  to the incident velocity  $v_i$ ,

$$e = -\frac{v_r}{v_i} \quad (1.10)$$

for a collision against a stationary wall. For a collision between a second particle, the relative velocities must be used. The coefficient of restitution, which must be a function of Stokes number and the properties of the two materials as is shown in Ruiz-Angulo (2008). For steel particles against a Zerodur wall, where both the wall and particles have high Young's moduli, the coefficient of restitution is well described by the empirical fit

$$e = 1 - \frac{8.65}{St^{0.75}} \quad (1.11)$$

as shown in Joseph (2003) and represents the elastic limit. For collisions involving greater plastic deformation, the coefficient of restitution will decrease. The elastic velocity is defined as

$$u_{el} = \frac{\pi^2}{2E^{*2}\sqrt{10\rho_p}}(1.65Y)^{5/2} \quad (1.12)$$

where  $Y$  is the yield strength and  $E^*$  is the reduced modulus, defined as  $E^* = [(1 - \nu_1^2)/E_1 + (1 - \nu_2^2)/E_2]^{-1}$ , which depends on the Young's modulus for each material  $E_i$  as well as Poisson's ratio  $\nu_i$ . For particle-particle collisions within the fluid, the two materials are identical and  $E^* = E/[2(1 - \nu^2)]$ . If the impact velocity is greater than the elastic velocity, deformation will occur. The elastic properties of each particle used are summarized in

section 3.3. For the materials used and the range of Stokes numbers tested, a reduction of less than 10% in the coefficient of restitution will occur.

## 1.2 Previous experiments

Bagnold (1954) first experimented with the rheology of fluid-particulate flows and proposed a non-dimensional number to govern variations between a rapidly sheared, high volume fraction region and a slow, low volume fraction region. The Bagnold number,

$$\begin{aligned} \text{Ba} &= \frac{\lambda^{\frac{1}{2}} \rho_p d^2 \dot{\gamma}}{\mu} \\ &= f(\phi) \text{Re} \frac{\rho_p}{\rho_f} \end{aligned} \quad (1.13)$$

is the product of the Reynolds number, the ratio of densities, and a function of the volume fraction. This “linear concentration,”  $\lambda$ , is a function of the volume fraction and the maximum obtainable volume fraction  $\phi_c$ ,

$$\lambda = \frac{1}{(\phi_c/\phi)^{1/3} - 1}. \quad (1.14)$$

Bagnold (1954, 1956) proposed that small Bagnold numbers represented a “macro-viscous” regime where the flow behaves like a Newtonian fluid and is considered non-collisional. In this region, the shear stress grow linearly with shear rate. On the other hand, the shear stress grows quadratically with shear rate in the “grain-inertia” regime at large Bagnold numbers. While the Bagnold number has been used to distinguish the transition between the non-collisional and continuous contact regimes, the transition observed by Bagnold was caused by the Reynolds number rather than volume fraction. The experiments of Bagnold (1954, 1956) were marred by the presence of secondary flows, as described in Hunt et al. (2002), which accounts for the transition in behavior Bagnold observed.

Bagnold’s apparatus, shown in Figure 1.5, was a Couette flow rheometer with the inner cylinder fixed and the top, bottom, and outer portions rotating. Liquid was allowed to fill the top and bottom gaps while particles were confined to the annulus using a knife-edge. The apparatus had a height to gap ratio ( $h/b$ ) of 4.6 and a ratio of gap to outer diameter ( $b/r_o$ ) of 0.189. The critical Reynolds number for the onset of Couette-Taylor flow for a



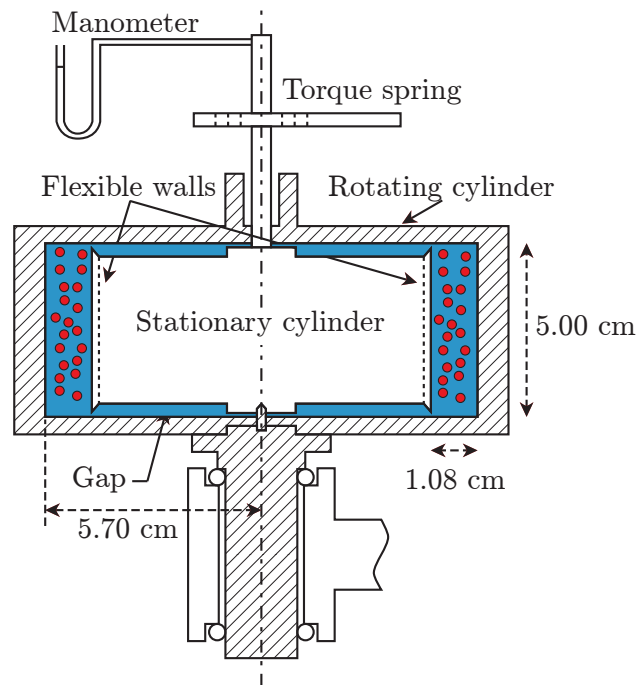


Figure 1.5. Cross-sectional view of the experimental apparatus used in Bagnold (1954, 1956). The thatched portions represent the rotating outer cylinder while the white portions represent stationary inner cylinder. Portions of the apparatus filled with fluid are represented in blue.

flow with these dimensions was approximately 18,000, well below the maximum operating gap Reynolds number of 33,000 (Hunt et al. 2002; Taylor 1936a,b). Secondary flows were present for some of Bagnold's experiments and accounted for the sharp increase in torque.

In addition to secondary flows in the annulus, the presence of fluid in the top and bottom gaps posed a complication. Using Bagnold's original data, Hunt et al. (2002) found that in the grain-inertia region, the normalized shear stress was best matched by the empirical relation:

$$\frac{\tau \rho_p d^2}{\mu^2 \lambda} = 0.35 \text{Ba}^{1.48}. \quad (1.15)$$

A laminar boundary layer induced by a spinning disk yields a torque of

$$M_{bl} \approx -4\pi \int_{r_i}^{r_o} r^2 \tau dr \approx 0.616\pi\rho \left( \frac{\mu\omega^3}{\rho} \right)^{1/2} (r_o^4 - r_i^4), \quad (1.16)$$

where  $\omega$  is the angular rotation rate of the disk (Schlichting 1951). This yields a shear stress that depends on the shear rate to the 3/2 power – very close to the 1.48 power of equation (1.15). Hunt et al. (2002) concluded that the transition observed between the macro-viscous and grain-inertia regions was not a transition in the fluid-particulate flow, but a Reynolds number effect where the flow became dominated by the laminar boundary layer present at the end caps and in the gaps.

Additionally, work by Chen and Ling (1996), found that the higher volume fractions tested by Bagnold ( $\phi = 0.606$  and  $\phi = 0.623$ ) were inconsistent with the lower volume fraction data. They hypothesized that this was due to the increase in particle slip against the cylinder walls. Thus only a portion of Bagnold's data – namely the low Reynolds number data – can be used as a comparison with the experiments presented in this thesis.

The rheology of fluid-solid flows using particles that are unaffected by Brownian motion were later studied by others: Acrivos et al. (1994); Hanes and Inman (1985); Savage and McKeown (1983); and Prasad and Kytömaa (1995), as shown in Table 1.2 and Figure 1.6.

### 1.2.1 Secondary flows

In addition to the the data of Bagnold (1954, 1956), the experiments of Savage and McKeown (1983) using an inner rotating concentric cylinder device (shown in Figure 1.7) were

Table 1.1. Previous experiments on non-Brownian shear flows.

Solid	d (mm)	Liquid	$\rho_p/\rho_f$	Type of Rheometer
Bagnold (1954, 1956) 50% paraffin wax and lead stearate	1.32	water	1.0	concentric cylinder, inner, top & bottom rotating
Savage and McKeown (1983)	0.97			
polystyrene	1.24 1.78	salt water	1.00	concentric cylinder, inner rotating
Hanes and Inman (1985)	1.1		2.48	
glass beads	1.85	water	2.78	annular gap, inner, outer & bottom rotating
Acrivos et al. (1994)				
PMMA <sup>a</sup>	0.1375	aqueous glycerine	1.00	Couette double gap, center rotating
acrylic	0.0905	Dow Corning FS-1265	0.95	
Prasad and Kytömaa (1995)				
acrylic	3.175	aqueous glycerine	1.12	annular gap, bottom rotating

<sup>a</sup>polymethyl methacrylate

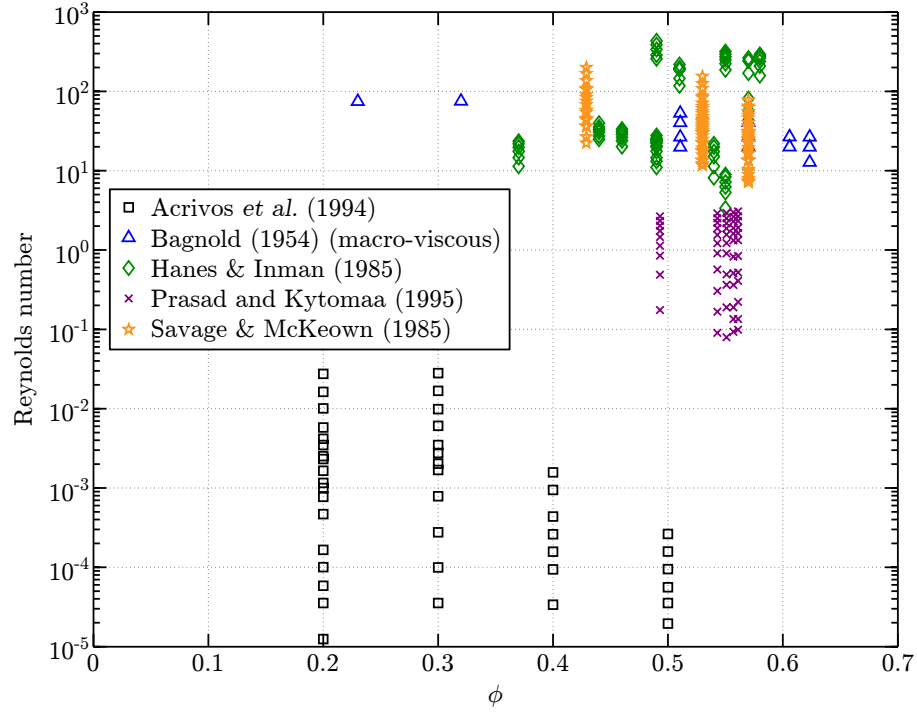


Figure 1.6. Reynolds number-volume fraction phase diagram of previous experiments. All of the data summarized in Table 1.2 is shown with the exception of the high Reynolds number data of Bagnold.

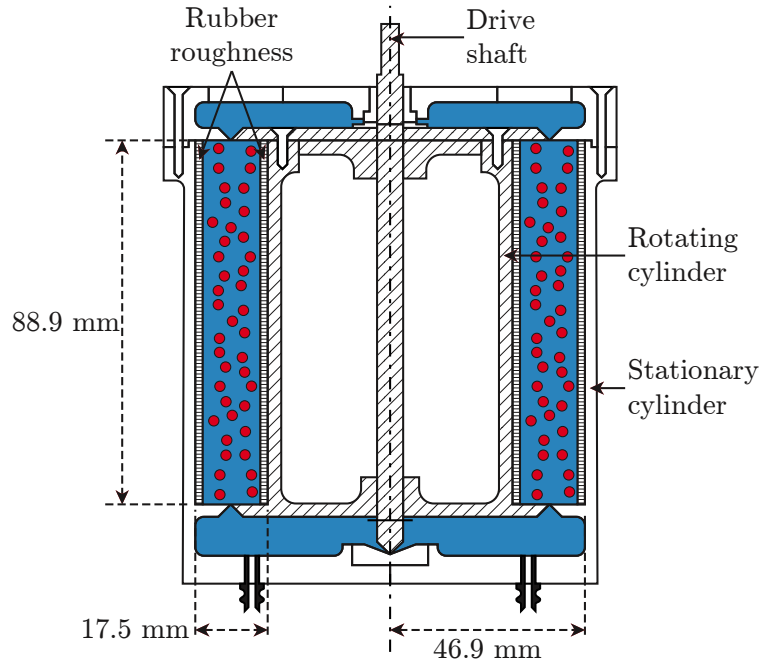


Figure 1.7. Cross-sectional view of the experimental apparatus used in Savage and McKeown (1983). The hatched portions represent the rotating inner cylinder while the white portions represent stationary outer cylinder. Portions of the apparatus filled with fluid are represented in blue.

affected by secondary flows. The pure fluid calibration for this apparatus showed evidence of Taylor-Couette flow and was nonlinear over the range of shear rates used. In their paper, Savage and McKeown (1983) normalized particle laden torques by the pure fluid torque measured at that shear rate without regard to the possible changes induced in the flow due to the particles. Their hypothesis was that the presence of non-zero concentrations would not significantly change the flow behavior, but as discussed in subsection 1.1.2, the presence of particles can either increase or decrease secondary flows. If the secondary flows increase in intensity at low volume fractions (as shown by Matas et al. 2003), the actual effective viscosity is lower than the measured value. For high volume fractions, the intensity of secondary flows is expected to decrease, increasing the effective viscosity. The degree to which the effective viscosity should be adjusted is difficult to estimate, however, without confirmation as to the type of Taylor-Couette flow present in the fluid-particulate cases or the strength of boundary layer flows. As no flow visualization or velocity measurement techniques were employed by Savage and McKeown (1983), their data is omitted when direct comparisons are made with the experimental data measured in this thesis.

### 1.2.2 Non-neutrally buoyant particles

In the present thesis, experiments with both neutrally buoyant and non-neutrally buoyant particles were conducted. As discussed in subsection 1.1.4, the mixing of particles is controlled by the Archimedes number, which depends on the difference in density between the particles and the fluid. Additionally, the flow may depend on the ratio of the densities,  $\rho_p/\rho_f$ . To avoid misinterpretations, the present neutrally buoyant experiments will only be compared with the neutrally buoyant experiments of Bagnold (1954, 1956) and Acrivos et al. (1994) in chapter 4. In chapter 5, the non-neutrally buoyant data of Acrivos et al. (1994), Hanes and Inman (1985), and Prasad and Kytömaa (1995) is matched with the non-neutrally buoyant data described in that chapter. A summary of all of the previously published experiments can be found in Table 1.2.

The experiments of Hanes and Inman (1985) were conducted in an annular, configuration where the sides and bottom rotated as shown in Figure 1.8(a). The top did not rotate, but was allowed to displace upwards as result of of the normal stress generated by the mixture. Volume fractions between 0.55 and 0.59 were recorded for the range of normal

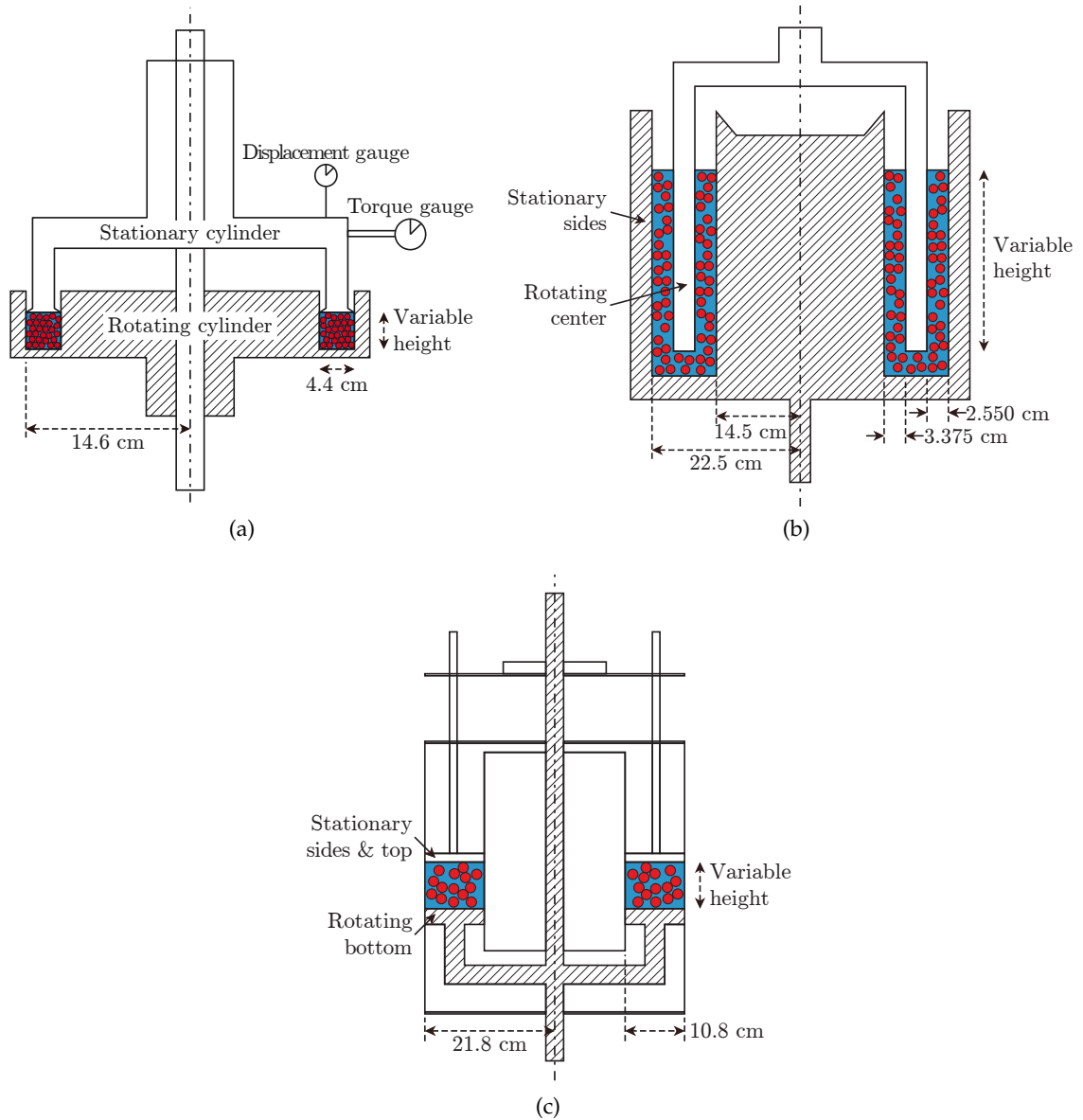


Figure 1.8. Cross-sectional view of the experimental apparatus used in (a) Hanes and Inman (1985), (b) Acrivos et al. (1994), and (c) Prasad and Kytömaa (1995). The thatched portions represent the rotating inner cylinder while the white portions represent stationary outer cylinder. Portions of the apparatus filled with fluid are represented in blue.

stresses used. The experiments used glass beads of two sizes in both water and air. Only the experiments in water are reported in this thesis. With the glass beads in water, the ratio of particle-to-fluid densities ranged from 2.48 to 2.78.

The non-neutrally buoyant experiments of Acrivos et al. (1994) used acrylic particles that were nearly neutrally buoyant; the particles were lighter than the fluid by only 5%. Volume fractions ranging from 0.2 to 0.5 were tested using the non-neutrally buoyant particles. (The neutrally buoyant polymethyl methacrylate experiments were limited to volume fractions of 0.2 and 0.3.) These experiments were conducted using a configuration Acrivos et al. (1994) termed the Couette double gap, wherein a rotating cylinder piece was lowered into a cup containing the particles and fluid (Figure 1.8b). The top was left as a free surface.

Using an annular gap where the bottom was allowed to rotate and the top and sides remained fixed (Figure 1.8c) Prasad and Kytömaa (1995) measured the effective viscosity of acrylic particles in an aqueous glycerine mixture. The top of this apparatus could be moved up and down (around  $h = 3$  cm) to vary the volume fraction between 0.49 and 0.56. Acrylic beads with  $\rho_p/\rho_f = 1.12$  were used in these experiments.

### 1.3 Thesis outline

The goal of the research documented in this thesis is to investigate the bulk behavior in flows composed of solid particles immersed in a fluid. Emphasis has been placed on measuring the effective viscosity of these flows at a constant shear rate as a function of the volume fraction of solids, size and shape of the solid particles, and the roughness of the exterior boundaries. A summary of other notable experiments investigating the effective viscosity of fluid-particulate flows was presented above.

The behavior of fluid-particulate flows is heavily influenced by the volume fraction of solids; it becomes more difficult for particles to move past their neighbors when the volume fraction nears maximum packing. This maximum packed state and another parameter, the loose-packed volume fraction, are considered in chapter 2. In addition to the effect of these volume fractions on the viscosity, methods for determining these volume fractions and actual measurements are also discussed in section 2.2 and section 2.3, respectively.

The work presented in this thesis is largely experimental and the experimental apparatus used is presented in chapter 3. Specific techniques used and the method for data pro-

cessing are discussed in section 3.2 with the data processing code included in appendix A. Five different particles were used in these experiments, the properties of which are discussed and characterized in section 3.3.

Experiments were conducted using neutrally buoyant particles (chapter 4) and non-neutrally buoyant particles (chapter 5). In both cases, the theory and expected results are presented first, followed by the experimental data, and followed by a summary of the results. Polystyrene has a density close to that of water allowing it to be used for both the neutrally buoyant and non-neutrally buoyant experiments. Since this is the case, the results with polystyrene particles are discussed first in both sections and in more detail.

Experiments using smooth walls in the Couette device are subject to the effects slip at the walls. Apparent slip is associated with a thin particle-free layer near the smooth walls. The influence of this particle-free layer on the measurements of the effective viscosity and particle velocities near the wall are discussed in chapter 6.

Finally, in chapter 7, a summary of the experimental results is presented. This summary is accompanied by several conclusions and a comparison with previously published data.





## Chapter 2

# Packing

The packing of particles in rigid containers is dependent on the shape of the particles, how the particles are configured, and on the size and shape of the container. Randomly packed particles generally fall between two well-defined limits: random loose-packing (RLP)  $\phi_l$ , where the particles are allowed to gradually come to rest against each other, and random close-packing (RCP)  $\phi_c$ , where the particles are compressed, generally through gentle shaking (Scott 1960). These two packing methods are highly repeatable – generally only varying by a few percent. The two random packed volume fractions have different implications for the flow properties as outlined in section 2.1.

One key feature of these packing states is their random nature: in the bulk of the material, there should be no short- or long-range ordering of particles. In a particulate flow, as exists in the present experiment, the particles are allowed to arrange themselves and do so in a semi-random nature. In the center of the flow, the particles should be randomly arranged, but near the walls of an enclosing container, the particles show a greater degree of order due to the influence on the walls. Near the walls, the measured volume fraction is different than in the bulk of the flow (see section 2.2).

The random packing volume fractions must be measured for each type of particle used in the present experiments or estimated for the previously published experiments. Measurements of the RCP and RLP for the current particles were conducted in a rectangular container with a width equal to the gap in the concentric cylinder rheometer. These measurements are highlighted in subsection 2.3.1. For the previously published data, the RCP is usually recorded from which the RLP can be estimated (subsection 2.3.2).

## 2.1 Implications for the effective viscosity

The effective viscosity for fluid-particulate flows is influenced by the volume fraction of particles,  $\phi$ . Specifically, these flows are influenced by the ratio of the volume fraction to the random loose-packing  $\phi/\phi_l$ , or to random close-packing  $\phi/\phi_c$ . As  $\phi/\phi_l$  nears unity, the number of particle collisions greatly increase and becomes a dominant force represented as a dramatic increase in the effective viscosity (subsection 2.1.1). As  $\phi/\phi_c$  nears unity, the particles are not able to move past each other without either increasing the order of the system or deforming the particles further increasing the effective viscosity (subsection 2.1.2).

### 2.1.1 Random loose-packing and the dilatancy onset

As particles are allowed to settle in a bed with no external forces, they settle into a random loose-packed state. Each sphere is touching and is partially supported by at least one neighbor. On average, each particle is touching 6 others (Cumberland and Crawford 1987; Yang et al. 1996). This configuration can only sustain small external forces and collapses into a denser packed state when subjected to external vibrations or external forces (Onoda and Liniger 1990). This configuration of particles is the driving force behind dry quicksand (Umbanhowar and Goldman 2006).

Granular fluids often dilate upon shearing. This behavior was first observed by Reynolds and is occasionally referred to as Reynolds' dilatancy (Reynolds 1885). If the particles are packed together, as in Figure 2.1, the particle bed must grow, or dilate, in order for

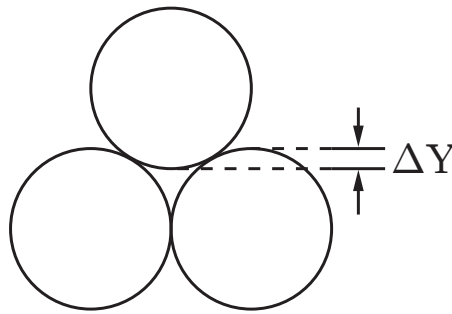


Figure 2.1. Dilatancy of particles in a packed state. To shear the top particle past either bottom particle, it must move up by  $\Delta Y$ .

the particles to freely shear past each other. This dilation is associated with the onset of movement (Pouliquen and Renaut 1996). Onoda and Liniger (1990) hypothesized that the

volume fraction at dilatancy onset corresponded to the random loose-packed volume fraction. Others have also noticed that these two points appear to correspond, but the physical reason for this convergence has not yet been determined (Cates et al. 2005; Wood 1991).

If the random loose-packing volume fraction corresponds to dilatancy onset, it represents a transition in the flow where particle collisions become increasingly common and important to the dynamics. With a sudden increase in the number of collisions, the effective viscosity should correspondingly increase. Dilatancy is not influenced by particle-particle friction, but is influenced slightly by particle shape (Bashir and Goddard 1991; Rowe 1962). Coussot and Ancey (1999) also suggest that dilatancy is associated with non-Newtonian shear thickening behavior.

### 2.1.2 Random close-packing and jamming

Random close-packing is the most compact state the particles can occupy without increasing the order of the system. Each particle, on average, is touching 9 others (Bennett 1972; Cumberland and Crawford 1987). The volume fraction of random close-packing ( $\phi_c = 0.637$ ) is less than the ordered hexagonal close-packed state ( $\phi_m = 0.7405$ ), which has a higher coordination number of 12. A close-packed state is at odds with a random state showing that there is some inherent balance between increasing density through increased order and randomness of the particles (Torquato et al. 2000). To reduce these ambiguities, RCP is taken as the point at which the flow jams (O'Hern et al. 2002; Torquato et al. 2000).

A jammed state is able to support very large external forces and is manifested as a sudden, rapid increase in the effective viscosity. Particles may be released from a jammed state through dilation of a free surface or deformation of either the particles or the constraining surface (Ruiz-Angulo 2008). There is also an increase in slip between the particles and the constraining surface (Barnes 1995, 2000). This increase in wall slip does not influence the actual viscosity of the fluid-particulate flow, but will reduce the measured effective viscosity (see chapter 6). Despite these effects, it is still expected that the measured shear stress dramatically increases as the packing approaches RCP (Stickel and Powell 2005).

It is expected that the slope of a  $\mu'/\mu = f(\phi)$  curve continually increases between  $\phi_l$  and  $\phi_c$ . This region is often modeled as an asymptotic approach to infinity (see subsection 5.4.2). While an increase to infinite shear stress is impossible, these points may be

difficult to measure as the force required to rotate the flow may be greater than can be provided by the motor.

## 2.2 Determination of random packing volume fractions

Since random close- and random close-packing states were first described by Scott (1960), there has been no definitive way to determine these volume fractions. Methods for determining these volume fractions and their results for spherical particles are described generally in subsection 2.2.1 for RCP and subsection 2.2.2 for RLP. The packing of particles is influenced by the particle shape as well as the size and shape of the container (Cumberland and Crawford 1987). The influence on container shape and size is discussed in subsection 2.2.3. Generalizations to non-spherical and nearly spherical particles are described in subsection 2.2.4 and subsection 2.2.5, respectively.

### 2.2.1 Random close-packing

Spherical particles can be arranged in an organized manner, in a hexagonally close-packed arrangement, to yield the absolute maximum packing volume fraction for spheres with all the same diameter of  $\phi = \frac{\pi}{3\sqrt{2}} \approx 0.7405$  (Figure 2.2). While this highly organized packing

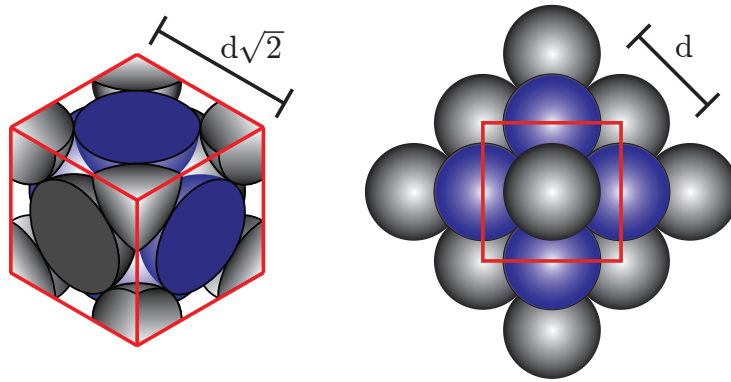


Figure 2.2. Hexagonally close-packed spheres.

is helpful to the understanding of the maximum volume fraction that particles can obtain, such a packing is rarely obtained in natural systems and cannot be sustained following shearing. When the spherical particles are allowed to randomly arrange themselves, the volume fraction is reduced from this theoretical maximum to a state called random close-

packing.

This close-packing state has been found to have a volume fraction between  $\phi_c = 0.606$  and  $\phi_c = 0.648$  (see Table 2.1) and is usually taken as  $\phi_c = 0.637$ . Such packings are

Table 2.1. Random close-packing volume fraction.

Reference	$\phi_c$	Method
Scott (1960)	0.637	Settling of ball bearings
Haughey and Beveridge (1966)	0.62–0.64	Sequential aggregation, $\geq 3$ contacts
Scott and Kilgour (1969)	$0.6366 \pm 0.0005$	Settling of ball bearings
Finney (1970)	$0.6366 \pm 0.0004$	Voronoi polyhedra model
Bennett (1972)	0.62	Sequential aggregation, $\geq 3$ contacts
LeFevre (1973)	0.6366	Monte Carlo and molecular dynamics models
Gotoh and Finney (1974)	0.610–0.647	Statistical polyhedra model
Woodcock (1976)	$0.637 \pm 0.002$	Equation of state
Berryman (1983)	$0.64 \pm 0.02$	Monte Carlo and molecular dynamics models
Torquato et al. (2000)	0.64	Lubachevsky-Stillinger compression model
Philippe and Bideau (2001)	0.606	Simulated tapping model
O'Hern et al. (2002)	0.648	Simulated settling model

often experimentally determined by pouring particles into a container and gently shaking or tapping until no more compaction is observed. For the purpose of this thesis, while the more common value of  $\phi_c = 0.637$  can be used, the slightly tighter compaction of  $\phi_c = 0.648$  appears to be better suited for the present data.

## 2.2.2 Random loose-packing

Random loose-packing is the loosest state that particles can obtain while still in contact. Particles in this state are sensitive to external forces and vibrations, which compacts the particles beyond RLP. Scott first found RLP by slowly tipping a graduated cylinder onto its horizontal axis, rotating it about its axis, and then slowly tipping the cylinder back to the vertical position. Using this method, a RLP volume fraction of  $\phi_l = 0.591$  and

$\phi_l = 0.608$  was found by Scott (1960); Scott and Kilgour (1969), and later  $\phi_l = 0.585$  by Zou and Yu (1995) (see Table 2.2). Realizing the influence of gravity on these experiments,

Table 2.2. Random loose-packing volume fraction.

Reference	$\phi_l$	Method
Scott (1960)	0.591	Tilting with ball bearings in air
Scott and Kilgour (1969)	0.608	Tilting with ball bearings in air
Visscher and Bolsteri (1972)	0.582	Monte Carlo model of serially dropped spheres
Bennett (1972)	0.61	Sequential aggregation, $\geq 3$ contacts
Matheson (1974)	$0.607 \pm 0.002$	Monte Carlo model of serially dropped spheres
Henley (1986)	0.5535	3D Penrose tiling model
Onoda and Liniger (1990)	$0.555 \pm 0.005$	Glass spheres dropped into matched density fluid
Zou and Yu (1995)	0.585	Tilting with glass spheres in air
Aste et al. (2004, 2005)	$0.586 \pm 0.005$	Acrylic beads poured around obstruction

Onoda and Liniger (1990) dropped glass spheres into a graduated cylinder containing a fluid with a density that closely matched that of the spheres. The density of the fluid could be adjusted to investigate the influence of gravity on the packing. A RLP volume fraction of  $\phi_l = 0.555 \pm 0.005$  was found using this method. Using acrylic beads poured around an obstruction that was later removed, a volume fraction of  $0.586 \pm 0.005$  was found by Aste et al. (2004, 2005).

In addition to experimental methods to determine the random loose-packing of spheres, several computational models have also been used. Using a Monte Carlo simulation of serially dropped spheres, Visscher and Bolsteri (1972) found a volume fraction of  $\phi_l = 0.582$  and Matheson (1974) found  $\phi_l = 0.607 \pm 0.002$ . Henley (1986) used a three dimensional Penrose tiling to find  $\phi_l = 0.5535$ .

No consensus has been reached on what value should be used for the random loose-packing volume fraction. For the purposes of this thesis, the RLP volume fraction is taken as the mean value of  $\phi_l = 0.584$ . For experimental determination of the volume fraction, a method such as was employed by Onoda and Liniger (1990) is used (see section 2.3).

### 2.2.3 Containers

The packing of particles depends on the container in which they are packed. Conforming to the walls of a container creates order near the walls, and places – such as the corners of a box – where particles cannot fit. This alignment near the walls is propagated inwards, changing the local volume fraction and, if the container is small, the average volume fraction. This trend was first observed by Scott (1960).

Two examples of two dimensional packing are shown in Figure 2.3. These contain-

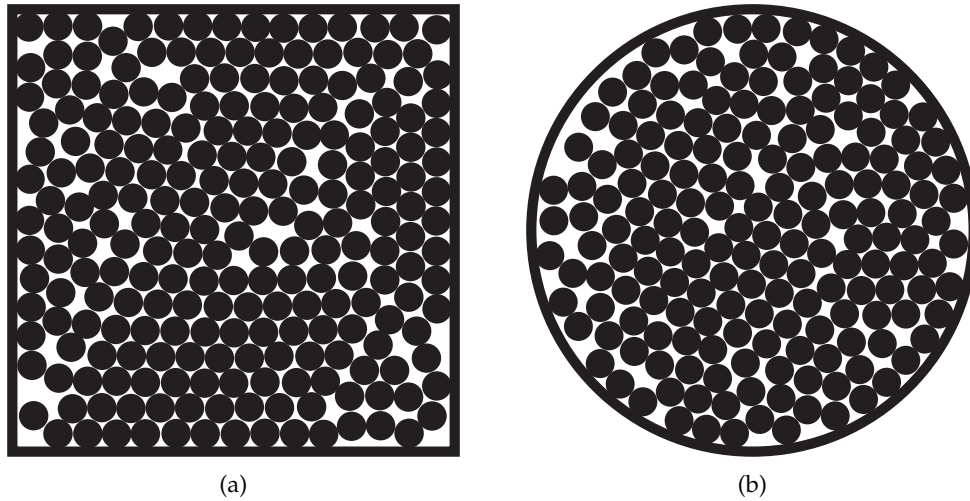


Figure 2.3. Images of 2D random packing in confined (a) square and (b) round containers with  $\phi_{2D} = 0.80$ .

ers are particularly small compared to the radius of the packed disks ( $D/d = 14.9$  and  $L/d = 14.9$ ) and show  $\phi_{2D} = 0.80$ . In the square container, particles tend to be located against the wall and regions of near close-packing propagate inwards (as on the lower side). Where these close-packing regions meet (as in the center), there are pockets that are not filled. There are also unfilled pockets located near the edges where the size of the container constricts the number of particles (as near the left side). The same trends can be observed in the round container with the added complication of the curved edges. In the the round container, regions of close-packing tend to propagate from the center outwards.

The tendency for particles to be located near walls can be further observed by measuring the volume fraction as a function of the distance from the wall, as in Figure 2.4. The volume fraction tends to oscillate near a wall: spheres are likely to be touching the wall creating a peak volume fraction at  $\frac{1}{2}d$  from the wall and trough at a distance  $d$  from the



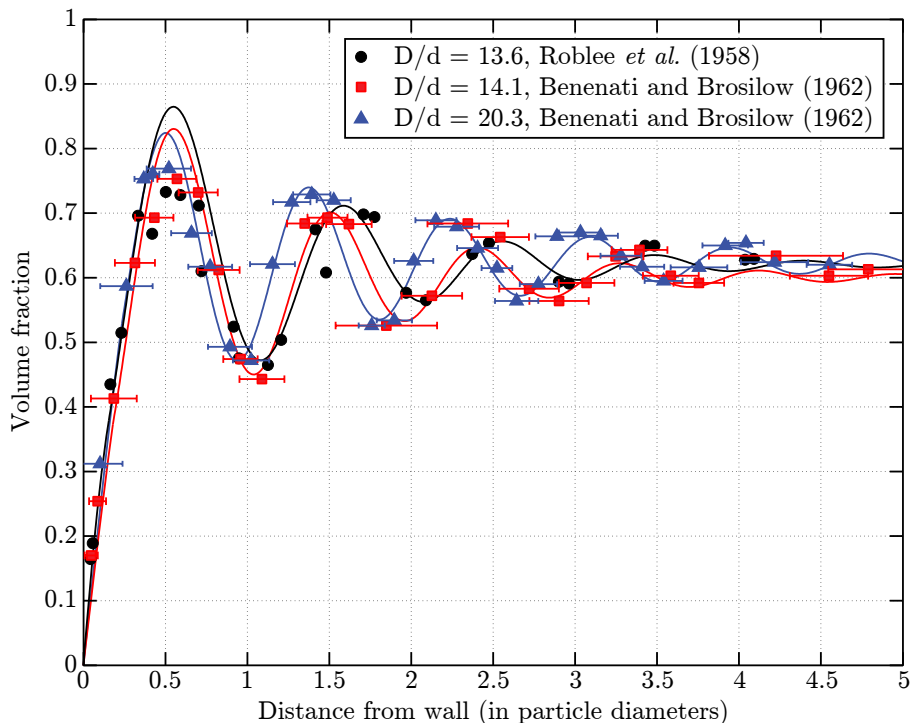


Figure 2.4. Volume fraction near the wall of a large cylinder. The oscillating behavior denotes areas where particles are more or less likely to be present.

wall. As one moves away from the wall, variations in particle location reduce this oscillatory effect. The influence of this behavior on the volume fraction for the entire cylinder is seen in Figure 2.5. For very small cylinders ( $D/d \lesssim 2$ ), the volume fraction is limited by the number of particles which can fit in the cylinder, thus there is no difference between the RLP and RCP packing. Past this point, these two packing densities diverge and asymptote to the values for infinite cylinders,  $\phi_l$  and  $\phi_c$ .

To avoid ambiguities, the random packing volume fraction is usually reported in terms of an infinite container size, or, as they relate to rheological measurements, measured *in situ* (see section 2.3).

## 2.2.4 Packing of non-spherical particles

For non-spherical particles, the maximum packing behavior is influenced by the particle shape and can be related directly to the sphericity (Zou and Yu 1996). The sphericity is defined as the ratio of surface area of an equivalent volume sphere divided by the actual

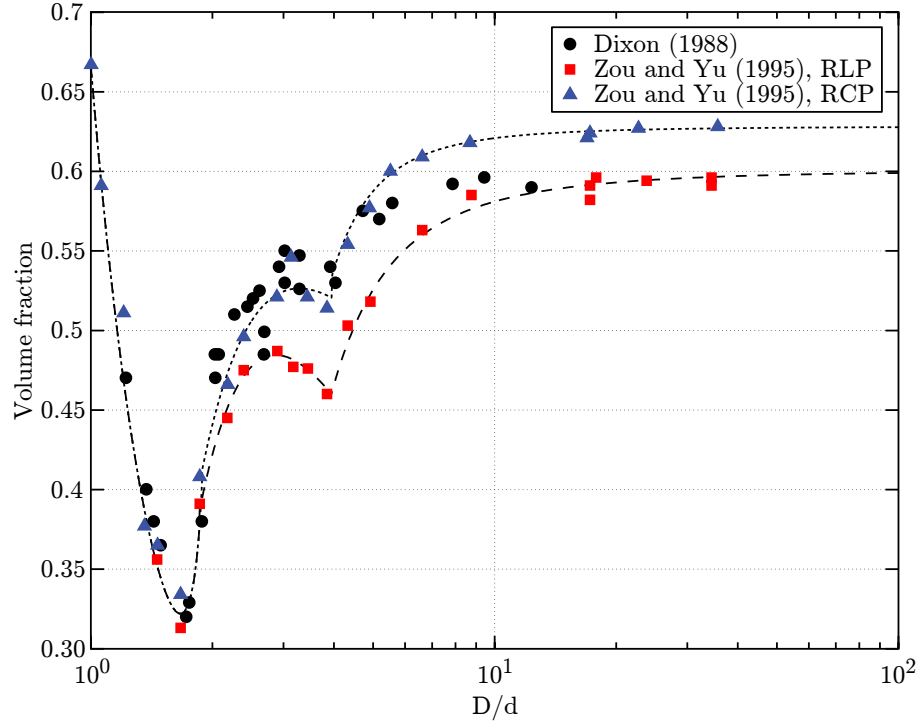


Figure 2.5. Influence of the diameter ratio on the volume fraction for RLP and RCP configurations. Curve fits are from Zou and Yu (1995).

surface area of the particle,

$$\psi = \frac{\pi^{\frac{1}{3}} (6V_p)^{\frac{2}{3}}}{A_p}. \quad (2.1)$$

Generally, as the sphericity increases toward one, the maximum volume fractions decrease, but near a sphericity of 1 ( $\psi \gtrsim 0.8$ ), the maximum volume fraction may increase slightly. The packing of arbitrary particle shapes falls between the limits of that of cylinders (long particles) and disks (short particles). Zou and Yu (1996) measured the RCP and RLP for several shapes of particles (all with the same volume) and found an appropriate curve fit. Based on a RCP and RLP volume fraction for equal volume spheres, designated  $\phi_{c,\infty}$  and  $\phi_{l,\infty}$  respectively, the fits of Zou and Yu (1996) can be adapted. The random loose-packing is

$$\ln(1 - \phi_{l,cylinder}) = \psi^{5.58} \exp[5.89(1 - \psi)] \ln(1 - \phi_{l,\infty}), \quad (2.2)$$

$$\ln(1 - \phi_{l,disk}) = \psi^{0.60} \exp[0.23(1 - \psi)^{0.45}] \ln(1 - \phi_{l,\infty}), \quad (2.3)$$

and the random close-packing is

$$\ln(1 - \phi_{c,cylinder}) = \psi^{6.74} \exp[8.00(1 - \psi)] \ln(1 - \phi_{c,\infty}), \quad (2.4)$$

$$\ln(1 - \phi_{c,disk}) = \psi^{0.63} \exp[0.64(1 - \psi)] \ln(1 - \phi_{c,\infty}). \quad (2.5)$$

For arbitrary convex particle shapes, the maximum volume fraction is a weighted average of these two points

$$\phi_m = \frac{I_{disk}}{I_{cylinder} + I_{disk}} \phi_{m,cylinder} + \frac{I_{cylinder}}{I_{cylinder} + I_{disk}} \phi_{m,disk}, \quad (2.6)$$

where  $m$  is either  $c$  for close-packing or  $l$  for loose-packing. The cylindrical index,  $I_{cylinder} = |\psi - \psi_{cylinder}|$ , is a measure of the difference in shape between the particle and a cylinder. The disk index,  $I_{disk} = |\psi - \psi_{disk}|$ , is a measure of the difference in shape between the particle and a disk. The cylindrical sphericity and disk sphericity are given by:

$$\text{For a cylinder, } \frac{d}{l} < 1 \quad \psi_{cylinder} = 12^{\frac{2}{3}} \frac{\left(\frac{d}{l}\right)^{\frac{1}{3}}}{4 + \frac{d}{l}}, \quad (2.7)$$

$$\text{For a disk, } \frac{l}{d} < 1 \quad \psi_{disk} = 12^{\frac{2}{3}} \frac{\left(\frac{l}{d}\right)^{\frac{2}{3}}}{1 + 4\frac{l}{d}}, \quad (2.8)$$

where  $l$  is the largest length for the cylinder and the shortest length for the disk. The diameter  $d$  is found using the projected area perpendicular to  $l$ .

### 2.2.5 Nearly spherical particles

For nearly spherical particles with a nominal diameter of  $d$  and perturbation in the diameter of  $\delta$ , the packing is close to that for a sphere, but with a slight variation. It is assumed that the largest measured diameter is  $d_{large} = d(1 + \delta)$ , where  $\delta \ll 1$ . To maintain the same volume, the smallest diameter  $d_{small} = \frac{d}{1+\delta}$ . The sphericity, assuming the surface area of a scalene ellipsoid with diameters  $\frac{d}{1+\delta}$ ,  $d$ , and  $d(1 + \delta)$ , is

$$\psi = 1 - \frac{1}{4}\delta - \frac{119}{60}\delta^2 + O(\delta^3). \quad (2.9)$$

The disk sphericity and cylindrical sphericity are

$$\psi_d = \left(\frac{3}{2}\right)^{\frac{2}{3}} \frac{(1+\delta)^{\frac{1}{2}}}{1 + \frac{1}{2}(1+\delta)^{\frac{3}{2}}}, \quad (2.10)$$

$$\psi_c = \left(\frac{3}{2}\right)^{\frac{2}{3}} \frac{(1+\delta)^{-\frac{1}{2}}}{1 + \frac{1}{2}(1+\delta)^{-\frac{3}{2}}}. \quad (2.11)$$

Using equation (2.6), the close-packing volume fraction is

$$\phi_c = \phi_{c,\infty} + 0.05839 \delta + 0.42066 \delta^2 + O(\delta^3), \quad (2.12)$$

and the loose-packing volume fraction is

$$\phi_c = \phi_{l,\infty} + 0.02259 \delta^{\frac{9}{20}} + 0.00012 \delta^{\frac{9}{10}} - 0.013286 \delta - 0.00005 \delta^{\frac{27}{20}} + O\left(\delta^{\frac{29}{20}}\right). \quad (2.13)$$

A comparison of the third and tenth order approximations for  $\phi_l$  and  $\phi_c$  as a function of the sphericity  $\psi$  is shown in Figure 2.6. For even large perturbations in the diameter,  $\delta < 0.15$

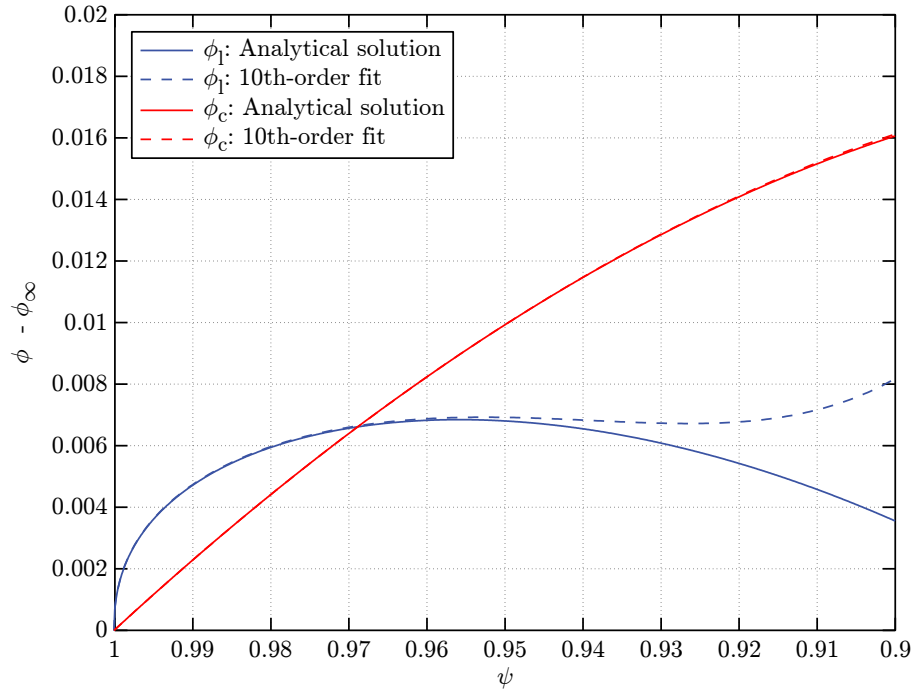


Figure 2.6. Approximations for close- and loose-packing for nearly spherical particles.

( $\psi = 0.925$ ), both the close- and loose-packing volume fractions remain accurate (less than

0.2% error). Using the tenth order approximation for the packing fractions, a loose-packing volume fraction can be found from previously published data if  $\phi_c$  is known.

## 2.3 Experimental data

### 2.3.1 Current particles

A rectangular container was constructed to measure both the close- and loose-packing volume fractions. To reduce any effect on the container shape between the counter-top and *in situ* measurements, the container was constructed with a width of 3.16 cm (1.25 in) to match the gap in the Couette shear cell and length much greater than the width (38.1 cm, 15 in). Volume fractions were measured by adding particles to a known volume of water and measuring the displaced volume. For loose-packing, the particles were slowly added without disturbing the container or interstitial fluid and allowed to come to rest in a loose, random orientation. For close-packing, the particles were added in small batches between which the container was tapped to encourage the particles to settle until no more visible compaction occurred. Again, the volume fraction was found by measuring the displaced volume of the fluid. The random packing volume fractions were repeated several times for each material and are summarized in Table 2.3.

Table 2.3. Random packing volume fractions for the currently used particles found by experimental measurement and calculated using the sphericity.

Property		Glass	Nylon	Polyester	Polystyrene	SAN
Size	$d$ (mm)	3.04	6.36	2.93	3.34	3.22
	$d/b$	0.0962	0.2013	0.0927	0.1057	0.1019
Sphericity	$\psi$	0.9998	0.9999	0.9910	0.7571	0.9798
	cylindrical, $\psi_c$	0.8736	0.8736	0.8690	0.8528	0.8658
	disk, $\psi_d$	0.8244	0.8254	0.8701	0.8356	0.8648
RLP, $\phi_l$	measured	0.597	0.568	0.593	0.553	0.611
	calculated	0.5844	0.5844	0.5883	0.5551	0.5898
	error	2.1%	2.9%	0.8%	0.4%	3.5%
RCP, $\phi_c$	measured	0.626	0.627	0.650	0.663	0.657
	calculated	0.6370	0.637	0.6500	0.6552	0.6524
	error	1.8%	1.6%	0.0%	1.2%	0.7%

Using the average particle dimensions and sphericity, the random packing volume

fraction can also be calculated from equation (2.6) using  $\phi_{c,\infty} = 0.648$  (based on the settling model of O'Hern et al. (2002)) and  $\phi_{l,\infty} = 0.584$ . These calculated packing fractions are shown in Table 2.3 accompanied by the error between the calculated and experimentally measured value. The average error for all particles is 1.5%.

### 2.3.2 Previously reported experiments

In previously reported experiments, researchers published the particle sizes or size distributions and the random close-packing volume fraction, which was either experimentally determined or estimated. The random loose-packing volume fraction was often not reported. As it is the hypothesis of this thesis that the random loose-packing volume fraction corresponds to a transition in the effective viscosity (as discussed in subsection 2.1.1) this volume fraction must be determined.

In order to estimate the random loose-packing volume fraction, the random close-packing volume fraction is used with the assumption that all of the reported particles are nearly spherical such that the equations outlined in subsection 2.2.5 can be used. The general agreement between the calculated and measured values shown in Table 2.3 reinforces the choice of this method for determining the RLP. Values for the random packing fractions are summarized in Table 2.4 and outlined in detail below:

Table 2.4. Previous experiments of non-Brownian shear flows

Experiments	Solid	d (mm)	$\phi$	$\phi_c$	$\phi_l$
Bagnold (1954)	50% paraffin & lead stearate	1.32	0.134–0.623	0.637	0.60
Savage and McKeown (1983)	polystyrene	0.97	0.429–0.570	0.642	0.590
		1.24		0.644	0.591
		1.78		0.641	0.590
Hanes and Inman (1985)	glass beads	1.1	0.55–0.58	0.64	0.544
		1.85	0.49–0.5	0.55	0.441
Acrivos et al. (1994)	PMMA acrylic	0.1375	0.20–0.30	0.58 <sup>a</sup>	0.58 <sup>a</sup>
		0.0905	0.20–0.50		
Prasad and Kytömaa (1995)	acrylic	3.175	0.493–0.561	0.565	0.512

<sup>a</sup>Based on a fit determined using 46  $\mu\text{m}$  polystyrene beads (Leighton and Acrivos 1987).

- *Bagnold (1954)*: In his paper, Bagnold normalized the volume fraction by the theoretical limit of  $\phi = 0.74$  for perfectly ordered spheres. In a later paper, Bagnold measured the “fluidity” packing fraction – below which the residual shear resistance at zero shear rate disappears – as  $\phi = 0.60$  (Bagnold 1966). In later analyses of his work, the RCP volume fraction has been taken as either the fluidity volume fraction (Savage and McKeown 1983) or as  $\phi = 0.65$  (Hanes and Inman 1985). As fluidity should correspond more closely to (but is not necessarily) the RLP volume fraction, Bagnold’s reported value of  $\phi = 0.60$  is used as the random loose-packing volume fraction. As no RCP value was reported, the theoretical value ( $\phi_c = 0.637$ ) was used for the close-packing volume fraction (Finney 1970).
- *Savage and McKeown (1983)*: Using the reported values for the RCP, the RLP was estimated for nearly spherical particles based on the 10th-order extrapolation using  $\phi_{c,\infty} = 0.637$  and  $\phi_{l,\infty} = 0.584$ . Values of  $\phi_l = 0.590, 0.591$ , and  $0.590$  were obtained for the  $d = 0.97, 1.24, 1.78$  mm particles, respectively.
- *Hanes and Inman (1985)*: In the experiment by Hanes and Inman, non-neutrally buoyant particles were confined to an annular region, the top plate of which was allowed to move axially, but was subjected to a non-zero load during the experiment. Due to this geometry, the measured volume fractions were all confined between  $\phi_l$  and  $\phi_c$ . Hanes and Inman report the RCP volume fractions, but do not report the RLP volume fractions. These values were estimated using the 10th-order extrapolation using  $\phi_{c,\infty} = 0.637$  and  $\phi_{l,\infty} = 0.584$ . For the  $d = 1.1$  and  $1.85$  mm particles, the extrapolation yielded values of  $\phi_l = 0.544$  and  $0.441$ . Both of these values are below the minimum volume fraction tested, as expected.
- *Acrivos et al. (1994)*: In their 1994 paper, Acrivos et al. did not determine  $\phi_c$  independently, but used the value obtained from a previous experiment. In Leighton and Acrivos (1987), using  $46 \mu\text{m}$  polystyrene beads,  $\phi_c$  was determined as a fitting parameter to be  $0.58$ . In their paper, Acrivos et al. claimed that this value is consistent with their results, but for two different types of particles ( $137.5 \mu\text{m}$  PMMA and  $90.5 \mu\text{m}$  acrylic). With no other information with which to make a determination, the value of  $0.58$  as reported in Leighton and Acrivos (1987) is used as  $\phi_c$  and  $\phi_l$ . This value is close to the values reported for RLP (Table 2.2), but does differ from the values for

RCP (Table 2.1).

- *Prasad and Kytömaa (1995)*: In the experiments by Prasad and Kytömaa, the RCP volume fraction was reported as  $\phi_c = 0.565$ . This reported value differs significantly from other values for RCP (Table 2.1), but may be due to the large particles ( $d/b = 0.294$ ). If the same reduction was present in RLP – as expected using the data presented in Figure 2.5 for the influence on packing fraction on diameter ratio – a value of  $\phi_l = 0.512$  is appropriate. This value is consistent with the transition shown in effective viscosity for their data.

## 2.4 Summary

The volume fraction of solids,  $\phi$ , can dramatically change the effective viscosity of the liquid-solid flow. The random close-packed (RCP) volume fraction  $\phi_c$  represents the volume fraction at which no more compaction occurs. At this volume fraction, the mixture is unable to shear without requiring deformation of either the particles or the surrounding cylinder walls. The random loose-packed (RLP) volume fraction  $\phi_l$  is the volume fraction where each particle is in contact with at least one adjacent particle. This volume fraction is the volume fraction obtained when shearing particles are allowed to freely dilate and represents the transition between an advective dominated diffusion and collision dominated diffusion. Above  $\phi_l$ , as the volume fraction approaches  $\phi_c$ , the effective viscosity is expected to asymptotically increase. Below  $\phi_l$ , a different, heretofore unknown, relation between the volume fraction and effective viscosity is expected.

These volume fractions depend on the particle size relative to the size of the container, particle shape, and on external forces. To avoid ambiguities, both the random close- and random loose-packed volume fractions for the particles used in this paper were measured in a container that mimicked the *in situ* conditions. For previously reported experiments,  $\phi_c$  was often reported without  $\phi_l$ . The RLP volume fraction was estimated from the corrections provided for slightly non-spherical particle and small container to diameter ratios.





## Chapter 3

# Apparatus and Experimental Procedure

To measure the influence of solids on the shear stress, a rheometer with a rotating outer cylinder was used. Particles are confined in an annular region between the inner, stationary cylinder and the outer, rotating cylinder. This rheometer was specifically designed to measure the effective viscosity of fluid-particulate flows, and special care was taken to minimize the effects of secondary flows on these measurements. As was discussed in subsection 1.1.2, secondary flows exist as Taylor-Couette vortices above a critical Reynolds number or as a boundary layer flow against the annular end caps and are manifested as an increase in the measured torque. The rheometer, which is discussed in more detail in section 3.1, was designed with a gap width to outer radius ratio to delay the onset of Taylor Couette flows and a ratio of gap width to height to reduce the influence of the boundary layer flows. In addition to these measures, the effective viscosity measurements are only made in a center region on the inner cylinder – the center, floating cylinder – to further isolate these measurements from the end cap boundary layers. Torque measurements are described in subsection 3.2.2 with the method for using these measurements to find the shear stress and effective viscosity for the fluid-particulate flow.

With non-neutrally buoyant particles, the volume fraction can vary axially and radially within the annulus. The shear stress and effective viscosity are measured at the center, floating cylinder. To correlate these force measurements with the volume fraction of solids over this region of the annulus, optical probes are mounted just above and below the floating cylinder. These probes were used to measure the volume fraction by measuring the frequency of particles crossing the optical probes and their velocity. The signals from the

optical sensors are filtered and analyzed using the algorithms described in subsection 3.2.1 with the MATLAB code included in appendix A.

Finally, this chapter also examines the properties of the particles that are used throughout these experiments in section 3.3. Properties including size, shape, and density are discussed in detail.

### 3.1 Rotating cylinder rheometer

The coaxial shear cell, which was constructed for the present experiment and is shown in Figure 3.1, consists of a fluid-particle mixture confined between two stainless steel concentric

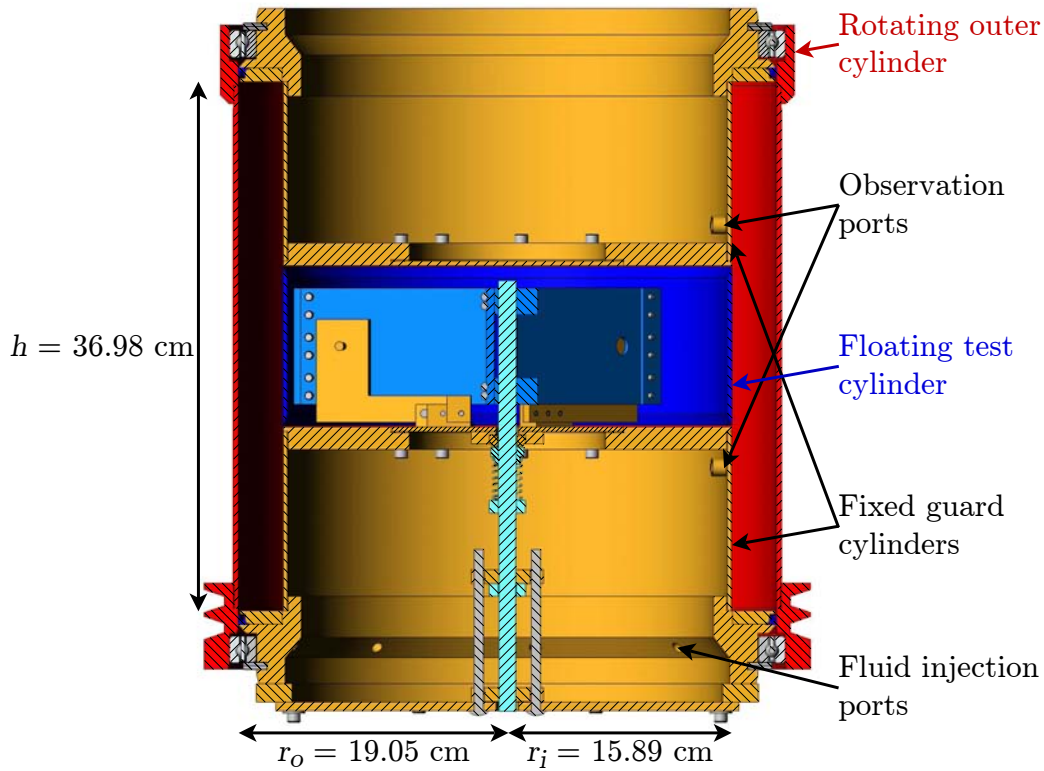


Figure 3.1. Coaxial rotating cylinder, Couette flow device. The outer cylinder rotates while the inner cylinder remains fixed. The center section of the inner cylinder (floating test section) is allowed to rotate slightly so as to measure the forces created by the flow

tric cylinders. The flow is driven by the rotation of the outer cylinder. The inner cylinder consists of three sections: rigid top and bottom sections, and a central, floating section, which deflects circumferentially to allow measurement of the shear stress. The floating cylinder is supported by a central axle. Knife-edge gaps between the floating section and

the upper and lower fixed sections prevent particles from leaving the annular region. A seal around the axle and seals above and below the annular gap prevent fluid from entering the bearings. Mechanical drawings of each part and assembly are included in appendix B and the properties of the experimental apparatus are summarized in Table 3.1. The inner cylinder radius  $r_i$  is 15.89 cm (6.26 in) and the outer cylinder radius  $r_o$  is 19.05 cm

Table 3.1. Dimensions and properties of the rotating cylinder rheometer.

Property	Value
radius of the inner drum, $r_i$	15.89 cm (6.26 in)
radius of the outer drum, $r_o$	19.05 cm (7.50 in)
annular gap width, $b = r_o - r_i$	3.15 cm (1.24 in)
height of the annular gap, $h$	36.98 cm (14.56 in)
height of the floating cylinder, $H$	11.22 cm (4.42 in)
ratio of annular height-to-gap, $h/b$	11.7
ratio of annular gap to outer radius, $b/r_o$	0.165
velocity of the outer, rotating cylinder, $V$	0.07 – 3.2 m/s
shear rate, $\dot{\gamma}$	2.2 – 100 1/s
gap Reynolds number, $Re = \rho\dot{\gamma}b^2/\mu$	$1.3 \times 10^3 - 6.2 \times 10^4$
critical gap Reynolds number for the onset of Taylor-Couette vortices	$1.8 \times 10^4$
shear stress, $\tau$	0.3 – 1000 N/m <sup>2</sup>

(7.50 in) leaving a gap between the two cylinders  $b$  of 3.15 cm (1.24 in). The annular gap has a height  $h$  of 36.98 cm (14.56 in) for a height to gap ratio  $h/b$  of 11.7 and a ratio of the gap to outer radius  $b/r_o$  of 0.165.

This annular Couette flow device was specifically designed to reduce the effect of secondary vortices on fluid measurements. These secondary flows and their influence on shear measurements is discussed in subsection 1.1.2. Several design choices were made to delay the onset of such secondary flows. First, the flow is driven through the rotation of the outer cylinder to delay the onset of Taylor-Couette vortices. Such vortices develop for an outer rotating Couette flow at a Reynolds number significantly higher than for an inner rotating flow on the same apparatus (Taylor 1936a,b; Wendt 1933). Further delay is achieved through the increase in the ratio of gap width to outer radius ( $b/r_o$ ). Using the data of Taylor or fit of Zeldovich, a critical gap Reynolds number of  $1.8 \times 10^4$  is found for the chosen ratio of  $b/r_o = 0.166$  (Taylor 1936a,b; Zeldovich 1981). Finally, for finite height Couette

flows, the presence of either rotating or stationary end caps can significantly increase the measured torque due to boundary layer flows at the end caps. Stationary end caps reduce the secondary flows as compared with rotating ends. The effects of these boundary layers is further reduced by increasing the height to gap ratio ( $h/b = 11.7$  for the present apparatus), which decreases the percentage of the inner cylinder affected by boundary layer flow, and by only taking measurements in the center of the annulus away from these stationary end caps and the associated boundary layer. In the case of the current apparatus, torque measurements are taken in the center 11.22 cm (4.42 in), four gap widths from each end cap.

## 3.2 Experimental measurements

The apparatus includes two observation ports located on the inner, fixed cylinders and centered at 2.86 cm (1.13 in) above and below the floating test cylinder. These ports were used with the optical probes, but can also be used with piezoelectric pressure sensors. The optical probes return a signal when a particle was in front of the probe face and are used to count the particles above and below the floating test cylinder. Additionally, two probes mounted side-by-side can measure the velocity of these particles. The velocity and particle count data are used to calculate the effective volume fraction in the center region of the annular gap. The probes and the algorithms used to find the particle velocity and volume fraction measurements are discussed in subsection 3.2.1.

Using the concentric cylinder apparatus, measurements of the torque on the inner, floating cylinder were completed. These measurements are discussed in detail in subsection 3.2.2 with the methods for calculating the shear stress and effective viscosity. A calibration of this data is also provided in subsection 3.2.3.

### 3.2.1 Particle velocity and volume fraction measurements

To evaluate the effective volume fraction adjacent to the floating cylinder, MTI 0623H optical probes were used. The optical sensors detect the presence of a particle close to the active face of the sensor (within 1 cm through a fluid or 3 cm in air). The sensors transmit light through a fiber optic cable, and the MTI KD-300 photonic sensor uses a photodetector to measure the light reflected back through the cable. The transmission and detection fibers

are arranged in a hemispherical pattern such that when a target is very close to the active face no light is reflected and no output is measured. The output rapidly increases before reaching a peak as the distance between the probe face and the particle is increased. After this peak, as the distance continues to increase, the voltage asymptotically approaches a low level representing the ambient light in the room. A typical calibration is shown in Figure 3.2.

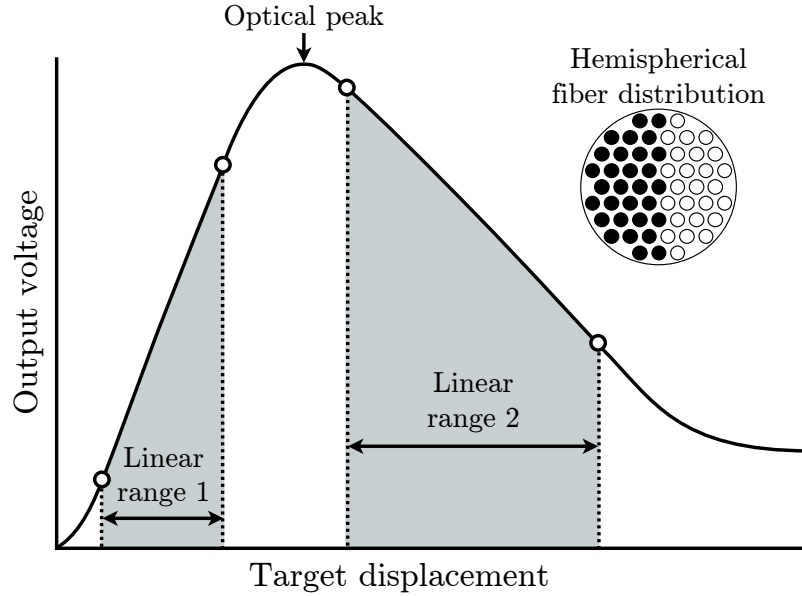


Figure 3.2. Typical response curve for the MTI KD-300 photonic sensors used with a MTI 0623H optical probe. The sensors are able to detect a particle passing the probe face and two adjacent sensors are used to find the particle velocity.

To estimate the local volume fraction, it is assumed that the particles are distributed evenly in all three directions and separated by some average distance,  $L$ , given by

$$L = \frac{u}{n}, \quad (3.1)$$

where  $u$  is the particle velocity and  $n$  is the number of particles that cross the probe per unit time. If the particles have a typical dimension,  $R$ , then the volume fraction,  $\phi$ , is given by

$$\phi = \frac{4}{3}\pi \left(\frac{R}{L}\right)^3. \quad (3.2)$$

The particle velocity and particle count must be measured in order to determine the volume fraction. Both of these tasks are accomplished by arranging two optical sensors

in line with the flow as shown in Figure 3.3. Two consecutive peaks are measured from

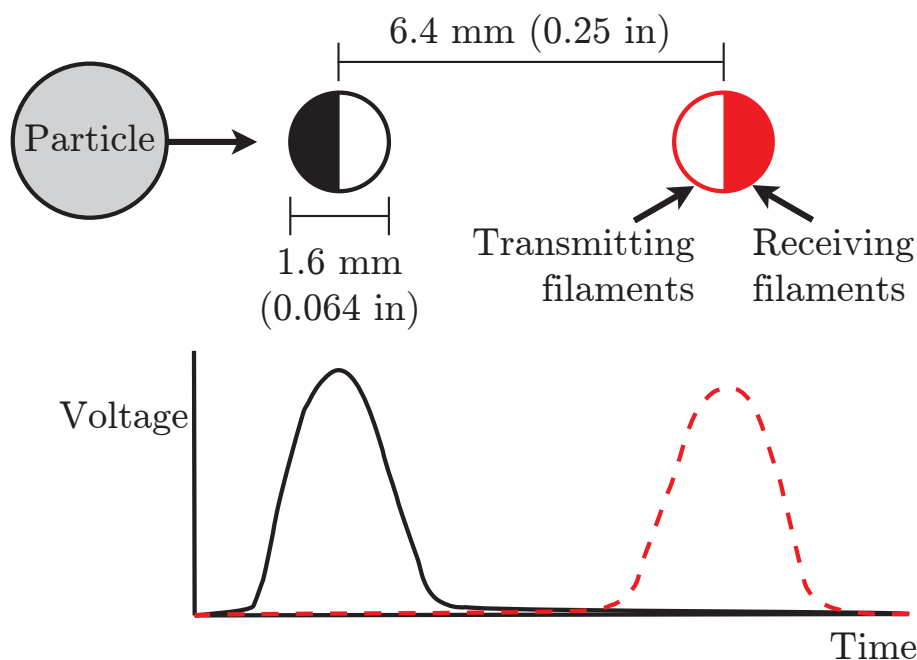


Figure 3.3. Schematic of the optical probe configuration to measure particle counts and velocities. The 1.6 mm (0.064 in) probes are arranged so that the transmitting fibers are toward the center, and are separated by 6.4 mm (0.25 in). Particles cross the probes from left to right yielding a voltage signal as shown in the lower graph.

the two probes corresponding to the particle passing each probe face in turn. The probes are oriented with the receiving filaments on the outside to reduce the strength of a signal registered from the second probe before the particle is directly in front of the probe. For the purposes of this discussion, the signals from the optical probes are considered as a part of a series, each individual measurement taken for singular rotational speed. The rotational speed was varied between measurements, while the number of particles in the annulus was kept constant.

The raw voltage signal from the optical probes was sampled at 10,000 Hz per channel using a 16-bit digital acquisition board (Measurement Computing PCI-DAS 6023) and processed digitally using MATLAB. At the highest speed recorded, a particle takes between 60 and 120 sample times to cross the optical probe. This digitized voltage is then normalized based on the average signal and filtered using a 9th order Butterworth lowpass filter (with a natural frequency of 185 Hz) and three third order Butterworth bandstop filters to reduce ambient electrical noise at 60 Hz and the first two harmonics at 120 Hz and 180 Hz.

The lowpass filter attenuated the signal at least 1 dB above 300 Hz, losing no more than 0.001 dB below 200 Hz. The Bode magnitude plot for this combined filter is shown in Figure 3.4 and the results of filtering are seen in Figure 3.5. The shape, width, and height

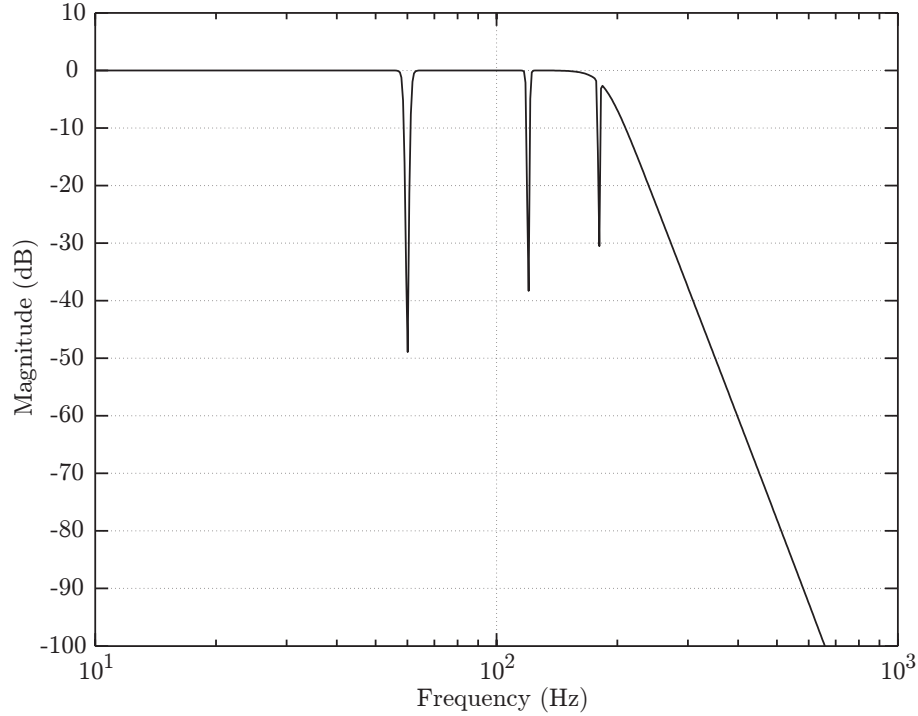


Figure 3.4. Bode magnitude plot for the combined lowpass and bandstop filter used to reduce experimental noise. The lowpass filter has a natural frequency of 185 Hz and the bandstop filters have natural frequencies of 60, 120, and 180 Hz.

of each particle peak signal are influenced by the particle shape, distance from the probe, and speed of the particle. In addition to these differences in peak height within a signal, the gain between signals can differ. In Figure 3.5, the oscillatory behavior in the unfiltered data corresponds to introduced 60 Hz noise from the supplied power and is significantly reduced in the filtered signals.

The filtered data is passed through a peak finding algorithm (see section A.1) to find the time locations of signals corresponding to particles conclusively passing by the probes. The peak finding algorithm looks for peaks within a certain range (*Range*) and with a peak width of  $2s$ . The initial threshold in voltage is set as 0.1 V over the mean value with a peak width of 40 time steps. Using these values, the maximum peak height for each optical probe, for each rotational speed measured, is recorded. This maximum peak height is then averaged over each rotational speed series to find `meanmaxpeak` and the new threshold is



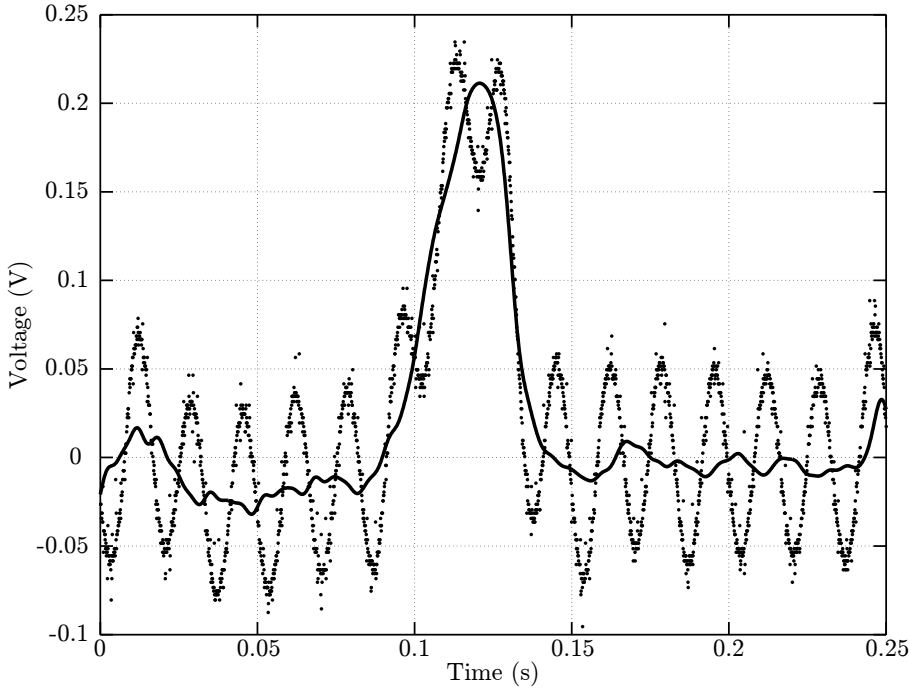


Figure 3.5. Filtered (–) and unfiltered (·) voltage data for an optical probe. The oscillatory behavior of the unfiltered signal corresponds with 60 Hz noise from AC supply and is significantly reduced in the filtered data.

then set as  $0.1 * \text{meanmaxpeak}$ . The new peak width is set as

$$2s = \frac{1}{10} \frac{d}{u} \text{ fs}, \quad (3.3)$$

where  $d$  and  $u$  are the particle diameter and velocity, respectively, and  $\text{fs}$  is the sample frequency. Using these new threshold values, the optical data is reanalyzed to find the peak number and locations using `fpeak.m` (section A.1). Typical results for an suspension of  $\phi = 0.30$  polystyrene ( $\text{St} = 52$ ) are shown in Figure 3.6 with the peaks shown as circles. The left signal (solid line) precedes the right (dashed line) by 0.0104 seconds. The typical optical sensor signal contain many slightly overlapping signals from many particles crossing the probes in quick succession.

To find the particle velocity, the peak locations and shapes from adjacent optical probes are cross-correlated using `correl_full.m` (see section A.2). Each signal is converted to one where each peak is normalized to a magnitude of 1 and only the area within the peak width  $s$  points of the center is non-zero (see lines 20–56 of `correl_full.m`). Figure 3.7 shows this converted signal for the same sample as seen in Figure 3.6. The results

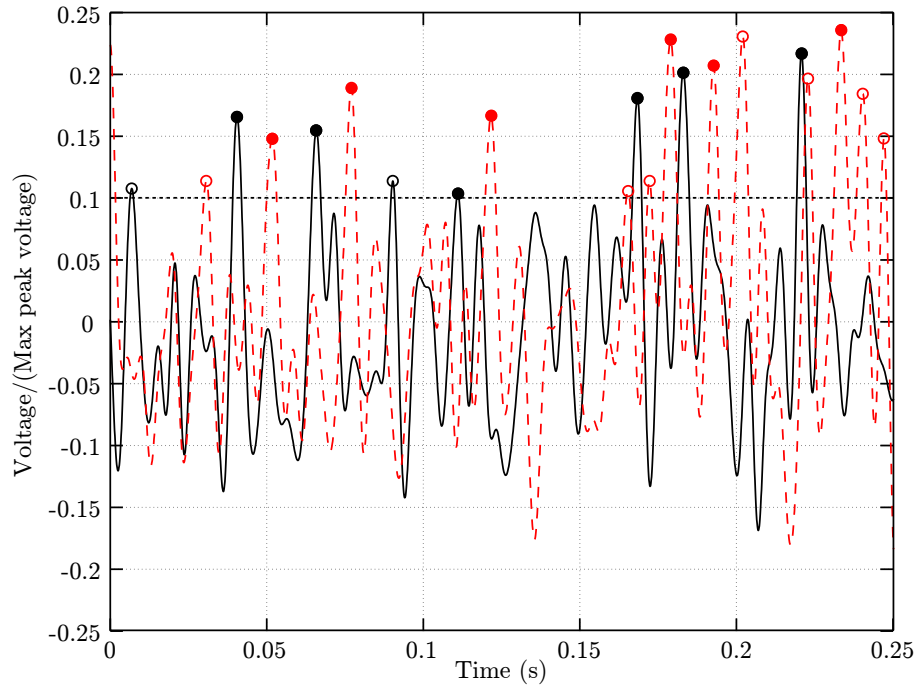


Figure 3.6. Filtered and normalized voltage signal from two probes located in the lower observation port. The flow proceeds from left to right, with particles crossing the left probe (solid line) 0.0104 seconds before the right probe (dashed line). Peaks detected and used to determine particle count are shown with circles (see section A.1). Peaks used for cross-correlation are shown with closed circles (see section A.2).

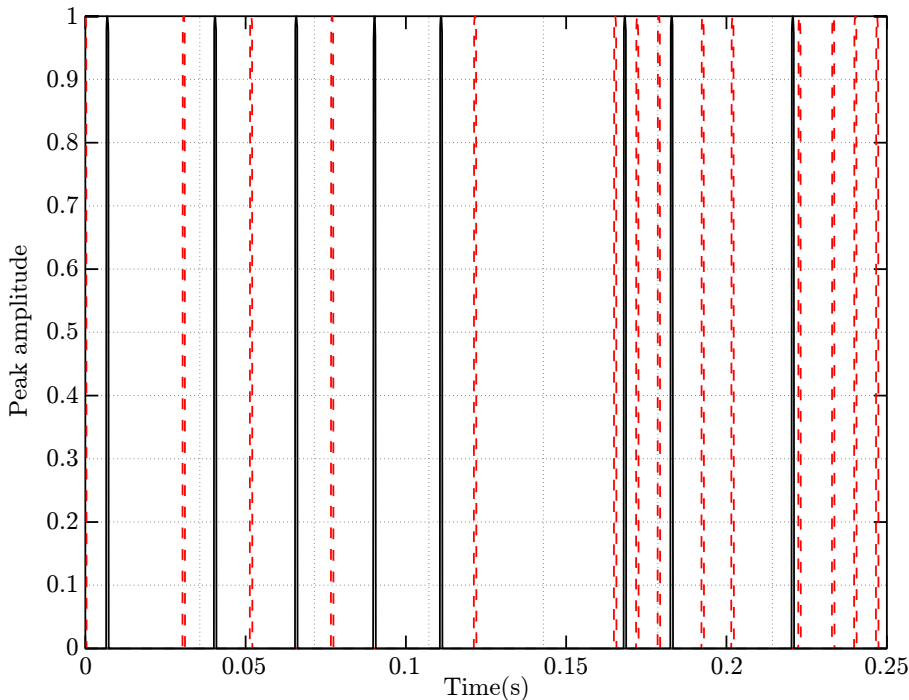


Figure 3.7. Converted voltage signal used for the cross-correlation of the full voltage signals for two adjacent optical probes. These are the same signals as appear in Figure 3.6. (See section A.2 for more information.)

of the cross-correlation are shown in Figure 3.8 with `offset` found to be  $t = 0.0104$  seconds. Using `correl.m`, the velocity of individual particles is determined through the cross-correlation of individual peak signals. For each peak from the first optical sensor `correl.m` looks for peaks between  $0.80 \times \text{offset}$  and  $1.33 \times \text{offset}$ , where `offset` is the time offset found using `correl_full.m`. Additionally, particle velocities cannot be greater than the rotational velocity of the outer (rotating) cylinder. A histogram of the particle velocities for the same example of a suspension of  $\phi = 0.30$  polystyrene ( $St = 40$ ) is shown in Figure 3.9. It is important to note that since peak width (also used for the cross-correlation to find the particle velocities) is a function of the velocity, an initial value of 40 time steps is used and then the data is reprocessed using the newly found velocity.

### 3.2.2 Shear stress

The floating inner cylinder (Figure 3.1) is allowed to deflect circumferentially so that the average shear stress on this cylinder is measured. The deflection is measured using the same type of optical probe and photonic sensor (MTI 0623H and MTI KD-300, respectively)

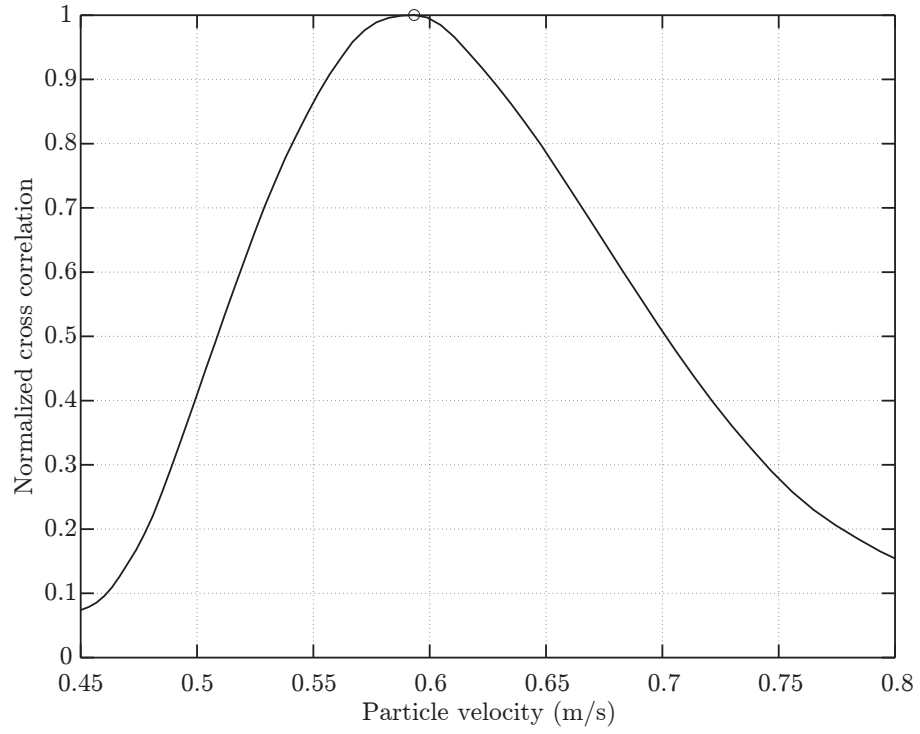


Figure 3.8. Normalized cross-correlation amplitude showing the likely particle velocities found by cross-correlating the entire optical signals with `correl_full.m` (see section A.2). The velocity found using the cross-correlation of the entire optical signals is  $u = 0.5935$  m/s.

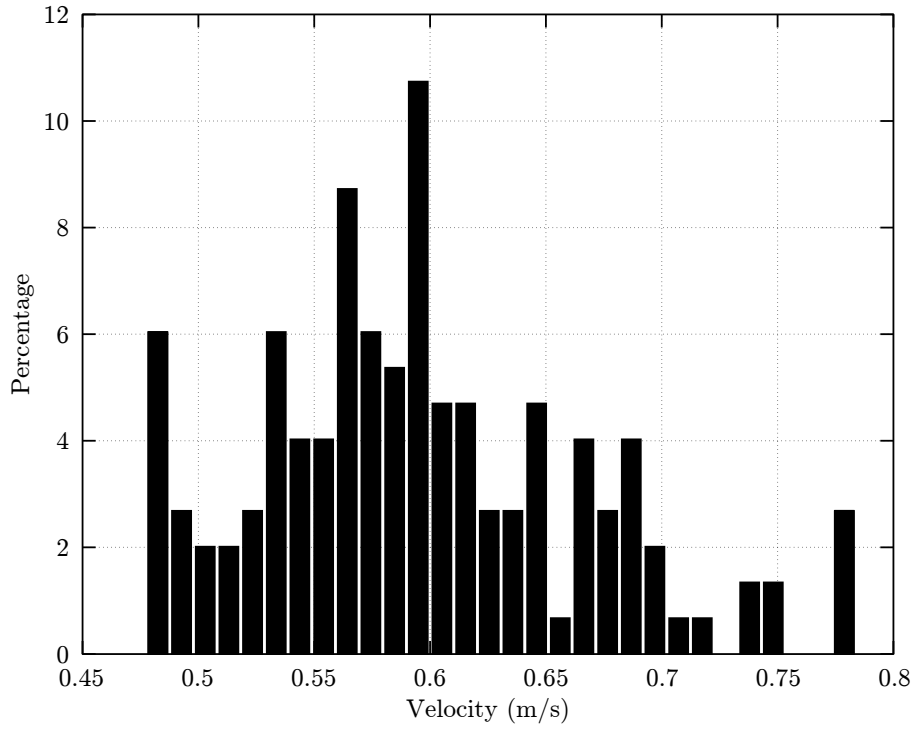


Figure 3.9. Histogram of particle velocities found using the `correl.m` script (see section A.3). The mean velocity ( $u = 0.5955$  m/s) found using this method closely matches the velocity found through the cross-correlation of the entire optical signals ( $u = 0.5935$  m/s).

as used to find the volume fraction. A small mirror is used as a moving target mounted to the floating inner cylinder, and the probe is mounted to a stationary reference. The optical sensor and target were initially displaced past the peak voltage (see Figure 3.2) ensuring that the measured signal would yield a singular displacement.

The calibration was obtained by recording the voltage for a variety of displacements measured separately by a dial gage. While the maximum measured voltage can change based on the initial separation between the sensor and target or optical sensor gain, the shape of the displacement curve is constant. An example of the normalized displacement curve is shown in Figure 3.10 and has a squared 2-norm of the residual of 0.0012 (R-squared value of  $1 - 1 \times 10^{-8}$ ). The displacement is fitted using an equation of the form

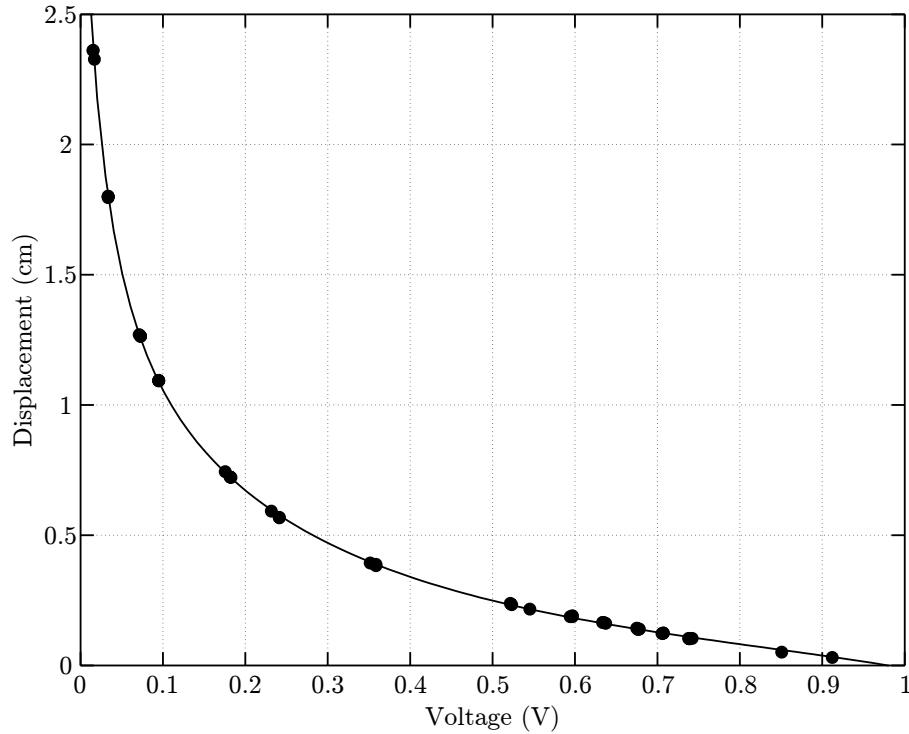


Figure 3.10. Post peak displacement as a function of normalized voltage for the MTI optical displacement sensors. Measured values are shown by the plotted points and the curve fit is shown by the line. The squared 2-norm of the residual is 0.0012 (R-squared value of  $1 - 1 \times 10^{-8}$ ) for this curve fit.

$$D = \frac{C_1 E^3 + C_2 E^2 + C_3 E + C_4}{C_5 E^4 + C_6 E^3 + C_7 E^2 + C_8 E + C_9} \quad (3.4)$$

This calibration was repeated several times, all with similar results.

The deflection of the floating inner cylinder is limited by a spring connecting the inner cylinder to a stationary reference. By adjusting the stiffness of the spring, it is possible to measure a range of torques corresponding to shear stresses between 0.3 and 1000 N/m<sup>2</sup>. The stiffness of each of these springs was calibrated *in situ* to account for any stiffness caused by the experimental apparatus itself. To measure the spring stiffness, known forces were applied to the torque arm using a set of calibrated masses. This test was performed while the rheometer was dry, wet, and wet with the outer cylinder rotating slowly ( $\sim 5$  rpm). While all three test conditions yielded similar results, completing the calibration wet with the outer cylinder rotating slowly was found to be the most repeatable.

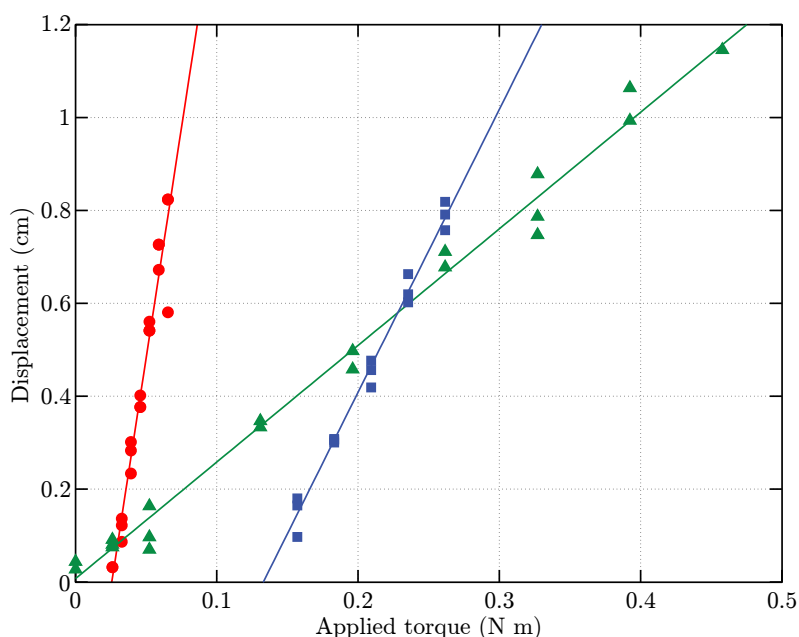


Figure 3.11. Plot of displacement as a function of applied torque for springs ▲ 167-A, ■ 170-A, and ● 176-A manufactured by Century Springs. The  $x$ -intercept for each spring is determined by the initial tautness of each spring and is not a spring property.

Each spring has a unique calibration constant (given by the slope in Figure 3.2.2) and an initial torque required to displace the spring. The initial torque ( $x$ -intercept) depends on the initial tautness when the spring is installed and is not a property of the spring. For some of the tests, it was necessary to preweight the system to avoid any errors caused by this initial torque. The value of this weight is unimportant as long as it remained constant for all of the tests in that series.

### 3.2.3 Pure fluid calibration

To test the experimental apparatus and data acquisition system, several tests were completed using an aqueous-glycerine mixture and no particles. These pure fluid measurements were expected to compare favorably with the theoretical results for Couette flow. Ignoring any end effects, an annular flow where the inner cylinder is stationary and the outer cylinder rotates has a velocity profile given by

$$v(r) = \frac{\Omega r_o^2}{r_o^2 - r_i^2} \left( r - \frac{r_i^2}{r} \right), \quad (3.5)$$

where  $r_i$  and  $r_o$  are the inner and outer radii, respectively, and  $\Omega$  is the angular rotation rate of the outer cylinder (Schlichting 1951). The shear stress, as measured on the inner cylinder, is given by

$$\tau|_{r=r_i} = 2\mu \frac{\Omega r_o^2}{r_o^2 - r_i^2}. \quad (3.6)$$

Thus, the torque on the inner, floating cylinder is

$$M_i = -M_o = 4\pi\mu H \frac{\Omega r_i^2 r_o^2}{r_o^2 - r_i^2}, \quad (3.7)$$

where  $H$  is the height of the floating cylinder. The fluid density and viscosity are a function of both the percentage of glycerine and the temperature. As seen in Figure 3.12 the experimentally obtained values for the shear stress compare well with the values predicted using this theoretical Couette flow solution with the curves for 68% and 75% glycerine easily distinguishable.

There is scatter in the calibration data caused by temperature variations and uncertainties in the experiment at low torques. As the temperature increases during the course of the experiment, the viscosity of the aqueous glycerine decreases, decreasing the measured shear stress. This temperature variation increases with an increase in the percentage of glycerine. The calculated pure fluid torque, used to normalize the measured torque, is corrected for temperature. Additional error is introduced due to the limitations of the experiment. This shear stress is at the lower range of the capabilities of this experimental apparatus (0.3–1000 N/m<sup>2</sup>). There is friction opposing the rotation of the center cylinder, primarily from the seal around the axle. This friction is small, but can interfere with small shear stress measurements. While there is some error in these measurements, they do not



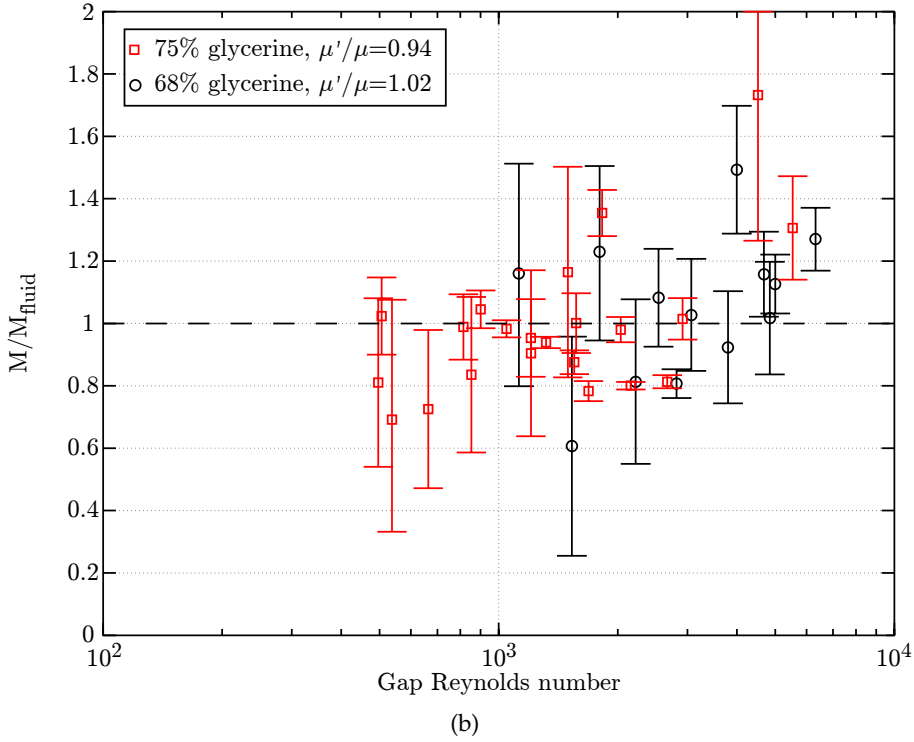
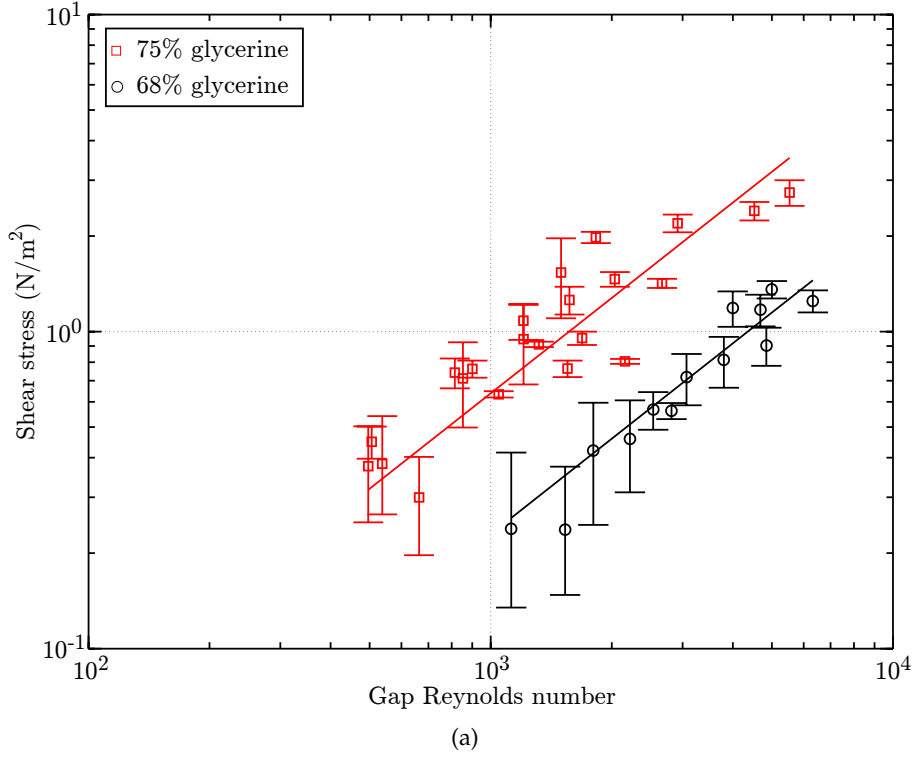


Figure 3.12. Pure fluid calibration showing (a) the measured shear stress and (b) the ratio of measured-to-pure fluid torque for aqueous glycerine mixtures with  $\circ$  68% and  $\square$  75% glycerine. The solid line represents the shear stress predicted using equation (3.6) with temperature adjusted values for the viscosity.

show the sudden increase in shear stress or torque that would occur if secondary flows are present.

### 3.3 Particle characterization

The present thesis includes measurements using five different types of particles. These particles, summarized in Table 3.2, vary in size, shape, and density. The particles also

Table 3.2. Properties for experiments

	Glass	Nylon	Polyester	Polystyrene	SAN
diameter, $d$ (mm)	3.04	6.36	2.93	3.34	3.22
diameter/gap width, $d/b$	0.0962	0.2013	0.0927	0.1057	0.1019
particle density, $\rho_p$ (kg/m <sup>3</sup> )	2520	1150	1400	1050	1070
fluid density, $\rho_f$ (kg/m <sup>3</sup> )	1200	1150	1200	1000 – 1070	1070
shape	spheres	spheres	ellipsoids	elliptical cylinders	ellipsoids
sphericity, $\psi$	0.9998	0.9999	0.9910	0.7571	0.9798
RLP, $\phi_l$	0.597	0.568	0.593	0.553	0.611
RCP, $\phi_c$	0.626	0.627	0.650	0.663	0.657
Young's modulus, $E$ (MPa)	72000	2100	2800	3000	
Yield strength, $Y$ (MPa)	50	45	55	40	
Poisson's ratio $\nu$	0.24	0.40	0.39	0.34	
elastic velocity $u_{el}$ (m/s)	0.001	1.40	1.20	0.592	

show variations in the random loose- and random close-packed volume fractions, but as shown in subsection 2.2.3 and 2.2.4, these volume fractions are influenced by the particle size relative to the container and the particle shape. These particles and their properties are described in detail in the following sections.

#### 3.3.1 Glass

Glass beads are commonly used in laboratory fluid-particulate flows due to their regularity and nearly spherical nature. Soda-lime glass has a density of 2520 kg/m<sup>3</sup> and therefore sinks in aqueous glycerine mixtures (pure glycerine has a density of 1260 kg/m<sup>3</sup>). The particles are nearly perfect spheres as seen in Figure 3.13.

The glass spheres used in this experiment are nearly spherical and by direct measurement of 200 particles, the glass beads were found to have a diameter of  $d = 3.04 \pm .04$  mm.



Figure 3.13. The glass spheres as used in the rheological experiments. The spheres have a specific gravity of 2.52 and have an equivalent spherical particle diameter of  $3.04 \pm .04$  mm. The ruler shown for reference measures in centimeters.

A histogram of the measured diameters is shown in Figure 3.14. As seen in this histogram, the particle diameters are unimodal. The volume was also found by directly measuring the displaced volume of 1000 particles. Using this method, the sphere of equal volume has a diameter  $d = 3.03$  mm. Weighing the sample and assuming a density of  $2520 \text{ kg/m}^3$ , sphere of equal volume is calculated to have a diameter  $d = 3.03$  mm. These methods for calculating the volume of the glass particles are in agreement, and the glass particles are taken to have a sphere of equal volume with a diameter of  $d = 3.03 \pm 0.04$  mm. The loose-packed volume fraction  $\phi_l$  is 0.597 and the close-packed volume fraction  $\phi_c$  is 0.626 (see section 2.3).

### 3.3.2 Nylon

Nylon is an opaque thermoplastic used as a fiber in clothing, ropes, and ladies' stockings as well as being used as the matrix in many composite materials. First produced in 1935 by DuPont, nylon 6-6 is usually championed for its resiliency as it is not vulnerable to chemical decomposition or weathering. Nylon plastic has a density of  $1150 \text{ kg/m}^3$  and is neutrally buoyant in an aqueous glycerine mixture with 58% glycerine by weight. The particles are nearly perfect spheres as seen in Figure 3.15.

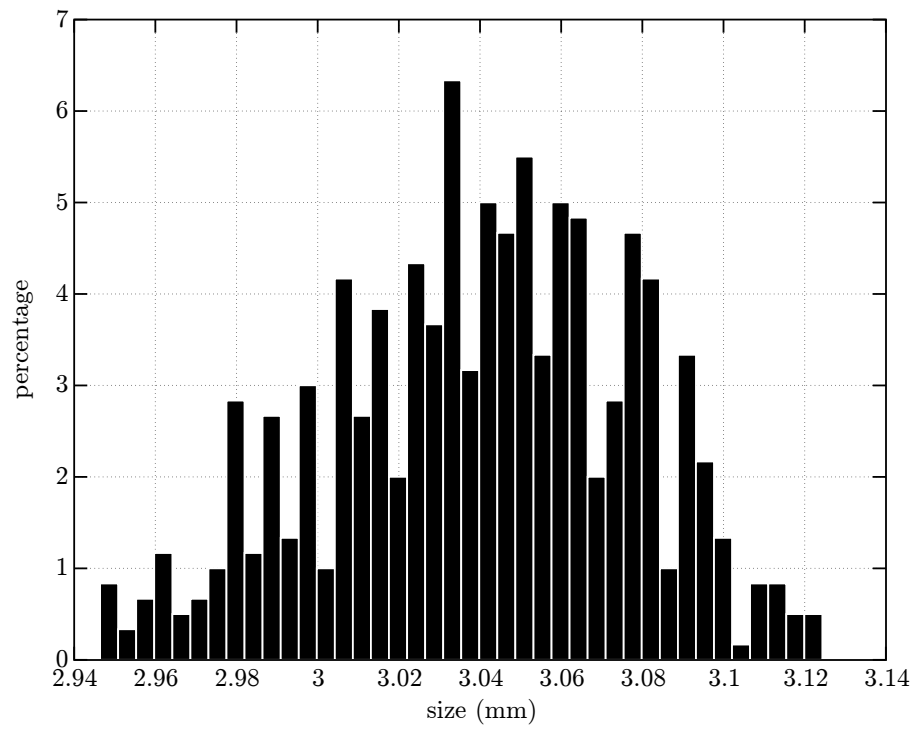


Figure 3.14. Histogram of particle diameters showing the unimodal distribution of particle diameters for 3 mm glass beads.



Figure 3.15. The nylon spheres as used in the rheological experiments. The spheres have a specific gravity of 1.15 and have an equivalent spherical particle diameter of  $6.36 \pm .02$  mm. The ruler shown for reference measures in centimeters.

These nylon spheres have a measured diameter of  $d = 6.36 \pm .02$  mm, as shown in Figure 3.16 for a sample of 200 particles. As seen in this histogram, the particle diameter is unimodal.

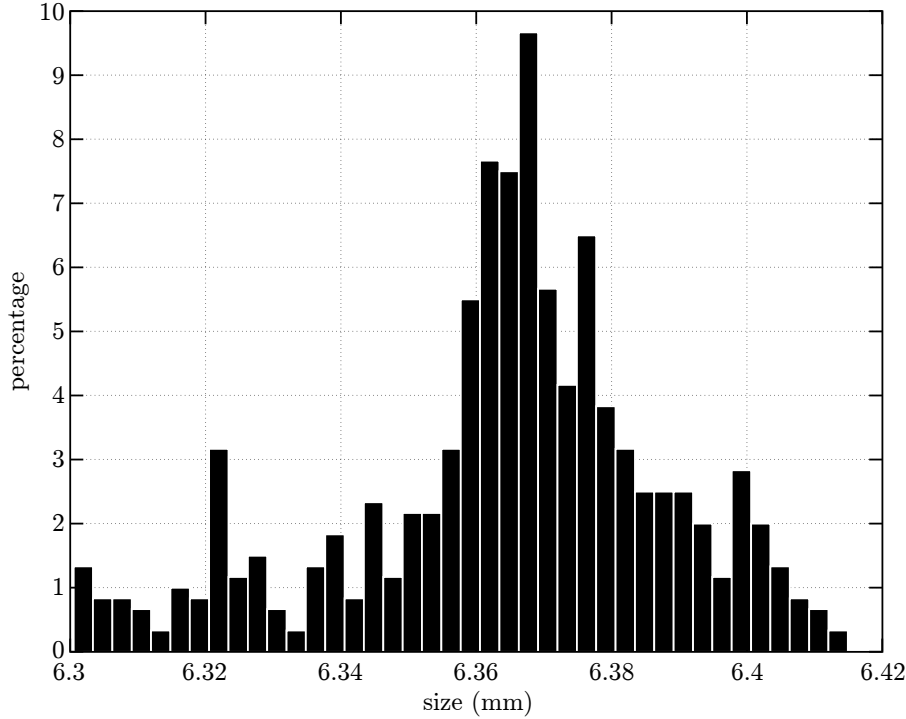


Figure 3.16. Histogram showing the unimodal distribution of nylon particle diameters.

The volume was also found by directly measuring the displaced volume of 1000 particles. Using this method, the sphere of equal volume has a diameter  $d = 6.36$  mm. Weighing this sample and assuming a density of  $1150 \text{ kg/m}^3$ , a sphere of equal volume is calculated to have a diameter  $d = 6.36$  mm. These methods for calculating the volume of the nylon particles are in agreement, and the nylon particles are taken to have a sphere of equal volume with a diameter of  $d = 6.36 \pm 0.02$  mm. The loose-packed volume fraction  $\phi_l$  is 0.568 and the close-packed volume fraction  $\phi_c$  is 0.627 (see section 2.3).

### 3.3.3 Polyester

Polyester resin is a hard, white plastic used in injection molding processes. Polyethylene terephthalate (PET), commonly referred to as polyester, was patented in 1941 by the Calico Printers' Association. It is found in textiles, plastic bottles, and as the matrix in many composite materials including fiberglass. Polyester plastic has a density of  $1400 \text{ kg/m}^3$

and therefore sinks in aqueous glycerine mixtures (pure glycerine has a density of 1260 kg/m<sup>3</sup>). The particles are scalene ellipsoids as seen in Figure 3.17.



Figure 3.17. The polyester scalene ellipsoids as used in the rheological experiments. The ellipsoids have a specific gravity of 1.40 and have an equivalent spherical particle diameter of  $2.93 \pm .02$  mm. The ruler shown for reference measures in centimeters.

These scalene ellipsoids of polyester have smooth sides, with semi-axes  $d_{small} = 2.60$ ,  $d_{medium} = 2.90$ , and  $d_{large} = 3.30$ . A histogram of the measured diameters is shown in Figure 3.18 for a sample of 200 particles. As seen in this histogram, the particle diameters are unimodal. The geometric mean of these three diameters yields the diameter of the sphere of equal volume,  $d = 2.93$  mm.

The volume was also found by directly measuring the displaced volume of 1000 particles. Using this method, the sphere of equal volume has a diameter  $d = 2.95$  mm. Weighing this sample and assuming a density of 1070 kg/m<sup>3</sup>, a sphere of equal volume has a diameter  $d = 2.91$  mm. These methods for calculating the volume of the polyester particles are in agreement, and the polyester particles are taken to have a sphere of equal volume with a diameter of  $d = 2.93 \pm 0.02$  mm. The loose-packed volume fraction  $\phi_l$  is 0.593 and the close-packed volume fraction  $\phi_c$  is 0.650 (see section 2.3).

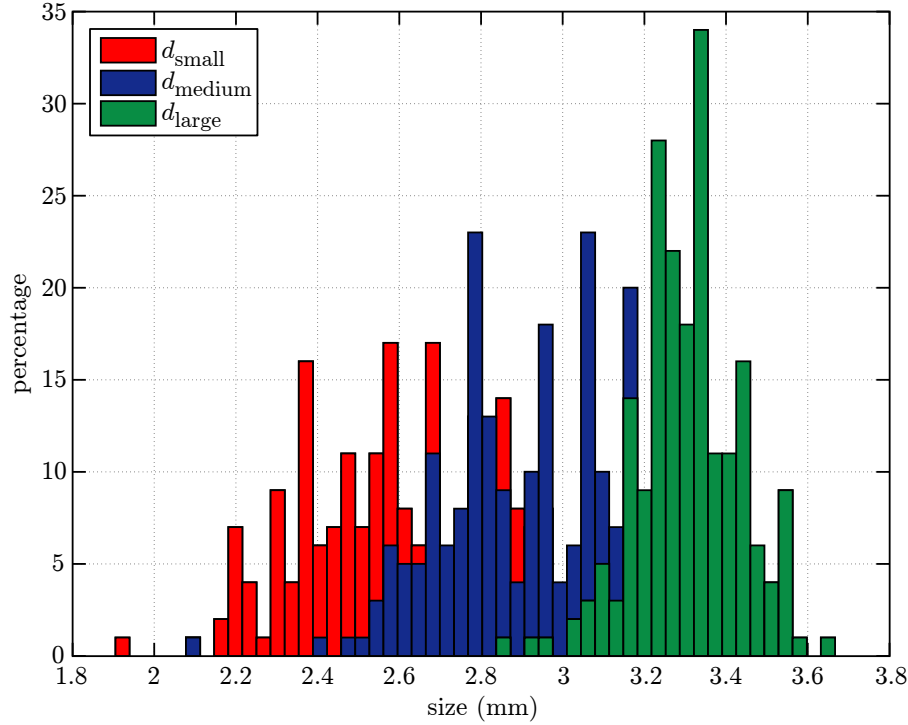


Figure 3.18. Histogram of polyester particle sizes showing the small, medium, and large diameters of the ellipsoid.

### 3.3.4 Polystyrene

Polystyrene is a colorless hard plastic used in injection molding processes that was discovered in 1839 by Eduard Simon. Uncompressed polystyrene, as used in this experiment, is molded into everything from CD cases to children's toys. When expanded with either carbon dioxide or pentane, the plastic is usually known by the trademarked name Styrofoam. Uncompressed polystyrene has a density of  $1050 \text{ kg/m}^3$  and is neutrally buoyant in an aqueous glycerine mixture of 21% glycerine. The polystyrene particles are elliptical cylinders as seen in Figure 3.19.

These elliptical cylinders of polystyrene have smooth sides, but are rough cut to varying lengths. A histogram of the particle diameters and lengths is shown in Figure 3.20 for a sample of 150 particles. This sample had an average small diameter  $d_{\text{small}} = 2.08 \text{ mm}$ , large diameter  $d_{\text{large}} = 2.92 \text{ mm}$ , and length  $l = 3.99 \text{ mm}$ . As seen in this histogram, the particle length is bimodal whereas the diameters are unimodal. Using these average lengths, a sphere of equal volume has a diameter  $d = 3.31 \text{ mm}$  where it is assumed that

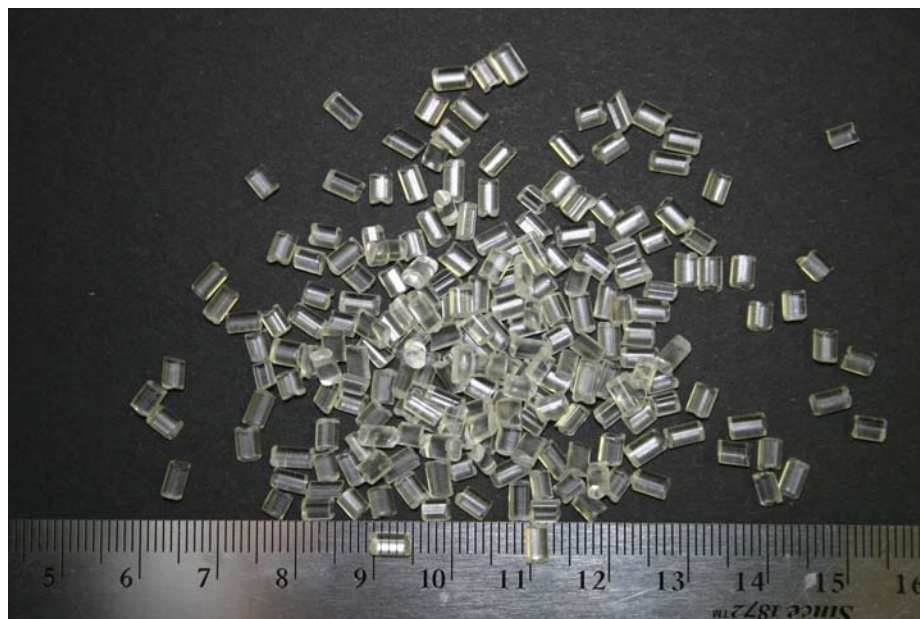


Figure 3.19. The polystyrene elliptical cylinders as used in the rheological experiments. The cylinders have a specific gravity of 1.05 and have an equivalent spherical particle diameter of  $3.34 \pm .02$  mm. The ruler shown for reference measures in centimeters.

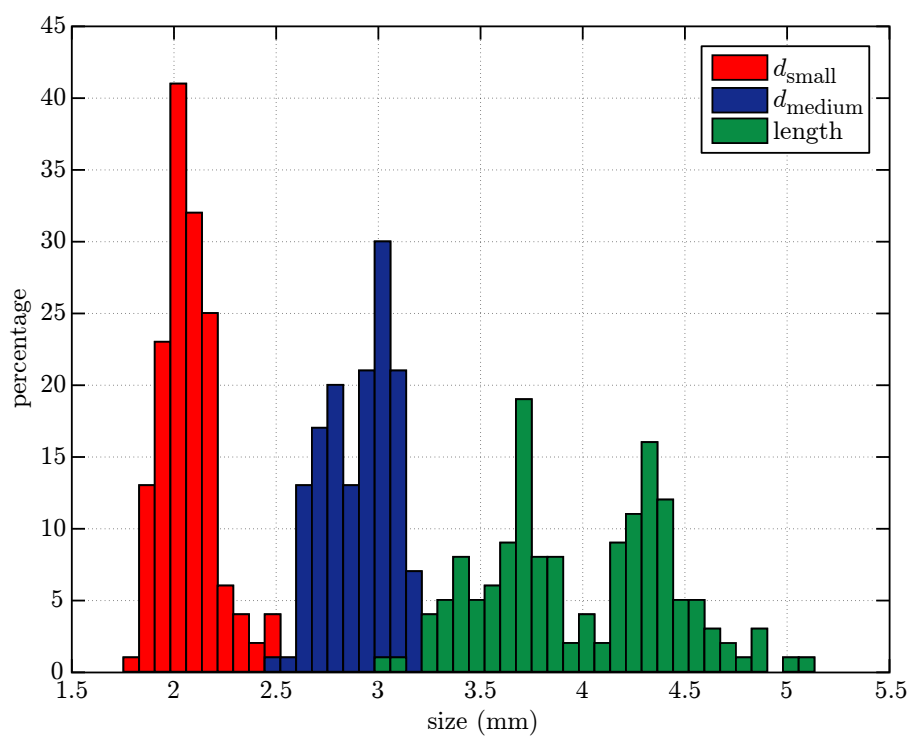


Figure 3.20. Histogram of polystyrene particle sizes showing the largest and smallest measured diameters and the cylinder length.



the volume of each particle is

$$V_p = \frac{\pi}{4} d_{small} d_{large} l. \quad (3.8)$$

The volume was also found by directly measuring the displaced volume of 1000 particles. Using this method, the sphere of equal volume has a diameter  $d = 3.35$  mm. Weighing this sample and assuming a density of  $1050 \text{ kg/m}^3$ , a sphere of equal volume has a diameter  $d = 3.34$  mm. These measurements of the volume of the polystyrene particles are in agreement, and the polystyrene particles are taken to have a sphere of equal volume with a diameter of  $d = 3.34 \pm 0.02$  mm. The loose-packed volume fraction  $\phi_l$  is 0.553 and the close-packed volume fraction  $\phi_c$  is 0.663. (See section 2.3 for more information on how these measurements were conducted.)

### 3.3.5 Styrene acrylonitrile

Styrene Acrylonitrile (SAN) plastic resin is a colorless hard plastic used in injection molding processes. SAN is used in many of the same applications as polystyrene, though it lacks some of the optical clarity. SAN is ideal for use as food containers, kitchenware, and computer products due to its high melting point. SAN resin has a density of  $1070 \text{ kg/m}^3$  and is neutrally buoyant in an aqueous glycerine mixture of 29% glycerine. The particles are flattened scalene ellipsoids as seen in Figure 3.21.

These scalene ellipsoids of SAN have smooth sides, with semi-axes  $a$ ,  $b$ , and  $c$  with the measured medium and large diameters corresponding to  $2b$  and  $2c$ , respectively. The ellipsoid is flattened such that the smallest measured diameter  $d_{small} < 2a$ . A histogram of the measured diameters is shown in Figure 3.22 for a sample of 200 particles. This sample had a peak small radius  $2a > d_{small} = 2.64$  mm, peak medium diameter  $2b = d_{medium} = 3.20$  mm, and peak large diameter  $2c = d_{large} = 3.86$  mm. As seen in this histogram, the particle diameters are unimodal. The geometric mean of these three diameters yields the radius of the sphere of equal volume, assuming that flattened portion of the scalene ellipse does not effect the total volume ( $2a = d_{small}$ ),  $d = 3.20$  mm.

The volume was also found by directly measuring the displaced volume of 1000 particles. Using this method, the sphere of equal volume has a diameter  $d = 3.25$  mm. Weighing this sample and assuming a density of  $1070 \text{ kg/m}^3$ , a sphere of equal volume has a diameter  $d = 3.22$  mm. These measurements are in agreement, and the SAN particles are



Figure 3.21. The SAN scalene ellipsoids as used in the rheological experiments. The ellipsoids have a specific gravity of 1.07 and have an equivalent spherical particle diameter of  $3.22 \pm .02$  mm. The ruler shown for reference measures in centimeters.

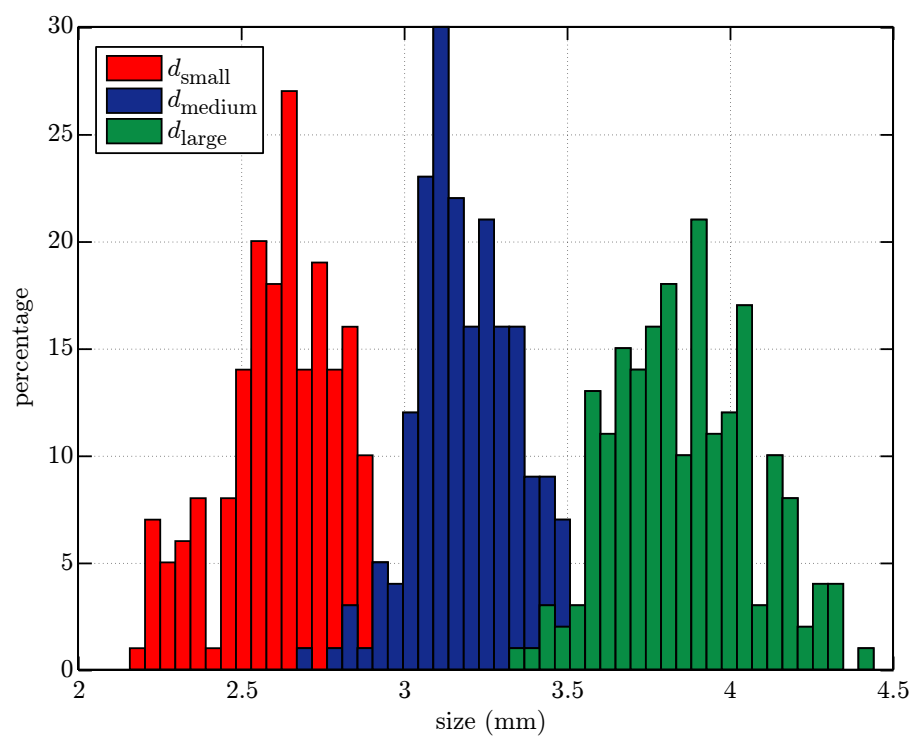


Figure 3.22. Histogram of SAN particle sizes showing the small, medium, and large diameters of the ellipsoid.

taken to have a sphere of equal volume with a diameter of  $d = 3.22 \pm 0.02$  mm. The loose-packed volume fraction  $\phi_l$  is 0.611 and the close-packed volume fraction  $\phi_c$  is 0.657. (See section 2.3 for a description of how these measurements were conducted.)

### 3.4 Summary

The bulk shear stress of the liquid-solid mixture is measured using a coaxial rheometer specifically designed to minimize the effects of secondary flows from these steady-state measurements. The critical design features include a height to gap ratio ( $b/r_o$ ) of 11.7 to delay the onset of Taylor-Couette flows and a gap to outer radius ratio ( $h/b$ ) of 0.166 to reduce the influence of boundary layers near the top and bottom end caps on shear stress measurements. Additionally, the shear stress is measured at the floating test cylinder, further isolating these measurements from the influence of secondary flows near the end caps. The shear stress on the inner cylinder was calculated through measurements of the displacement of the center, floating cylinder. This displacement was opposed by a linear spring, each spring allowing for a specific range of force measurements. Using these measurements of the shear stress, the effective viscosity, relative to the viscosity of the liquid, is calculated. The effective viscosity is measured for five different types of neutrally buoyant and non-neutrally buoyant particles in aqueous glycerine. Each particle is characterized to find its size, sphericity, random close- and loose-packing volume fractions, and density.

In addition to effective viscosity measurements, the particle velocities and volume fraction is measured using optical probes mounted just above and below the center cylinder. These optical probes record a voltage peak due to the reflection of light as a particle passed the probe face. The voltage signals from two adjacent probes is filtered and cross-correlated to find the mean and individual velocities of the particles. These velocity measurements, combined with the count of the number of particles passing each probe and particle size, are used to find the volume fraction of solids. These volume fraction measurements are used in the following sections to investigate the influence of the resuspension of particles on effective viscosity data.

## Chapter 4

# Neutrally buoyant particles

In order to determine the effective viscosity of a fluid-particulate flow, experiments with neutrally buoyant particles are considered first. If the particles are neutrally buoyant, they will be evenly distributed axially within the annulus of the concentric cylinder rheometer. The theory of these flows is discussed first in section 4.1, followed by the experimental results for three different types of particles. The experiments with polystyrene are discussed first and in the most detail (subsection 4.2.1) followed by experiments with nylon (subsection 4.2.2) and SAN (subsection 4.2.3). The results from all three experiments are compared in section 4.3.

### 4.1 Theory

It is the goal of this thesis to examine the shear stresses as a function of the volume fraction of solids  $\phi$ , the Reynolds number, the ratio of fluid-to-particle density, and the Archimedes number, as discussed in section 1.1, where the flow is non-Brownian. If the particles and the fluid are the same density, the Archimedes number is equal to zero and the density ratio is one for all cases, thus the effective viscosity should only depend on the volume fraction and Reynolds number.

At very low volume fractions,  $\phi \ll 1$ , the dynamics of the fluid-particulate mixture deviates only slightly from the dynamics of the fluid alone. These dilute suspensions were studied in detail by Einstein (1906), Batchelor (1970, 1977), Batchelor and Green (1972) among many others. For non-Brownian suspensions of rigid spheres, Batchelor and Green

added a second order correction to Einstein's effective viscosity,

$$\mu'/\mu = 1 + 2.5\phi + 7.6\phi^2 \quad (4.1)$$

where  $\mu$  is the fluid viscosity and  $\mu'$  is the effective viscosity of the fluid-particulate mixture.

At higher volume fractions, particles collide with increasing frequency. For rigid particles, as the volume fraction nears the maximum packing volume fraction, the force required to slide particles past each other tends toward infinity. For the current experiments, the particles are not perfectly rigid, but the force required still increases dramatically as the volume fraction nears maximum packing. The force required to deform the mixture can be expressed in terms of an effective viscosity for the bulk fluid  $\mu'$ .

It was hypothesized in section 2.1 that there should be a transition between flows with a volume fraction less than the random loose-packing volume fraction and those between the RLP and RCP. While the form of either curve is not known, the curves should match the limits for  $\phi \ll 1$ ,  $\phi \approx \phi_c$ , and each other at  $\phi_l$ . Furthermore, each curve should show an increasing dependence on volume fraction.

In addition to a dependence on volume fraction, there may also be a dependence on Reynolds number. The fluid itself is Newtonian, having a constant viscosity, but the interactions between particles may depend on the rate of rotation of the outer cylinder,

$$\mu'/\mu = f\left(\phi, \text{Re}, \frac{d}{b}\right). \quad (4.2)$$

Such interactions certainly do depend on the rate of rotation for non-neutrally buoyant particles, but for these neutrally buoyant particles, this dependence will need to be experimentally determined.

## 4.2 Experiments

Using an aqueous glycerine mixtures matched to the density of the particles, experiments were conducted in the concentric cylinder rheometer. In these experiments, the volume fraction of particles was varied while the resulting shear stress  $\tau$  on the inner, floating

cylinder was calculated from measurements of the torque using

$$M = 2\pi H r_i^2 \tau, \quad (4.3)$$

as a function of Reynolds number, where the floating cylinder height  $H$  is 11.22 cm (4.42 in), the inner radius of the annulus  $r_i$  is 15.89 cm (6.26 in), and the outer radius of the annulus  $r_o$  is 19.05 cm (7.50 in). All torque measurements were made several minutes after the onset of the shearing motion and are considered to be steady-state measurements.

The measured shear stress is compared to the shear stress for the fluid alone to find an effective viscosity ratio. For an annular geometry with the outer cylinder rotating and the inner cylinder stationary, the shear stress  $\tau$ , as measured on the inner cylinder, can be related to the viscosity through (Schlichting 1951)

$$\tau = 2\mu \frac{\Omega r_o^2}{r_o^2 - r_i^2}. \quad (4.4)$$

The shear stress measured for several aqueous glycerine mixtures compared favorably with the shear stress predicted using equation (4.4), and thus this equation is used to normalize the measured shear stresses.

The experimental apparatus is designed to record the torque by measuring the displacement of a target attached to the center, floating cylinder relative to a stationary base. The initial displacement of the target is held stationary for each experiment with a constant volume fraction, but is not necessarily constant between series of experiments. In addition to uncertainty in the initial displacement, the displacement is opposed by a linear spring, which may require an initial force based on the spring's tautness before any displacement is recorded. To overcome these uncertainties in determining the torque for any individual measurement, the experiment can either be calibrated for each experiment, as it was with the pure fluid measurements, or the slope between points in each experiment can be used to adjust this curve-fit through the origin.

Any error in the  $y$ -intercept in a shear stress versus Reynolds number graph can affect the recorded shear stress values, but does not influence the measurement of the effective viscosity. The shear stress data is found using equation (4.3) and any error in zeroing the torque data adds a constant offset shear stress. The effective viscosity for each volume

fraction experiment is found using the slope of the shear stress curve-fit, a value that does not change with any error in the initial offset.

#### 4.2.1 Polystyrene

The shear stress measurements taken for a range of volume fractions are shown in Figure 4.1 on a log-log plot. Each point represents the mean value of at least five individually recorded measurements shown with error bars representing the standard deviation in these measurements. For each volume fraction, the shear stress is shown with its linear fit. The shear stress increases rapidly with the volume fraction, varying by several orders of magnitude between the smallest and largest volume fraction. The dependance on the volume fraction appears to be more pronounced as the volume fraction increases. The linear

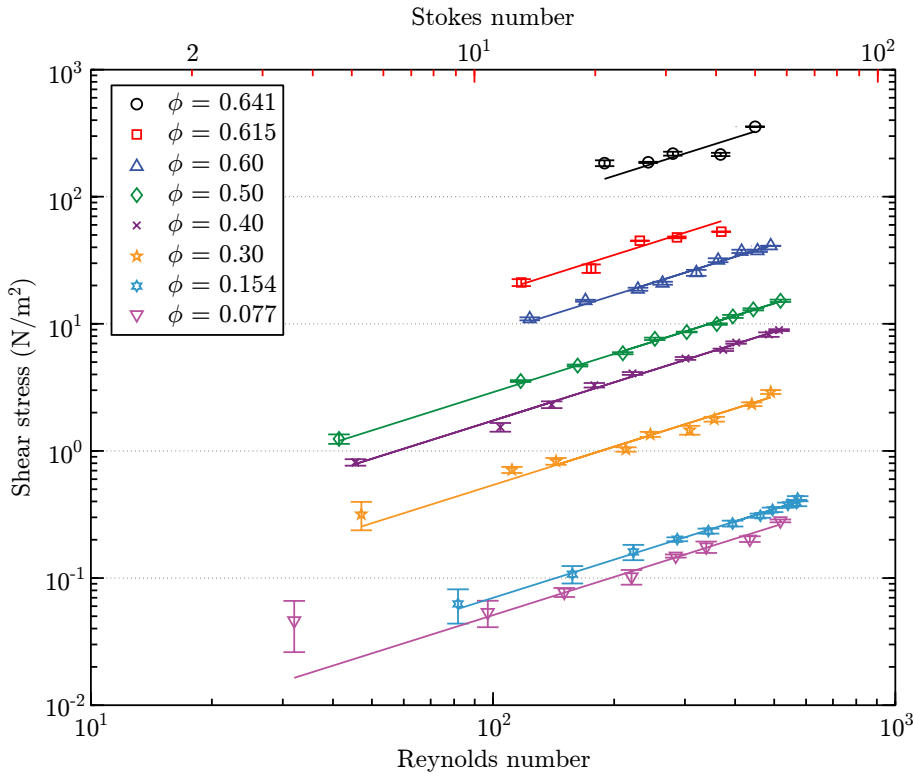


Figure 4.1. Shear stress measurements for suspensions of polystyrene particles in aqueous glycerine. The lines represent linear fits for each volume fraction, fits that are constrained to pass through the origin.

increase in shear stress with the Reynolds number implies that fluid-particulate flow, like the pure fluid flow, is Newtonian ( $\tau = \mu' \dot{\gamma}$ ) with the particles as it is with the pure fluid alone.

For neutrally buoyant particles, the Stokes number is equal to one-ninth of the Reynolds number. For the polystyrene, the Stokes number ranges from 3.5 to 63. For all but the lowest Stokes numbers, the collisions between particles will show a clear rebound. The coefficient of restitution between plastic particles colliding at these low Stokes numbers will be small – less than 0.6. For these low coefficients of restitution, particles collisions represent significant damping of the particle velocities.

The nature of the effective viscosity can easily be seen by considering the ratio of measured torque to the torque predicted using the pure fluid viscosity, as seen in Figure 4.2. The ratio of torques,  $M/M_{\text{fluid}}$ , is clearly a function of the volume fraction, but does not

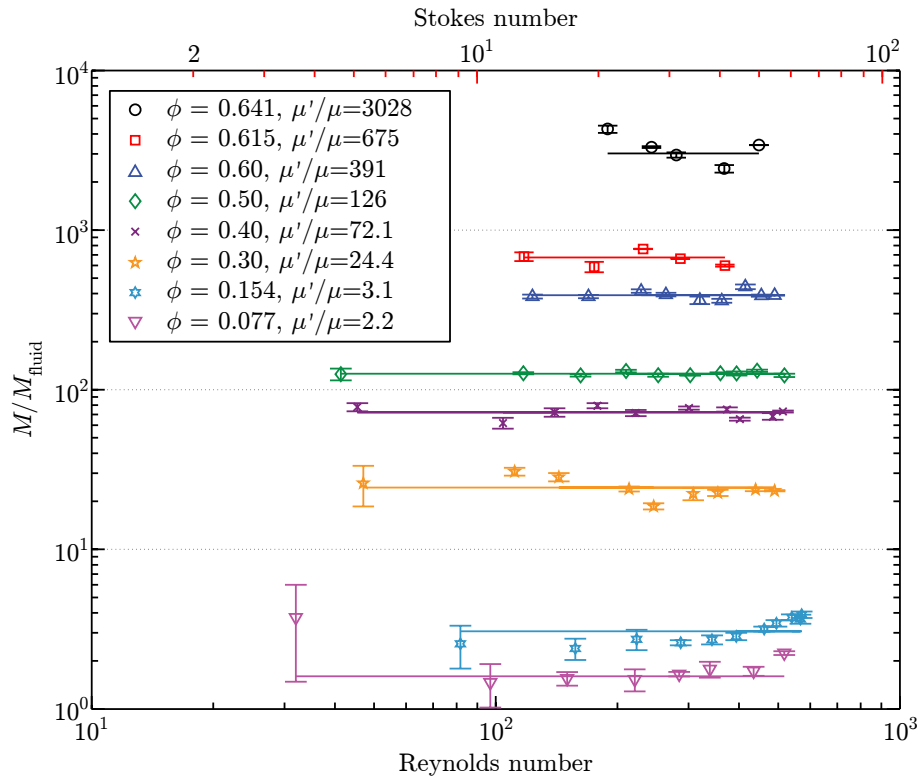


Figure 4.2. Ratio of measured-to-pure fluid torques for suspensions of polystyrene particles in aqueous glycerine. This ratio is fitted by a constant, unique to each volume fraction  $\phi$ . This constant is the ratio of the effective viscosity to the pure fluid viscosity,  $\mu'/\mu$ .

appear to depend greatly on the Reynolds number. For most volume fractions, the ratio of torques is fairly constant as would be expected with a Newtonian fluid. For the two lowest volume fractions ( $\phi = 0.077$  and  $\phi = 0.154$ ), the ratio of torques does increase slightly with Reynolds number, which may be due to the onset of secondary flows in the fluid (see discussion below). Additionally, for the largest volume fraction measured, the particles stick



and slip against the inner cylinder creating torque that is more uneven and may depend on the Reynolds number.

The ratio of torques  $M/M_{\text{fluid}}$  is equal to the effective viscosity ratio  $\mu'/\mu$ . It can be seen to be a function of the volume fraction, but does not appear to vary dramatically with the Reynolds number. The effective viscosity is thus taken as only a function of the volume fraction of solids

$$\mu'/\mu = f(\phi), \quad (4.5)$$

as in Figure 4.3. For points below  $\phi_l$ , the effective viscosity is fitted by an exponential

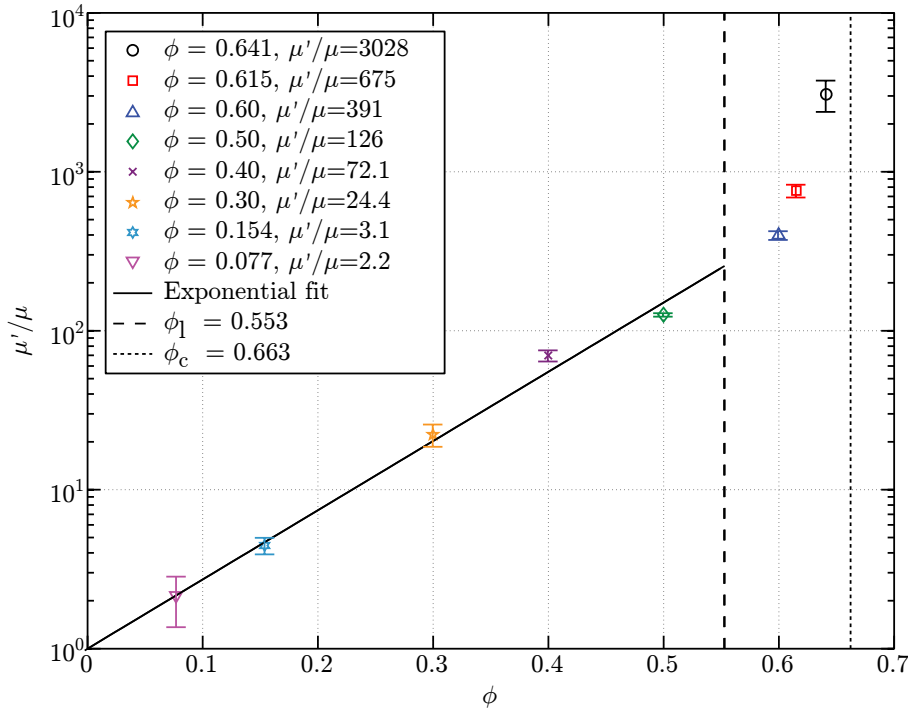


Figure 4.3. Effective viscosity ratio for neutrally buoyant polystyrene particles in aqueous glycerine solutions. The black line is an exponential fit for the points below  $\phi_l$ , dashed vertical lines denote the loose-packing and close-packing volume fractions.

$$\mu'/\mu = \exp\left(5.41 \frac{\phi}{\phi_l}\right). \quad (4.6)$$

For volume fractions greater than  $\phi_l$ , the effective viscosity grows more quickly than the exponential fit. This deviation is expected as the particles near a region of jamming where more force is required to shear the particle layers.

In the experiments with the lowest volume fractions ( $\phi = 0.077$  and  $\phi = 0.154$ ), there

was a slight increase in effective viscosity with the Reynolds number (Figure 4.2). This increase begins for gap Reynolds numbers between  $1 \times 10^4$  and  $3 \times 10^4$ . For the apparatus used in these experiments, the critical Reynolds number for the onset of Taylor-Couette flow is at  $1.8 \times 10^4$ , certainly within the range of the increase measured. The higher volume fractions do not see such an increase in effective viscosity beyond this critical Reynolds number. If the variation in the data is considered as a function of the Reynolds number using the mean effective viscosity and gap width

$$\text{Re}'_b = \frac{\rho \dot{\gamma} b^2}{\mu'} \quad (4.7)$$

as in Figure 4.4, the increase from the mean value for these low volume fraction exper-

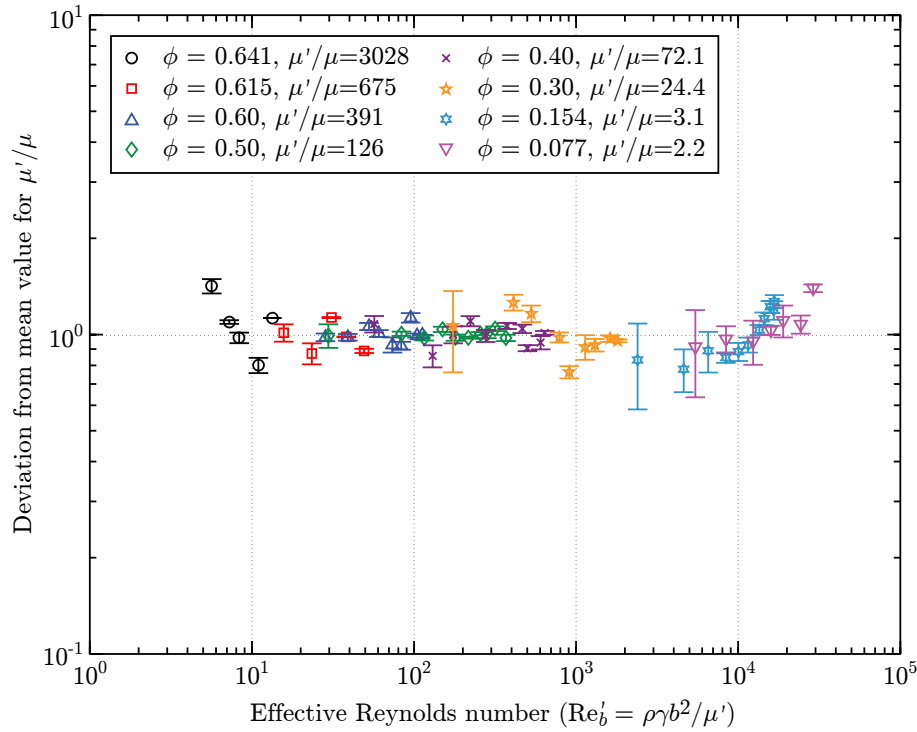


Figure 4.4. Deviation from the mean effective viscosity ratio for neutrally buoyant polystyrene particles in aqueous glycerine solutions as a function of the Reynolds number based on the mean effective viscosity.

iments is clearly observed. The much lower effective viscosity measured for these low volume fraction cases separates these two cases from the others in terms of the  $\text{Re}'_b$ . The increase in effective viscosity with Reynolds number present in two lowest volume fraction experiments may be due to the onset of secondary flows. In these two experiments,

there is an increase at a  $Re'_b \approx 1 \times 10^4$ . This is below the Reynolds number for the onset of Taylor vortices for the present experimental apparatus ( $Re_b = 1.8 \times 10^4$ ), and may represent the point at which the vortices caused by the stationary end caps begins to impinge on the floating cylinder.

In addition to the experiments with neutrally buoyant polystyrene, experiments were also conducted with nylon and styrene acrylonitrile (SAN). The results from these additional experiments are summarized in the following sections.

#### 4.2.2 Nylon particles

Experiments with nylon particles were conducted using an aqueous glycerine mixture of 56% glycerine by weight. The nylon particles were very nearly spherical ( $\psi = 1.0$ ) and had a diameter of 6.36 mm, about twice the size of the polystyrene. Lower volume fractions ( $\phi = 0.10, 0.20$  and  $0.295$ ) were tested using the nylon as seen in Figure 4.5. Only these

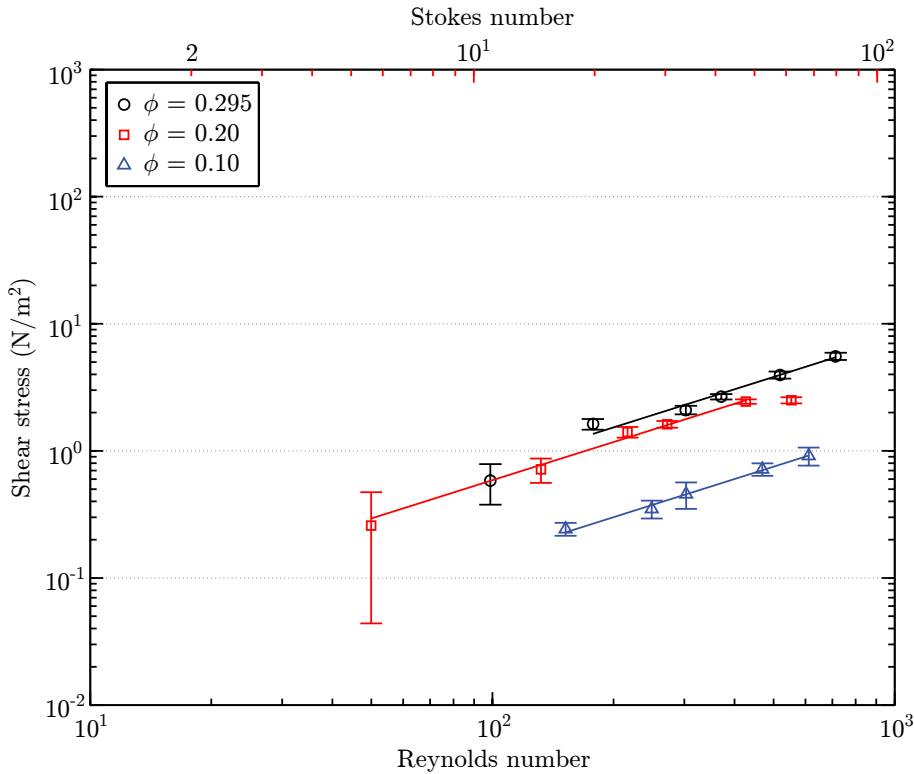


Figure 4.5. Shear stress measurements for suspensions of nylon particles in aqueous glycerine. The lines represent linear fits for each volume fraction, fits that are constrained to pass through the origin.

volume fractions were tested due to the limited availability of these particles. As with the

polystyrene measurements (Figure 4.1), the shear stress grows linearly with the Reynolds number and shows a strong dependence on the volume fraction.

For this neutrally buoyant nylon, the Stokes number ranges from 5.5 to 80. All of the collisions between particles will show a clear rebound. The coefficient of restitution between plastic particles colliding at these low Stokes numbers will be small – less than 0.7. For these low coefficients of restitution, particles collisions represent significant damping of the particle velocities.

The ratio of torques, Figure 4.6, is nearly constant implying that this flow may also

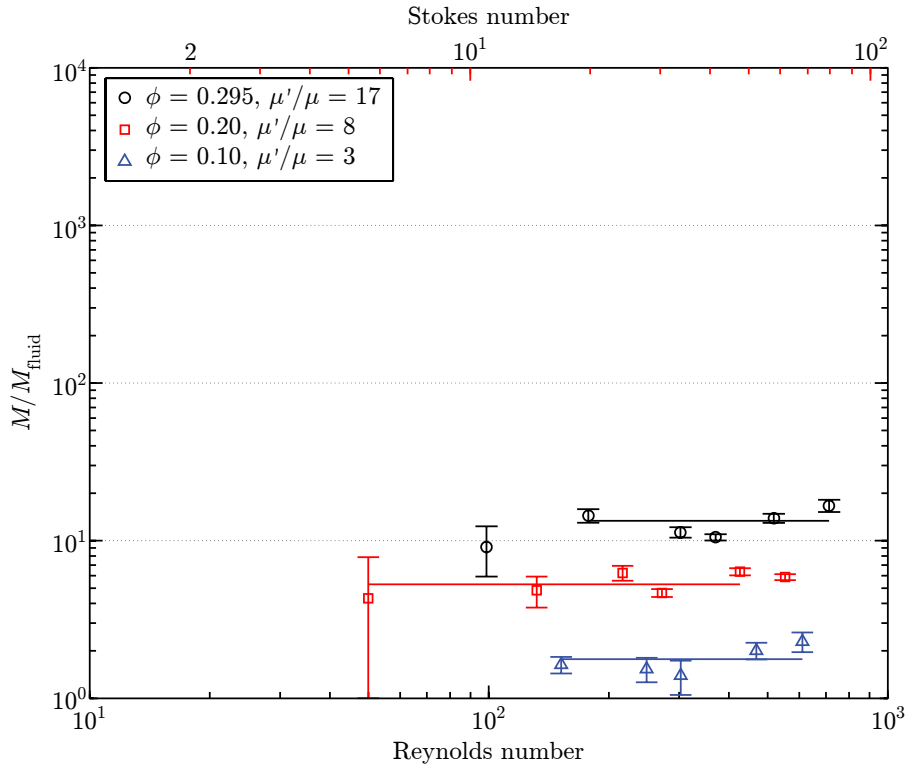


Figure 4.6. Ratio of measured-to-pure fluid torques for suspensions of nylon particles in aqueous glycerine. This ratio is fitted by a constant, unique to each volume fraction  $\phi$ . This constant is the ratio of the effective viscosity to the pure fluid viscosity,  $\mu'/\mu$ .

be considered Newtonian where the effective viscosity is only a function of the volume fraction, as shown in Figure 4.7. All of the volume fractions measured are below  $\phi_l$ , and are fitted by an exponential

$$\mu'/\mu = \exp\left(5.49 \frac{\phi}{\phi_l}\right). \quad (4.8)$$

For reference, the loose-packing and close-packing volume fractions are denoted with dashed and dotted vertical lines.

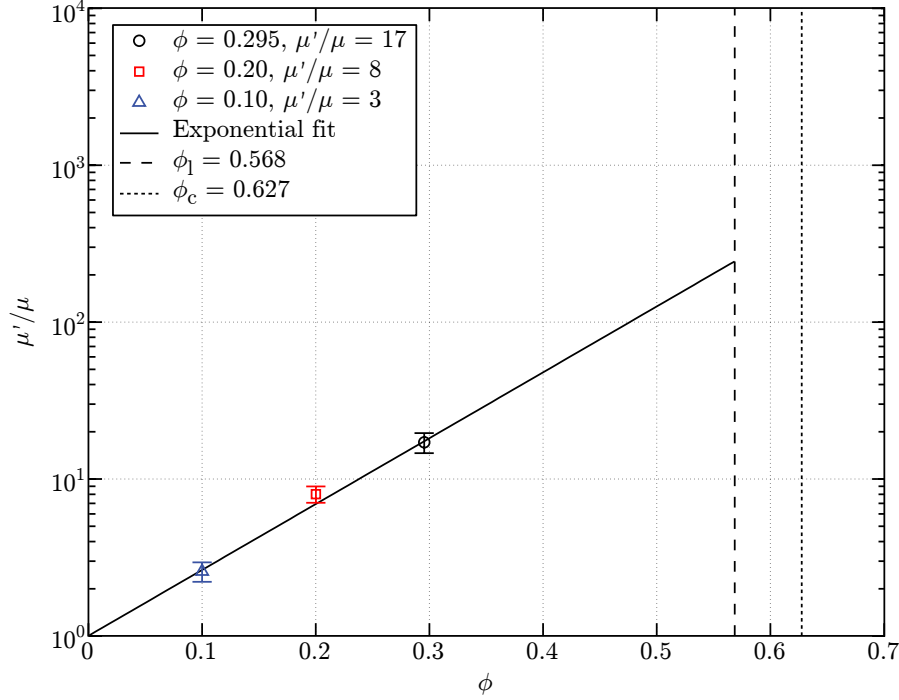


Figure 4.7. Effective viscosity ratio for neutrally buoyant nylon particles in aqueous glycerine solutions. The black line is an exponential fit for the points below  $\phi_l$ , dashed vertical lines denote the loose-packing and close-packing volume fractions.

### 4.2.3 Styrene Acrylonitrile

Using an aqueous glycerine mixture of 29% glycerine by weight, matched to the density of the SAN particles, experiments were conducted for volume fractions of  $\phi = 0.40, 0.50, 0.60$ , and  $0.657$ . The SAN particles are flattened ellipsoids with sphericity  $\psi = 0.98$  and a diameter of  $3.22$  mm, close to the diameter of the polystyrene.

The shear stress measurements are shown in Figure 4.8 with the linear fits and the ratio of torques are shown in Figure 4.9. For the neutrally buoyant SAN, the Stokes number ranges from  $2.6$  to  $60$ . The lowest Stokes numbers ( $St \lesssim 9$ ) there will be a clear point of contact between the particles, but no clear rebound. This behavior results in the coalescence of particles during interactions. At higher Stokes numbers, collisions between particles will show a clear rebound. The coefficient of restitution between plastic particles colliding at these low Stokes numbers will be small – less than  $0.6$ . For these low coefficients of restitution, particles collisions represent significant damping of the particle velocities.

The ratio of torques,  $M/M_{\text{fluid}}$ , are constant with the Reynolds number and are taken as only a function of the volume fraction as shown in Figure 4.10. For points below  $\phi_l$ , the

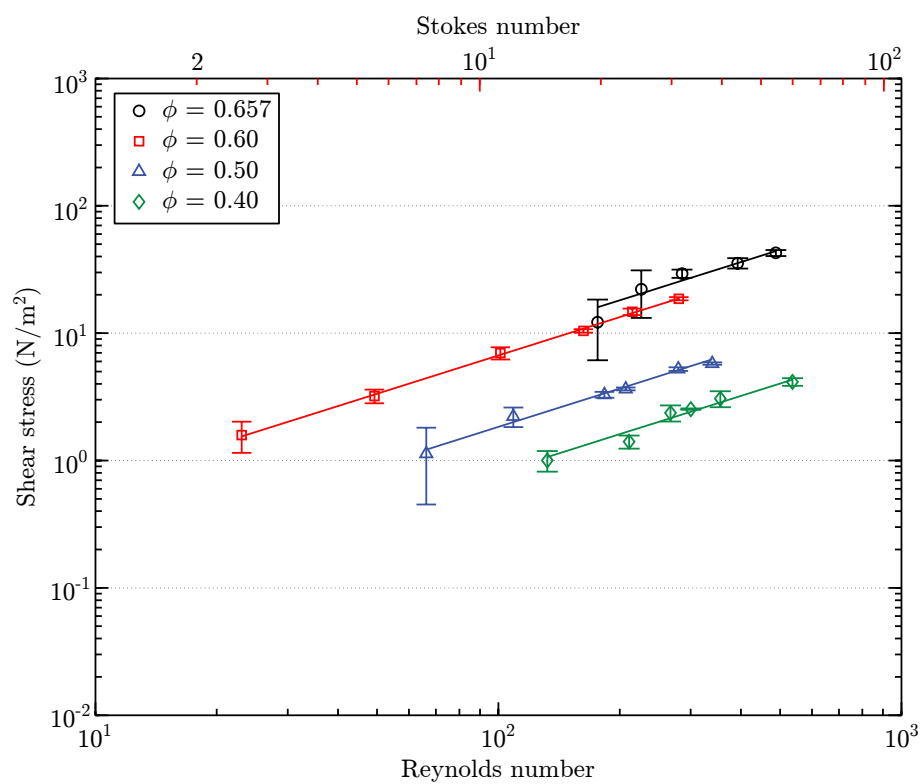


Figure 4.8. Shear stress measurements for neutrally buoyant SAN particles in aqueous glycerine. The lines represent linear fits for each volume fraction, which are constrained to pass through the origin.

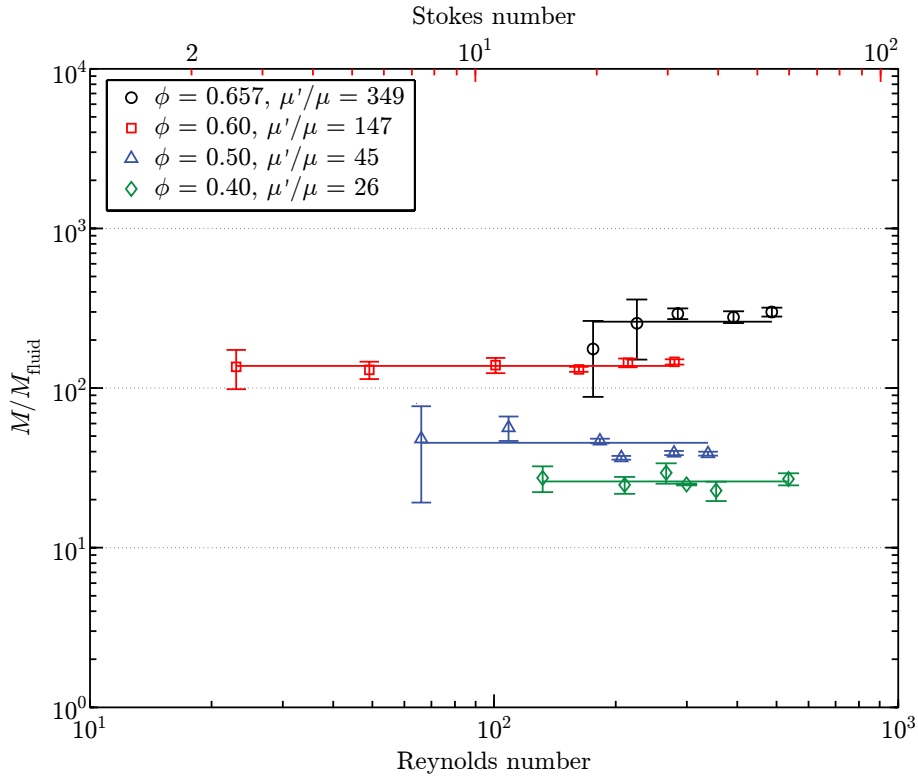


Figure 4.9. Ratio of measured-to-pure fluid torques for suspensions of SAN particles in aqueous glycerine. This ratio is fitted by a constant, unique to each volume fraction  $\phi$ . This constant is the ratio of the effective viscosity to the pure fluid viscosity,  $\mu'/\mu$ .

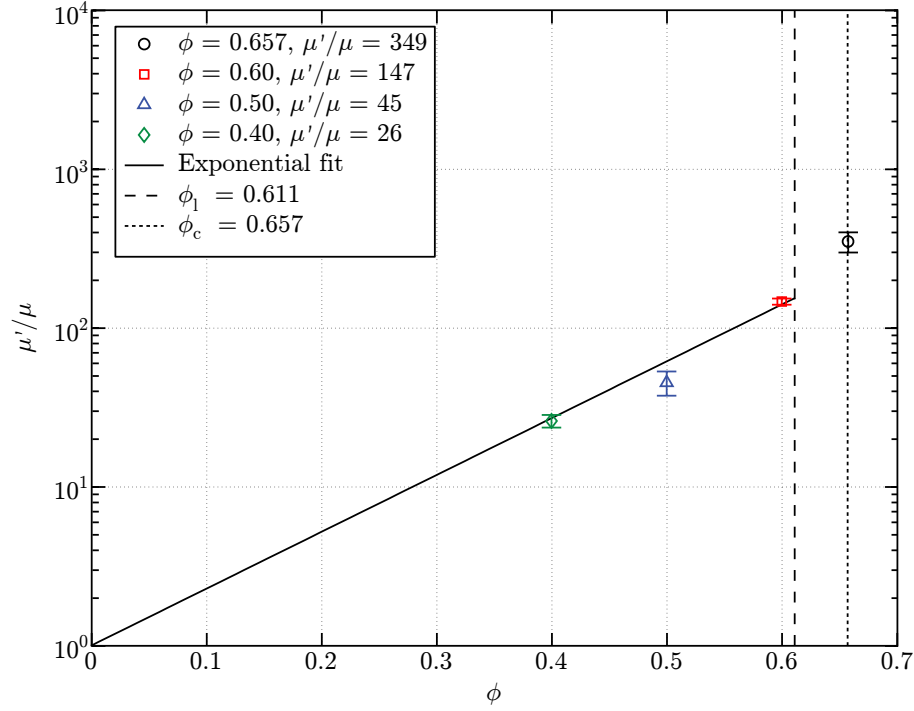


Figure 4.10. Effective viscosity ratio for neutrally buoyant SAN particles in aqueous glycerine solutions. The black line is an exponential fit for the points below  $\phi_l$ , dashed vertical lines denote the loose-packing and close-packing volume fractions.

effective viscosity is fitted by an exponential. For the higher volume fraction point which lies near the close-packed volume fraction, the effective viscosity is greater than predicted using the exponential fit

$$\mu'/\mu = \exp\left(5.04 \frac{\phi}{\phi_l}\right). \quad (4.9)$$

The loose-packing and close-packing volume fractions are shown in Figure 4.10 with a dashed and dotted line, respectively.

### 4.3 Summary

The effective viscosity for three different neutrally buoyant particles was experimentally determined in the preceding section (section 4.2). It was hypothesized in section 4.1 that the effective viscosity should transition at the random loose-packed volume fraction, a proposition that appears to be substantiated by the experimental data. In order to compare the three experiments, the volume fraction is normalized by the RLP as shown in Figure 4.11. For all of the particles tested, the effective viscosity is only a function of this



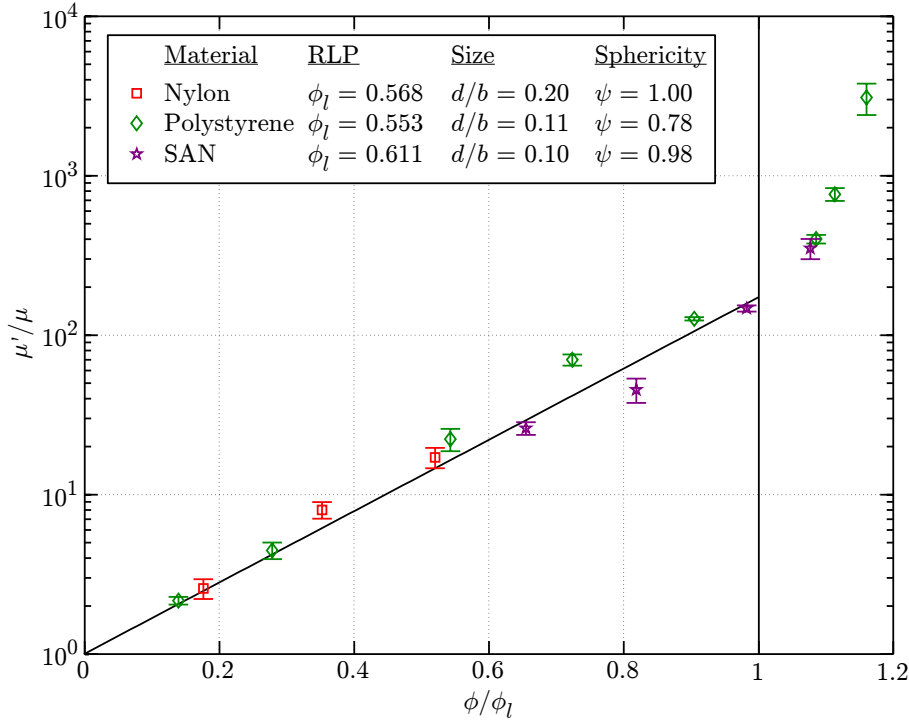


Figure 4.11. Effective viscosity for neutrally buoyant particles in aqueous glycerine.

volume fraction ratio and is fitted well by an exponential for  $\phi < \phi_l$

$$\mu'/\mu = \exp\left(5.15 \frac{\phi}{\phi_l}\right). \quad (4.10)$$

For larger volume fractions, the effective viscosity grows faster than exponentially as the volume fraction nears the RCP.

When normalized by the size and shape dependent RLP, the effective viscosity shows no further influence from the particle size or shape. Comparing the nylon to the SAN, both have a high sphericity ( $\psi = 1.00$  and  $0.98$ ), but the nylon are nearly twice the size of the SAN ( $d = 6.36$  and  $3.22$  mm). Almost 10 SAN particles can fit across the gap while only 5 nylon beads are able to fit. Despite this drastic difference in size, when normalized by their respective RLP volume fractions, both experiments show the same effective viscosity. Comparing the rod-shaped polystyrene to the nearly spherical SAN, it can be seen that there is also no deviation for sphericity for the particles tested. As discussed in subsection 2.2.3 and 2.2.4, the volume fraction is dependent on the particle size and shape. Thus, it is consistent that by normalizing against the RLP, any influence on the particle size or

shape would be eliminated from the effective viscosity.

The results from the present experiments can be compared to the previously published experiments, as shown in Figure 4.12. In this figure, only the neutrally buoyant exper-

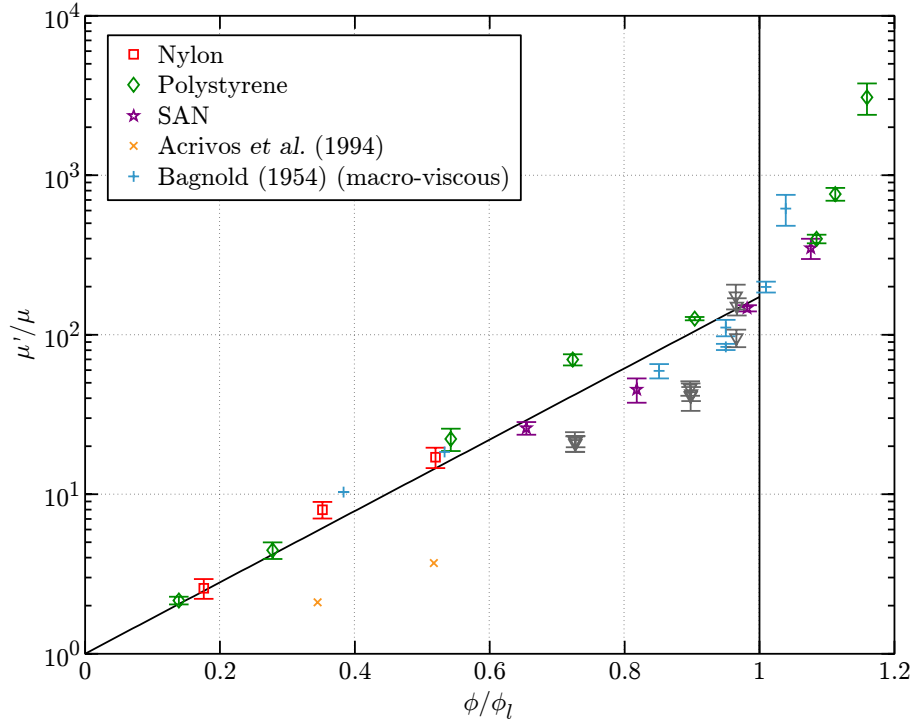


Figure 4.12. Effective viscosity for neutrally buoyant particles in aqueous glycerine.

iments of Acrivos *et al.* (1994) and the macro-viscous experiments of Bagnold (1954) are considered. As discussed in section 1.2, these are the experiments that are both neutrally buoyant and without secondary flows. The macro-viscous data from Bagnold compares favorably with the current experiments showing a similar transition at the RLP volume fraction. The PMMA used in the experiments of Acrivos *et al.* were significantly smaller ( $d = 0.1375$  mm) and were tested at a much lower Reynolds number (0.3–13) implying that the fluid-particulate flow may be in a different flow regime.

Additional data on neutrally buoyant polystyrene is included in chapter 6. In this chapter, the influence of slip against the cylinder walls is investigated.



## Chapter 5

# Non-neutrally buoyant particles

The effective viscosity of a flow consisting of neutrally buoyant particles in a Newtonian fluid was discussed in chapter 4. These experiments showed that the effective viscosity grows exponentially with the volume fraction for volume fractions less than the random loose-packing volume fraction, and that the effective viscosity transitions to a faster region of growth for the region between the random loose- and the random close-packed volume fractions.

In this chapter, these flows are examined with the added complexity of non-neutrally buoyant particles. The theory regarding this change is discussed first, in section 5.1 followed by the experimental results for three different types of particles: polystyrene (subsection 5.2.1), glass (subsection 5.2.2), and polyester (subsection 5.2.3). As with the previous chapter, the experiments with polystyrene are discussed in the greatest detail and the results of these experiments are used for the other particles.

### 5.1 Theory

As with neutrally buoyant particles in a Newtonian fluid for non-neutrally buoyant particles, the volume fraction of solids has a dramatic influence on the effective viscosity. In all of the experiments outlined in the previous chapter, measurements were taken when the experiment reached a steady state. For particles with a density different than the interstitial fluid, the particles tend to float or sink away from the floating cylinder, at which the shear stress measurements are taken. As the particles migrate away from the central, floating cylinder, the local volume fraction decreases, a change that is likely to alter the effective viscosity ratio.

The migration of particles in the fluid creates several flow regimes. When the settling velocity of the particles is much less than the mixing velocities in the shear cell, the mixture becomes homogeneous. This homogeneous mixture may be obtained in these experiments through a combination of using a fluid density close to that of the particle velocity (thereby reducing the settling velocity) or by increasing the rate of rotation (thereby increasing the mixing velocity). If mixing is decreased or if the density ratio differs greatly from unity, the particles settle into a heterogeneous mixture. The Archimedes and Reynolds numbers, discussed in subsection 1.1.4, determine the rate of mixing. In these current experiments, the mixture is assumed to be heterogeneous and the volume fraction is directly measured.

By adjusting for the actual volume fraction across the floating cylinder, the effective viscosity for non-neutrally buoyant particles should match that obtained for neutrally buoyant particles.

## 5.2 Experiments

For non-neutrally buoyant mixtures of particles in aqueous glycerine, the torque on the inner cylinder is recorded and used to find the effective viscosity. This process is identical to the methods for neutrally buoyant particles. As the particles are not evenly distributed axially in the annulus, optical sensors are used to record particle counts and velocities near the inner cylinder. This data from the optical sensors is used to determine the volume fraction of particles across the floating cylinder. The method for determining the volume fraction using the optical sensor data is discussed in detail in subsection 3.2.1. For all of the experiments discussed in the following sections, the particles are not fluidized using inflow from the bottom of the annulus.

In the following sections, non-neutrally buoyant experiments for polystyrene, glass, and polyester are described. The polystyrene experiments are discussed first and in the most detail, as they were for the neutrally buoyant experiments. In section 5.3, all of the non-neutrally buoyant experiments are compared with the neutrally buoyant experiments of this thesis and with previously published data.

### 5.2.1 Polystyrene

The polystyrene particles used in the non-neutrally buoyant experiments are identical to those used in the neutrally buoyant experiments. These particles are elliptical cylinders with a diameter of equal volume of  $d = 3.34$  mm and sphericity  $\psi = 0.76$ . The particles have a density  $\rho = 1050$  kg/m<sup>3</sup>, and experiments were conducted in aqueous glycerine mixtures with a density between  $\rho_f = 1000$  and 1070 kg/m<sup>3</sup>. By varying the fluid density, specific relations for the volume fraction can be determined based on the particle buoyancy. In this section, the data from the optical sensors is discussed first (subsection 5.2.1.1 and 5.2.1.2) followed by measurements for the effective viscosity (subsection 5.2.1.3).

#### 5.2.1.1 Particle velocity

Using two MTI optical sensors, the particle velocity is found at the observation ports above and below the center, floating cylinder. The probes are located 2.86 cm (1.13 in) above and below the floating test cylinder, where the velocity is measured at the lower probes and the particle counts are measured both above and below the test cylinder. The velocity was only measured on the lower signals in order to maximize the number of particles passing the sensors. The method for finding the velocity is described in detail in subsection 3.2.1, but entails the cross correlation of both a full ten second signal and individual particle peaks to find both the mean velocity and individual velocities for each particle, a process that is repeated for each rotational speed.

The mean particle velocities are shown in Figure 5.1(a). The particle velocity shows a positive dependence on the rotational velocity of the outer cylinder, but does not follow perfectly the velocity predicted using laminar Couette flow (dotted black line). The particles in a fluid with a density within 1% of the particle density ( $\rho_f/\rho_p = 0.997 - 1.009$ ) follow the fluid closely at higher speeds, but deviate at lower speeds. The particle velocity shows increased slip as the density of the fluid departs from the particle density with the greatest slip occurring for particles in water ( $\rho_f/\rho_p = 0.951$ ). This slip is investigated further in chapter 6.

For the fluids that are not within 1% of the particle density, there appears to be a transition between a region of rapid growth in particle velocity for low rotational velocities and a region of more slowed growth in particle velocity for high rotational velocities. In

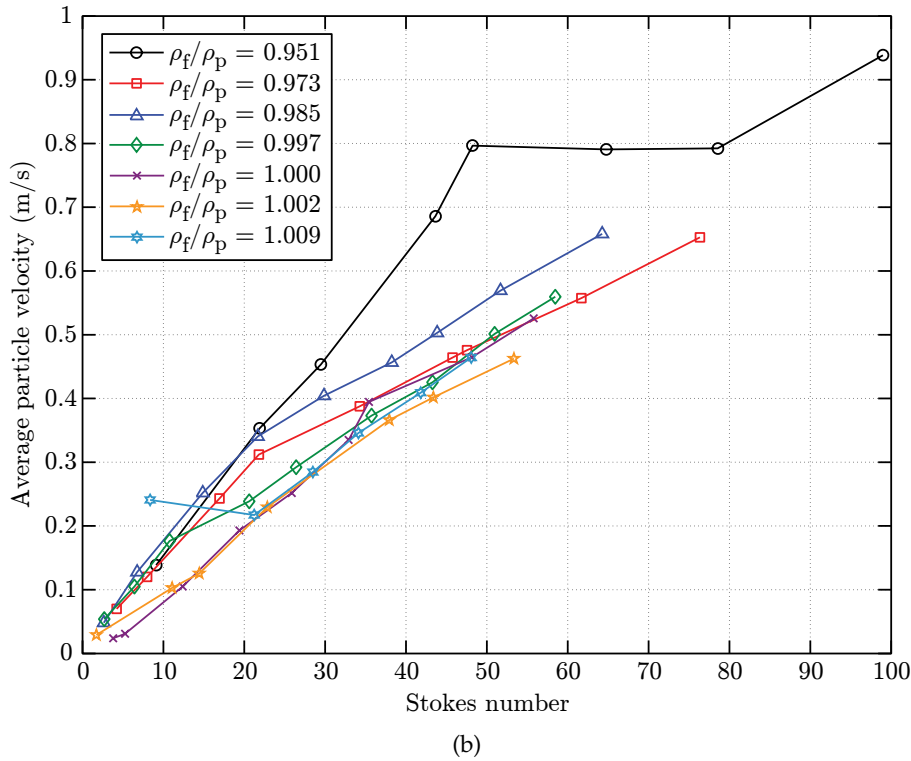
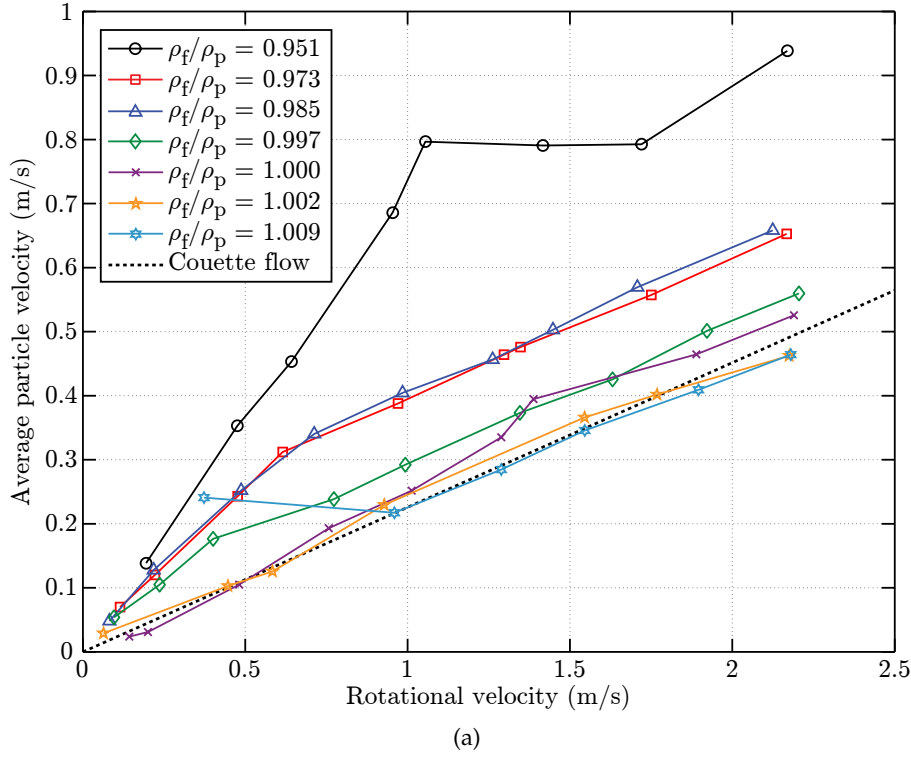


Figure 5.1. Graph of the particle velocity as a function of the (a) rotational velocity of the outer cylinder and (b) Stokes number. The dotted line in (a) represents the velocity predicted for laminar Couette flow for a particle located two diameters away from the stationary inner cylinder

the region of slow growth, all of the curves appear to be parallel to each other and to the laminar Couette line. While the particles in the lower fluid density curves are physically moving faster, they have the same acceleration with rotational velocity. The low fluid density curves collapse in the low rotational velocity region when viewed as a function of the Stokes number (Figure 5.1b) to remove any dependence on the fluid viscosity. The collapse of these curves with Stokes number implies that the particle velocity is limited by the ability of the particles to track the fluid. For these low rotations, the particle count and volume fraction are rapidly increasing from less than half of the average volume fraction in the annulus. At low rotational speeds, the particles are able to track the fluid, but as the number of particles begins to increase, particle interactions become much more frequent and slow the average particle velocity. For the curves in which the density difference between the fluid and particles is small, the particles are well distributed within the annulus, even at low rotational speeds, and follow the laminar Couette line throughout the experiment.

The mean particle velocities can also be normalized against the laminar Couette velocity, as seen in Figure 5.2. The slip is greater for lower rotational velocities and for greater

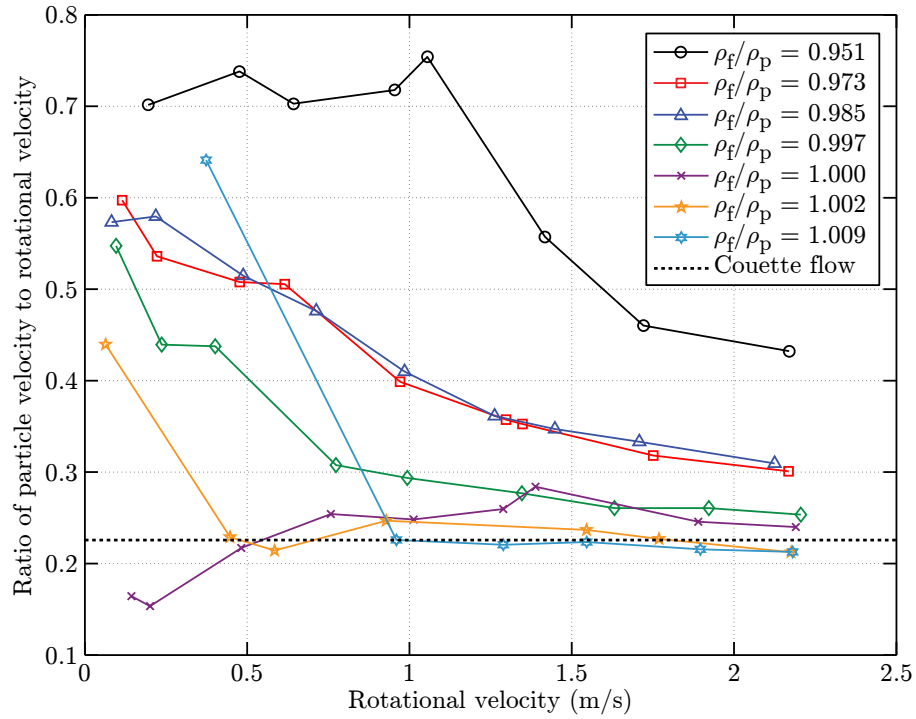


Figure 5.2. Graph of the particle velocity normalized by the rotational velocity of the outer cylinder. These velocities were obtained from optical probes mounted below the stationary floating cylinder.



density offsets. As the rotational velocity is increased, the particles begin to fluidize allowing the particles to follow the fluid more closely.

In addition to the average velocities recorded for all of the particles in the measurement period, individual particle speeds were also recorded. The velocity of individual particles is represented as a histogram, as seen in Figure 5.3, or since the spread is well represented by a Gaussian, by the standard deviation as in Figure 5.4. For all but the lowest veloci-

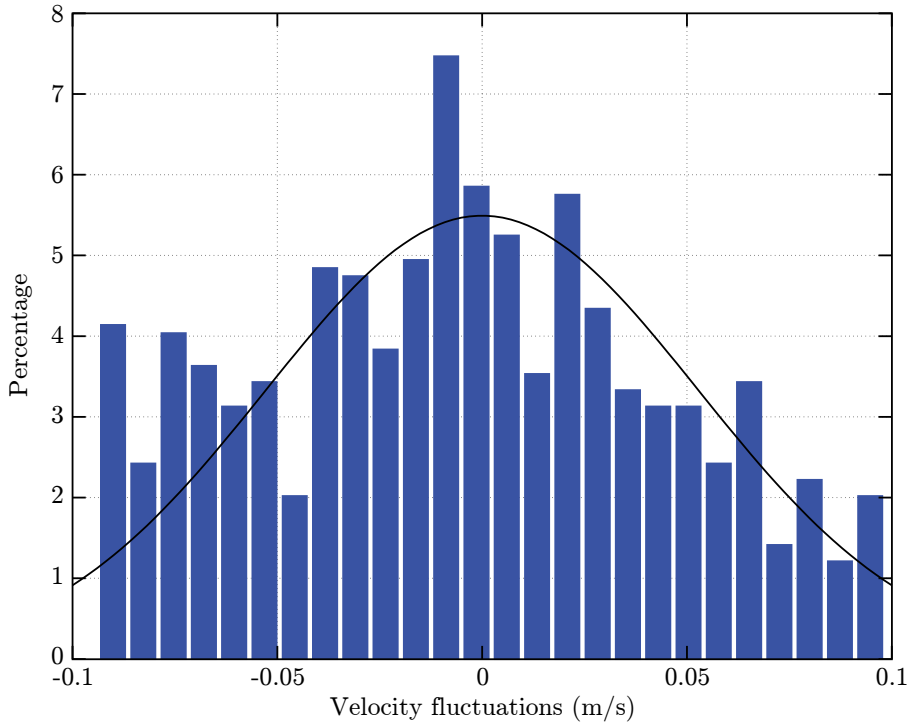


Figure 5.3. Histogram of velocity fluctuations – the individual particle velocities minus the mean value – for 30% polystyrene in 21% glycerine ( $\rho_f/\rho_p = 1.000$ ) rotating at 1.4 m/s. The histogram is well fitted by a Gaussian normal distribution with a standard deviation of 0.053 m/s.

ties, the standard deviation remains a constant percentage of the mean velocity (between 12% and 18%). This deviation in particle speeds may represent some variation in particle distance from the wall, changes in momentum due to collisions between slower moving particles and the stationary wall, collisions with faster particles radially inward, or some combination of all of these factors. A 20% variation in particle velocity from the mean value can be the result of a  $0.1d$ – $0.5d$  movement in particle radial position.

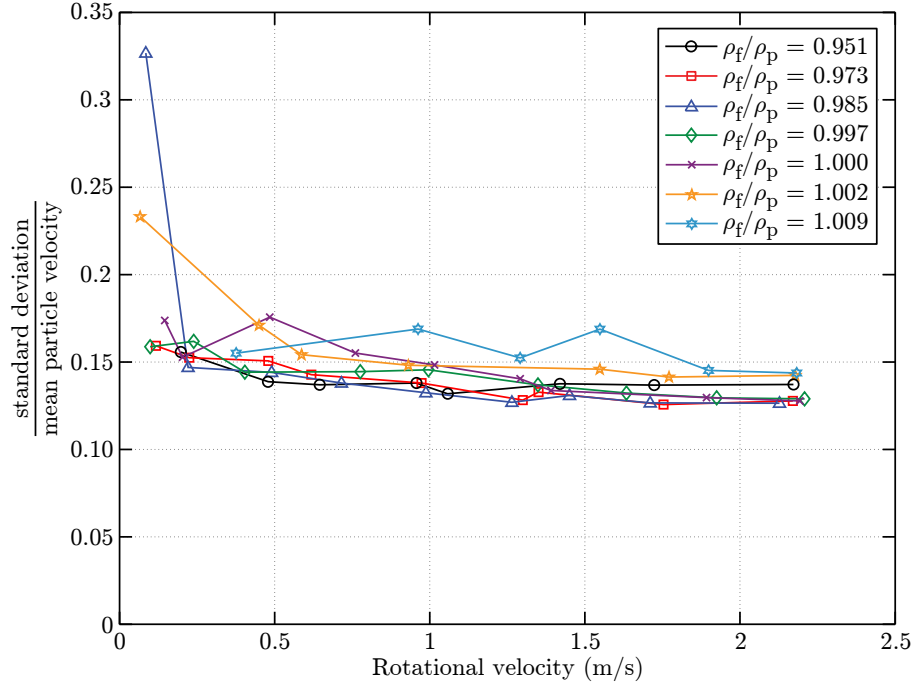


Figure 5.4. Standard deviation in particle velocity normalized by the mean value for an average volume fraction in the annulus of  $\bar{\phi} = 0.30$ . With the exception of the low rotational velocity points, the spread in the particle velocities remains fairly constant.

### 5.2.1.2 Volume fraction

As the interstitial fluid is varied and the rotational speed is allowed to change, the distribution of particles within the annular gap correspondingly changes. The particles migrate toward the top or bottom of the annulus and toward the outer cylinder. The highest rotational speed gives rise to a centripetal acceleration four times larger than the acceleration due to gravity. The optical probes measure the volume fraction near the inner, stationary cylinder where measurements of the shear stress are made. The particle counts are measured via optical probes just above (Figure 5.5a) and below (Figure 5.5b) the floating cylinder. Above the floating cylinder, the tests in 21% glycerine ( $\rho_f/\rho_p = 1.000$ ) start out with higher particle counts and remain higher throughout the experiment. The experiments where the fluid density is within 1% of the particle density register a nonzero particle count throughout the experiment, but did not achieve the same high counts as in the matched density case. Tests with  $\rho_f/\rho_p \leq 0.985$  (in which the polystyrene sink) only begin to register particles at the upper cylinder at higher rotational speeds. The particle counts just below the floating cylinder are close for every fluid tested. There is a slight trend to-

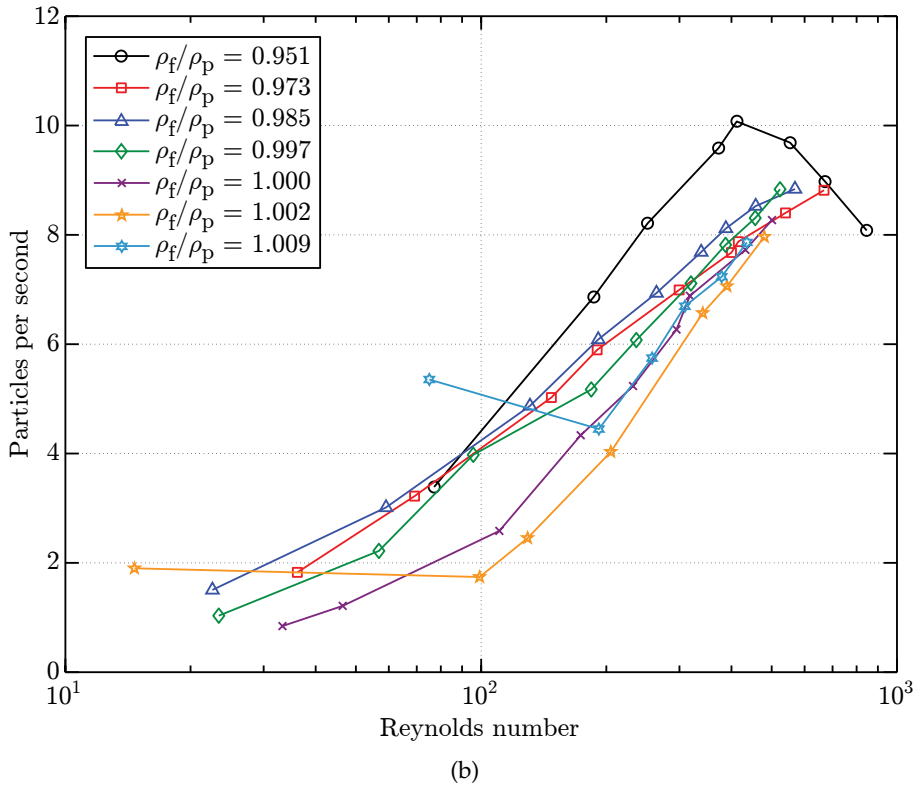
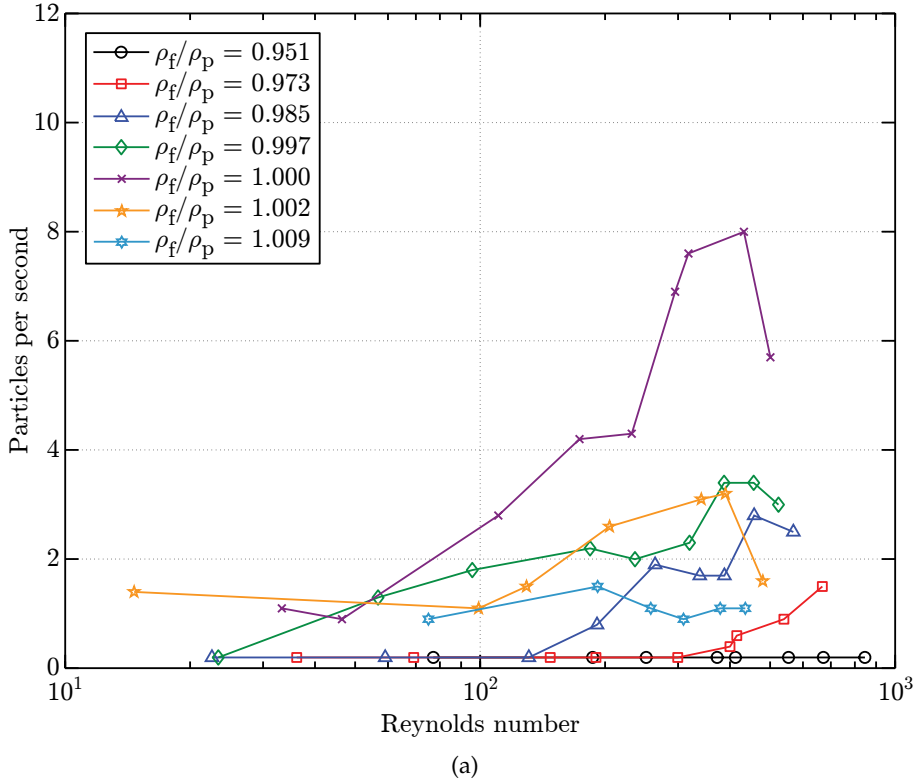


Figure 5.5. Graph of the particle counts obtained from optical probes mounted (a) above and (b) below the stationary floating cylinder.

ward a higher particle count for the lighter fluids (e.g.  $\rho_f/\rho_p = 0.951$ ) than the heavier fluids ( $\rho_f/\rho_p = 1.009$ ). The particle counts at the bottom probe are generally higher than at the top, the exception being for the  $\rho_f/\rho_p = 1.00$  where the number of particles measured at the top probe match the number of particles measured at the bottom probe throughout the experiment. This even distribution of particles throughout the experiment is congruent with particles that are neutrally buoyant.

From the particle count and particle velocity measurements, the local volume fraction is found using equation (3.2),

$$\phi = \frac{4}{3}\pi \left(\frac{R}{L}\right)^3, \quad (5.1)$$

where

$$L = \frac{u}{n}.$$

The volume fraction averaged over the floating cylinder is shown in Figure 5.6 as a function of the Reynolds number based on the rotational velocity and annular gap. The ex-

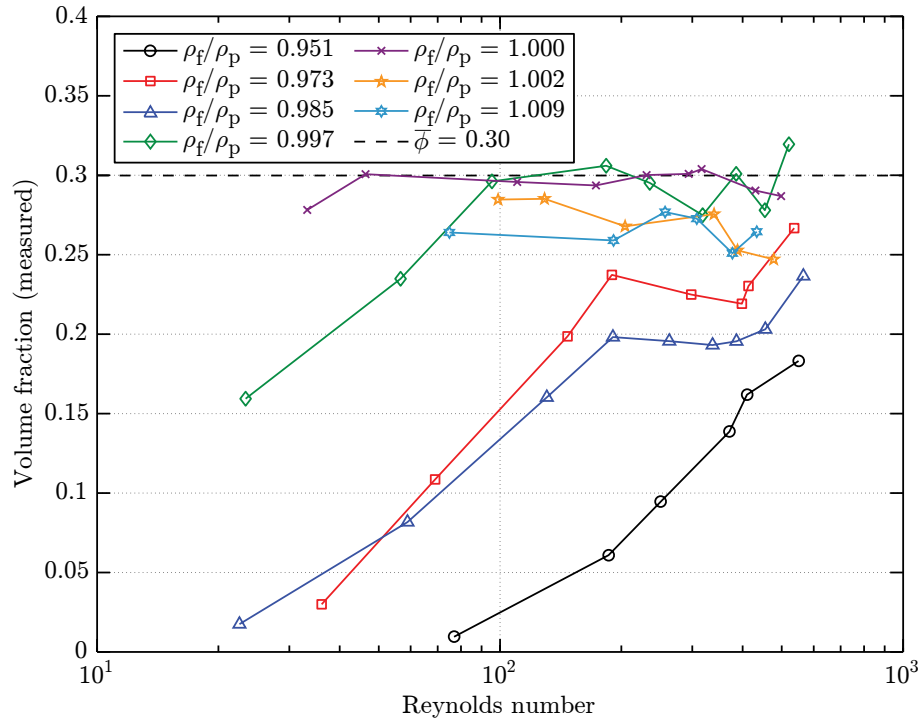


Figure 5.6. Average volume fraction across the floating cylinder for various aqueous glycerine solutions. The volume fraction was obtained from the particle counts and particle velocities using equation (3.2). The dashed line represents the average volume in the entire annulus,  $\bar{\phi} = 0.30$ .

periment was conducted with a total number of particles such that, if they were evenly distributed, a volume fraction of  $\bar{\phi} = 0.30$  would be obtained. For the experiments with neutrally buoyant polystyrene, the measured volume fraction remains near the average volume fraction throughout the experiment. As the fluid density deviates from the particle density, the volume fraction across the floating cylinder decreases. As it is readily apparent in the experiments with  $\rho_f/\rho_p \leq 0.985$ , there is a positive influence on the rotational velocity as the particles begin to fluidize. This effect is less prevalent for the cases where the fluid density is near to the particle density, but may still influence the results. For these lighter fluids, the measured volume fraction increases due to fluidization, but never increases to the 0.30 average volume fraction.

The volume fraction should depend on the speed of rotation, in the form of the Reynolds number, as well as the difference in density between the fluid and particles. To account for the buoyancy effects, the Archimedes number is introduced,

$$\text{Ar} = \frac{gd^3\rho_f|\rho_p - \rho_f|}{\mu^2}. \quad (5.2)$$

The magnitude of the density difference is used to force the Archimedes number to always be positive. In Figure 5.7, the measured volume fraction is plotted against the Reynolds number divided by the Archimedes number. This composite number, similar to that used by Acrivos et al. (1994), collapses the volume fraction measurements.

In addition to variations in volume fraction in the axial direction, the volume fraction could vary in the circumferential and radial directions. While neither of these variations were measured, hypotheses can be made about their magnitude. Particles should be equally distributed in the circumferential direction. No external force exists to induce such a variation, though one might exist due to how the particles were added to the tank. Before taking measurements, the cylinder is allowed to rotate for several minutes allowing the particles to redistribute. In the radial direction for neutrally buoyant particles Abbott et al. (1991) using nuclear magnetic resonance (NMR) imaging and Shapley et al. (2002) using laser Doppler velocimetry (LDV) of a center rotating Couette flow found that particles did cluster around the outer, stationary cylinder. The distribution of particles in the radial direction is amplified by the density difference between the fluid and particles. The variation of particles in the radial direction creates particle-free layers near the walls and

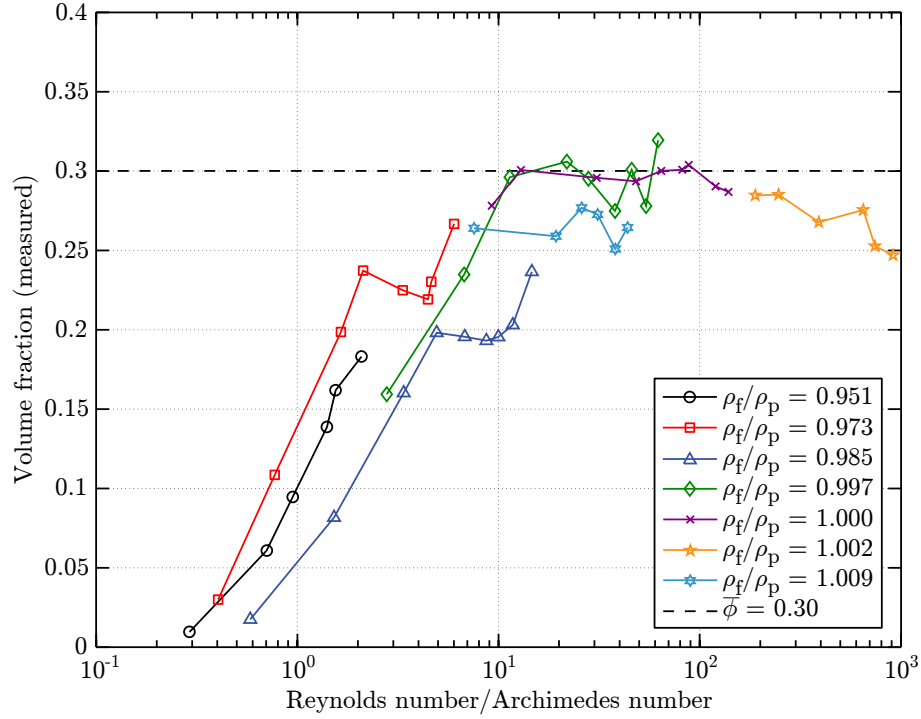
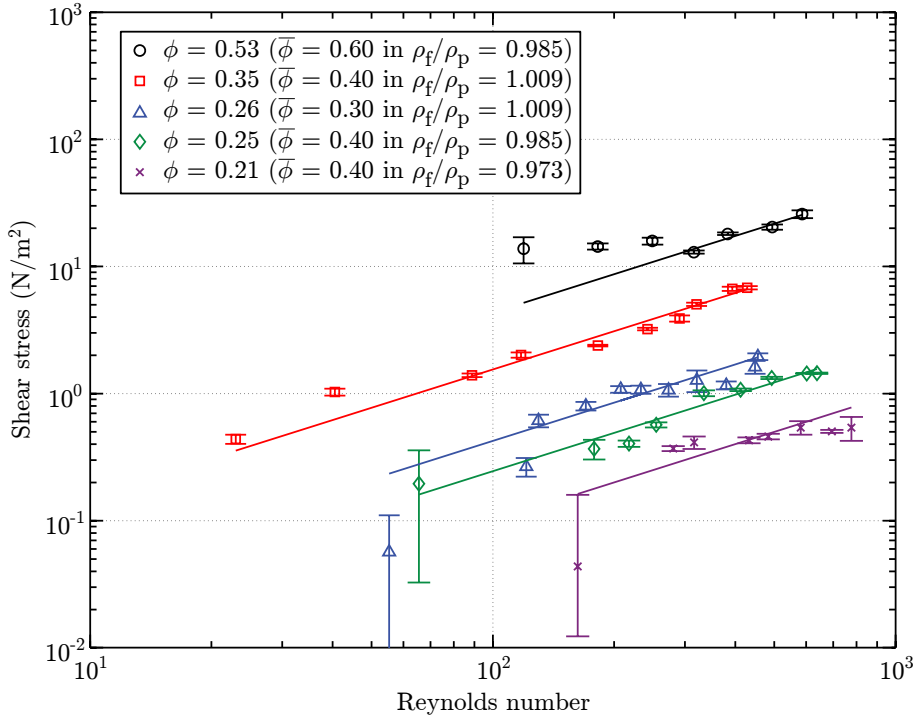


Figure 5.7. Volume fraction across the floating cylinder as a function of the Reynolds number divided by the Archimedes number.

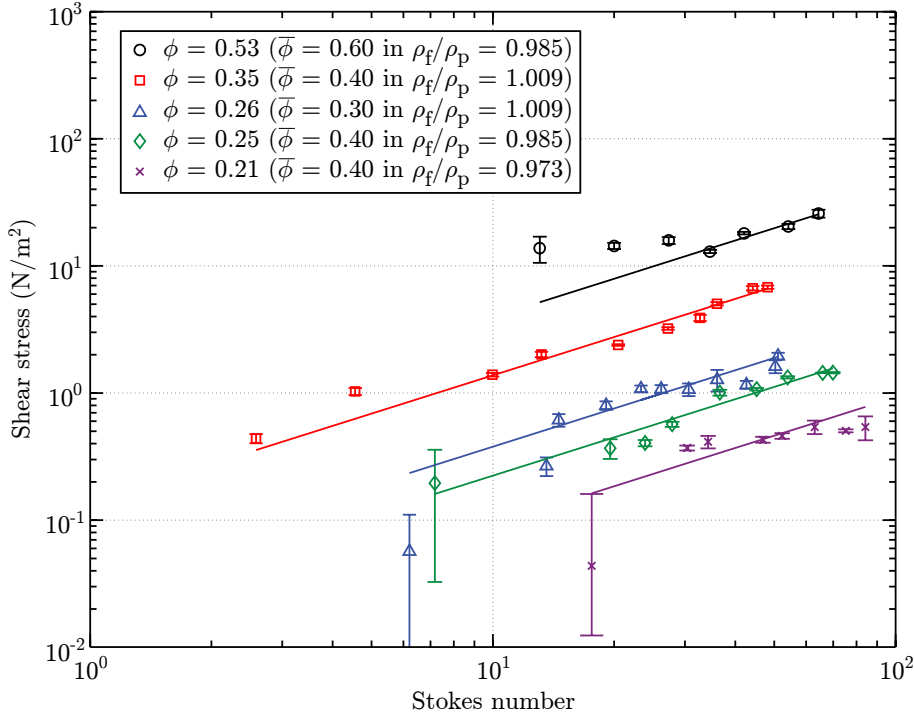
contributes to the appearance of slip. Slip against these cylinders decreases the measured shear stress and is explored further in chapter 6.

### 5.2.1.3 Effective viscosity

As with the experiments using neutrally buoyant particles, the goal of the experiments using non-neutrally buoyant particles is to determine the effective viscosity ratio. This is accomplished by measuring the torque on the inner, floating cylinder and comparing this value to the pure fluid torque. The measured shear stress as a function of the Reynolds number is shown in Figure 5.8. Each experiment represents an experiment of non-neutrally buoyant polystyrene. For example, the black circles ( $\circ$ ) denote 7.8 liters of polystyrene solids, corresponding to a volume fraction  $\bar{\phi} = 0.60$  if evenly distributed, in a mixture of 15% glycerine and water by weight ( $\rho_f/\rho_p = 0.985$ ). For this case, the actual volume fraction over the floating cylinder is  $\phi = 0.53$ . The large error bars present for the lowest shear stress measurements represent variations in the measured force due to limitations of the experimental apparatus. At higher Reynolds numbers, the experiments are fitted



(a)



(b)

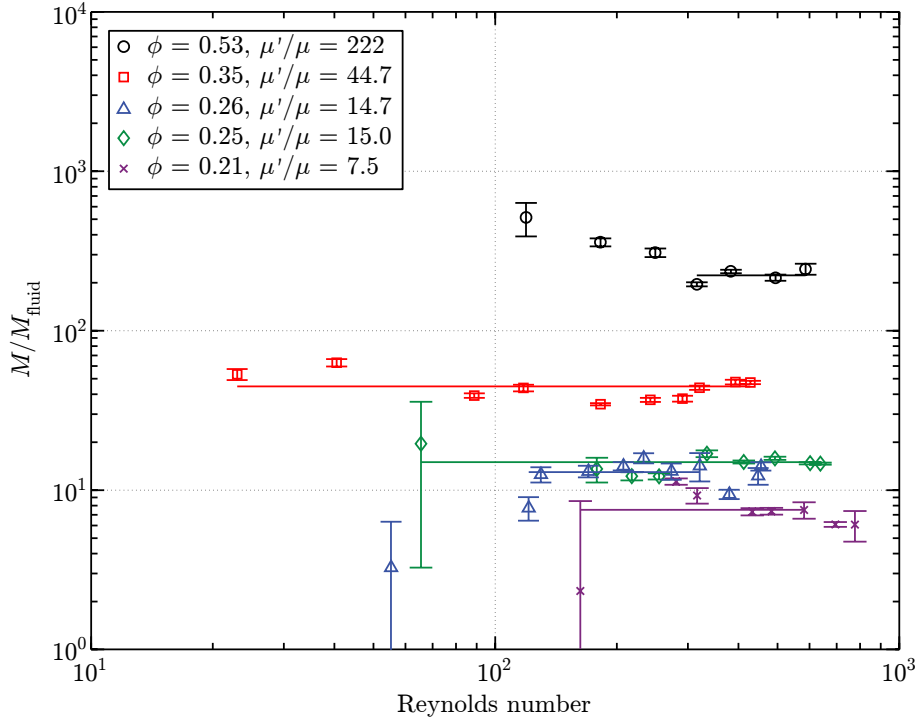
Figure 5.8. Shear stress measurements of polystyrene particles in varying concentrations of aqueous glycerine as a function of (a) the Reynolds number and (b) the Stokes number. The lines represent linear fits for each volume fraction, fits that are constrained to pass through the origin.

well by a line, but at lower Reynolds numbers, the shear stress deviates from the line. This trend is easily apparent in the graph of the ratio of measured-to-pure fluid torques (Figure 5.9). The deviation at low Reynolds numbers from the constant effective viscosity is consistent with a rotational velocity that is not high enough to fluidize the particles. For the experiment with  $\phi = 0.53$  (black circles), the volume fraction for an experiment with the same density offset (Figure 5.6) becomes linear near  $Re = 2 \times 10^2$ . For this same configuration flow, the shear stress only becomes linear above  $Re = 3 \times 10^2$ . Ideally these values should correspond (within the discretization of the velocity), but as long as the shear stress becomes linear after the particles have fluidized, the slope can be used to find the effective viscosity.

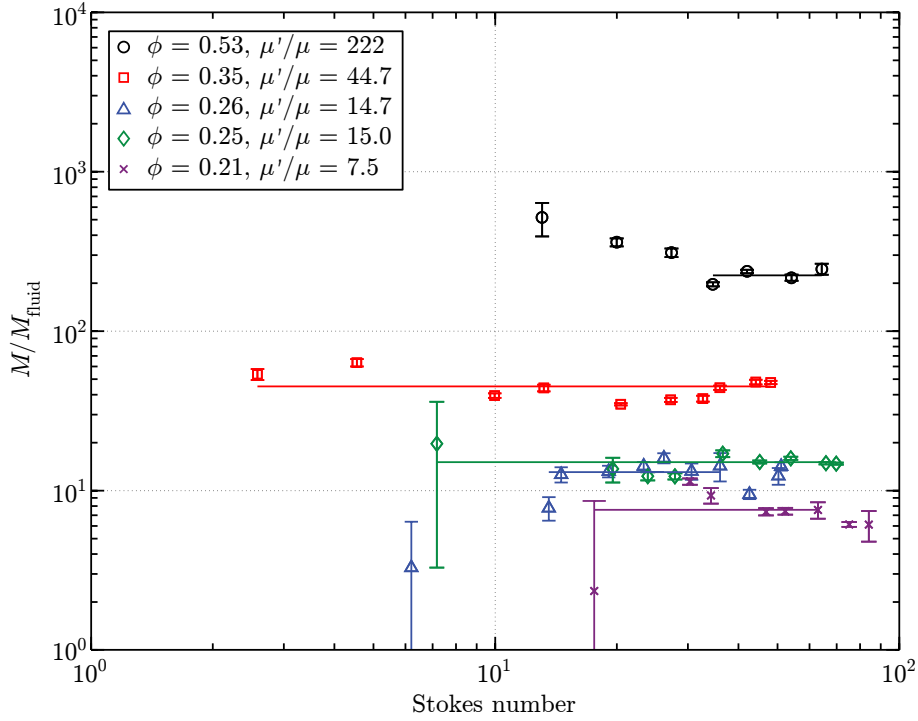
The direct dependance on the fluid density can be seen in Figure 5.10. It is important to note that every point on Figure 5.9 is plotted on this figure, including those points where the particles are not fluidized. The lines represent the constant value fits for the fluidized data. For each of the average volume fractions, the effective viscosity ratio is highest when the ratio of fluid-to-particle densities is unity. As was hypothesized in section 5.1, as the density ratio of the fluid diverges from unity, the particles float or sink away from the central cylinder. As the volume fraction decreases around this center section, the measured torque also decreases. Comparing the experiments with a volume fraction  $\bar{\phi} = 0.60$  ( $\triangle$ ) to those with a volume fraction of  $\bar{\phi} = 0.40$  ( $\circ$ ), shows that for a reduction in fluid density (15% glycerine,  $\rho_f/\rho_p = 0.985$ ), the  $\bar{\phi} = 0.60$  case shows a greater drop in effective viscosity by 43% (from  $\mu'/\mu = 391$  to  $\mu'/\mu = 222$ ) whereas the  $\bar{\phi} = 0.40$  case drops by 68% (from  $\mu'/\mu = 47.6$  to  $\mu'/\mu = 15.0$ ). As the average volume fraction in the annular gap approaches and passes the loose-packing volume fraction, the difference between the fluid and particle density becomes less important. The difference in density can affect the random packing of particles, but this difference is smaller than the settling of particles in a sparsely populated flow.

Using the measured volume fraction over the center, floating cylinder, the viscosity ratio is plotted on the same graph as the neutrally buoyant cases (Figure 5.11). As can be seen in the apparent viscosity graph, the experiments with non-neutrally buoyant particles show strong agreement with the neutrally buoyant particles when the volume fraction is adjusted based on the fluidization of particles.





(a)



(b)

Figure 5.9. Ratio of measured-to-pure fluid torques of polystyrene particles in varying concentrations of aqueous glycerine as a function of (a) the Reynolds number and (b) the Stokes number. This ratio is fitted by a constant, unique to each volume fraction  $\phi$ . This constant is the ratio of the effective viscosity to the pure fluid viscosity,  $\mu'/\mu$ .

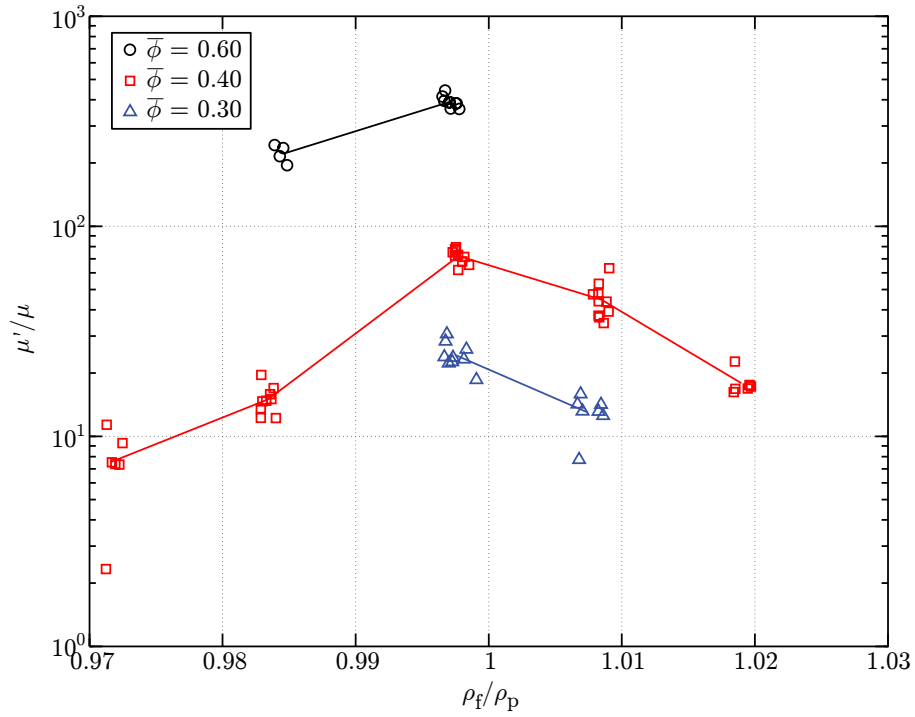


Figure 5.10. Effective viscosity ratio as a function of the density of the interstitial fluid normalized by the particle density. The points on this graph represents the data from each Reynolds number variation, including the particles are not fluidized. The lines represent the constant value fits for the fluidized data. The effective viscosity is the largest when the fluid density matches the particle velocity. At this point, the volume fraction across the floating cylinder is highest.

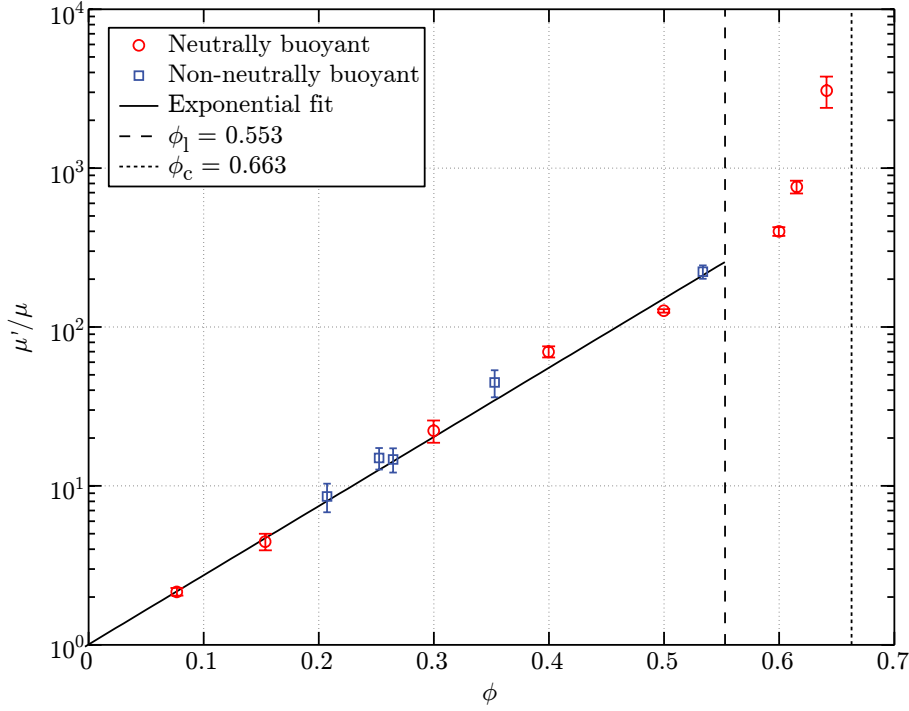


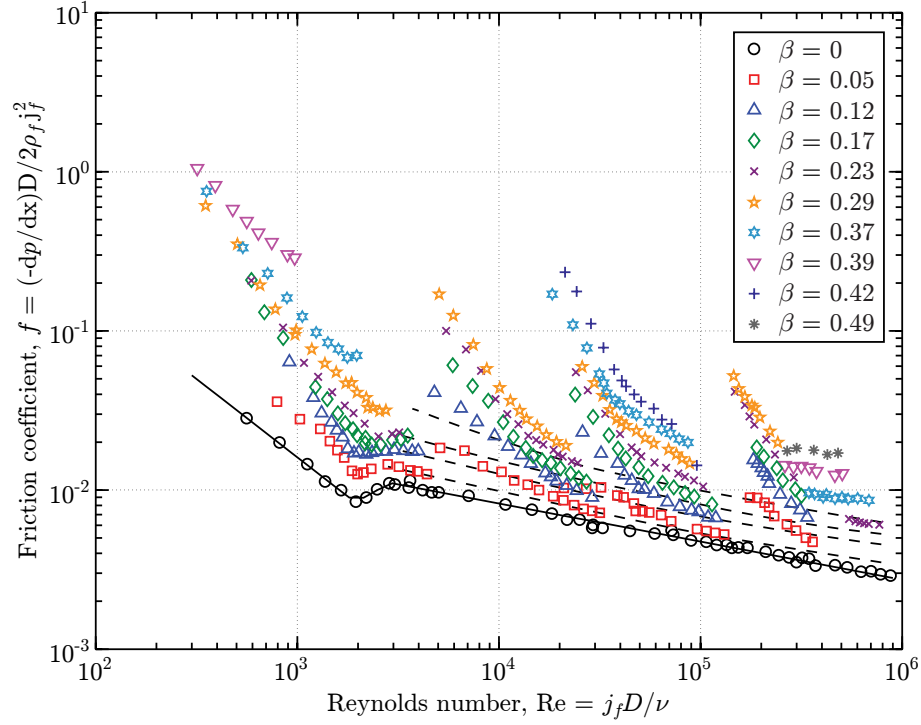
Figure 5.11. Effective viscosity ratio for both neutrally buoyant and non-neutrally buoyant experiments of polystyrene in aqueous glycerine solutions.

#### 5.2.1.4 Coefficient of friction

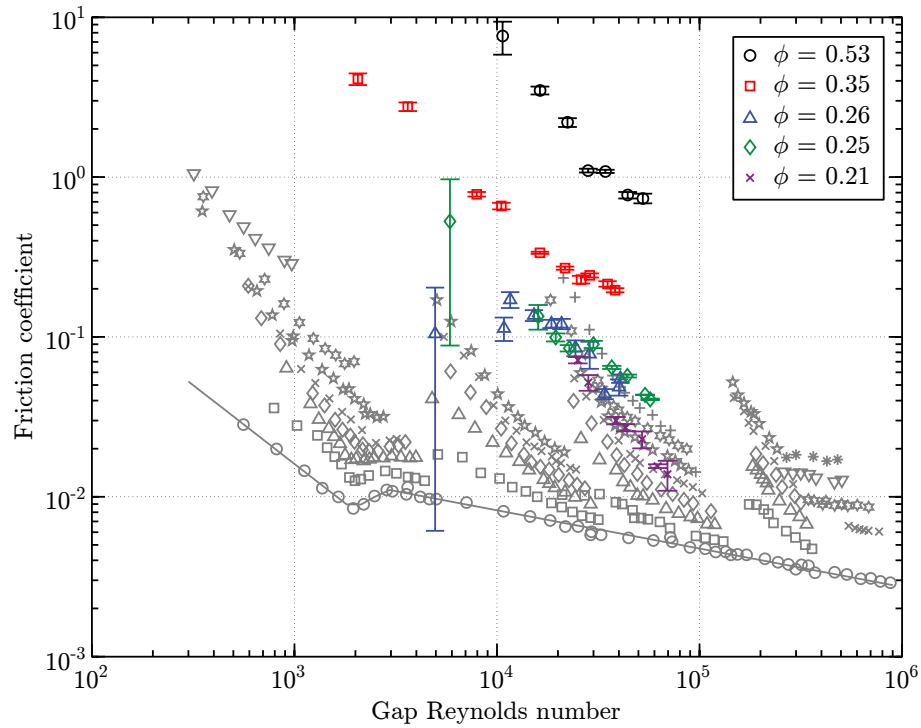
Using the shear stress data obtained for the non-neutrally buoyant polystyrene particles, the coefficient of friction for these flows can be calculated. The coefficient of friction  $C_f$  is given by

$$C_f = \frac{4\tau}{\rho_f \dot{\gamma} b^2}. \quad (5.3)$$

This friction data, shown in Figure 5.12, is compared with the coefficient of friction data obtained by Lazarus and Neilson (1978) for solid particles in horizontal pipe flow. The data from the present experiment shows the same decrease in coefficient of friction with Reynolds number as the data from Lazarus and Neilson, but the data for each volume fraction in the present data is higher than the corresponding volume quality from Lazarus and Neilson. Some of this discrepancy may be due to the difference between volume quality and volume fraction – these values will match when the particle velocities match the velocity of the fluid. One key feature from the Lazarus and Neilson data is the presence of the asymptotic approaches (shown in dashed lines in Figure 5.12a). These approaches represent the fluidized data for different types of particles, all at the same volume qual-



(a)



(b)

Figure 5.12. Coefficient of friction versus gap Reynolds number (a) for the data of Lazarus and Neilson (1978) and (b) for the present non-neutrally buoyant polystyrene data. The data of Lazarus and Neilson (1978) is expressed as a function of the volume quality  $\beta$ . The volume quality is defined as the ratio of volumetric flux of solids to the total volumetric flux. The volume quality equals the volume fraction when the particle velocities are equal to the fluid velocities.

ity. These asymptotic approaches are not present in the current data due to the generally large Archimedes numbers. When the coefficient of friction is shown as a function of the Reynolds number divided by the Archimedes number, as in Figure 5.13, the current data

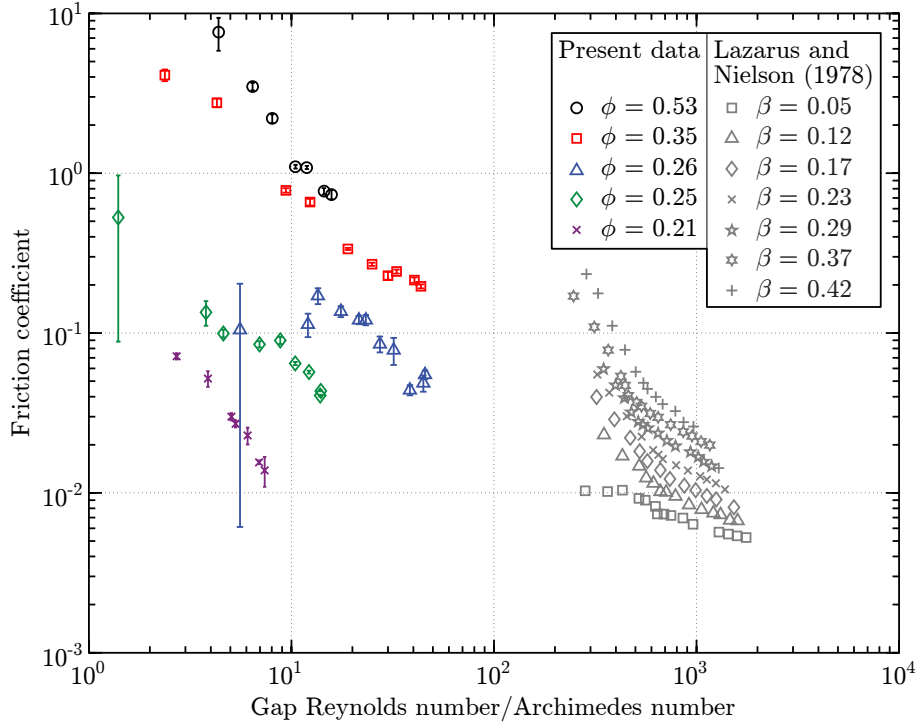


Figure 5.13. Coefficient of friction versus the gap Reynolds number divided by the Archimedes number for the present non-neutrally buoyant polystyrene data ( $Ar = 200$ – $20000$ ) and the 60/100 sand in water ( $Ar = 74$ ) data from Lazarus and Neilson (1978).

appears to approach the curves of Lazarus and Neilson (1978) if higher Reynolds numbers or lower Archimedes numbers were tested. In Figure 5.13, only the data using 60/100 sand in water was included, as that is the only data reported separately for which the ratio of Reynolds number to Archimedes number could be conclusively calculated. The Archimedes numbers for the other particles shown in Figure 5.12 range from the steel shot with  $Ar = 1.6 \times 10^6$  to the 60/100 sand in ethylene glycol with  $Ar = 0.07$  (Lazarus and Neilson 1978).

## 5.2.2 Glass

Experiments were conducted in the concentric cylinder rheometer using an aqueous glycerine mixture of 77% glycerine in which the glass particles would sink ( $\rho_f/\rho_p = 0.476$ ). The Archimedes number for these tests is 200 for the 3.04 mm beads. Due to the high den-

sity of the glass beads, only one volume fraction was able to be tested:  $\phi = 0.626$ . The shear stress measurements are shown in Figure 5.14 with the linear fit, constrained to pass

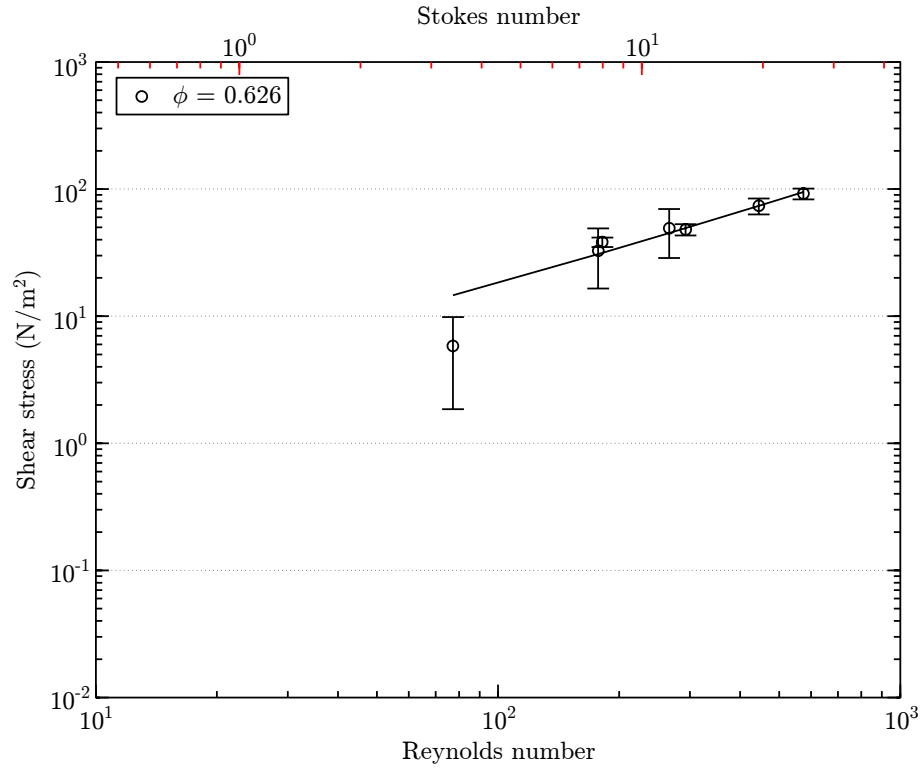


Figure 5.14. Shear stress measurements for non-neutrally buoyant glass particles in aqueous glycerine. The line represents a linear fit that is constrained to pass through the origin.

through the origin. The ratio of measured-to-pure fluid torque, a measurement is equivalent to the effective viscosity for the sample (shown in Figure 5.15). The ratio of torques,  $M/M_{\text{fluid}}$ , does not appear to depend greatly on the Reynolds number as one would expect for a Newtonian fluid.

### 5.2.3 Polyester

Experiments were conducted in the concentric cylinder rheometer using an aqueous glycerine mixture of 77% glycerine ( $\rho_f/\rho_p = 0.857$ ). The Archimedes number for these tests is 30. The shear stress measurements, taken for a range of volume fractions, are shown in Figure 5.16. For each volume fraction, the shear stress is shown with its linear fit. The shear stress increases rapidly with with volume fraction, varying by three orders of magnitude between the smallest and largest volume fraction. The ratio of measured torque to the

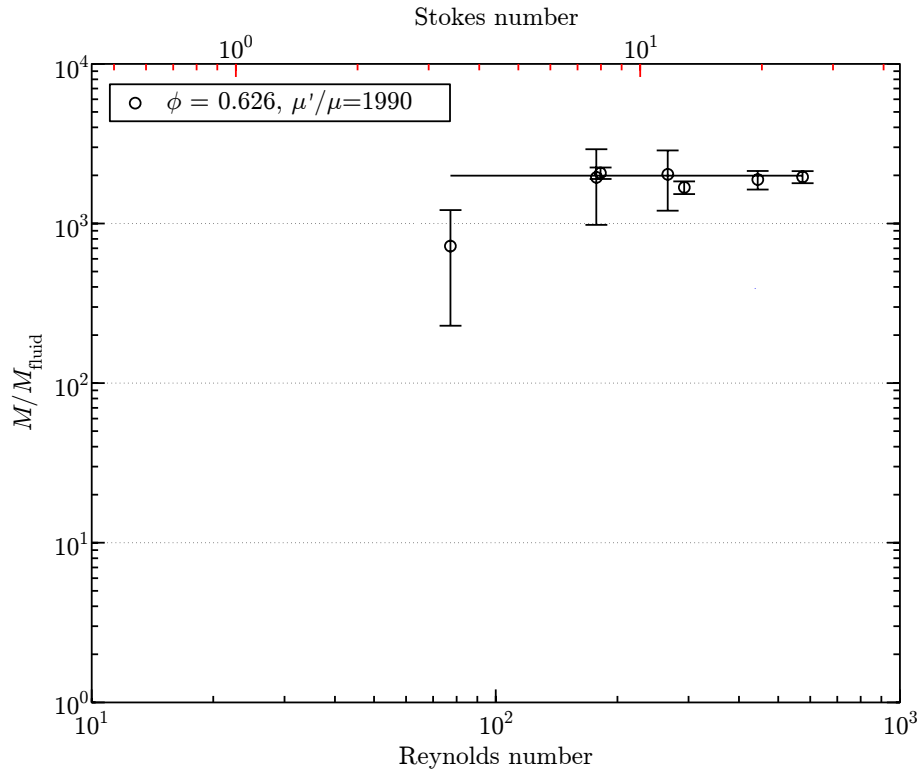


Figure 5.15. Ratio of measured-to-pure fluid torque for non-neutrally buoyant glass particles in aqueous glycerine. This ratio is fitted by a constant, which is equivalent to the ratio of the effective viscosity to the pure fluid viscosity,  $\mu'/\mu$ .

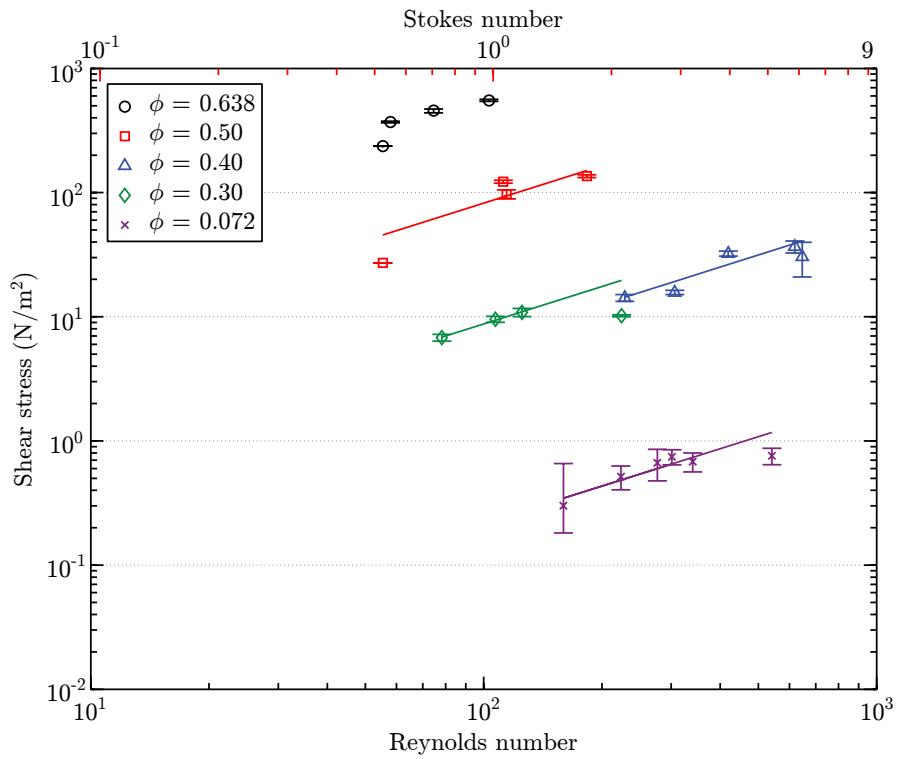


Figure 5.16. Shear stress measurements for non-neutrally buoyant polyester particles in aqueous glycerine. The lines represent linear fits for each volume fraction, fits that are constrained to pass through the origin.



torque predicted using the pure fluid viscosity, as seen in Figure 5.17, yields values for the

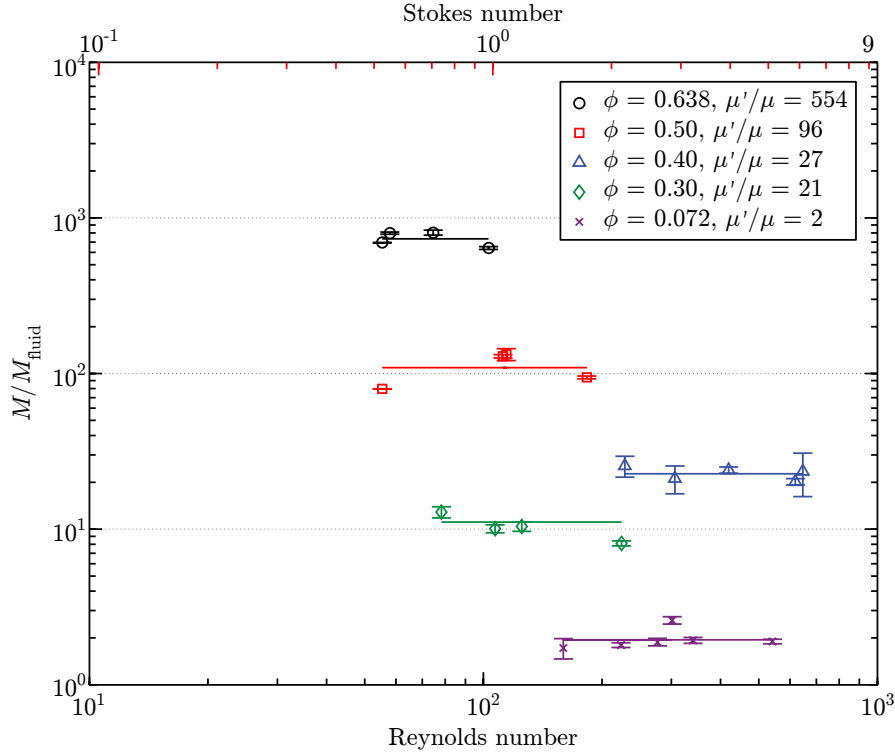


Figure 5.17. Ratio of measured-to-pure fluid torques for non-neutrally buoyant polyester particles in aqueous glycerine. This ratio is fitted by a constant, unique to each volume fraction  $\phi$ . This constant is the ratio of the effective viscosity to the pure fluid viscosity  $\mu'/\mu$ .

ratio of the effective to pure fluid viscosity,  $\mu'/\mu$ . The ratio of torques,  $M/M_{\text{fluid}}$ , is clearly a function of the volume fraction, but does not appear to depend greatly on the Reynolds number. For most volume fractions, the ratio of torques is fairly constant as expected with a Newtonian fluid.

For the non-neutrally buoyant polyester, the Stokes number is small for all of the experiments conducted. For very small Stokes numbers (less than about 2), there is no clear collision. For slightly larger Stokes numbers (between about 3 and 9), there is a clear point of collision, but there is no rebound: the two particles will move with the velocity of the slower particle. For all of these experiments, any interaction between particles results in significant loss of energy.

As the effective viscosity remains constant for the Reynolds numbers tested in the experiment, it is taken as only a function of the volume fraction of solids (Figure 5.18). For points below  $\phi_l$ , the effective viscosity is fitted by an exponential. The point above the ran-

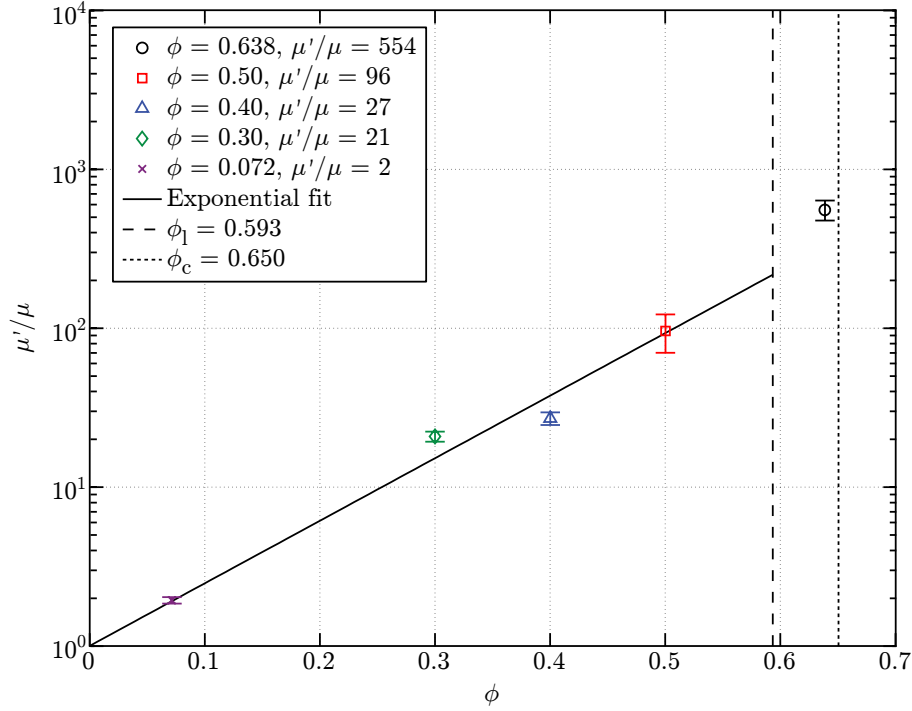


Figure 5.18. Effective viscosity ratio for neutrally buoyant polyester particles in aqueous glycerine solutions. The black line is an exponential fit for the points below  $\phi_l$ . Dashed vertical lines denote the loose-packing and close-packing volume fractions.

dom loose-packed volume fraction has a higher effective viscosity than the exponential fit for the lower volume fraction points. For reference, the loose-packing and close-packing volume fractions are denoted with dashed and dotted vertical lines.

### 5.3 Summary of experimental data

In the previous chapter, experiments for several neutrally buoyant particles were compared by normalizing the volume fractions by the loose-packed volume fraction for each particle (section 4.3). For the non-neutrally buoyant experiments discussed in the previous section (section 5.2), the volume fractions again are normalized by the RLP, but rather than using the average volume fraction  $\bar{\phi}$ , the volume fraction measured using the optical probes is used. The adjustment to the average volume fraction accounts for the migration of particles away from the center, floating cylinder during torque measurements, movement that is dependent on the Archimedes and Reynolds numbers for the flow. The neutrally buoyant and non-neutrally buoyant experiments are shown in Figure 5.19. The

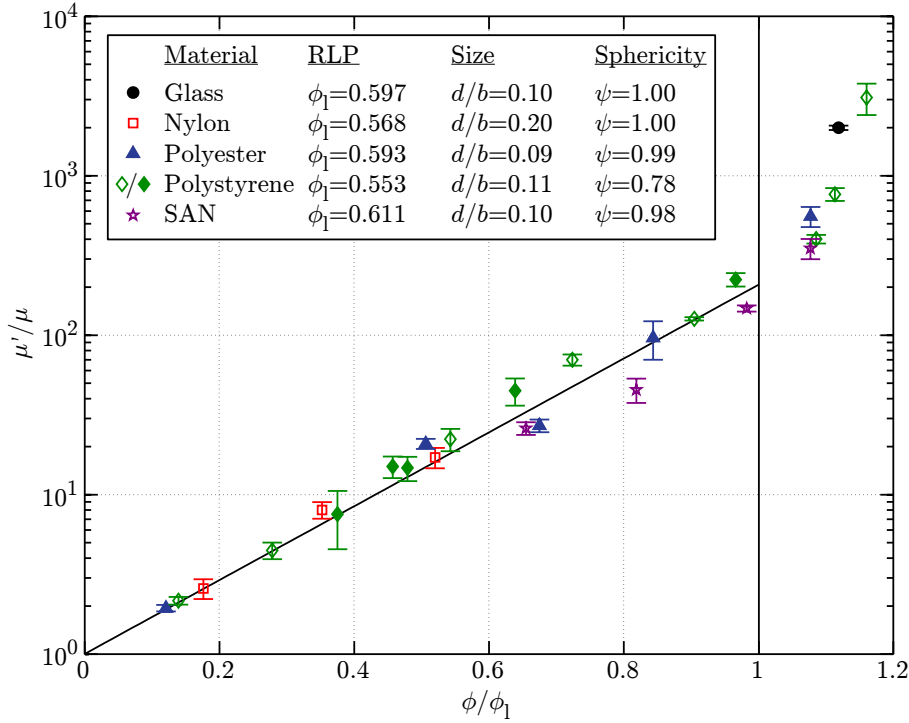


Figure 5.19. Effective viscosity for all neutrally buoyant (open symbols) and non-neutrally buoyant (filled symbols) particles where the volume fraction is normalized by the RLP.

neutrally buoyant experiments are denoted using open symbols while the non-neutrally buoyant particles are shown with filled symbols. All of the experiments show a characteristic change in effective viscosity with volume fraction: an exponential rise for  $\phi < \phi_l$  and the deviation from this exponential slope for  $\phi > \phi_l$ .

As with the neutrally buoyant experiments, there appears to be no change in the effective viscosity based on the particle size or shape. Additionally, there is not dependence on the density offset of the particle and fluid, as long as the average volume fraction is corrected to accurately represent the volume fraction over the measurement area.

The present data may be compared to both neutrally buoyant and non-neutrally buoyant experimental results that were previously published. This comparison, Figure 5.20, shows that the previous experiments compare favorably to the present experiments. The one exception is the experiments of Acrivos et al. (1994) which, as discussed earlier in section 4.3, were for experiments conducted at much lower Reynolds numbers using much smaller particles.

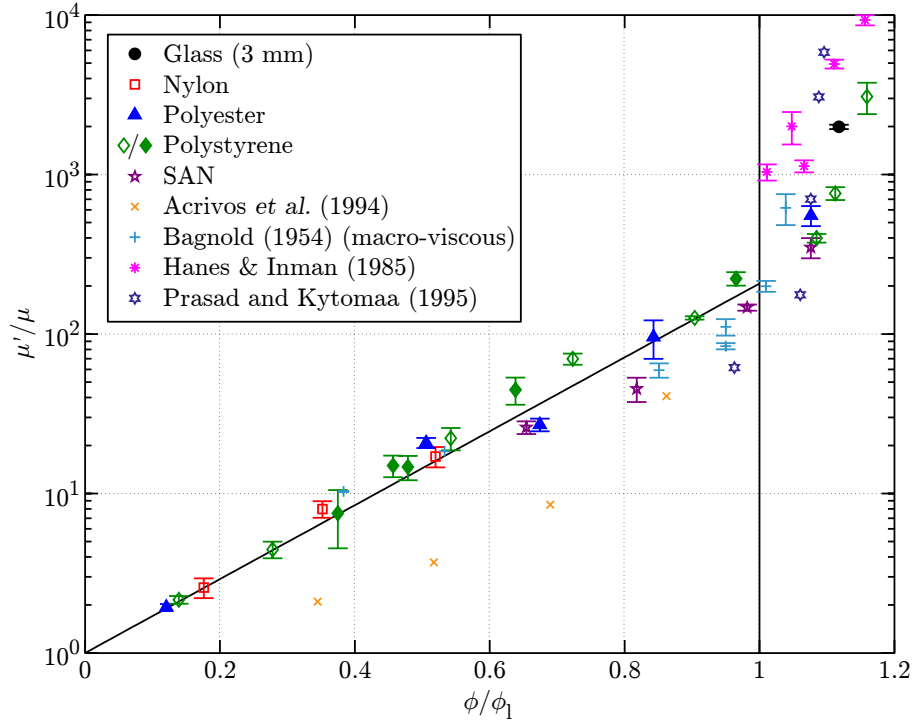


Figure 5.20. Effective viscosity for all neutrally buoyant (open symbols) and non-neutrally buoyant (filled symbols) particles compared with other experimental data.

## 5.4 Experimental fits

In the dilute and dense packing regions, the experimental data is well represented by an exponential fit. This fit is given by the equation

$$\frac{\mu'}{\mu} = \exp\left(C \frac{\phi}{\phi_l}\right), \quad (5.4)$$

where the fitting parameter  $C$  is found to be  $5.3 \pm 0.1$ . When the volume fraction transitions to the continuous contact regime, the effective viscosity increases more rapidly with the volume fraction and is no longer fitted by the same exponential. In the following sections, other fitting parameters are discussed.

### 5.4.1 Dilute curve fits

In the dilute region, the presence of the particles has a small impact on the velocity and viscosity of the bulk fluid. In the limit of small  $\phi$ , the viscosity of the fluid-particulate flow is close to the viscosity of the pure fluid. Einstein (1906) considered a small perturbation in

the velocity created by the movement of a few randomly distributed spheres that did not collide and found that the energy loss due to this random motion would produce a flow with a viscosity

$$\frac{\mu'}{\mu} = 1 + \frac{5}{2}\phi. \quad (5.5)$$

Einstein's relation does not account for interactions between particles and is considered accurate only for  $\phi < 0.02$  (Rutgers 1962). This equation was later modified to the second order to account for two-particle interactions by Batchelor and Green (1972)

$$\frac{\mu'}{\mu} = 1 + \frac{5}{2}\phi + 7.6\phi^2. \quad (5.6)$$

This correction yields a more accurate relation for particles in the dilute region, but can only be used when near collisions are binary (Batchelor and Green 1972). If more than one neighboring particle is within a few sphere radii or direct collisions occur, this approximation cannot be used. The theoretical fit of Einstein and the correction by Batchelor and Green is shown below, in Figure 5.21.

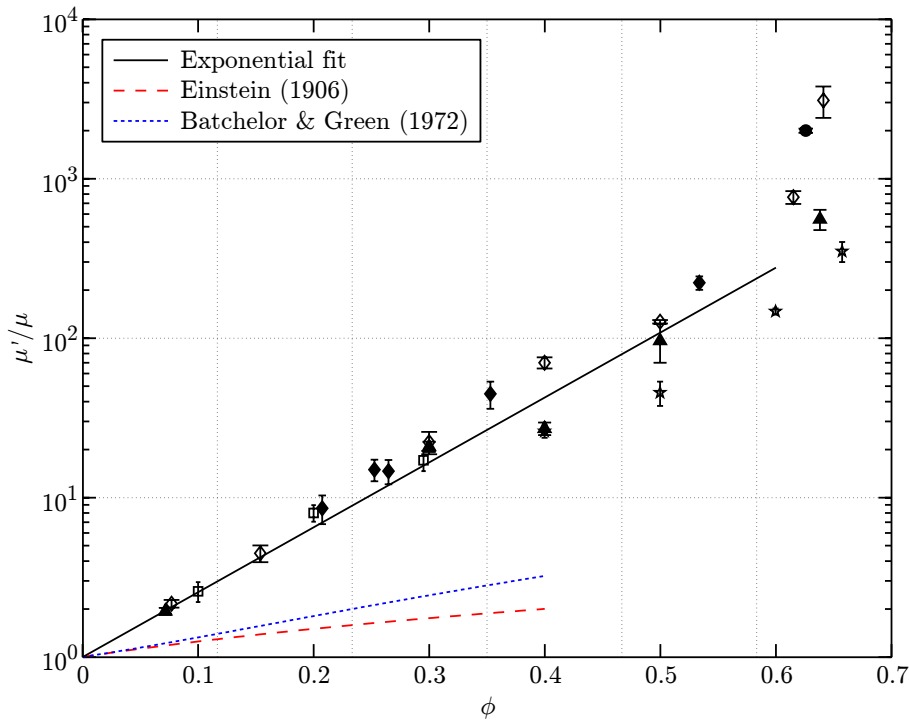


Figure 5.21. Theoretical curve fits for dilute particle concentrations of Einstein (1906) and Batchelor and Green (1972) graphed with the experimental data and the experimentally determined exponential fit.

### 5.4.2 Continuous contact curve fits

In addition to considering the low volume fraction region, it is also useful to consider the limit of high volume fractions. In the region of continuous particle contacts, the effective viscosity increases rapidly with the volume fraction and for hard spheres tend toward infinity as the volume fraction nears random close-packing.

For his data, Bagnold (1954) devised a curve fit using the linear concentration,  $\lambda$

$$\frac{\mu'}{\mu} = C\lambda^{\frac{3}{2}} \quad (5.7)$$

$$= C \left[ \left( \frac{\phi_c}{\phi} \right)^{\frac{1}{3}} - 1 \right]^{-\frac{3}{2}}, \quad (5.8)$$

where the empirical constant was experimentally determined as  $C = 2.25$ . Using viscous fluid energy dissipation in a concentrated suspension, Frankel and Acrivos (1967) devised a power law fit of the form

$$\frac{\mu'}{\mu} = C \left[ \frac{\left( \frac{\phi}{\phi_c} \right)^{\frac{1}{3}}}{1 - \left( \frac{\phi}{\phi_c} \right)^{\frac{1}{3}}} \right], \quad (5.9)$$

where the constant  $C = 9/8$ . Early work by Eilers (1941) for dense emulsions also yielded a fit which in addition to satisfying the condition at  $\phi = \phi_c$  also gives  $\mu' = \mu$  when  $\phi = 0$ . This equation was modified by Ferrini et al. (1979) to account for the rigidity of solid particles,

$$\frac{\mu'}{\mu} = \left[ 1 + \frac{C\phi}{1 - \frac{\phi}{\phi_c}} \right]^2, \quad (5.10)$$

where the constant  $C$  ranges from 1.25 to 1.5 (Acrivos et al. 1994; Leighton 1985).

These fits are plotted with the smooth wall experimental data in Figure 5.22 using least squared fitting parameters for the present experimental data. Additionally, a master power law of the form

$$\frac{\mu'}{\mu} = \left[ 1 + \frac{C_1 \left( \frac{\phi}{\phi_l} \right)^n}{1 - C_2 \left( \frac{\phi}{\phi_l} \right)^n} \right]^m \quad (5.11)$$

where the constants  $C_1$  and  $C_2$  and the exponents  $n$  and  $m$  are fitting parameters is plotted. In the continuous contact regime, the fits agree well with each other and with the experimental data. Batchelor and Green's correction (equation (5.6)) to Einstein's equation

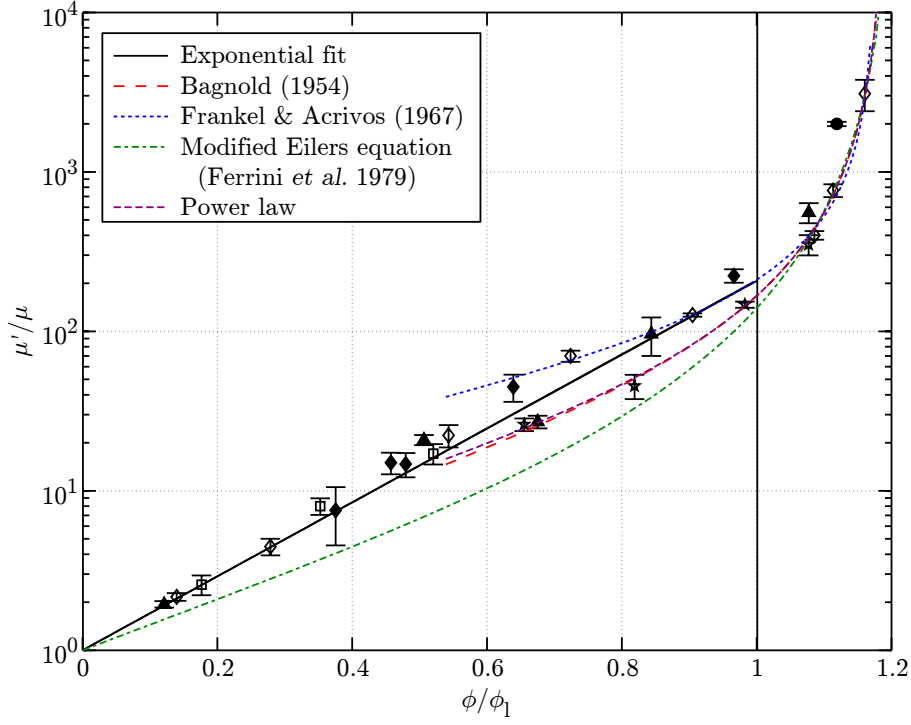


Figure 5.22. Curve fits using experimentally determined fitting parameters.

(equation (5.5)) agrees well with the experimental data in the dilute regime. In the dense regime, however, the previously recorded fits do not coincide with the experimental data. In this region, the exponential fit (equation (5.4)) best matches the experimental data.

## Chapter 6

# Slip layer and the influence of surface roughness

When treated as an effective single phase, liquid-particle flows may appear to violate the non-slip condition at a solid wall (Acrivos 1992). While the interstitial fluid does not violate no-slip, the solid particles are able to roll and slide against the wall, creating behavior in the bulk fluid-particulate flow akin to slip against the solid wall. There may also be a thin layer near the wall where solid particles are not present and that has a lower viscosity than the bulk flow. This thin particle depletion layer creates the appearance of slip in the bulk flow.

This slip occurs most often in experiments with smooth walls and exhibits an increasing dependence on volume fraction (Yilmazer and Kalyon 1989). The conclusions from an experiment may be marred if apparent viscosity is not corrected for the presence of slip (Barnes 2000). Slip has been observed in most multi-phase flows and is a particularly important phenomena in blood flow. Due to the aggregation of red blood cells, the flow in capillaries is subjected to periodic stopping and starting. The duration of this stasis increases without slip, resulting in tissue damage (Picart et al. 1978)

### 6.1 Theory

The slip against a smooth wall may be thought of as being composed of two types. In the first type, “rolling slip,” solid particles are able to roll over stationary walls with a non-zero velocity creating a particle slip velocity,  $v_{slip}$ . This type of slip is often present in granular flows (Brennen 2005) and is likely to occur in densely packed flows ( $\phi > \phi_l$ ). The second



type of slip, “apparent slip” is caused by the migration of particles away from the walls. Because of the decrease in particles near the wall, the effective viscosity drops resulting in a higher velocity gradient. While the resulting particle deficient layers may be very small (less than a particle diameter), they may significantly change the apparent viscosity of the system (Barnes 1995). The two types of slip are illustrated in Figure 6.1. In addition,

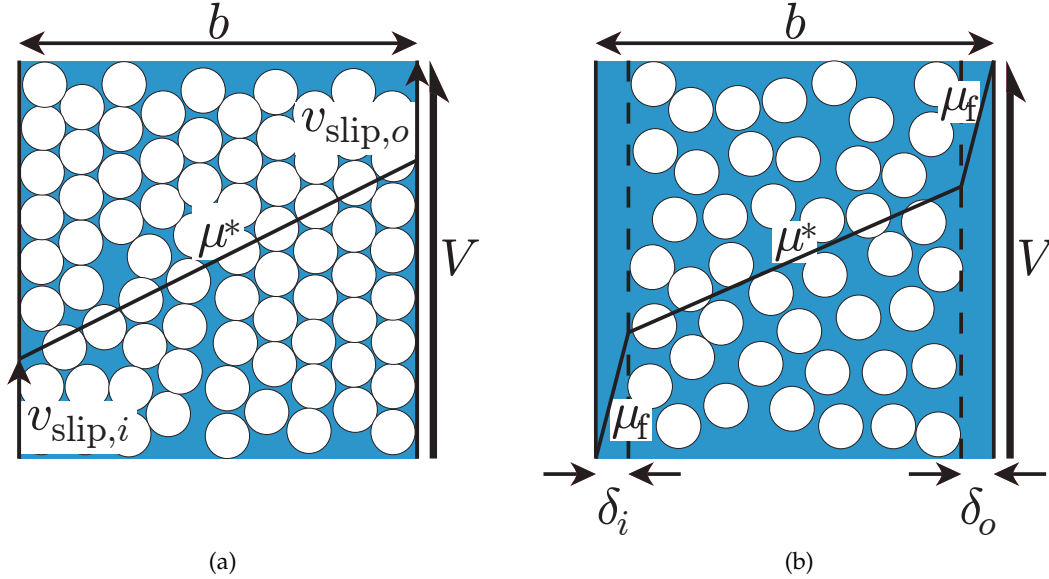


Figure 6.1. (a) Rolling slip caused by rolling or sliding particles in direct contact with the walls. (b) Apparent slip caused by particle deficient layers near the walls.

we note that in concentric cylinder devices, any outward force (such as that on particles denser than the fluid), will tend to push particles toward the outer cylinder wall, thereby reducing the depletion layer thickness on the outer wall and increasing the depletion layer thickness on the inner wall. For large volume fractions, experimentalists have found that the slip on the outer cylinder wall is negligible and that roughening the inner cylinder is sufficient to reduce the total slip in the experiment. (Barnes 1995; Buscall et al. 1993).

The depletion layer thickness is generally smaller than one particle diameter. The thickness of this layer grows linearly with the particle diameter and, while the volume fraction is constant, increases linearly with the shear stress (Soltani and Yilmazer 1998). Typical depletion layer thicknesses are shown in Figure 6.2 for the inner cylinder wall of a concentric cylinder device.

As the depletion layer thickness decreases with the volume fraction, it has been theo-

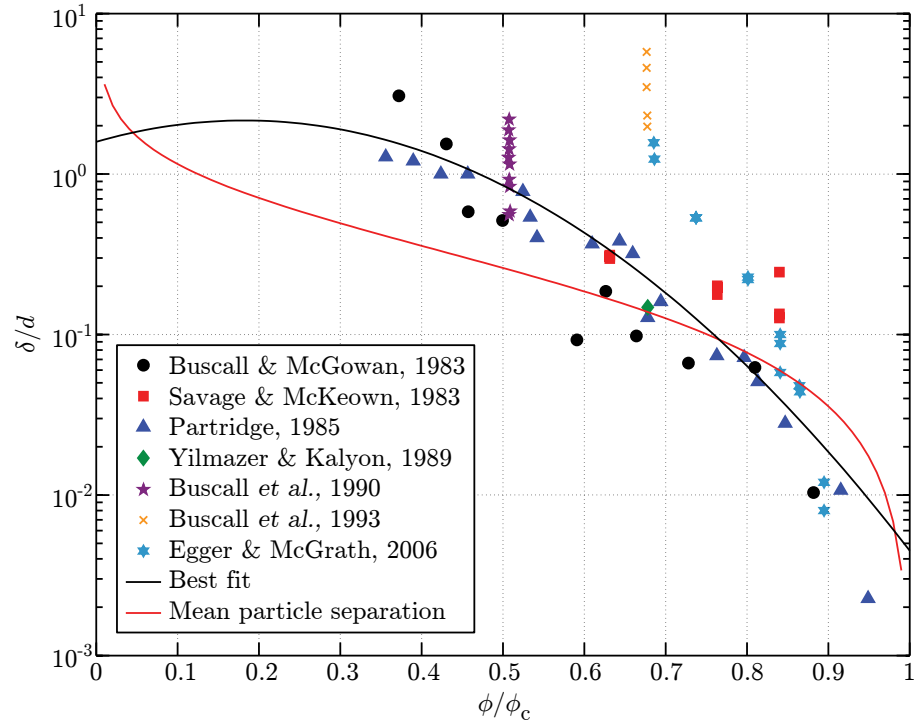


Figure 6.2. Typical depletion layer thicknesses (divided by the particle diameter) on the inner cylinder of a concentric cylinder device. Data from Savage and McKeown (1983) and Egger and McGrath (2006) were calculated from shear stress measurements (assuming slip on the inner cylinder only) for  $d \approx 1$  mm polystyrene beads and a  $d \approx 0.5 \mu\text{m}$  emulsion, respectively. The other data were calculated from shear stress measurements for  $d \approx 1 \mu\text{m}$  polystyrene as reported in Buscall *et al.* (1993).

rized by Buscall et al. (1993) that the mean particle separation in the core region,

$$\frac{\delta}{d} = \left( \frac{\phi_c}{\phi} \right)^{1/3} - 1, \quad (6.1)$$

might be a heuristic estimate of the gap thickness. The mean particle separation tends to zero as the volume fraction increases toward maximum packing and increases rapidly for smaller volume fractions. This dependence is shown in Figure 6.2 with values for the depletion layer thickness estimated from measurements of the effective viscosity (see subsection 6.1.1). The mean particle separation compares favorably at high volume fractions, but deviates from the mean value for the depletion layer thickness at lower volume fractions. At low volume fractions, the particles are able to migrate away from the stationary walls, but at higher volume fractions, this movement is impeded by the presence of the other particles in the core region.

While rolling slip may occur at high volume fractions ( $\phi > \phi_l$ ), and is investigated in subsection 6.2.2, this thesis focuses on the influence of apparent slip on the bulk properties. Apparent slip can influence measurements of the effective viscosity, particle velocities, and to a lesser degree, the volume fraction of solids. Several assumptions must be made to elucidate the influence of slip on these bulk properties:

1. *Both the depletion layer and core region are treated as Newtonian.* Viscosity is treated as uniform in each region and assumed to be independent of the shear stress. Note that in the present experiments, the fluid used is Newtonian and the bulk effective viscosity does not exhibit Reynolds number effects (chapter 4).
2. *There is no slip at the wall.* The depletion layer is composed of the continuous (fluid) phase that must satisfy the nonslip condition at the wall.
3. *The shear stress is continuous at the depletion layer-core region interface.* The present experiments were conducted under steady-state conditions where no such discontinuities should exist.
4. *The depletion layers are small compared with the cylinder radii.* In the present experiments, the depletion layer should be of the order of (or much smaller than) the particle diameter.

If both regions of the flow can be treated as Newtonian, the velocity in each region can be written as:

$$u(r) = C_1 r + \frac{C_2}{r}, \quad r_i \leq r \leq r_i + \delta_i, \quad (6.2)$$

$$u(r) = C_3 r + \frac{C_4}{r}, \quad r_i + \delta_i \leq r \leq r_o - \delta_o, \quad (6.3)$$

$$u(r) = C_5 r + \frac{C_6}{r}, \quad r_o - \delta_o \leq r \leq r_o, \quad (6.4)$$

where from the no-slip conditions on the inner and outer wall,

$$C_1 r_i + \frac{C_2}{r_i} = 0, \quad (6.5)$$

$$C_5 r_o + \frac{C_6}{r_o} = 0. \quad (6.6)$$

Continuity of the velocity at the depletion layer-core region interface yields

$$C_1 (r_i + \delta_i) + \frac{C_2}{r_i + \delta_i} = C_3 (r_i + \delta_i) + \frac{C_4}{r_i + \delta_i}, \quad (6.7)$$

$$C_3 (r_o - \delta_o) + \frac{C_4}{r_o - \delta_o} = C_5 (r_o - \delta_o) + \frac{C_6}{r_o - \delta_o}, \quad (6.8)$$

and continuity of the shear stress at the interface,

$$\mu_f \frac{C_2}{(r_i + \delta_i)^2} = \mu^* \frac{C_4}{(r_i + \delta_i)^2}, \quad (6.9)$$

$$\mu^* \frac{C_4}{(r_o - \delta_o)^2} = \mu_f \frac{C_6}{(r_o - \delta_o)^2}. \quad (6.10)$$

This system of equations can be simplified if the depletion layer thicknesses are small. Using these equations, relations can be found between the measured (apparent) viscosity, the actual viscosities of each fluid layer (subsection 6.1.1) and the depletion layer thickness. A relation can also be found between measured particle velocity and the depletion layer thickness (subsection 6.1.2).

### 6.1.1 Apparent viscosity

From the equations of the last section, the apparent shear rate is

$$\gamma_{app} = 2V \frac{r_o}{r_o^2 - r_i^2}, \quad (6.11)$$

where  $V$  is the velocity of the outer cylinder. The shear stress at the inner cylinder is thus

$$\tau_i = \mu_{app} \gamma_{app}, \quad (6.12)$$

where  $\mu_{app}$  is the apparent viscosity of the mixture. Assuming that there is a thin layer without particles, the shear stress is

$$\tau_i = \mu_f \gamma_i, \quad (6.13)$$

where  $\gamma_i$  is the shear rate of the inner depletion layer. This shear rate is a function of the fluid viscosity  $\mu_f$ , the effective viscosity of the fluid-particulate mixture  $\mu^*$ , and the boundary conditions on the flow subjected to the assumptions mentioned in the previous section. Equating these two equations for the shear stress at the inner cylinder yields

$$\mu_{app} = \frac{\mu^*}{a \left( \frac{\mu^*}{\mu_f} - 1 \right) + 1}, \quad (6.14)$$

where  $a$  is a function of the depletion layer thicknesses,  $\delta_i$  and  $\delta_o$  on the inner and outer walls, respectively:

$$a = \frac{\left( \frac{\delta_i}{b} r_o^3 + \frac{\delta_o}{b} r_i^3 \right)}{r_o r_i (r_o + r_i)}. \quad (6.15)$$

If the depletion layer thicknesses are the same thickness and denoted by  $\delta$ ,

$$a = \frac{\delta}{b} \frac{r_o^3 + r_i^3}{r_o r_i (r_o + r_i)}. \quad (6.16)$$

If the slip only occurs on the inner cylinder,

$$a = \frac{\delta_i}{b} \frac{r_o^2}{r_i (r_o + r_i)}. \quad (6.17)$$

Finally, if the Couette flow can be simplified as a simple shear flow ( $b \ll r_o$ ),

$$a = \frac{\delta_i + \delta_o}{b}. \quad (6.18)$$

The error in the apparent viscosity, for several depletion layer thicknesses and the geometry of the present experiment, is shown in Figure 6.3. The difference between the measured

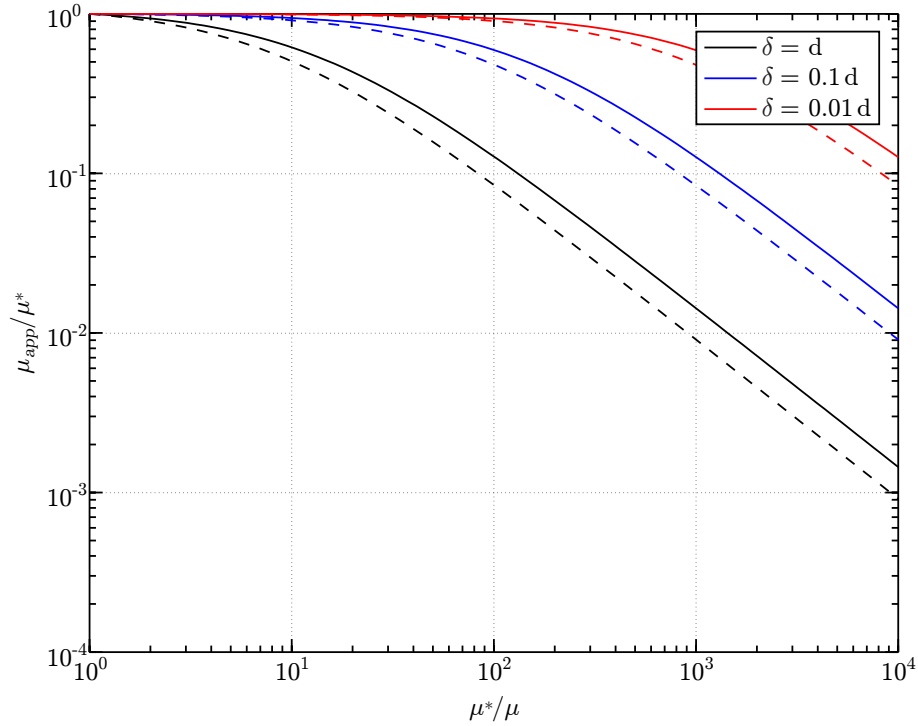


Figure 6.3. Ratio of the apparent viscosity to the actual bulk viscosity as a function of the ratio of the bulk viscosity to the fluid viscosity for several depletion layer thicknesses. Solid lines represent slip occurring on only one cylinder wall while dashed lines represent slip on both walls. The depletion layer thickness is given as a percentage of the particle diameter where, for the polystyrene particles,  $d/b = 0.1057$ .

apparent viscosity and actual bulk viscosity is smallest for small actual bulk viscosities such that the difference in the viscosity between the slip layers and core region are small and for smaller depletion layer widths. As seen in Figure 6.2, the depletion layer decreases with volume fraction while the actual viscosity increases. These two effects together work to temper the uncertainty in the measured viscosity as a function of the volume fraction, but this error can still be significant. Direct measurements of either the slip layer thickness or measurements of both the actual and apparent viscosities must be made in order to quantify this error.

### 6.1.2 Particle velocity

The depletion layer on the inner cylinder can also be calculated from measurements of the particle velocities near that surface on the inner cylinder. Since there are no particles in the depletion layer, the particles viewable from the stationary cylinder are those at the depletion layer-core region interface. Using the velocity at the inner interface ( $r = r_i + \delta_i$ ) and the assumption that the particles located at this radius are moving at the same velocity as the fluid, equation (6.2) and equation (6.13) can be used to express the particle velocity  $u$  as,

$$\frac{u}{V} = \frac{2\delta_i}{b} \frac{\mu_{app}}{\mu_f} \frac{r_o^2}{r_i(r_o + r_i)}. \quad (6.19)$$

This relation for the ratio of velocities is equivalent to

$$\frac{u}{V} = 2 \frac{\mu_{app}}{\mu_f} a, \quad (6.20)$$

where  $a$  is the function obtained for slip on the inner cylinder (equation (6.17)). Thus, the inner depletion layer thickness can be estimated using a particle velocity measured near the inner cylinder. Using equation (6.14), the ratio of velocities can also be expressed as a function of the actual viscosity of the core region.

## 6.2 Experiments with polystyrene

To investigate the influence of slip on the effective viscosity measurements, the cylinder walls were roughened. As the slip is significantly reduced when the surface roughness is the same size as or larger than the diameter of the particles the cylinder walls were roughened using particles glued to that surface (Gulmus and Yilmazer 2007). Particles were glued to thin rubber sheets, which were attached to both the inner and outer cylinders. The particles are oriented randomly at a surface volume fraction  $\phi_{2D} = 0.70$ . A typical image of the glued particles is included in Figure 6.4. The roughened cylinders are expected to significantly reduce the slip. For simplicity, the roughened surface is considered a “no-slip” boundary in which there is no depletion layer and the measured viscosity is the actual bulk viscosity of a fluid-particulate mixture at that volume fraction. This assumption is verified in subsection 6.2.3.



Figure 6.4. Photograph of the surface roughness added to inner and outer cylinders. The surface volume fraction is 0.70. Markings on the ruler are in centimeters.



As was discussed in section 6.1, there are two ways of calculating the thickness of the depletion layer: using the difference in shear stress measurements (subsection 6.1.1) and using the measured slip velocity (subsection 6.1.2). In subsection 6.2.1, the measured shear stress and effective viscosity for the rough wall experiments is found. This effective viscosity for the rough walls is detailed, and it is assumed that this corresponds to the no-slip measurements. The effective viscosity from the rough wall experiments is compared with the smooth wall experiments and a depletion layer thickness is calculated. In subsection 6.2.2, the slip velocity found in subsection 5.2.1.1 is combined with the effective viscosity (subsection 5.2.1.3) to calculate the depletion layer thickness. Finally, in subsection 6.2.3, the velocity near the inner, stationary rough wall is measured to confirm that the slip is virtually nonexistent in the rough wall case.

### 6.2.1 Actual viscosity measurements

Rough wall experiments were conducted using polystyrene particles glued to the both the inner and outer cylinders. As was described in section 3.2, torque measurements were taken on the inner, stationary cylinder and used to calculate the shear stress and effective viscosity using polystyrene particles in a equal density aqueous glycerine mixture. These measurements of effective viscosity are considered to be measurements of the actual bulk viscosity as slip is non-existent at the rough wall.

The experimental apparatus is designed to record torque through the displacement of a target attached to the center, floating cylinder. As the static position of this target is somewhat indeterminate and varies from experiment to experiment, it is the displacement from an initial position that is recorded for each volume fraction. The slope is found for lines passing through the origin so as to guarantee that the shear stress is zero when the cylinder is stationary. This adjustment affects the deduced values for shear stress, but does not influence the measurements of the effective viscosity. The effective viscosity for each volume fraction is determined from the slope of the shear stress curvefit, a value unchanged by any uncertainty in the initial target position.

The shear stress measurements for a range of volume fractions is shown in Figure 6.5 on a log-log plot. The shear stress varies by several orders of magnitude between the low volume fraction measurements and the highest volume fractions. For each volume

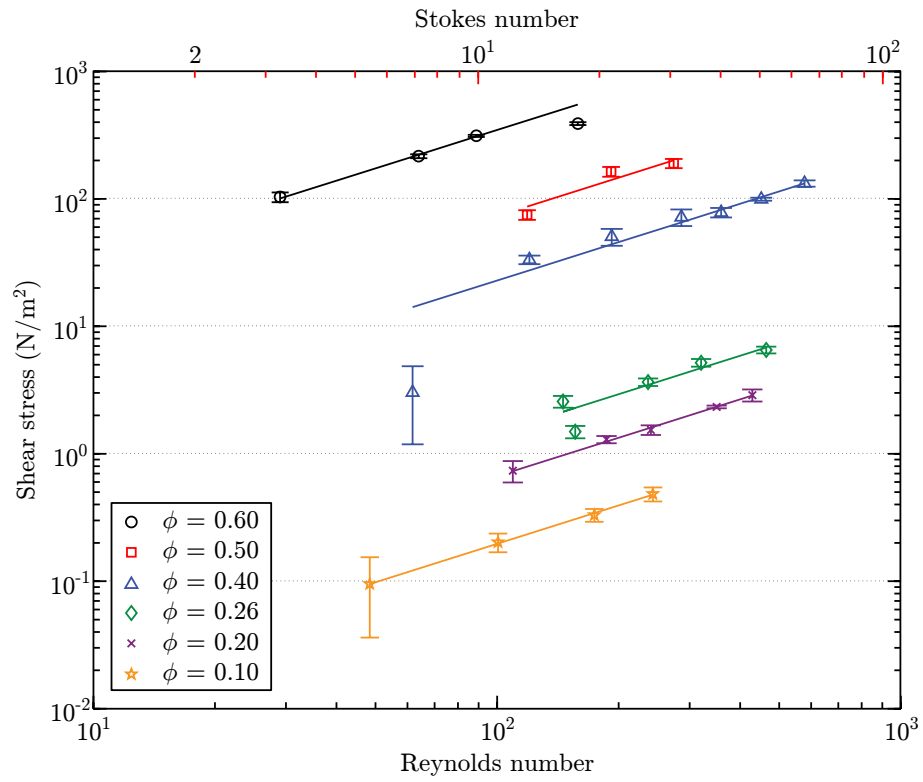


Figure 6.5. Shear stress measurements for suspensions of polystyrene particles in aqueous glycerine with rough cylinder walls. The lines represent linear fits, constrained by the condition that the shear stress must be zero at  $\text{Re} = 0$ , for each volume fraction.

fraction, the shear stress is a linear function of the Reynolds number as one would expect for a Newtonian fluid. This behavior is also consistent with the smooth wall neutrally buoyant experiments (section 4.2). At the highest volume fraction ( $\phi = 0.60$ ), there is a reduction in shear stress at the highest Reynolds number. This behavior is consistent with the same reduction shown for the smooth wall case (Figure 4.1).

The torque measurements are normalized by the torque from the pure fluid viscosity (corrected for any temperature variations). and the resulting normalized torque measurements are shown in Figure 6.6. The ratio of torques is equivalent to an effective viscosity

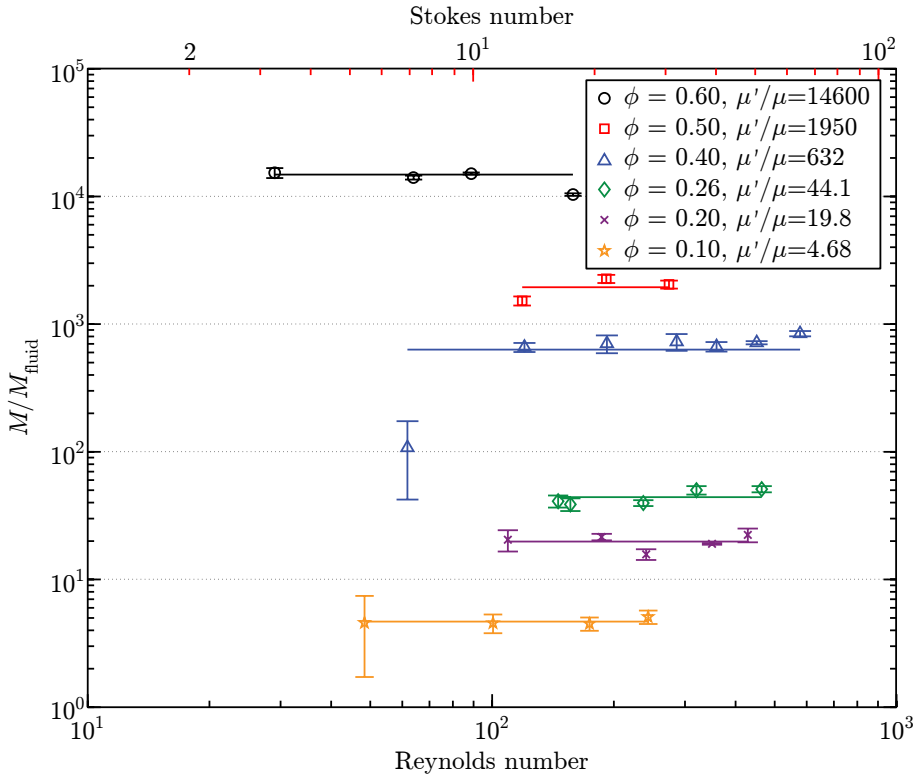


Figure 6.6. Ratio of measured torque to pure fluid torques for suspensions of polystyrene particles with rough cylinder walls. The horizontal lines are fits to the data and represent the value of the ratio of effective viscosity to pure fluid viscosity  $\mu'/\mu$ .

ratio. The effective viscosity ratio remains relatively constant with Reynolds number with the exception of the highest volume fractions (as noted earlier). The effective viscosity increases by almost four orders of magnitude between the lowest volume fraction and the highest volume fraction. This large increase in effective viscosity is similar to that exhibited in the smooth wall experiments.

The effective viscosities corresponding to the horizontal lines in Figure 6.6 are plot-

ted against the volume fraction of particles in Figure 6.7. This figure shows that the rough wall experimental data exhibits an exponential increase with the volume fraction below the loose-packed volume fraction. Between the loose-packed and close-packed volume fractions, the effective viscosity is expected to increase significantly, but this behavior could not be confirmed due to limitations in the experimental apparatus that prevented operation at such high torques.

The effective viscosity for rough wall experiments is higher at every volume fraction than the equivalent from the smooth wall experiments (gray six-pointed stars). If the smooth wall experiments are subjected to slip, it would logically follow that the measured viscosity for the rough wall (non-slip) experiments would be higher. The apparent viscosity for the smooth wall experiments would be reduced by a factor which includes the size of the slip layer (equation (6.14)). Furthermore, this difference between the two measurements is expected to increase as the effective viscosity (volume fraction) increases. Using the difference between the smooth (apparent) and the rough (actual) viscosity curves, the function  $a$  can be calculated for each volume fraction. From this function, the depletion layer thickness can be calculated assuming some relationship between the depletion layer on the inner cylinder and the outer cylinder. In Figure 6.8 the depletion layer thicknesses thus calculated are plotted assuming that slip occurs either on the inner cylinder alone or that the depletion thicknesses are the same on both the inner and outer cylinders. The calculated depletion layer thickness is slightly lower than previously recorded data ( $\bullet$ ), but is consistent with those measurements. The difference in depletion layer thickness between the cases if slip occurs on both walls or just only on the inner cylinder is small, but the inner wall data better matches previously recorded data. As the previous data was calculated assuming just slip on the inner cylinder, this is not surprising. However, no information presently exists with which definitive statements on the presence of a slip layer against the outer cylinder may be made. Measurements of the slip velocity – with which the depletion layer thickness on the inner cylinder may be calculated – can help to elucidate if slip occurs on one or both of the cylinders.

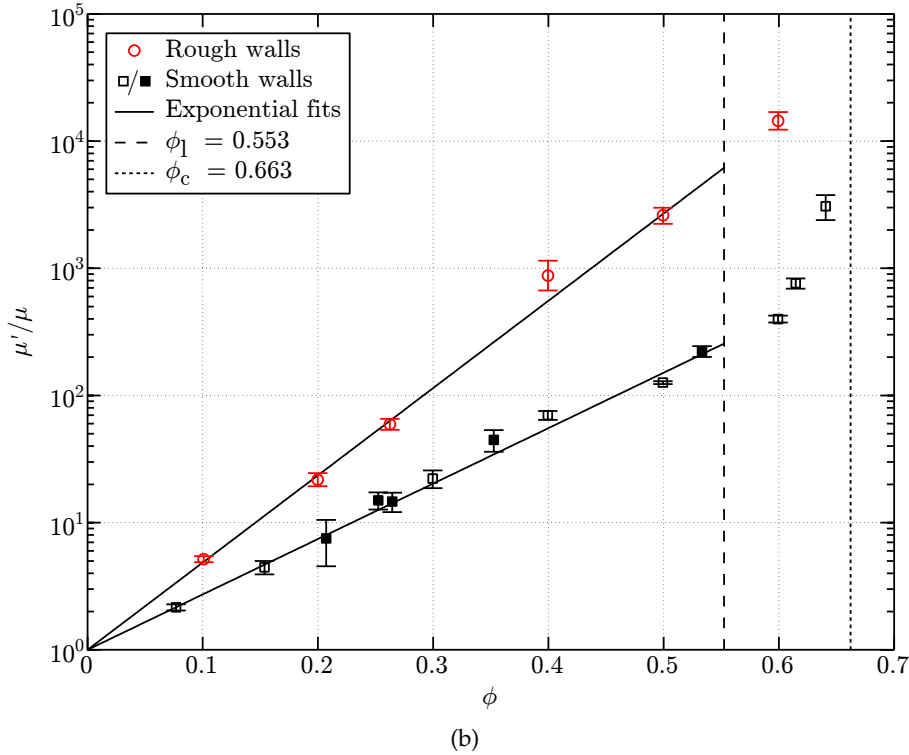
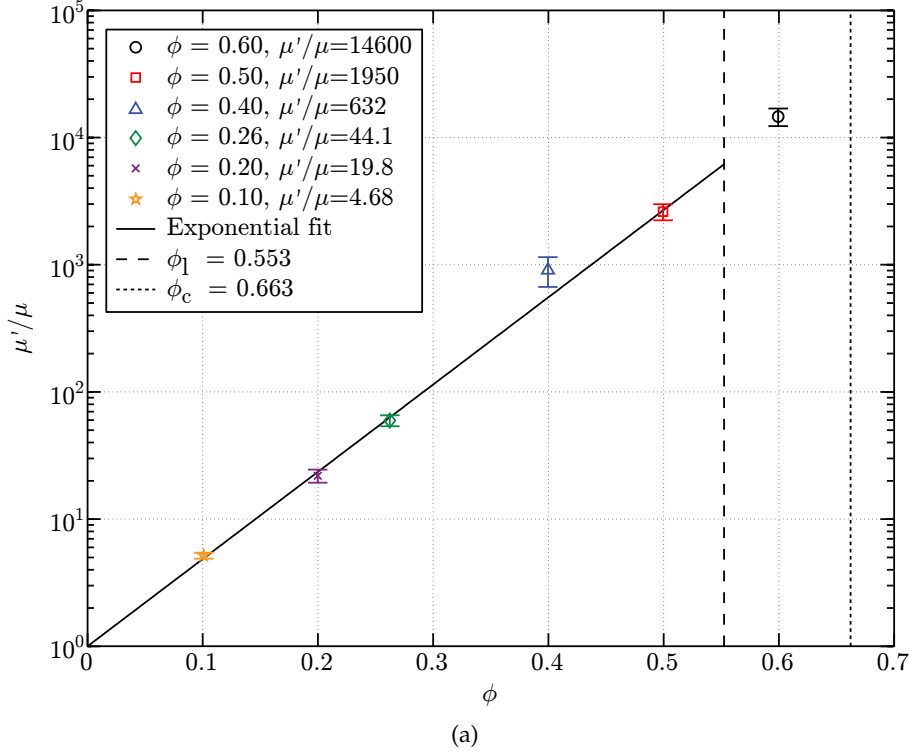


Figure 6.7. Effective viscosity ratio for neutrally buoyant polystyrene particles in aqueous glycerine solutions with (a) rough and (b) rough and smooth cylinder walls. The black line is an exponential fit for the points below  $\phi = \phi_l$ . Dashed vertical lines denote the loose-packing and close-packing volume fractions.

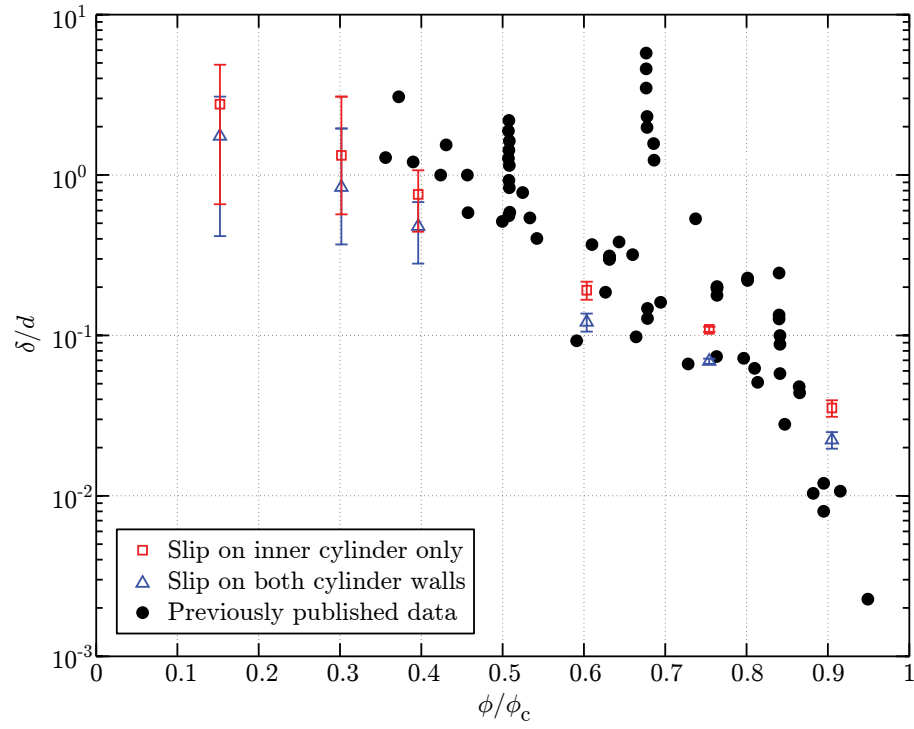


Figure 6.8. Depletion layer thicknesses (— and —) calculated from apparent and actual viscosity measurements using equation (6.14) shown with previously reported experimental values (•, Figure 6.2).

### 6.2.2 Particle velocity

Using non-neutrally buoyant polystyrene particles in various aqueous glycerine mixtures with different densities, particle velocities and effective viscosities were recorded as described in subsection 5.2.1. This data is shown in Figure 6.9, plotted as a function of the Reynolds number (based on the speed of the outer, rotating cylinder). As the Reynolds

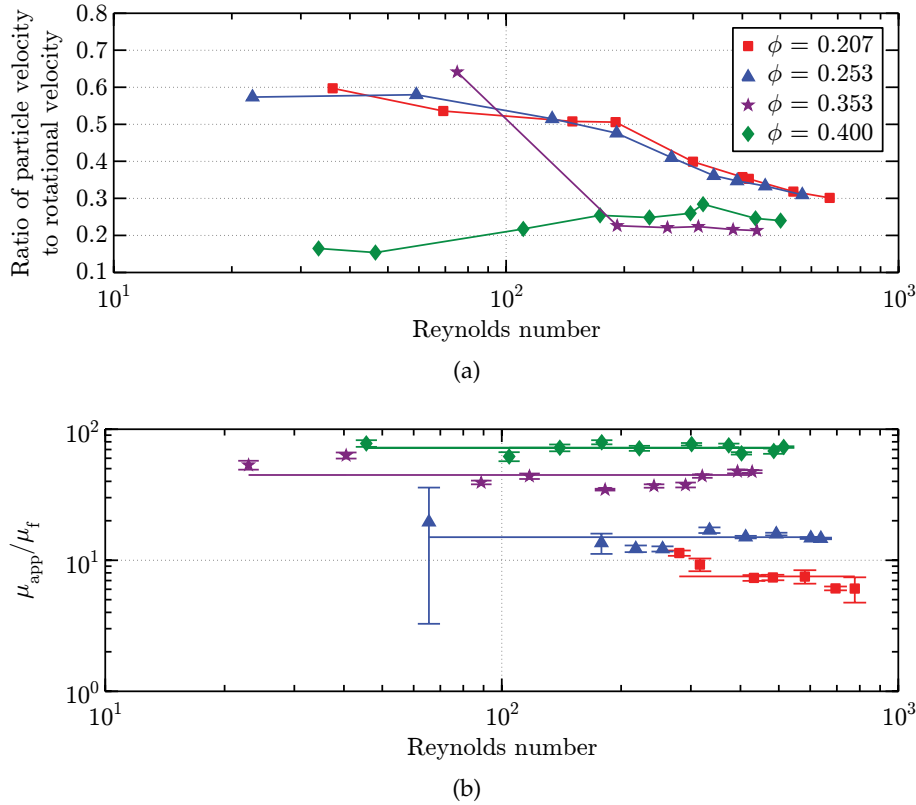


Figure 6.9. (a) Particle velocities (reprinted from Figure 5.1) and (b) measured apparent viscosities (reprinted from Figure 5.9) for non-neutrally buoyant polystyrene particles.

number increases, the normalized particle velocity changes while the apparent viscosity remains fairly constant. The thickness of the inner depletion layer can be found using these two data sets and equation (6.19). This thickness (normalized by the mean particle diameter) is shown as a function of the Reynolds number in Figure 6.10. The depletion layer thickness remains fairly constant with Reynolds number and clearly varies with the density of the fluid. The thickness increases as the fluid to particle density increases with the neutrally buoyant particles exhibiting the smallest thickness (more than an order of magnitude smaller than the greatest density ratio case). Increasing the density ratio in-

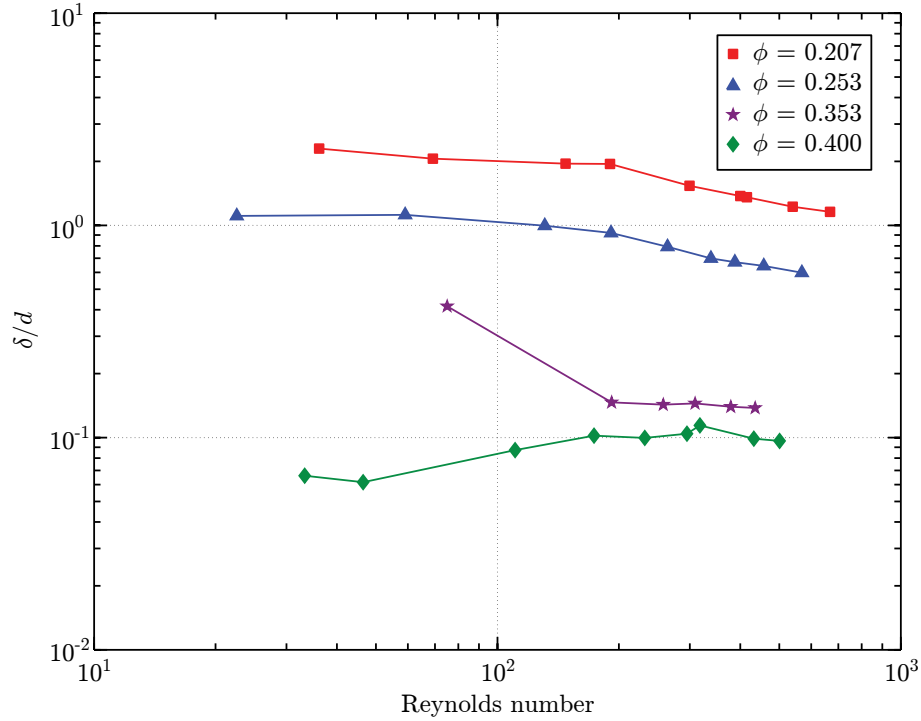


Figure 6.10. Depletion layer thickness calculated from the velocity measurements shown as a function of the Reynolds number.

hibits the fluidization of particles within the annular gap. When the particles are not fully fluidized, they have a lower local volume fraction, as was discussed in subsection 5.2.1.2 (and shown in Figure 5.6). The depletion layer thickness as a function of this effective volume fraction is shown in Figure 6.11. The depletion layer thickness decreases as the volume fraction increases toward the random close-packed volume fraction,  $\phi_c$ . The values for the depletion layer thickness calculated using the velocity data compare favorably to the calculations using the difference in the apparent and actual effective viscosities (subsection 6.2.1) and imply that for low volume fractions, slip occurs on just the inner cylinder wall, but for higher volume fractions, slip occurs on both cylinder walls. The measured values are slightly lower than previously reported values, but are the same order of magnitude. As discussed in section 6.1 and shown in Figure 6.2, the previously reported values for the depletion layer thickness ( $\bullet$ ) were calculated using the effective viscosity measurements and assumed that slip occurs only on the inner cylinder wall. If it was assumed that slip occurred on both walls (as one would expect for dense volume fractions) then the previously reported data would shift downward slightly, placing these values more in line



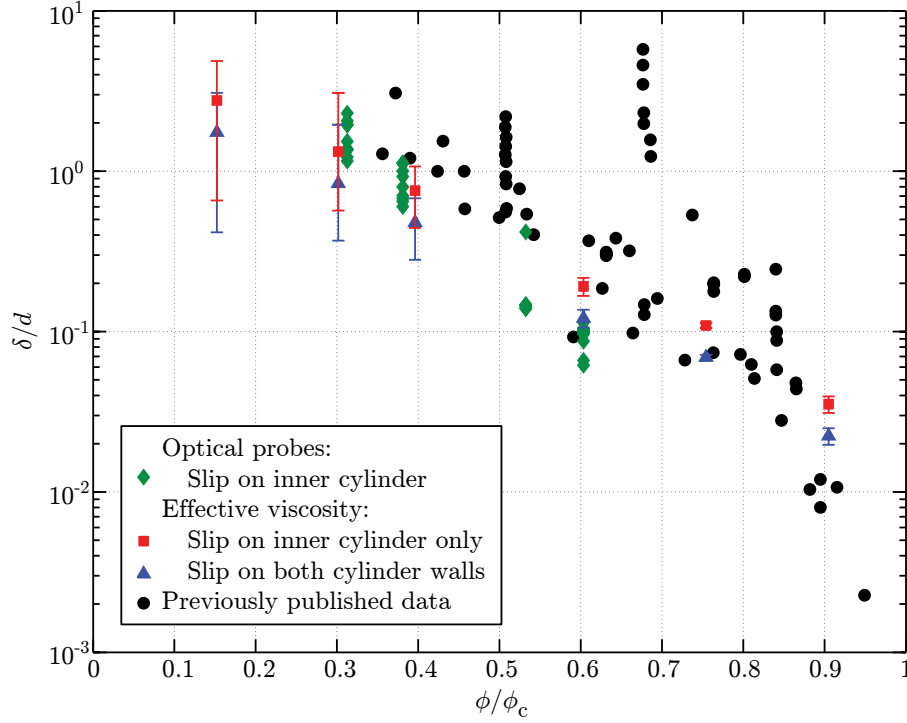


Figure 6.11. Depletion layer thickness calculated from the velocity measurements using equation (6.19).

with the values obtained using the velocity data.

### 6.2.3 Smooth and rough wall boundary conditions

The previous sections assumed that liquid-solid flow experiments conducted with rough walls were characterized by not having slip against the cylinder walls. If this non-slip condition was in effect, there is no particle depletion layers and the measured effective viscosity is equal to the actual bulk viscosity for the fluid-particulate flow. To confirm that there is little or no slip near the stationary cylinder, the particle velocities were measured using the MTI optical probes (subsection 3.2.1) for an flow with an average volume fraction of  $\phi = 0.30$  in various density aqueous glycerine mixtures.

The particle velocity, normalized by the rotational velocity of the cylinder, is displayed in Figure 6.12b for rough walls and Figure 6.12a for smooth walls. These measured velocity ratios are shown with the value predicted for a Couette flow at a given radius, if no depletion layers are present and the velocity profile within the annular gap is uniform. If the particles perfectly follow the fluid, these lines represent the velocity of the particle

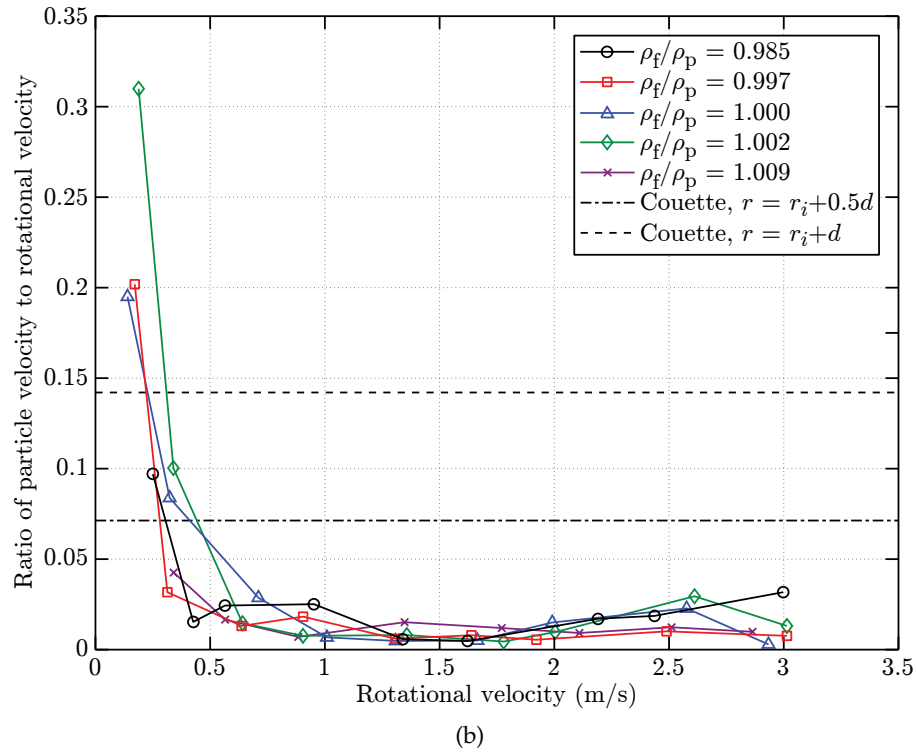
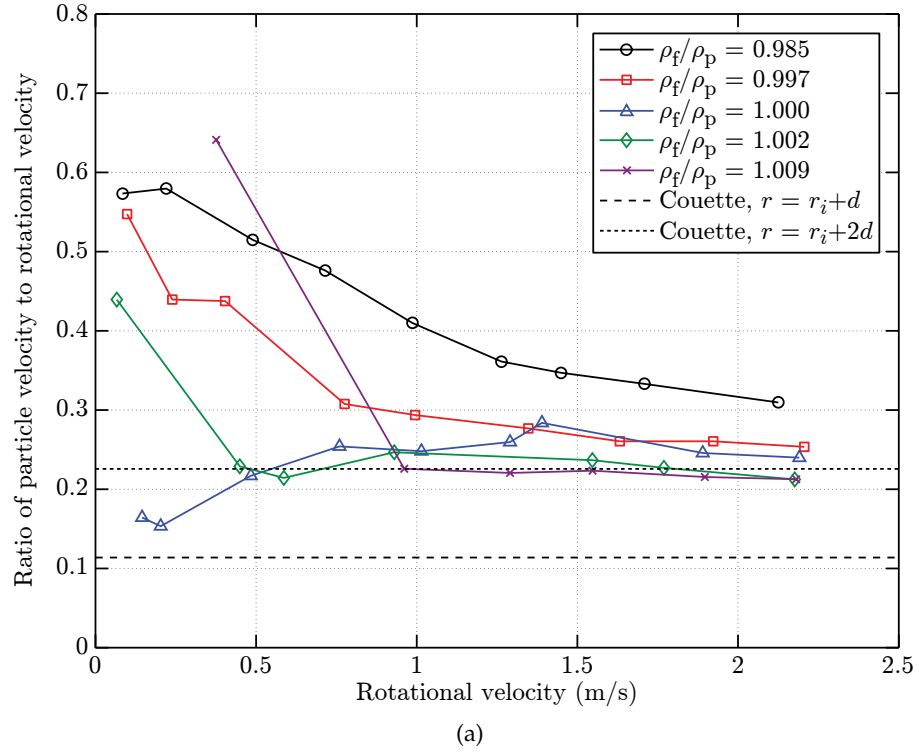


Figure 6.12. Ratio of particle velocity to the rotational velocity of the outer cylinder, as measured near the stationary wall, for (a) smooth walls and (b) rough walls. Both graphs are shown with the velocity predicted if the particle, centered at  $r$ , was moving with the velocity of a Couette flow without slip layers.

centers at those points. If depletion layers are present, the actual distance between the stationary cylinder and the particle centers is smaller than  $r - r_i$  and is calculated as in the previous section.

The measured particle velocities in the smooth wall case are much higher than for the rough wall case. For smooth walls, the velocities appear to asymptotically approach a velocity close to the  $r = r_i + 2d$  uniform Couette velocity. In the smooth wall experiments, the depletion layer thickness is calculated to be  $\delta = 2d$  for a volume fraction of  $\phi = 0.25$  (Figure 6.10). For the roughened walls, the measured particle velocities are much smaller and approach a very small velocity asymptote. This asymptote is below Couette velocity without the presence of slip layers for a radius  $r = r_i + 0.5d$ , implying that the particles have very little velocity near the stationary cylinder. If a depletion layer were still to exist, a depletion layer thickness below  $\delta = 0.01d$  is calculated (for  $\phi = 0.26$ ) – two orders of magnitude smaller than for the smooth wall case. With the addition of particles to roughen the inner and outer cylinder walls, the slip is significantly reduced implying that any error in the measured apparent viscosity is also very small. These rough wall measurements are considered to represent the actual bulk effective viscosity for the fluid-particulate flows.

### 6.3 Corrections for smooth walls

Smooth wall experiments are subject to apparent slip. This apparent slip – caused by a small particle-free layer near the smooth walls – can significantly lower the measured viscosity. The actual viscosity is related to the measured, apparent viscosity by

$$\mu^* = \frac{\mu_{app}(a - 1)}{\mu_{app}a - 1}, \quad (6.21)$$

where the slip parameter  $a$  is a function of the depletion layer thickness. If this depletion layer thickness can be estimated, as was done in section 6.2, the actual effective viscosity can be determined from smooth wall experiments. One such estimation yields the relation shown in Figure 6.13. This corrected data compares favorably for small volume fractions, but as the volume fraction increases, the difference between the corrected smooth wall data and the measured rough wall data becomes more pronounced. As the volume fraction increases, the depletion layer and thus the slip parameter becomes smaller. This parameter

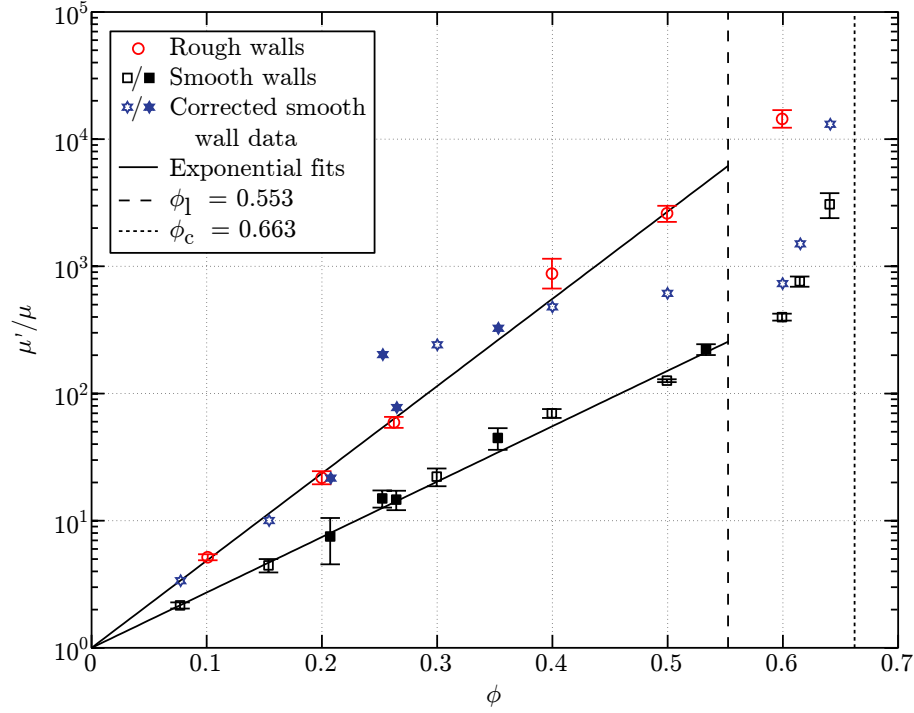


Figure 6.13. Smooth wall data corrected for the presence of particle depletion layers and plotted as a function of the volume fraction of polystyrene. The corrected data is shown with the measured effective viscosity for rough and smooth walls.

multiplied by the apparent viscosity approaches unity, driving the calculated effective viscosity toward infinity. This mathematical artifact causes erroneous results in the regions around  $\phi = 0.31$  and  $\phi = 0.56$ . This correction is best confined to low volume fraction measurements.

## 6.4 Summary

The slip of particles against smooth wall cylinders can dramatically reduce effective viscosity measurements. For volume fractions less than  $\phi_l$ , the slip appears to be caused by a small particle depletion layer near the cylinder walls. Slip can be eliminated if roughness with a typical length equal to or greater than the particle diameter is added to the cylinder walls. Particles are glued to both the inner and outer cylinder walls and the effective viscosity as well as particle velocities are measured for this configuration. The particle velocities show that near the stationary wall, the particle velocity is small (less than 5% of the rotational velocity of the outer cylinder); less than if the particle centers moved at

a velocity coincident with a uniform Couette flow at a particle radius from the stationary wall.

The depletion layer thickness is measured through comparisons between smooth and rough wall effective viscosity measurements and through measurements of the particle velocities near the inner cylinder wall. This depletion layer thickness decreases as the volume fraction is increased with slip on the inner cylinder dominating for  $\phi < 0.5\phi_c$ . Above  $\phi = 0.5\phi_c$ , slip on the outer cylinder wall is also important. For  $\phi > \phi_l$ , slip caused by particles rolling over the cylinder walls appears to dominate and is able to contribute significantly to differences found between smooth and rough wall experiments.

## Chapter 7

# Summary and conclusions

This thesis describes experiments with neutrally buoyant and non-neutrally buoyant particles in a concentric cylinder apparatus, which could be equipped with either smooth or rough walls. The goal of these experiments was to determine the effective viscosity of the fluid-particulate mixture as a function of the key parameters. For these non-Brownian flows, the effective viscosity ratio may depend on the Archimedes number, Reynolds number, the volume fraction of solids, a size or shape parameter, and the ratio of the particle-to-fluid densities:

$$\frac{\mu'}{\mu} = f \left( \text{Ar}, \text{Re}, \phi, \frac{d}{L^*} \frac{\rho_p}{\rho_f} \right). \quad (7.1)$$

In the following sections, these dimensionless parameters are discussed to elucidate their effects on the flow and its effective viscosity.

### 7.1 Neutrally buoyant particles

For neutrally buoyant particles, the effective viscosity does not depend on the ratio of particle-to-fluid densities nor on the Archimedes number. The effective viscosity can depend on the Reynolds number, the volume fraction, and on the size or shape parameter.

$$\frac{\mu'}{\mu} = f \left( \text{Re}, \phi, \frac{d}{L^*} \right). \quad (7.2)$$

In chapter 4, the specific influence of the Reynolds number and volume fraction were examined. These results are summarized below.

### 7.1.1 Reynolds number

For all of the different particles tested, the effective viscosity was measured as a function of the Reynolds number based on the shear rate within the annulus and the width of the annular gap. As demonstrated with the polystyrene particles in a matched density fluid (Figure 4.2), there was very little dependence on the Reynolds number. Like the pure fluid, the fluid-particulate flows are Newtonian with a constant viscosity for the range of Reynolds numbers tested. There was no Bagnold-like transition between “grain-inertia” and “macro-viscous” flows. (As discussed in section 1.2, the boundary layer effects in Bagnold’s experiments were responsible for this transition and caused his erroneous conclusion (Hunt et al. 2002).)

That is not to say that there was no dependence on the Reynolds number. The lowest volume fractions in Figure 4.4 did show a slight increase in effective viscosity at the highest Reynolds numbers as the secondary flows in the present experimental apparatus started to gain strength and impinge on the measurements taken at the center, floating cylinder. There also appeared to be some influence on the Reynolds number for the very highest volume fraction tested using neutrally buoyant polystyrene ( $\phi = 0.641$ ). For this test, the effective viscosity decreased slightly with Reynolds number. This effect was most likely due to slip between the polystyrene particles and the smooth walls. The influence of slip was examined in chapter 6 and is summarized below in section 7.3.

It was the intent of this thesis to determine if a collisional regime contributed to the effective stresses. Unfortunately, the maximum rate of rotation for the experimental apparatus limited the use of particle materials – especially at low volume fractions – to plastics where the particle density was close to or matched to the fluid density. This limited the particle Stokes number below 100 for the glass, nylon, polystyrene, and SAN particles and below 10 for the polyester particles. As discussed in subsection 1.1.5, the coefficient of restitution for a particle collision depends very strongly on the relative Stokes number between two colliding particles. For Stokes numbers less than 9, no rebound occurs and the coefficient of restitution is zero. For larger Stokes numbers, a clear rebound exists, but the coefficient of restitution may still be small: only for collisions above a Stokes number of about 1000 does the coefficient of restitution approach unity. In the present thesis, there was no clear dependence on the particle Stokes or Reynolds numbers, but since we could

not conduct experiments for a wide range of shear rates within this collisional regime, this dependence is still undetermined.

### 7.1.2 Volume fraction of solids

For Newtonian flows, the effective viscosity seems to depend only on the volume fraction of particles. This class of flows can be divided into three subregions: dilute, dense, and continuous contact volume fractions as seen in the phase diagram, Figure 7.1. Dilute

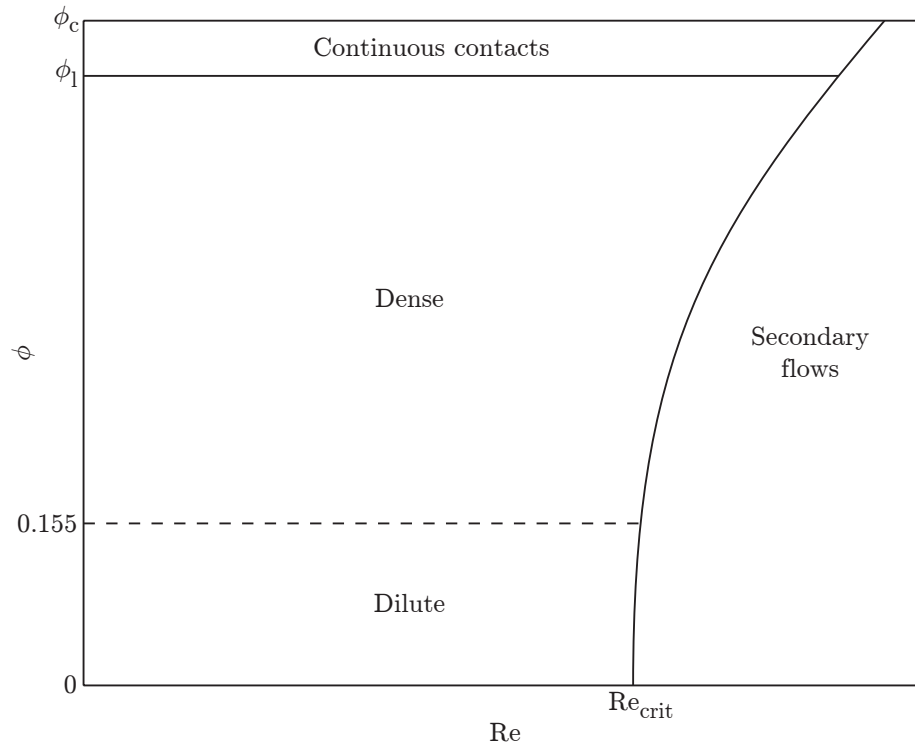


Figure 7.1. Phase diagram for fluid-particulate flows showing delimitations in the volume fraction and Reynolds number. (Based on the figure by Coussot and Ancey 1999).

particle mixtures are those where particle collisions are infrequent and the effective viscosity is close to the fluid viscosity. The upper boundary of this regime appears to be about  $\phi = 0.155$ , the point at which the distance separating particles is a particle radius. Continuous contact behavior exists in the region between the random loose-packed volume fraction ( $\phi_l$ ) and the random close-packed volume fraction ( $\phi_c$ ) where particle collisions become a dominant factor and the effective viscosity increases rapidly. The regime between dilute and continuous contact behaviors is referred to as a dense suspension.

In the dilute region, particle collisions are rare, and the effective viscosity is a perturba-



tion from the pure fluid viscosity. Advection dominates over diffusion caused by particle interactions in this region due to the minimal collisions. In the dense region, advection continues to be the dominant form of diffusion. While the perturbative formulas for the effective viscosity cannot be used in the dense region, no transition is expected to occur. The random loose-packing volume fraction marks the boundary between the dense and continuous contact regimes. Above  $\phi_l$ , the particles are always in contact with at least one neighbor and collisional diffusion dominates. As the movement of one shear layer depends on adjusting the placement of many neighboring particles, the effective viscosity is expected to increase rapidly with the solids fraction in this region. At the random close-packing volume fraction, there is no free room for additional particle movement. At this point, the movement of particles in a shear layer requires the deformation of either the particles or the walls.

Different sized and shaped particles were examined in the present experiment. For each of the particles, the random packed volume fractions can vary, as discussed in chapter 2. In order to eliminate variations due to changes in these parameters, they are used as a normalization for the volume fraction of solids. As the random loose-packing volume fraction represents the change between advection dominated and collisional dominated behavior, it is the logical choice for normalization and indeed shows the best ability to collapse all of the data.

Through the normalization using  $\phi_l$ , the particle size and shape factors are eliminated. While the sphericity for the previously published experiments was not recorded, all should be close to unity with the exception of the experiments of Bagnold. The data from all of the experiments is in good agreement when normalized by  $\phi_l$ . If there is a dependence on the size or shape of particles beyond their influence on  $\phi_c$ , these effects are small and secondary.

## 7.2 Non-neutrally buoyant particles

In mixtures composed of particles that are a different density than the fluid, particle segregation occurs. Experiments with non-neutrally buoyant particles were described in chapter 5. In the apparatus used for the present experiments, when the particles are heavier than the fluid, they settle to the bottom of the annulus and require mixing as a result of

cylinder rotation in order to rise up from the lower end cap. Force measurements were taken in the middle 11.22 cm (4.42 in) of the annulus, four gap widths from each end cap. This means that for low volume fractions there may be no particles in the measurement volume, but as the rate of rotation increases, the particles begin to fluidize and the local volume fraction increases. In this configuration, the effective viscosity ratio increases from unity as the volume fraction increases until the flow becomes homogenized and a constant effective viscosity is approached. For high volume fractions with no rotation, when the center portion of the cylinder is covered, the volume fraction is near the random loose-packing volume fraction and the effective viscosity ratio is high. As the flow becomes fluidized, the volume fraction decreases in the center region and the effective viscosity ratio similarly decreases.

How quickly the bed becomes fluidized depends on the Archimedes number, which describes the ratio of gravitational forces to viscous forces. In subsection 5.2.1.2, the local volume fraction at the floating cylinder was measured. When this local volume fraction is plotted against the Reynolds number divided by the Archimedes number, as in Figure 5.7, all of the curves collapse. For  $Re/Ar \gtrsim 10^4$  the volume fraction plateaus near the average volume fraction implying that the mixture is homogeneously mixed. For  $10^3 \lesssim Re/Ar \lesssim 10^4$  there also appears to be a slight plateau for the cases where the fluid and particle densities differ by more than a percent. This plateau is at a lower volume fraction and implies some heterogeneous mixing.

When the effective viscosity is plotted against the local volume fraction in the heterogeneously or homogeneously mixed cases, these experiments match the data obtained for neutrally buoyant experiments. This comparison, shown in Figure 5.19, shows that the fluid-particle and particle-particle interactions within well-mixed non-neutrally buoyant configurations do not differ from their neutrally buoyant counterparts. This seems to imply that the particle inertia does not matter as long as the local volume fraction is used to determine the effective viscosity.

### 7.3 Surface roughness

One of the size parameters that is important in determining the dynamics of fluid-particulate flows is the ratio of the particle diameter to the characteristic length scale of the surface

roughness at the boundaries. In chapter 6, these effects were examined more closely. When the surface is smooth compared to the particle diameter, there is an apparent slip caused by a particle depletion layer near the surface. In this depletion layer, the local viscosity is the viscosity of the fluid, which is undergoing a higher local shear rate. The bulk of the flow outside the depletion layer has a higher viscosity, namely the viscosity of the fluid-particulate mixture. Depending on the thickness of the depletion layer, the slip can significantly alter the measured torque and therefore the measured apparent viscosity.

To examine these effects more closely, the smooth wall data was compared with results from experiments using rough walls to eliminate slip. Using both of these data sets, a thickness for the particle depletion layer could be calculated and was displayed in Figure 6.8. The calculated depletion layer thickness compares favorably with data obtained in a similar fashion by other researchers. The depletion layer thickness could also be inferred from measurements of the particle velocities obtained using non-neutrally buoyant particles (Figure 6.11). These measurements of the depletion layer thickness agree with those obtained using the effective viscosity data. Using the effective viscosity to calculate the depletion layer required the assumption that slip either occurred on only the inner layer or equally on both layers. Comparing these results with the measured slip on the inner layer (from the velocity data) implies that for low volume fractions ( $\phi < 0.5\phi_c$ ), slip only occurs on the inner cylinder wall. For high volume fractions ( $\phi > 0.5\phi_c$ ) slip occurs on both the inner and outer cylinder walls.

## 7.4 Topics for future investigation

In this thesis, experiments concentrated on the influence of various parameters on the effective viscosity for fluid-particulate flows. Experiments with both neutrally buoyant and non-neutrally buoyant particles, with smooth and rough walls, and with varying particle size and shape were conducted. These experiments were able to show that the effective viscosity depended primarily on the local volume fraction and the conditions of the containing walls.

Experiments at higher Stokes numbers should be conducted to determine if a shear rate dependence on the effective stresses exists in the collisional regime. The current configuration of the apparatus limited the experiments conducted to lower Stokes numbers,

outside of an elastic collisional regime. If the apparatus can be modified to allow for the use of higher shear rates or much denser particles while still maintaining a mostly homogeneous distribution of particles within the annulus, the effects of the collisional regime may be determined.

The collisions of particles in a fluid are much more likely to occur in the direction of shear, but oblique collisions are able to impart particle motion orthogonal to the direction of bulk motion. This random motion, known as a granular temperature, is able to impart a force on the containing walls either through direct particle-wall collisions or particle-particle collisions near a wall (Zenit et al. 1997). This force, analogous to a pressure, is not present in the pure fluid flow. Individual collisions were investigated by Zenit et al., but the bulk behavior was not recorded. Recording these pressure forces would be of interest.

The rebound of particles against a solid wall was extensively studied by Joseph and Hunt (2004); Joseph et al. (2001) for both normal and oblique collisions. This work was extended by Ruiz-Angulo and Hunt (2009) to investigate the influence of deformation on the collisional dynamics. Ruiz-Angulo and Hunt found that the rebound was reduced due to the energy loss from deformation. Further investigations into the effects of deformable particles or deformable walls on the effective viscosity or pressure forces would be of interest.

While no effect on particle size was shown in this thesis, the experiments were conducted using only one particle size in each flow. If mixtures are created with many different types of particle sizes, their effects might be greater. This variation in particle size distribution is the first step in investigating the influence of particle cohesiveness on the fluid-particulate flow. Cohesive particles are found in many different natural and industrial flows and would be an interesting addition to the understanding of this field.

Finally, this thesis used optical probes mounted above and below the test section to elucidate the particle velocities (in the direction of the flow) and vertical movement of particles. This limited work was instrumental to the understanding of these flows, but clearly with better equipment much more work can be completed in these areas. One of the limitations of the concentric cylinder apparatus is its stainless steel construction. While durable, it impedes the experimentalists ability to visualize the flow. The center, floating test section can be easily replaced with an equivalent acrylic or polycarbonate part. The clear plastic section can be used for particle visualization to determine the movement of

particles vertically or combined with laser doppler velocimetry to determine two of the velocity components (circumferential and vertical). The top (or bottom) end caps can also be replaced such that the radial component could not be resolved, but this is impractical for the current design.

## Appendix A

# MATLAB source code

### A.1 Peak finding algorithm (fpeak.m and getPeak.m)

The following MATLAB functions take as input the time data ( $x$ ), one data signal ( $y$ ), the peak half-width ( $s$ ), and the range to be considered ( $\text{Range}$ ). The output is a matrix corresponding to the  $x$  and  $y$  values of peaks within  $\text{Range}$ . The function includes documentation, which can be accessed through the `help` command in MATLAB.

```

1 function peak=fpeak(x,y,s,Range)
2 % based on the peak finding algorithm developed by Geng Jun at USTB, China.
3 % Modified by Erin Koos, Version 3: 1/24/08
4 %
5 % INPUTS
6 % x = time data [1/fs:1/fs:T]
7 % y = filtered data vector (one signal only)
8 % s = peak width threshold (in number of data points)
9 % Range = [x1, x2, y1, y2], where peaks are located between
10 %   x1 < x < x2, and have a height y1 < y < y2
11 %
12 % RETURNS
13 % peak = peak data for signal of the form [x, y]
14
15 % compare vector sizes to make sure size(x)=size(y) and transpose if
16 % necessary.
17 [rx,cx]=size(x);
18 [ry,cy]=size(y);
19 if rx==1

```

```

20     x=x';
21     rx=length(x);
22 end
23 if ry==1;
24     y=y';
25     ry=length(y);
26 end
27 if rx~=ry
28     fprintf('%s','Vector lengths must agree');
29     return
30 end
31
32 % Reduce the x and y vectors to those points within Range
33 numP=1;
34 Data=[x,y];
35 Data=Data(find(Data(:,2)≥Range(3) & Data(:,2)≤Range(4)),:);
36 Data=Data(find(Data(:,1)≥Range(1) & Data(:,1)≤Range(2)),:);
37 Data=sortrows(Data);
38 x=Data(:,1);
39 y=Data(:,2);
40
41 % Determine if each point in Data is a peak
42 peak=[];
43 for i=1:length(x)
44     isP=getPeak(x,y,i,s);
45     if sum(isnan(isP))==0
46         peak(numP,:)=isP;
47         numP=numP+1;
48     end
49 end
50
51 % Return the locations and values of each peak
52 if isempty(peak)==0
53     peak=peak(find(peak(:,1)),:);
54     peak=peak(find(peak(:,1)≥Range(1) & peak(:,1)≤Range(2)),:);
55     peak=peak(find(peak(:,2)≥Range(3) & peak(:,2)≤Range(4)),:);
56
57 else
58     peak=[0 0];

```

59 `end`

```

1 function p=getPeak(x,y,i,s)
2 % based on the peak findng algorithm developed by Geng Jun at USTB, China.
3 % Modified by Erin Koos, Version 3: 1/24/08
4 %
5 % INPUTS
6 % x = time data [1/fs:1/fs:T]
7 % y = filtered data vector (one signal only)
8 % i = index of interest
9 % s = peak width threshold (in number of data ponts)
10 %
11 % RETURNS
12 % p = [x(i), y(i)] if i is a peak, p = [nan,nan] otherwise
13
14 if i-s>1
15     top=i-s;
16 else
17     top=1;
18 end
19 if i+s>length(y)
20     bottom=length(y);
21 else
22     bottom=i+s;
23 end
24
25 tP=(sum(y(top:bottom)>=y(i))==1);
26
27 if tP==1
28     p=[x(i), y(i)];
29 else
30     p=[nan,nan];
31 end

```



## A.2 Cross-correlation for the entire signal (`correl_full.m`)

The following MATLAB function takes as input the time data (`x`), the two data signal to be cross-correlated (`yf`), the peak locations for two signals (`peak1` and `peak2`), and the peak half-width (`s`). The output is a vector of the top three signal offsets (`offset`), a matrix (`yy`) of the converted data signals (see Figure 3.7), a matrix of the cross-correlation magnitude (`c`), and the cross-correlation peak data (`cpeak`). The function includes documentation, which can be accessed through the `help` command in MATLAB.

```

1 function [offset,yy,c,cpeak]=correl_full(x,yf,peak1,peak2,s)
2 % cross correlation of the entire signal.
3 %
4 % INPUTS
5 % x = time data [1/fs:1/fs:T]
6 % yf = filtered data where yf(:,1;2) are the signals to be compared
7 % peak1 = peak data for signal 1 of the form [x, y] (from fpeak)
8 % peak2 = peak data for signal 2 of the form [x, y] (from fpeak)
9 % s = peak width threshold (in number of data points) as used to identify peaks
10 %
11 % RETURNS
12 % offset = vector of top three time offsets between signal 1 and 2
13 % yy = modified data vector to be only nonzero near peaks
14 % c = [time, cross correlation sequence] which yields the locations of
15 %     probable offsets
16 % cpeak = [time, value] locations of peaks in c
17
18 global fs %sample frequency
19
20 % Each signal is modified such that only the regions around peaks are
21 % nonzero. Each peak is also normalized such that the maximum height is 1.
22 yy=zeros(size(yf));
23 for i=1:length(peak1(:,1))
24     n=find(x==peak1(i,1));
25     if n-s>=1
26         if (n+s)<=length(x)
27             yy(n-s:n+s,1)=yf(n-s:n+s,1)/peak1(i,2);
28         else

```

```

29         yy(n-s:length(x),1)=yf(n-s:length(x),1)/peak1(i,2);
30     end
31 else
32     if (n+s)≤length(x)
33         yy(1:n+s,1)=yf(1:n+s,1)/peak1(i,2);
34     else
35         yy(1:length(x),1)=yf(1:length(x),1)/peak1(i,2);
36     end
37 end
38 end
39
40 for i=1:length(peak2(:,1))
41     n=find(x==peak2(i,1));
42     if n-s≥1
43         if (n+s)≤length(x)
44             yy(n-s:n+s,2)=yf(n-s:n+s,2)/peak2(i,2);
45         else
46             yy(n-s:length(x),2)=yf(n-s:length(x),2)/peak2(i,2);
47         end
48     else
49         if (n+s)≤length(x)
50             yy(1:n+s,2)=yf(1:n+s,2)/peak2(i,2);
51         else
52             yy(1:length(x),2)=yf(1:length(x),2)/peak2(i,2);
53         end
54     end
55 end
56 clear i
57
58 % use Matlab's xcorr function to complete the cross correlation between
59 % one peak from the y1 signal and all peaks from the y2 signal.
60 % c = [time, cross correlation sequence] which yields the locations of
61 %     probable offsets
62 [b, a] = xcorr(yy(:,1),yy(:,2));
63 c=[a' b];
64 clear a, clear b
65 c(:,1)=c(:,1)/fs;
66 c(:,2)=c(:,2)/max(c(:,2));
67

```

```

68
69 % Limit probable offsets to peaks located between  $-1 \leq \text{offset}(i) \leq 0$ 
70 %   with a peak width greater than  $s$ , and with a cross correlation sequence
71 %   of at least 35% of the maximum.
72 cpeak=fpeak(c(:,1),c(:,2),s,[-1,0,.35,1]);
73 cpeak=sortrows(cpeak,2);
74
75 % Return only the top three peaks (in order of likelihood)
76 offset=zeros(3,1);
77 if length(cpeak(:,1))>3
78     for i=1:3
79         n=find(c(:,2)==cpeak(length(cpeak(:,1))-i+1,2));
80         offset(i)=c(n,1);
81     end
82 else
83     if isequal(cpeak,[0,0])==0
84         for i=1:length(cpeak(:,1))
85             n=find(c(:,2)==cpeak(length(cpeak(:,1))-i+1,2));
86             offset(i)=c(n,1);
87         end
88     end
89 end

```

### A.3 Cross-correlation for individual peaks (correl.m)

The following MATLAB function takes as input the time data ( $x$ ), the two data signal to be cross-correlated ( $yf$ ), the peak locations for two signals ( $\text{peak1}$  and  $\text{peak2}$ ), the peak half-width ( $s$ ), the signal offset found using `correl_full.m` ( $\text{offset}$ ), and the time for the outer cylinder to rotate the distance between the two probes ( $\text{rotime}$ ). The output is a vector signal offsets for each peak ( $\text{offset2}$ ). The function includes documentation, which can be accessed through the `help` command in MATLAB.

```

1 function [offset2,y1,y2]=correl(x,yf,peak1,peak2,s,offset,rotime)
2 % based on the cross correlation of the entire signal (from correl_full),
3 % cross correlate individual peaks.
4 %

```

```

5 % INPUTS
6 % x = time data [1/fs:1/fs:T]
7 % yf = filtered data where yf(:,1;2) are the signals to be compared
8 % peak1 = peak data for signal 1 of the form [x, y] (from fpeak)
9 % peak2 = peak data for signal 2 of the form [x, y] (from fpeak)
10 % s = peak width threshold (in number of data points) as used to identify peaks
11 % offset = time offset between signal 1 and 2 as found by cross
12 %           correlating the entire signal (from correl_full)
13 % rotime = time for the outer cylinder to rotate the distance between the
14 %           two optical probes.
15 %
16 % RETURNS
17 % offset2 = vector of time offsets between signal 1 and 2 for each peak
18 % y1 = peak only data for signal 1
19 % y2 = peak only data for signal 2
20
21
22 global fs %sample frequency
23
24 % look for peaks within the range lowlimit ≤ offset2(i) ≤ highlimit
25 lowlimit=min(rotime,.8*offset);
26 highlimit=1.33*offset;
27
28 % y1 will be used as the base signal and correlated against y2. Each
29 % signal is modified such that only the regions around peaks are nonzero.
30 % Each peak is also normalized such that the maximum height is 1.
31 y2=zeros(length(x),1);
32 y1=zeros(length(x),length(peak1(:,1)));
33
34 for j=1:length(peak2(:,1))
35     n=find(x==peak2(j,1));
36     if n-s≥1
37         if (n+s)≤length(x)
38             y2(n-s:n+s)=yf(n-s:n+s,2)/peak2(j,2);
39         else
40             y2(n-s:length(x))=yf(n-s:length(x),2)/peak2(j,2);
41         end
42     else
43         if (n+s)≤length(x)

```

```

44         y2(1:n+s)=yf(1:n+s,2)/peak2(j,2);
45     else
46         y2(1:length(x))=yf(1:length(x),2)/peak2(j,2);
47     end
48 end
49 end
50
51 for i=1:length(peak1(:,1))
52     m=find(x==peak1(i,1));
53
54     if m-s≥1
55         if (m+s)≤length(x)
56             y1(m-s:m+s,i)=yf(m-s:m+s,1)/peak1(i,2);
57         else
58             y1(m-s:length(x),i)=yf(m-s:length(x),1)/peak1(i,2);
59         end
60     else
61         if (m+s)≤length(x)
62             y1(1:m+s,i)=yf(1:m+s,1)/peak1(i,2);
63         else
64             y1(1:length(x),i)=yf(1:length(x),1)/peak1(i,2);
65         end
66     end
67
68     % use Matlab's xcorr function to complete the cross correlation between
69     % one peak from the y1 signal and all peaks from the y2 signal.
70     % c = [time, cross correlation sequence] which yields the locations of
71     %     probable offsets
72     [b, a] = xcorr(y1(:,i),y2);
73     c=[a' b];
74     clear a, clear b
75     c(:,1)=c(:,1)/fs;
76     c(:,2)=c(:,2)/max(c(:,2));
77
78     % Limit probable offsets to peaks located between
79     %     lowlimit ≤ offset2(i) ≤ highlimit,
80     %     with a peak width greater than s, and with a cross correlation
81     %     sequence of at least 70% of the maximum.
82     cpeak=[];

```

```
83     cpeak=fpeak(c(:,1),c(:,2),s,[highlimit,lowlimit,.7,1]);
84     cpeak=sortrows(cpeak,2);
85     if isempty(cpeak)==0
86         if cpeak*cpeak'≠0
87             m=find(c(:,2)==cpeak(length(cpeak(:,1)),2));
88             offset2(i)=c(m,1);
89         else
90             offset2(i)=0;
91         end
92     else
93         offset2(i)=0;
94     end
95
96 end
```



## Appendix B

# Drawings

This section includes the schematics for the concentric cylinder Couette device. This device was originally designed by Jim Cory. Some parts were later modified for the experiments discussed in this thesis. The following tables summarize each part and should be used as a guide.

Table B.1. Drawings.

Num.	Rev.	Drawing Title	Date Created	Date Modified
01001	1	<b>Floating Drum:</b> Thin walled floating drum. The shear stress applied to this surface by the fluid is measured.	11/22/00	01/20/01
01002	–	<b>Shaft:</b> The floating drum (01001) is suspended using this shaft.	10/28/05	
01003	–	<b>Shaft collars:</b> These collars attach to the shaft (01002) and support the sensor mounts (01006).	10/20/05	
01004	–	<b>Sensor Mounting Bracket:</b> These brackets are furnace brazed to the floating drum (01001).	10/24/00	
01005	–	<b>Target Mounting Bracket:</b> These brackets attach to the lower cap plate (01020) and support the target mount (01007).	11/04/05	
01006	–	<b>Sensor Mount:</b> This drawing shows the mount for the non-contact displacement sensor.	10/20/04	
01007	–	<b>Target Mount:</b> These mounts support the non-contact displacement sensor targets (01008).	11/08/05	
01008	1	<b>Sensor Target:</b> Slightly magnetic target for the non-contact displacement sensor	04/02/02	11/14/04

Continued on next page



Table B.1 – continued from previous page

Num.	Rev.	Drawing Title	Date Created	Date Modified
01009	3	<b>Assembly of the Inner Floating Drum:</b> This drawing shows the assembly and rendered view of the floating drum (01001) mounted on the shaft (01002) using the shaft collars (01003), sensor mounting brackets (01004), and the sensor mounts (01006). The target mounts (01007), which are supported by the lower cap plate (01020) and the target mounting brackets (01005) are also shown.	04/02/02	11/10/05
01010	1	<b>Upper Drum Shoulder:</b> The upper drum shoulder supports upper inner drum wall (01011). The bolted flange is sealed with a flat treated paper gasket against the upper cap plate (01013).	10/25/00	05/08/01
01011	–	<b>Upper Inner Drum Wall:</b> Similar to the lower inner drum wall (01018) except for a bored hole to allow the mounting of the filling port boss (01015).	05/28/02	
01012	–	<b>Upper Hub:</b> This upper hub is adhesively bonded to the upper inner drum wall (01011). It supports the inner diameter of the bearing and seal.	09/18/01	
01013	–	<b>Upper Cap Plate:</b> This plate attaches to the upper drum shoulder (01014) and forms a barrier to seal fluids into the inner floating drum (01009).	10/26/05	
01014	1	<b>Pressure Sensor Boss:</b> The pressure sensor bosses are adhesively bonded to the inner drum walls (01018, 01011).	04/08/01	09/15/01
01015	–	<b>Filling Port Boss:</b> This boss is adhesively bonded into the upper inner drum wall (01012) and allows the annulus to be filled with the maximum solids fraction. During use, it is sealed with an SAE standard hydraulic plug.	05/28/02	
01016	3	<b>Assembly of the Upper Inner Drum:</b> This drawing shows the brazed assembly of the upper inner drum (01010, 01011, 01012, 01013, 01014, and 01015).	04/03/01	10/20/05
01017	1	<b>Lower Drum Shoulder:</b> Similar to the upper drum shoulder (01014) except for the inclusion of a tapped NPT hole to allow the installation of an extraction port for the fluid circulation system and three holes for the non-contact displacement sensor wires.	10/25/00	05/08/01
01018	–	<b>Lower Inner Drum Wall:</b> This inner drum wall mounts on the lower side of the inner floating drum (01009). It contains a mounting point for a dynamic pressure sensor and is adhesively bonded to the lower shoulder (01017) and to the lower hub (01019).	04/03/01	
01019	1	<b>Lower Hub:</b> This lower hub is similar to the upper hub (01012), but includes the addition of mounting holes for fluid connectors around the base. These holes will be used to rotate fluid in the annulus during the high gravity portions of the flight, minimizing the settling of the bed. This hub also has mounting holes to secure the inner drum assembly to the frame.	08/10/01	07/31/03
01020	–	<b>Lower Cap Plate:</b> This part is similar to the upper cap plate (01013), but it contains a hole for the shaft (01004) to pass through the plate and attaches to the seal seat (01021).	10/26/05	

Continued on next page

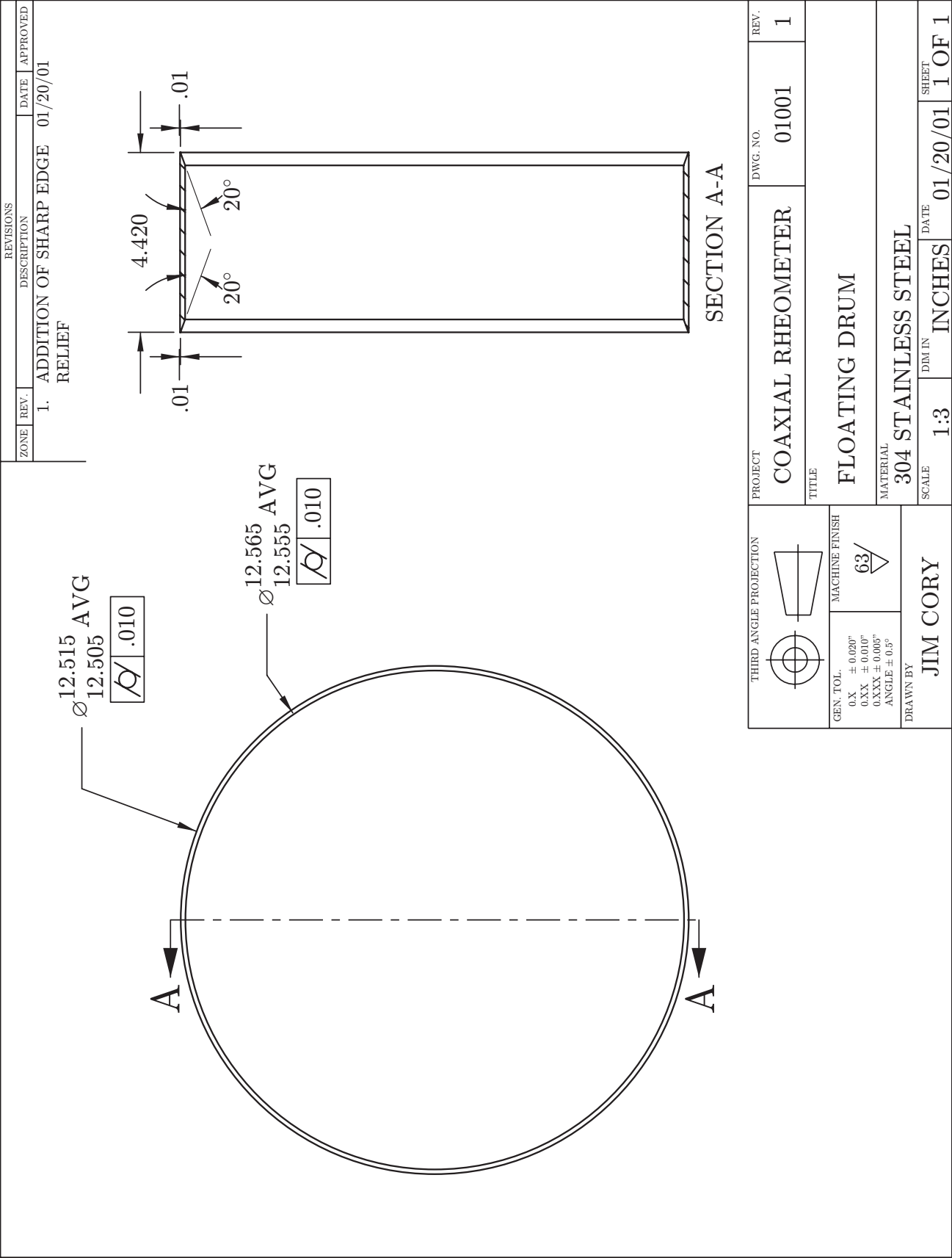
Table B.1 – continued from previous page

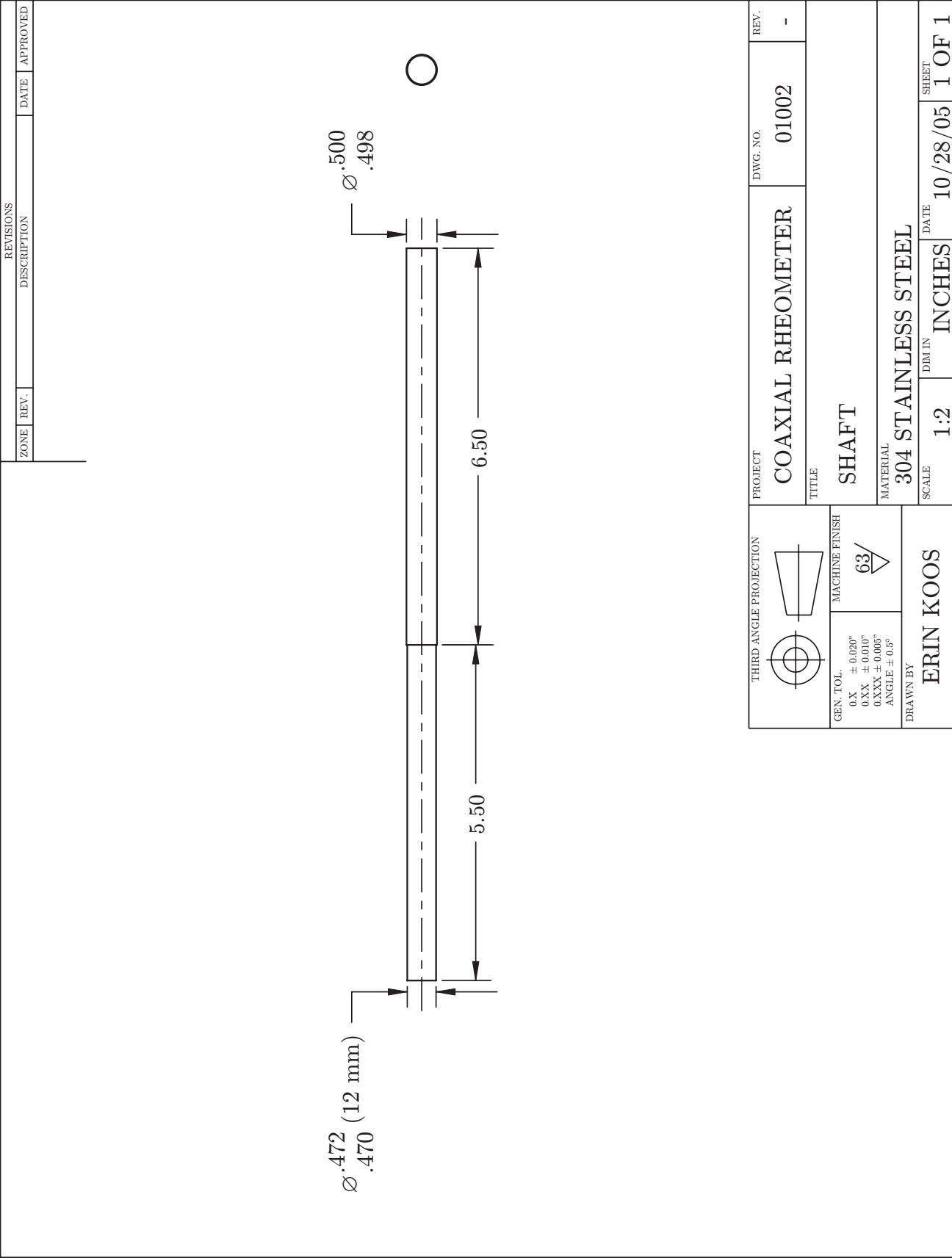
Num.	Rev.	Drawing Title	Date Created	Date Modified
01021	–	<b>Seal Seat:</b> The shaft is sealed at this point to keep any fluid contained in the inner floating drum (01009).	10/20/05	
01022	3	<b>Assembly of the Lower Inner Drum:</b> This drawing shows the brazed assembly of the lower inner drum end (01017, 01018, 01019, 01010, and 01021).	05/29/02	10/10/05
01023	–	<b>Upper Seal Cover:</b> This component clamps to the upper lip seal and provides a knife edge low clearance gap around the outer wall to prevent particles from contacting the sealing lip.	09/18/01	
01024	–	<b>Lower Seal Cover:</b> This part is similar to the upper seal cover (01023) and clamps to the lower lip seal, but it contains small diameter jets to direct the circulating fluid.	08/13/01	
01025	3	<b>Inner Drum Complete Assembly:</b> This drawing shows the full assembly of the inner drum (01009, 01022, 01016, 01023, 01024).	10/25/00	10/27/05
01026	1	<b>Rotating Drum Upper Flange:</b> This component is similar to the lower flange (01028). It does not include the drive belt grooves, but does include a series of holes around the circumference to allow magnetic dowels to be pressed into the drum. These pegs will be used in conjunction with a magnetic proximity sensor to measure the rotating speed of the drum.	04/03/01	05/09/02
01027	–	<b>Rotating Drum:</b> This drawing shows the thin walled section of the rotating outer drum.	04/03/01	
01028	1	<b>Rotating Drum Lower Flange:</b> This component is adhesively bonded to the outer drum center (01027) and supports the OD of the bearing and the sealing lip of the seal. Two B-section v-belt grooves are cut into the flange that allows the outer drum to be driven.	04/03/01	02/04/02
01029	1	<b>Rotating Drum Assembly:</b> Brazed assembly of the outer drum (01026, 01027, 01028). A bleed hole must be machined into the assembly after brazing to allow air in the annulus to bleed out during filling.	04/03/01	05/10/02
01030	2	<b>Complete Drum Assembly:</b> Cross section and rendered view of the complete drum assembly. It shows the major mechanical parts, the pressure sensor mounting locations, and the fluid connector locations at the base of the annulus.	04/03/01	11/10/05
01031	–	<b>Base Plate:</b> The base plate is securely bolted to the top of the extruded aluminum frame. The rheometer drum assembly is then bolted into this plate.	08/01/02	
01032	–	<b>Top Plate:</b> This drawing shows the top plate which is bolted to the top of the extruded aluminum frame. The located plate (01033) bolts to this plate and in turn supports to the top of the rheometer drum assembly	08/01/02	
01033	–	<b>Locating Plate:</b> The locating plate supports the top of the rheometer drum assembly by locating in the inside diameter of the upper hub (01012). This plate is then bolted to the top plate (01032).	08/01/02	

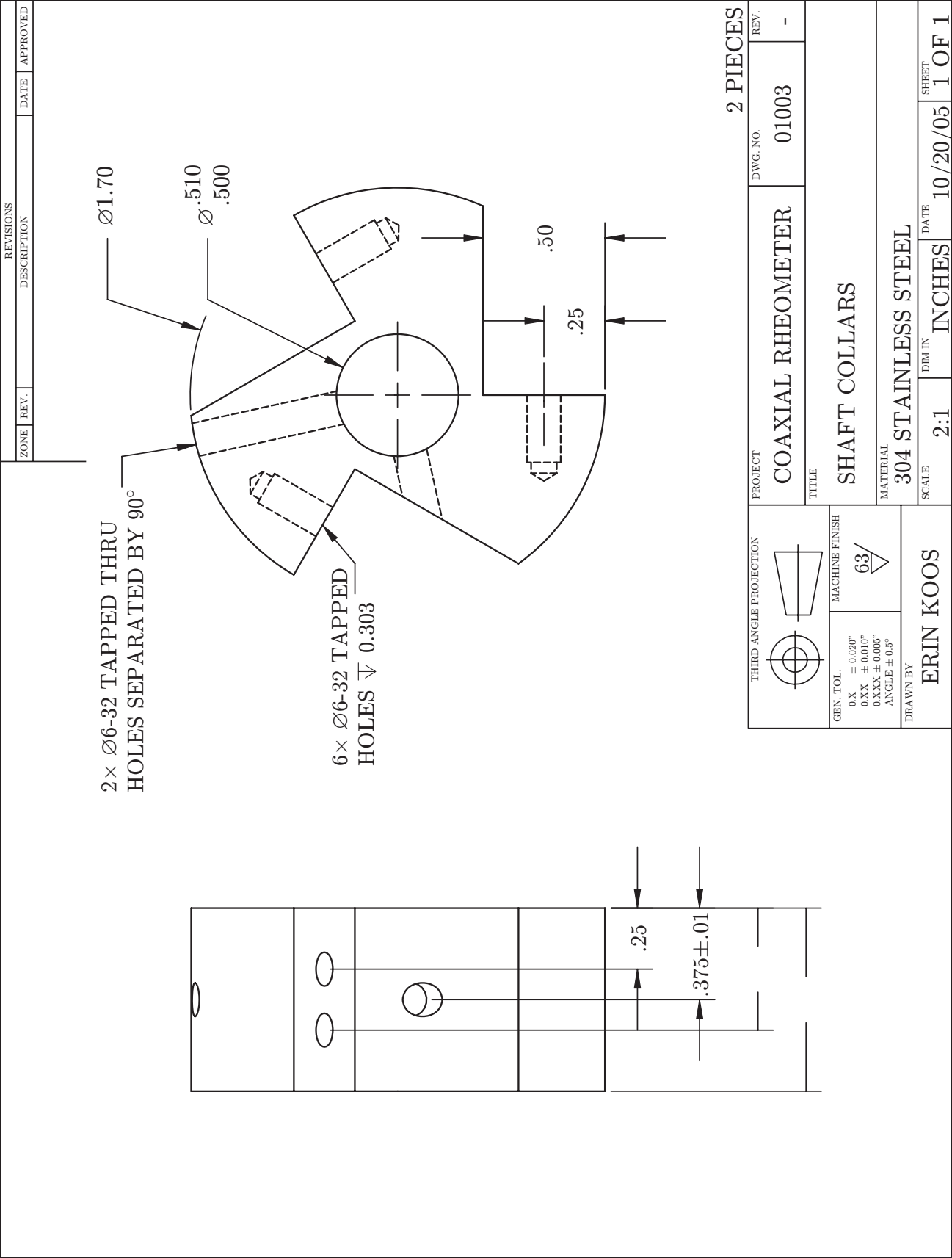
Continued on next page

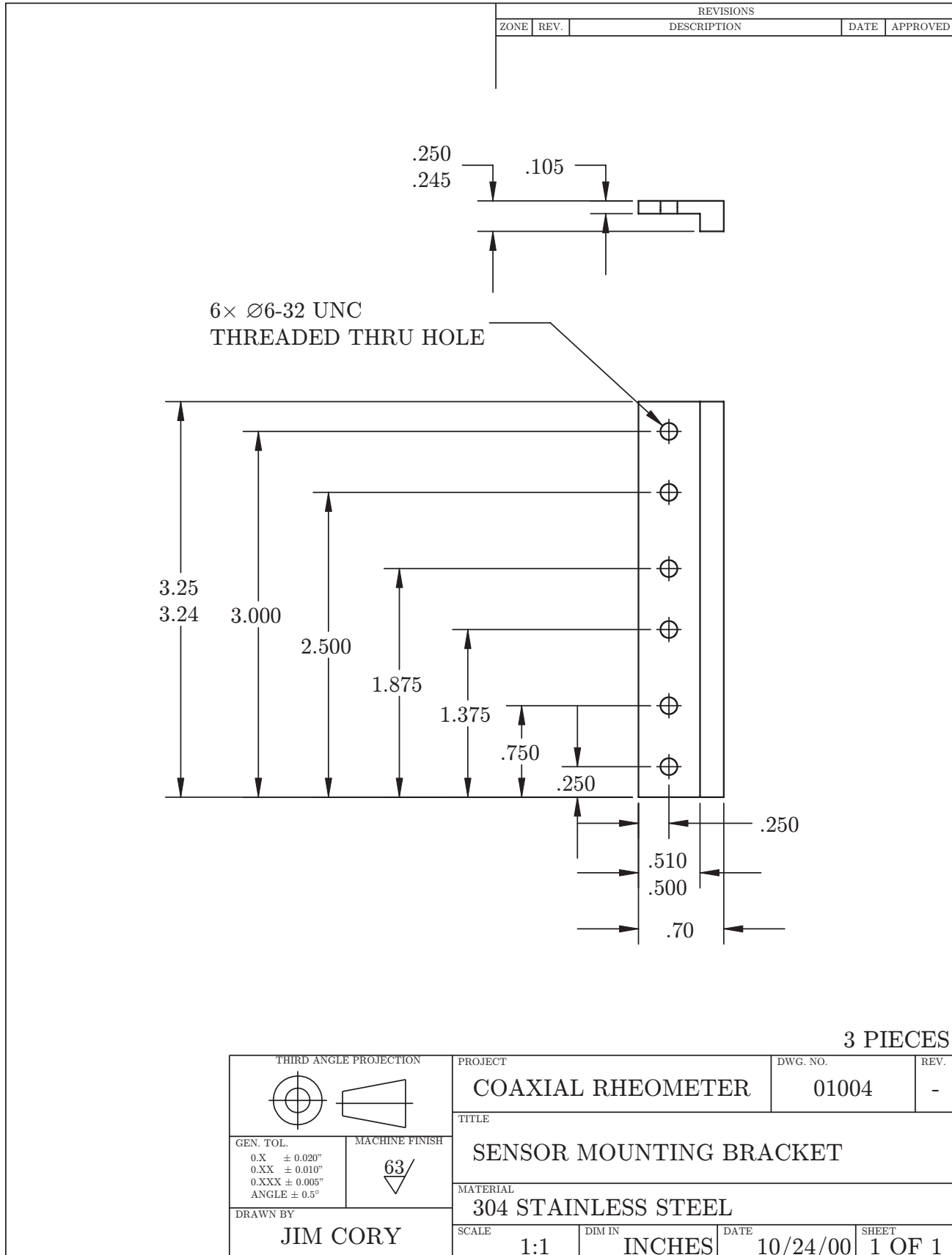
Table B.1 – continued from previous page

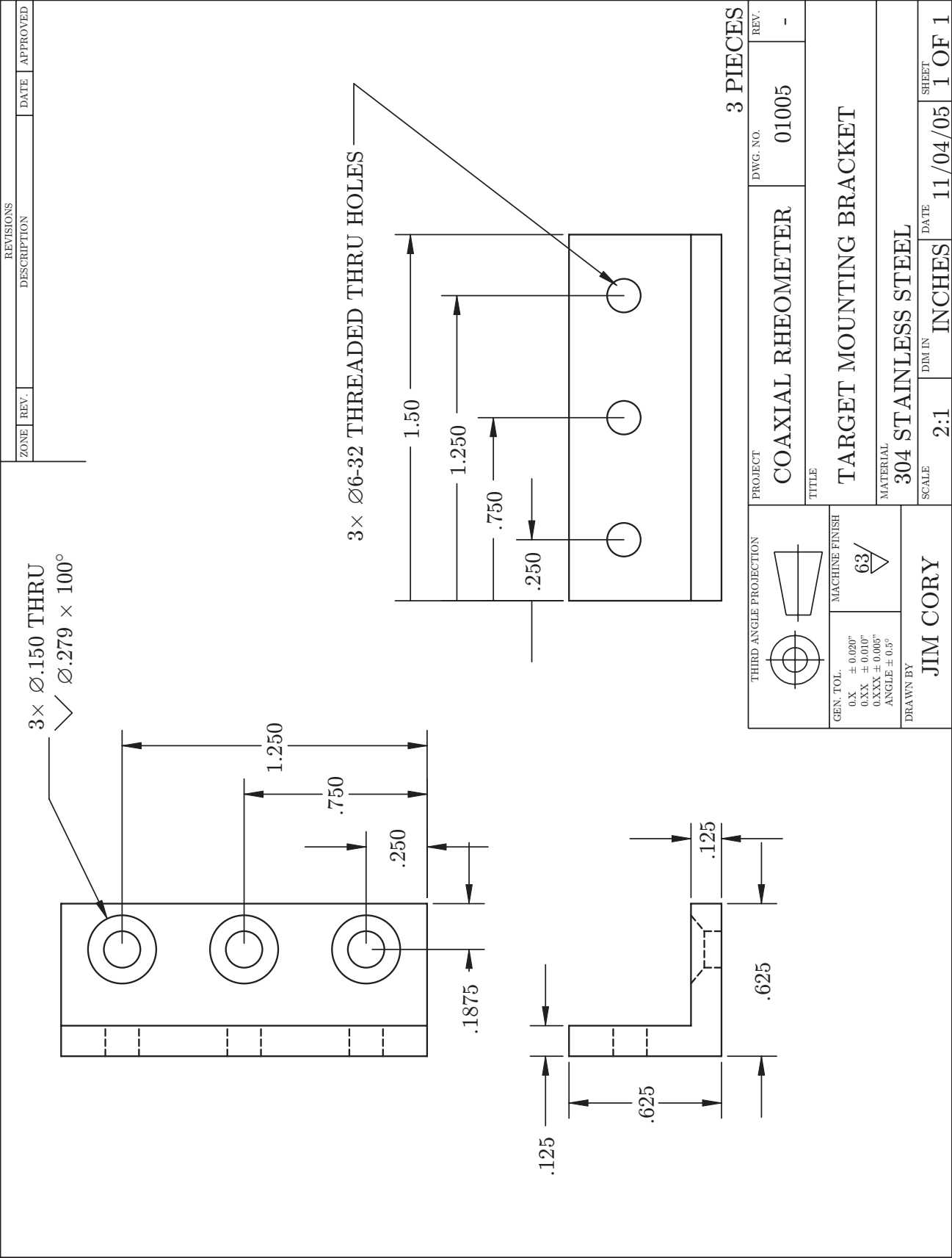
Num.	Rev.	Drawing Title	Date Created	Date Modified
01034	–	<b>Motor Plate:</b> This plate supports the motor and is bolted to the extruded aluminum frame in a way so that it can be adjusted towards and away from the rheometer drum assembly. A screw thread is machined into the edge of the plate to allow for the adjustment of this separation in conjunction with the tensioner block (01035). The motor mounts to this plate via its face.	08/01/02	
01035	–	<b>Tensioner Block:</b> The tensioner block is mounted securely to the end of the extruded aluminum frame. It acts as an anchor against which the motor plate (01034) can be adjusted towards or away from the rheometer drum assembly. This allows the drive belt to be tensioned.	08/01/02	
01036	–	<b>Bearing Locating Plate:</b> This plate attaches to the base plate (01031) and supports the bearing and shaft system.	11/10/05	
01037	–	<b>Bearing Ring:</b> The bearings are press fitted into these rings and the rings are bolted to the bearing locating plate (01036)	11/10/05	
01038	3	<b>Rendered Assembly Including Frame:</b> Rendered impression of the drum assembly mounted in the extruded aluminum frame.	10/26/02	11/15/05
01039	–	<b>Hydraulic Schematic:</b> Schematic representation of the fluid circulation system for the equipment.	02/28/04	





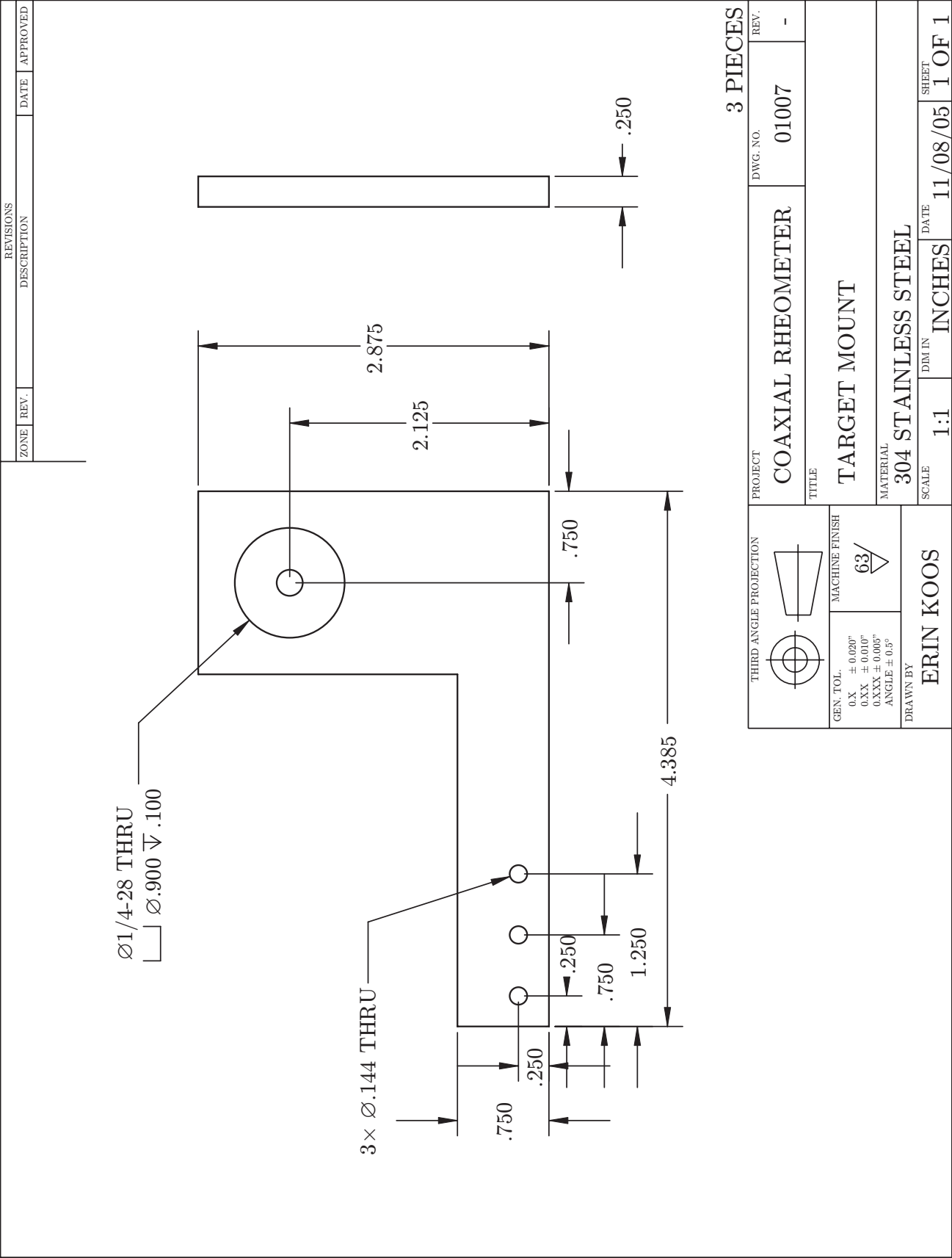


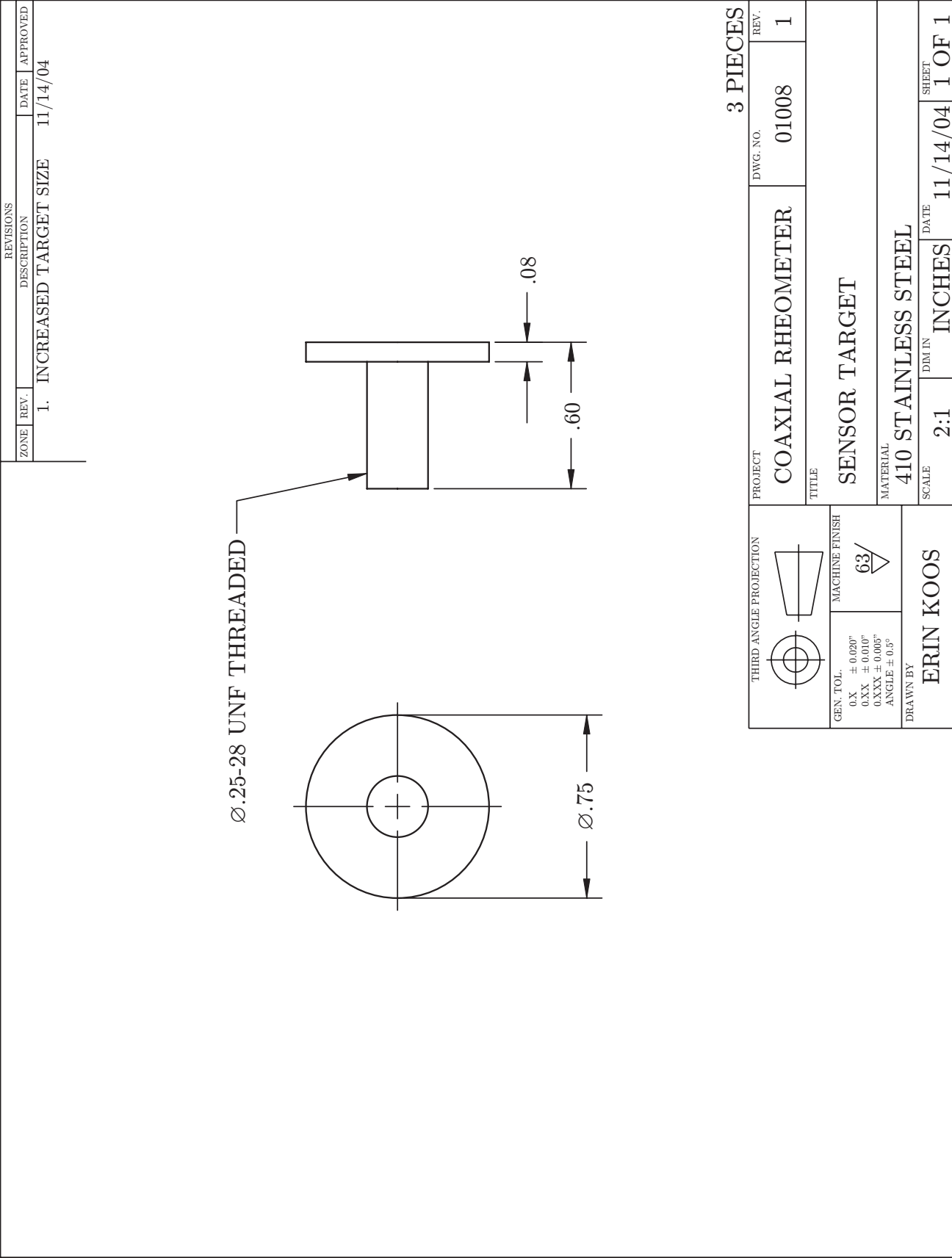








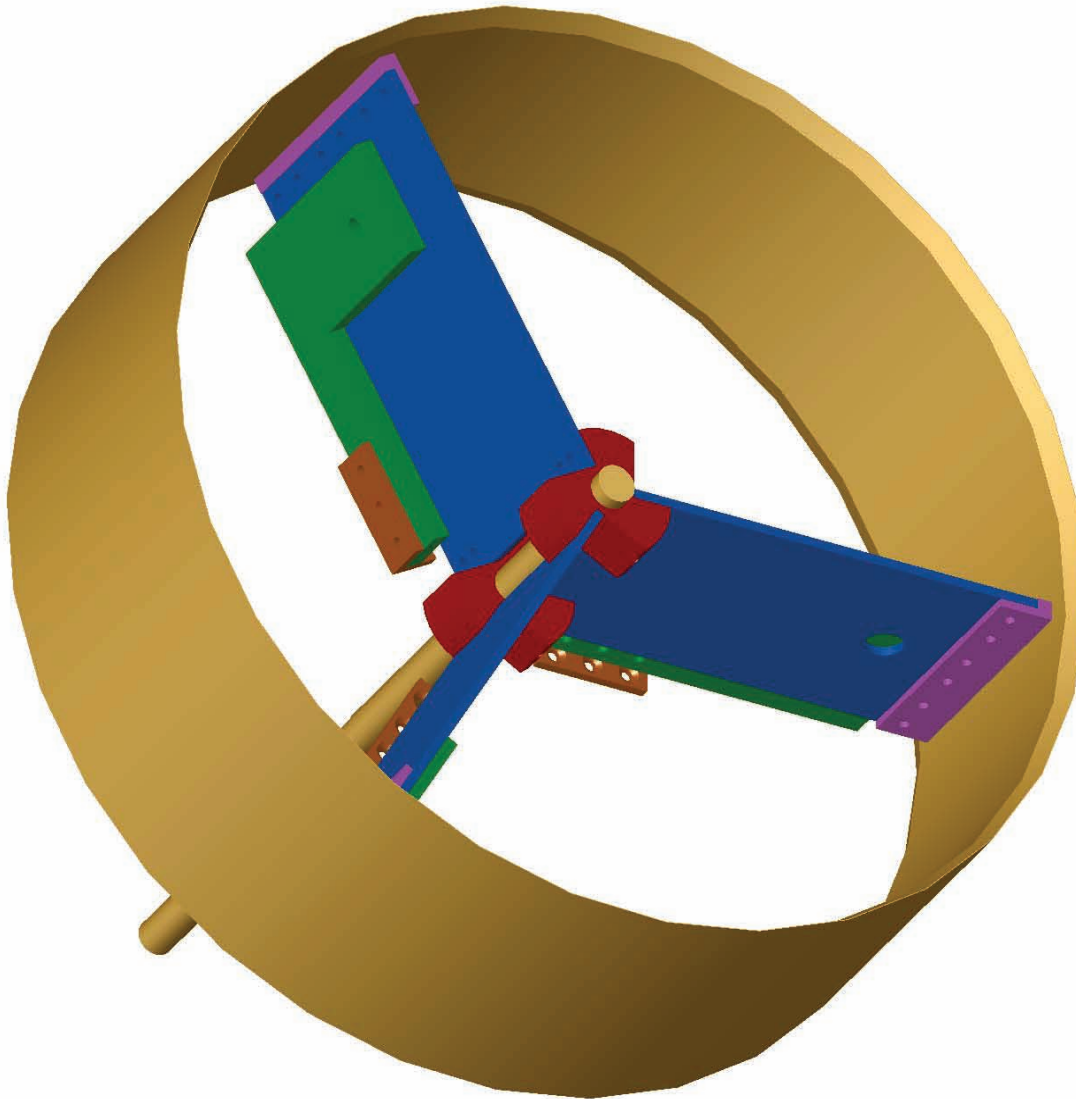




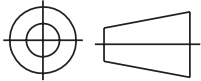

3 PIECES

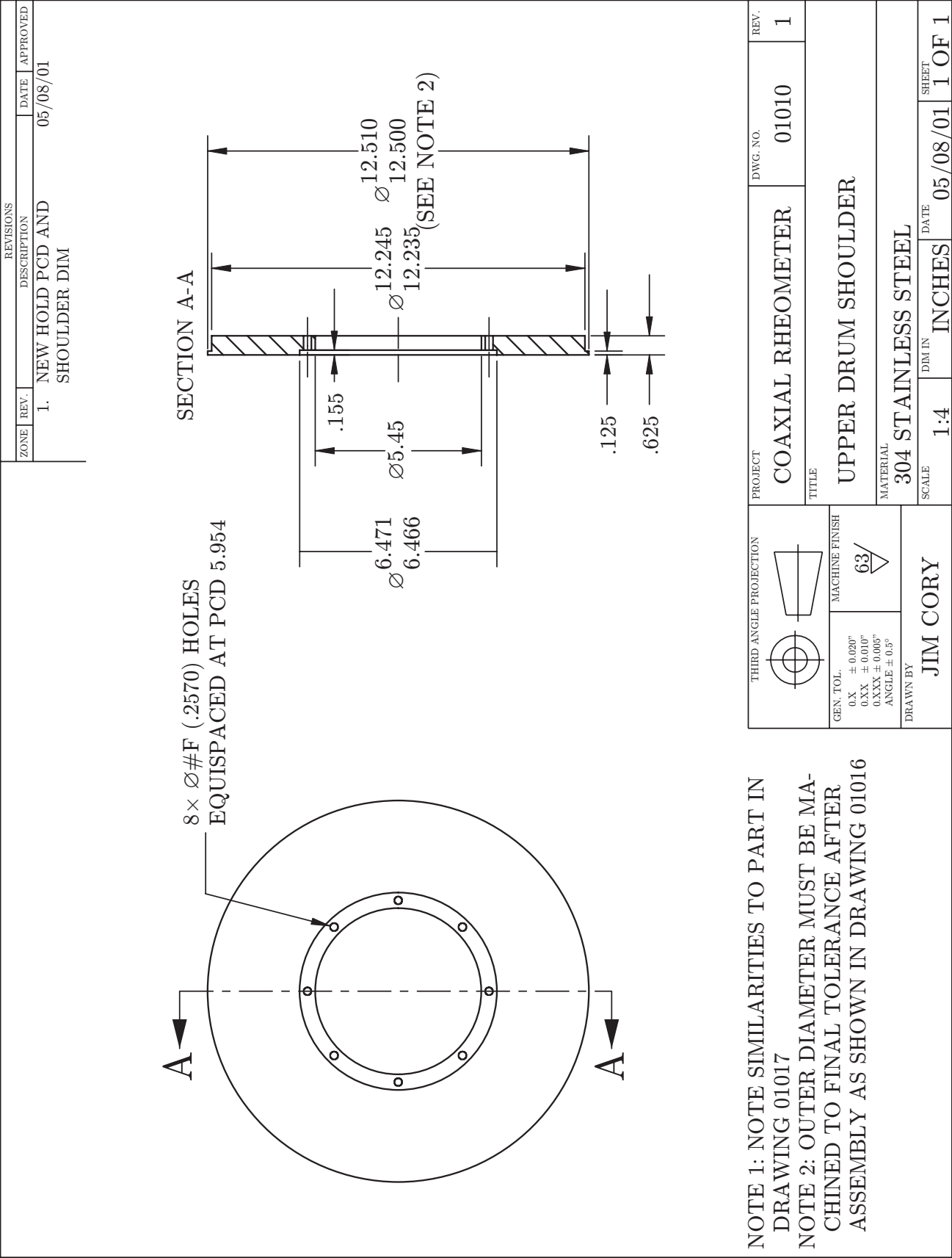


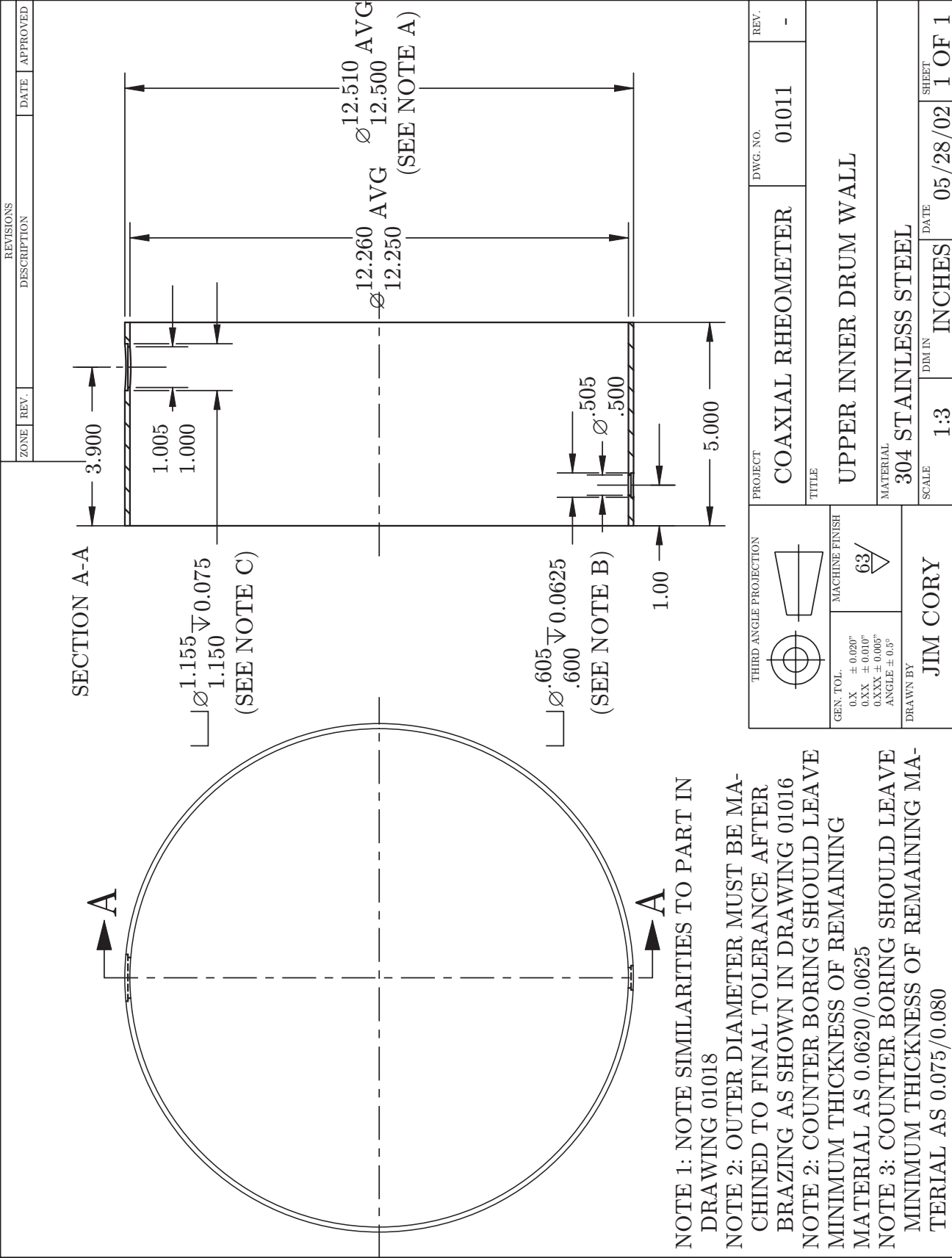
REVISIONS				
ZONE	REV.	DESCRIPTION	DATE	APPROVED
	1.	REVISION TO PART 01001	01/20/01	
	2.	REVISION TO PART 01008	11/14/04	
	3.	ADDITION OF PARTS 01002, 01003, 01006, AND 01007	11/10/05	

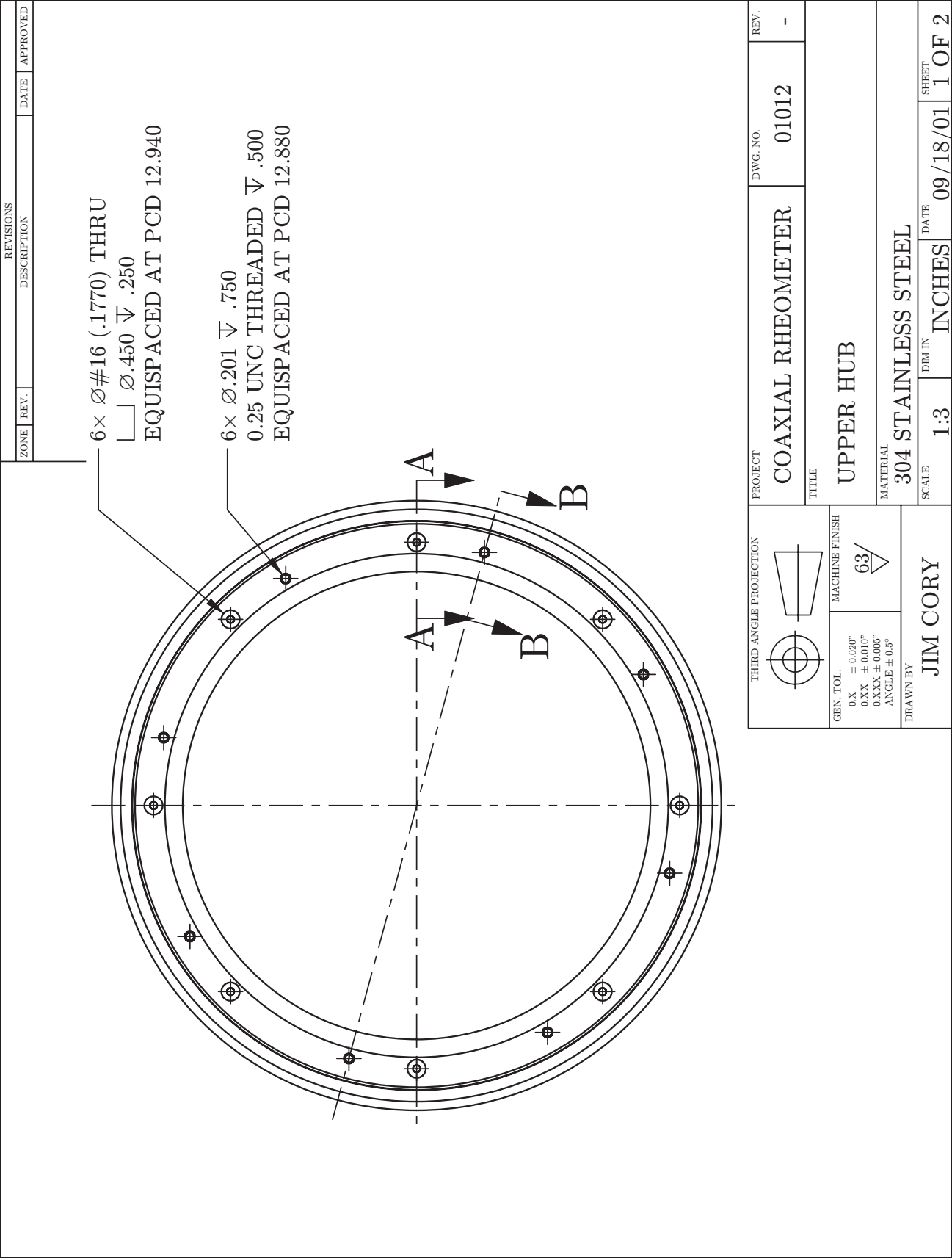


NOTE: THIS IS PURELY AN IMPRESSION OF THE ASSEMBLED  
DEVICE. DO NOT SCALE OR USE AS AN ASSEMBLY GUIDE

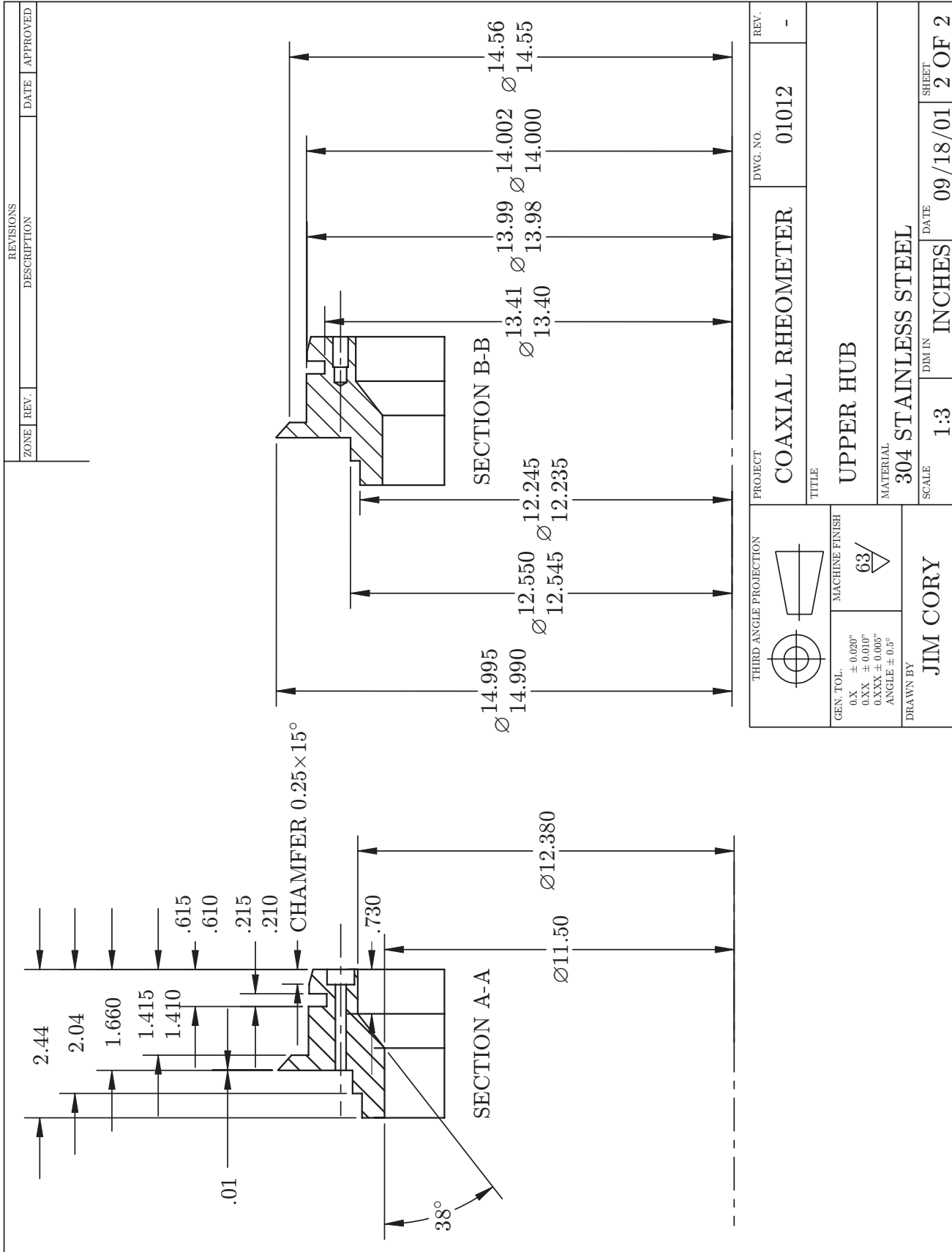
THIRD ANGLE PROJECTION		PROJECT	DWG. NO.	REV.
		COAXIAL RHEOMETER	01009	3
GEN. TOL. 0.X $\pm 0.020''$ 0.XX $\pm 0.010''$ 0.XXX $\pm 0.005''$ ANGLE $\pm 0.5^\circ$		TITLE ASSEMBLY OF THE INNER FLOATING DRUM		
MACHINE FINISH 		MATERIAL VARIOUS		
DRAWN BY ERIN KOOS		SCALE 1:3	DIM IN INCHES	DATE 11/10/05
				SHEET 2 OF 2

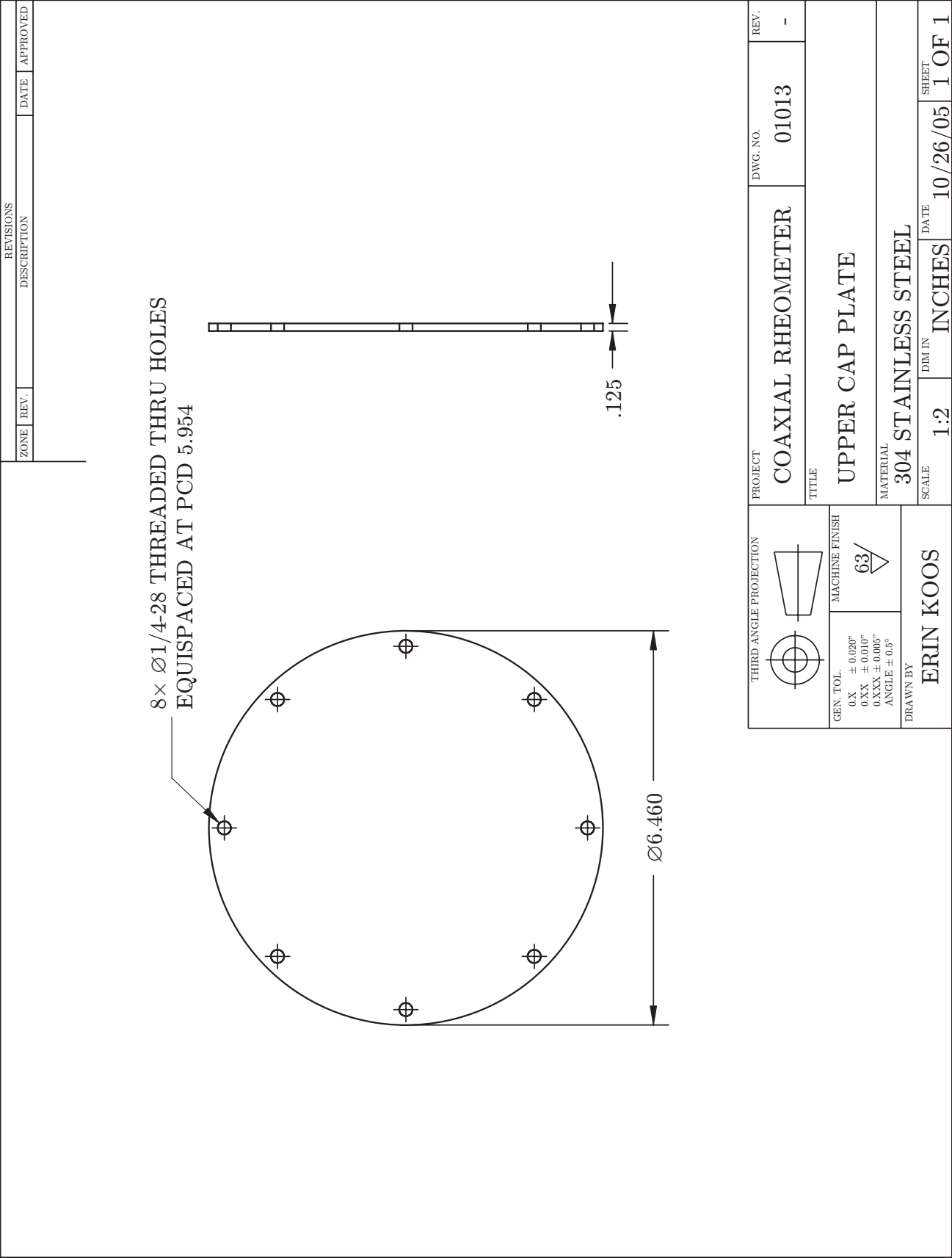


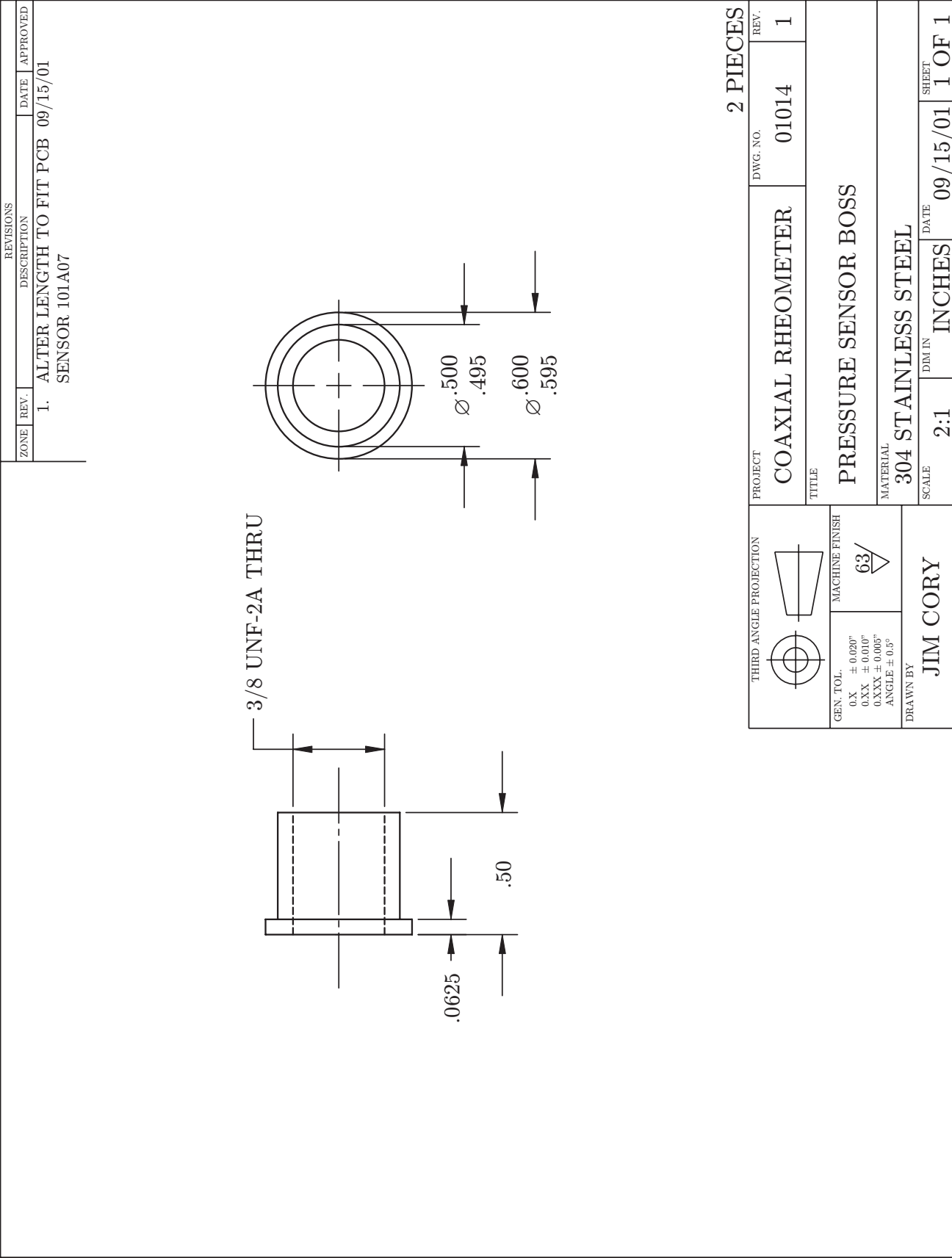


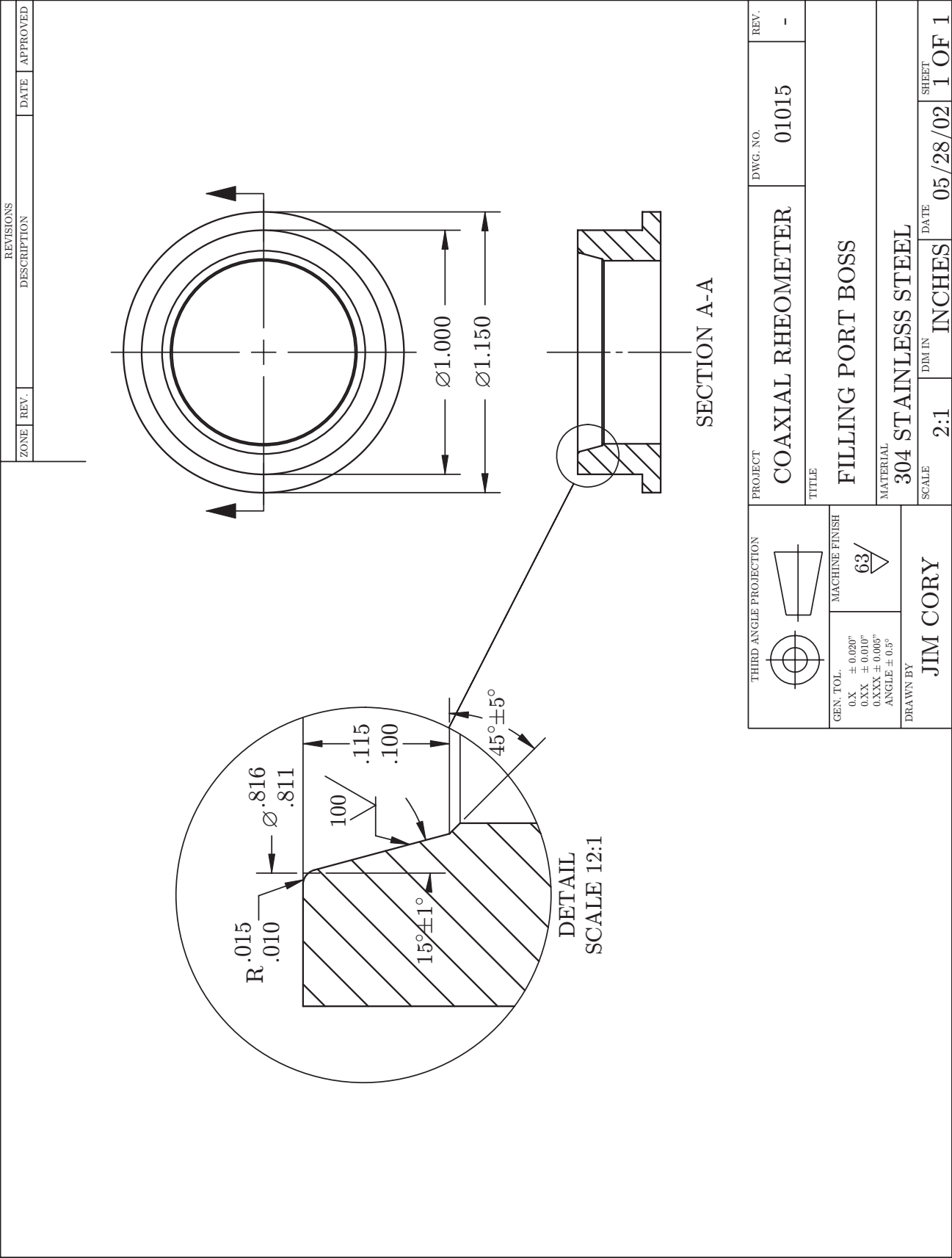


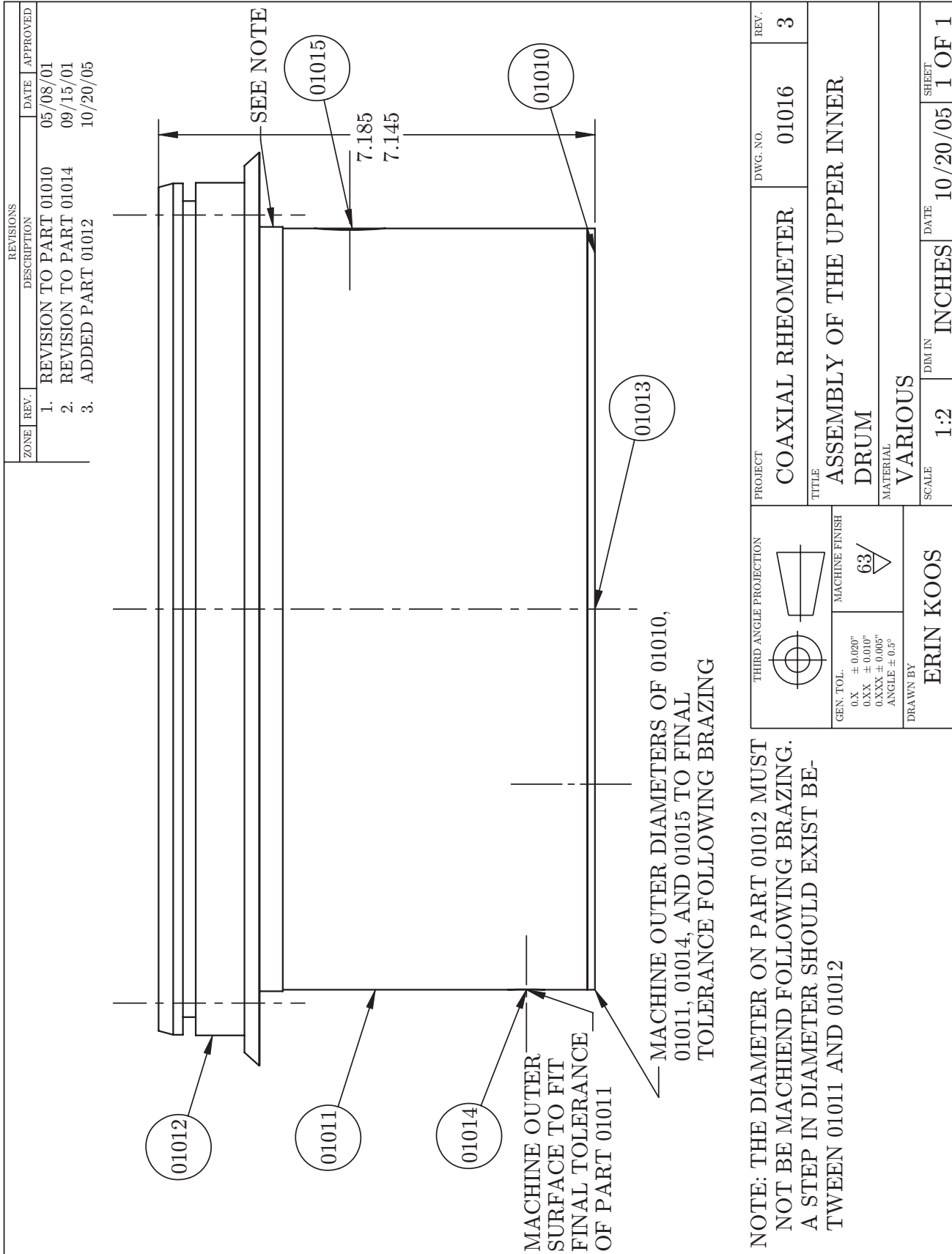




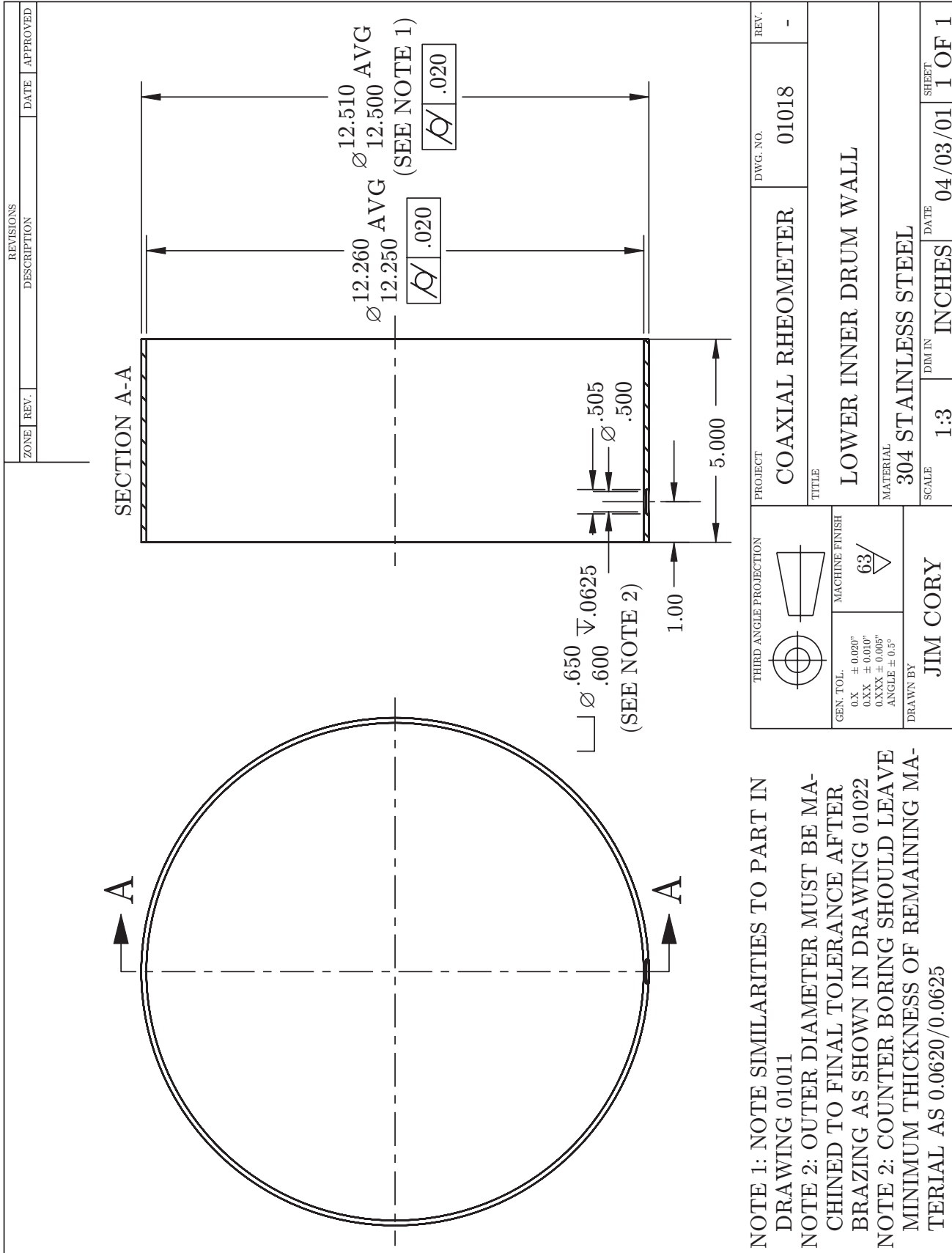


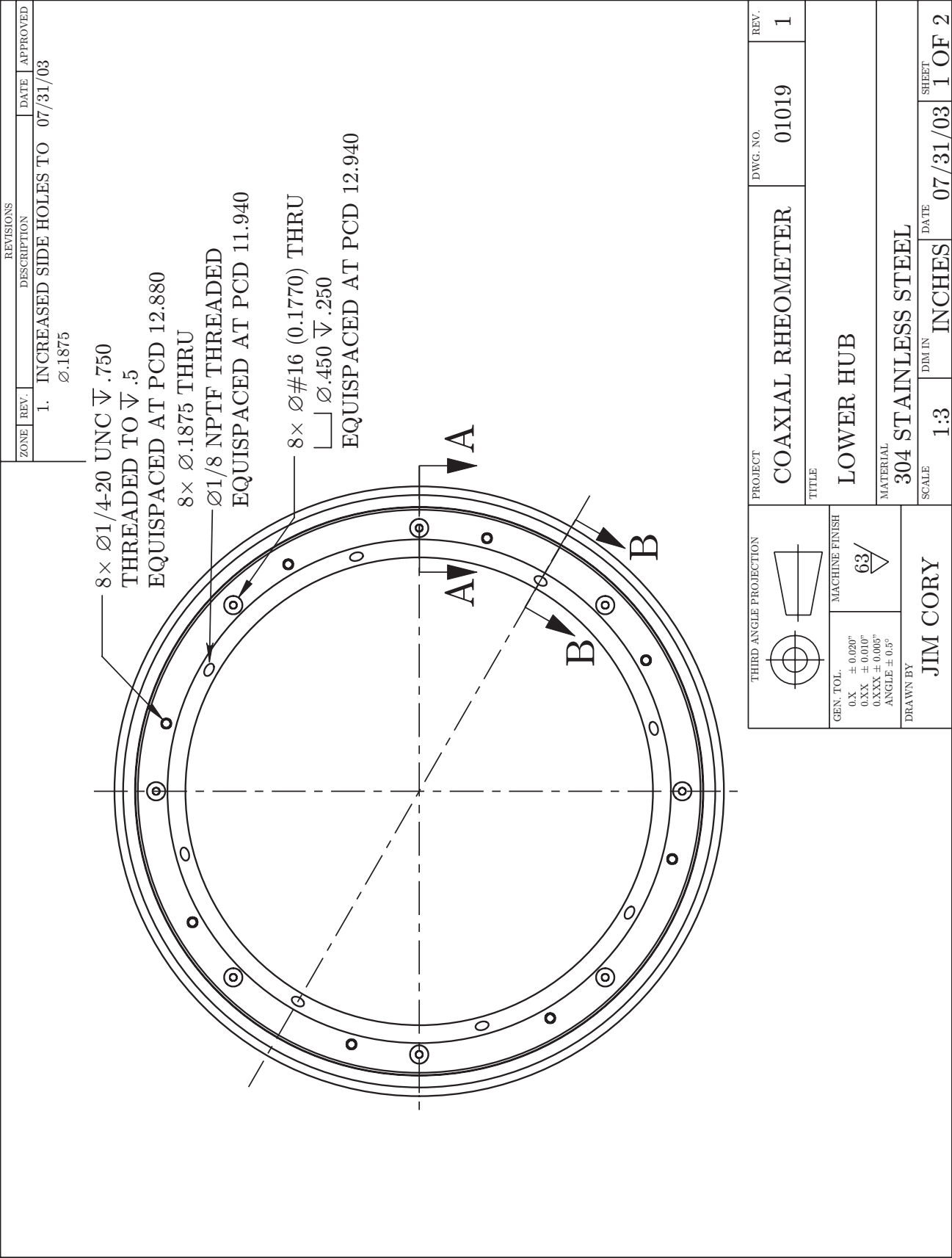




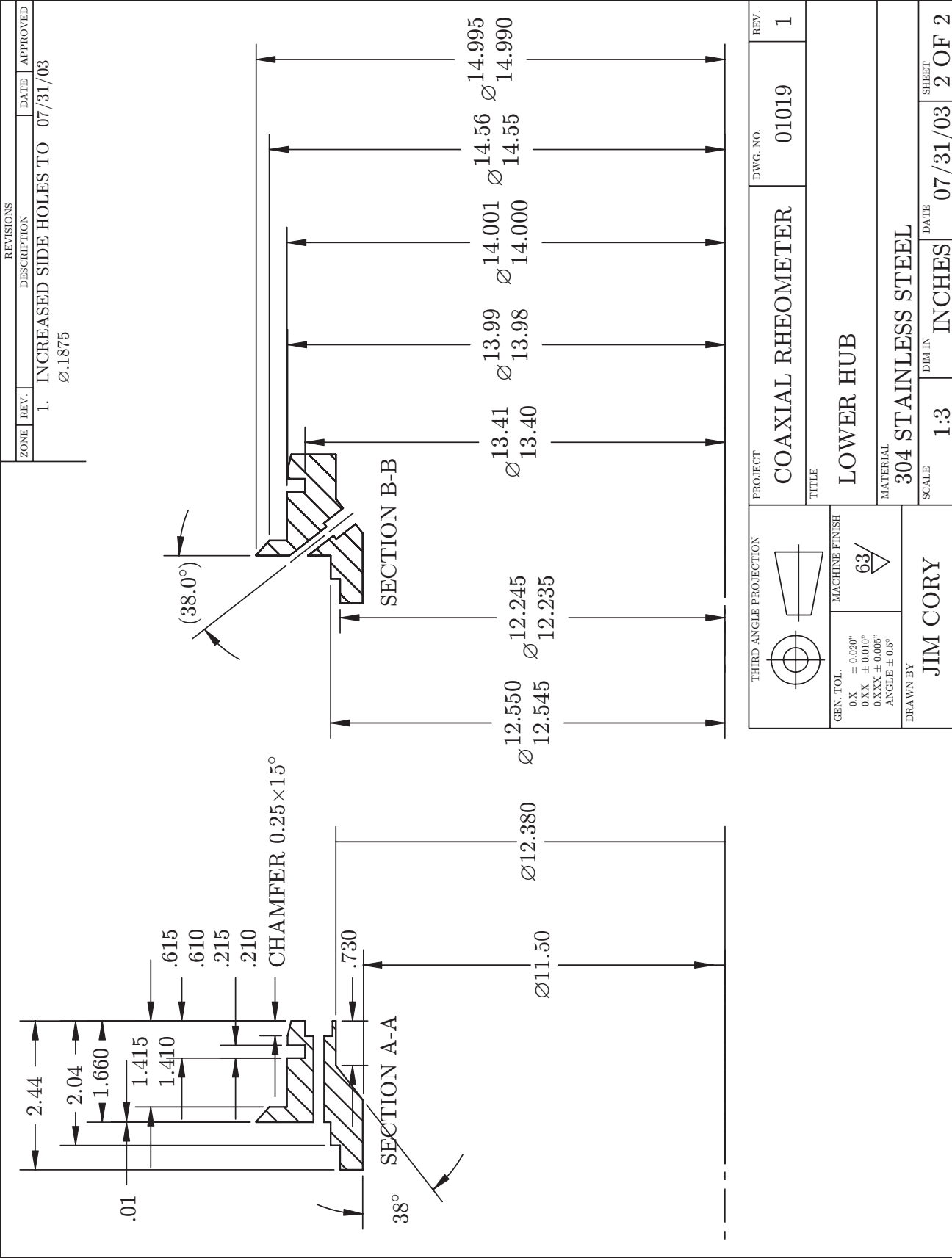


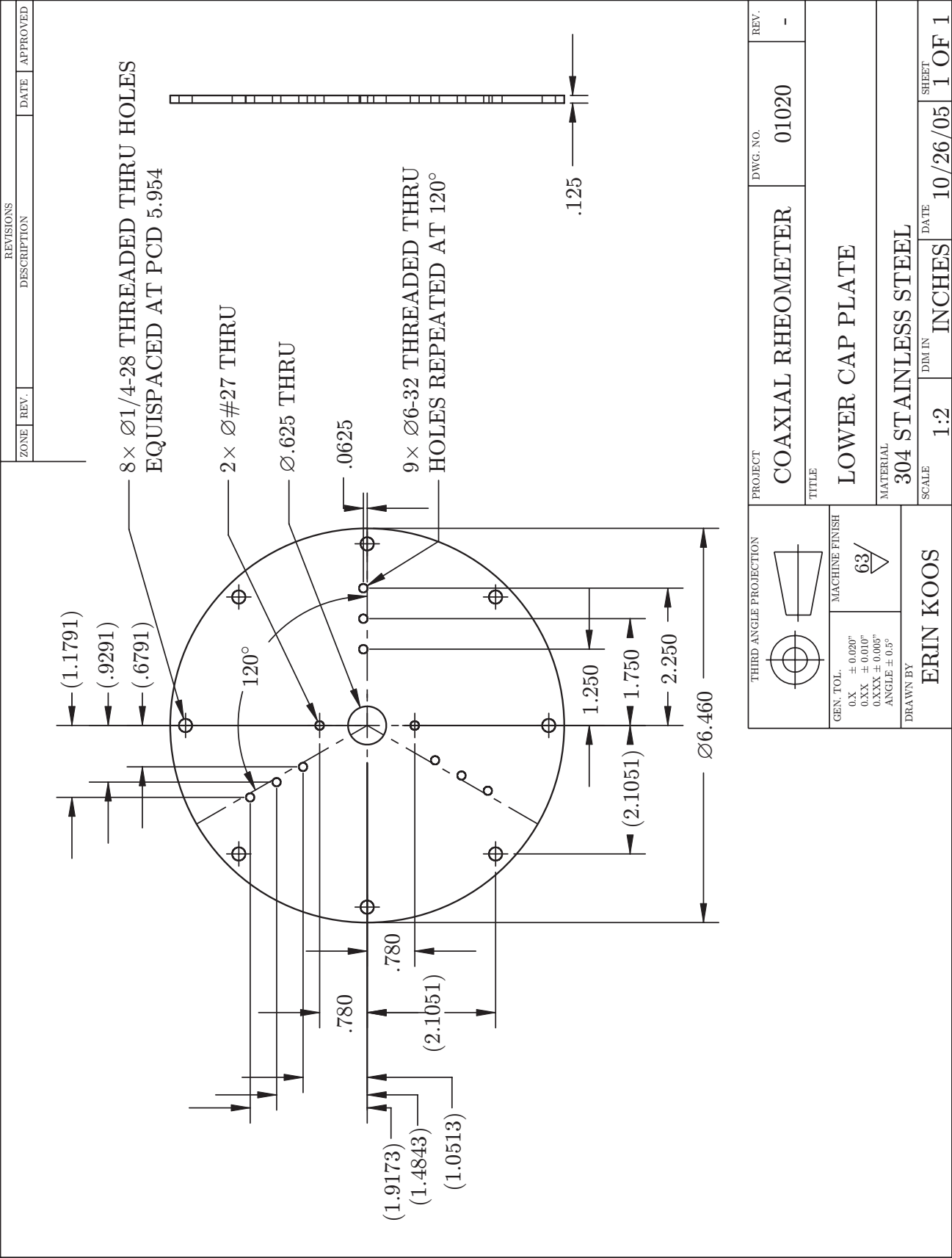


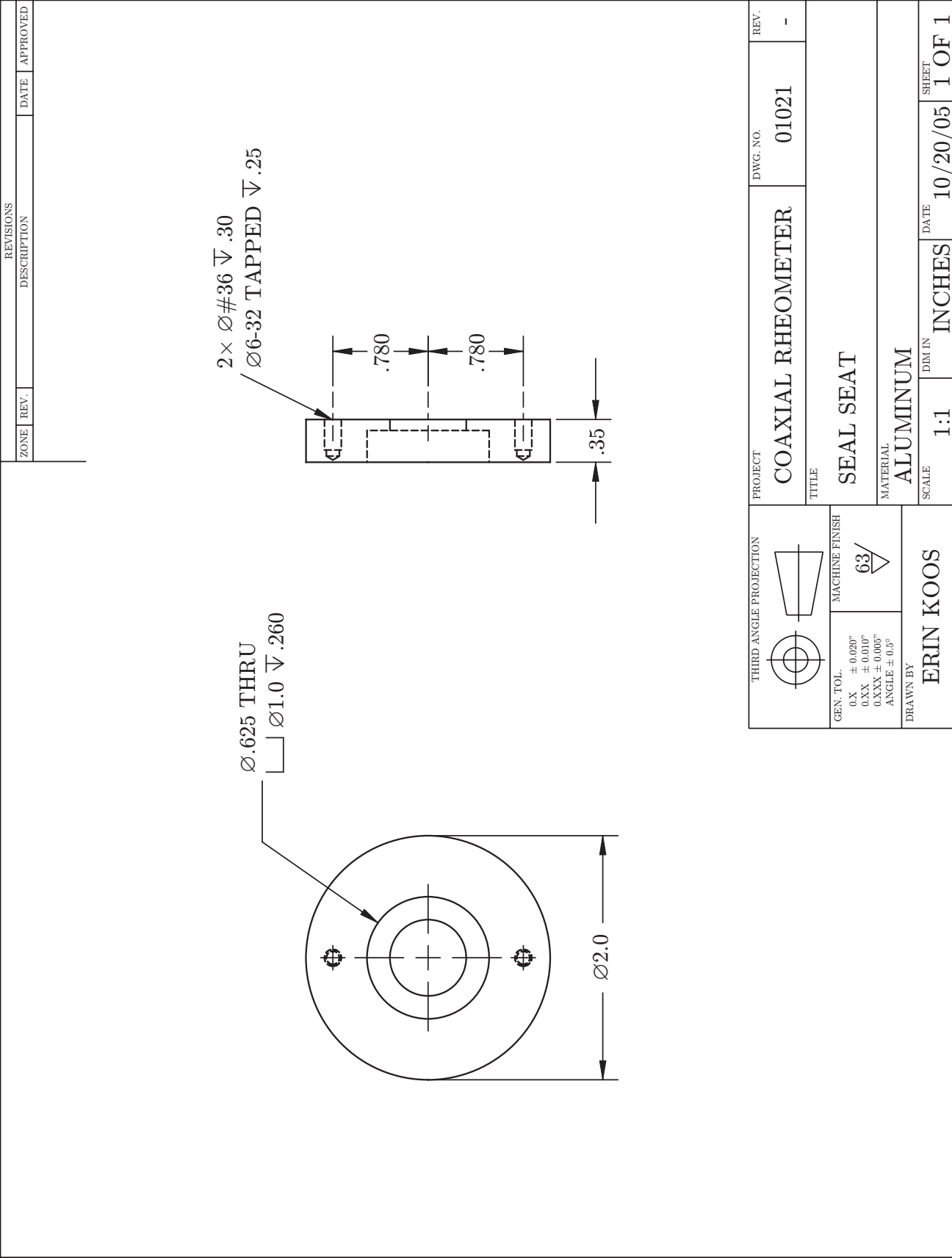


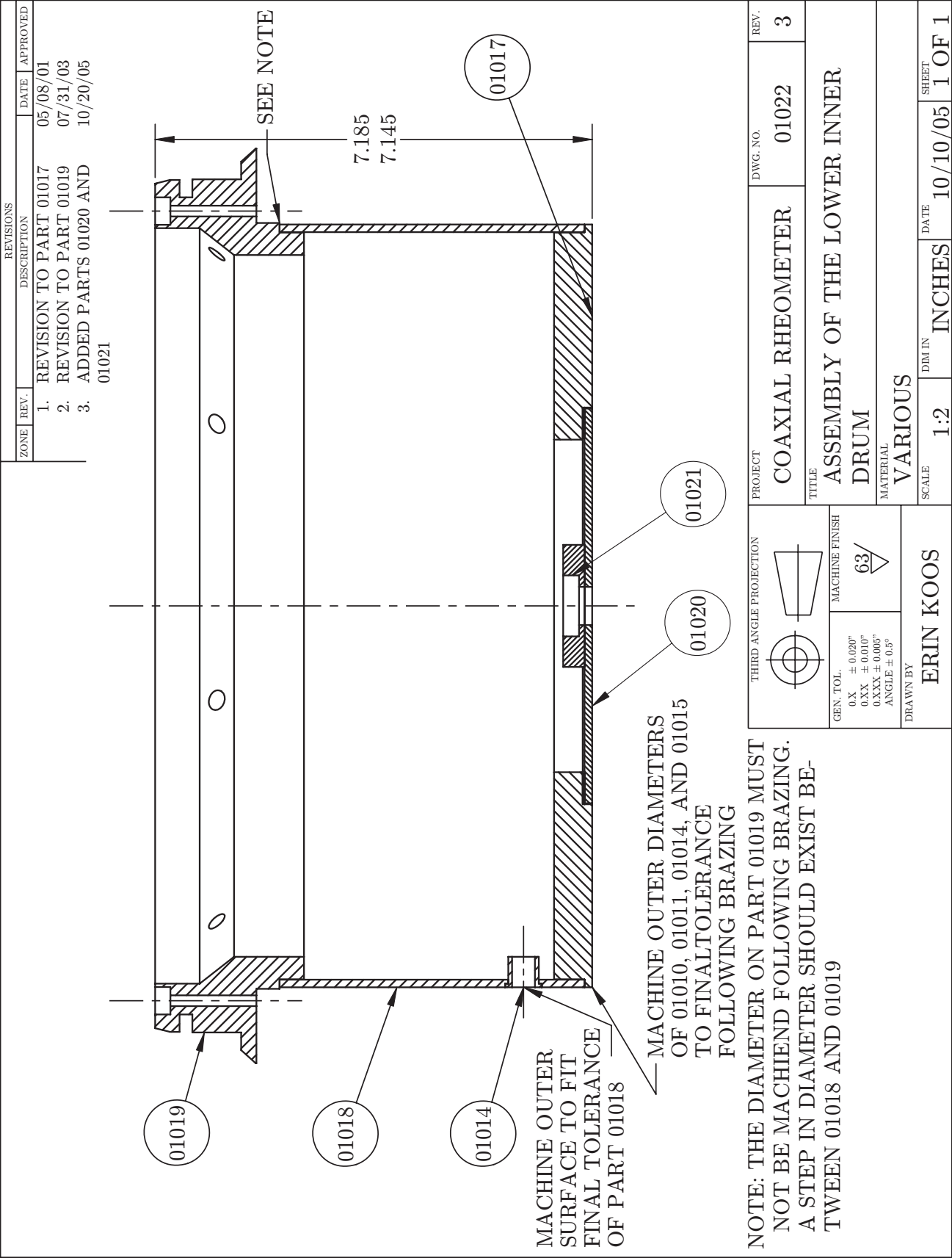


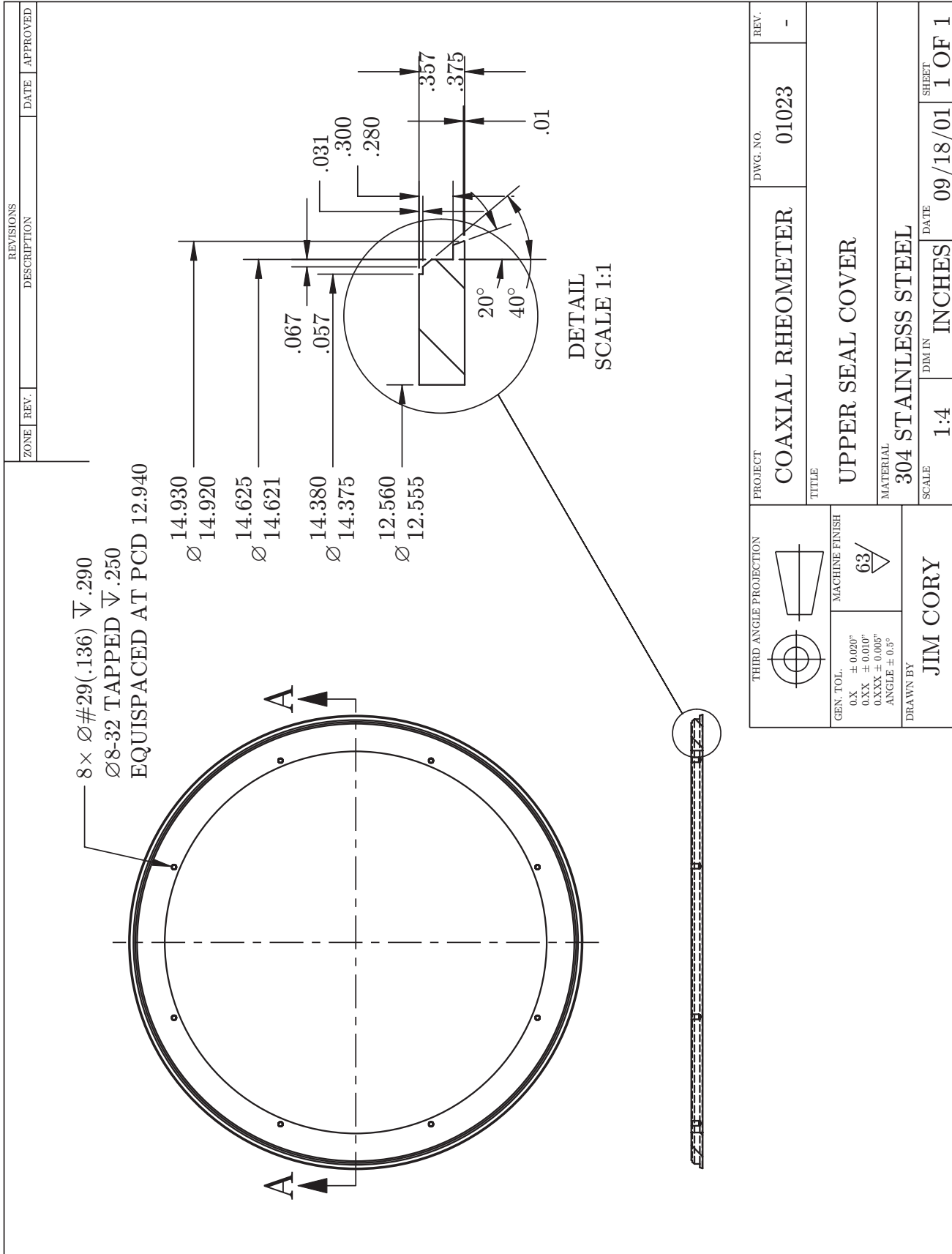


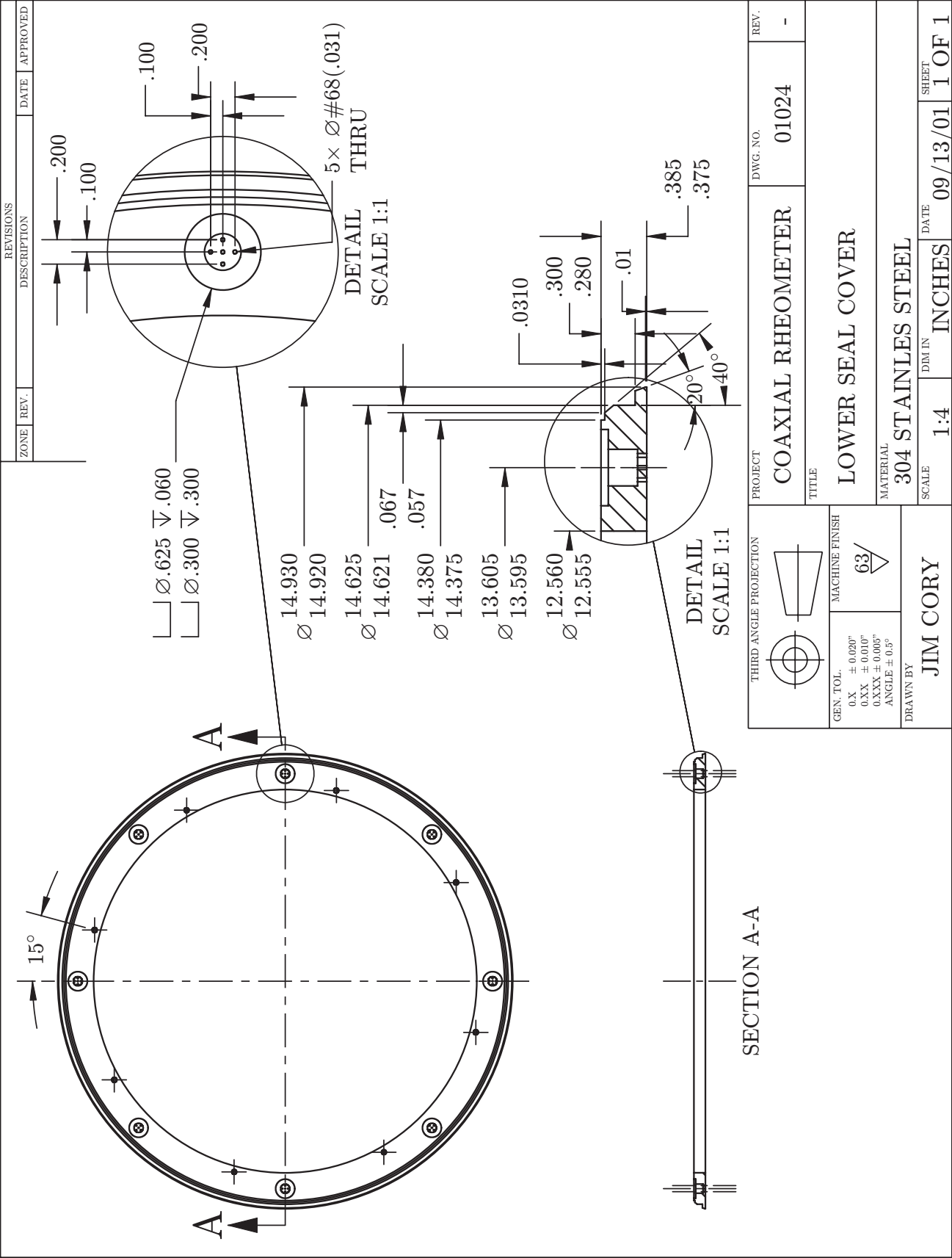


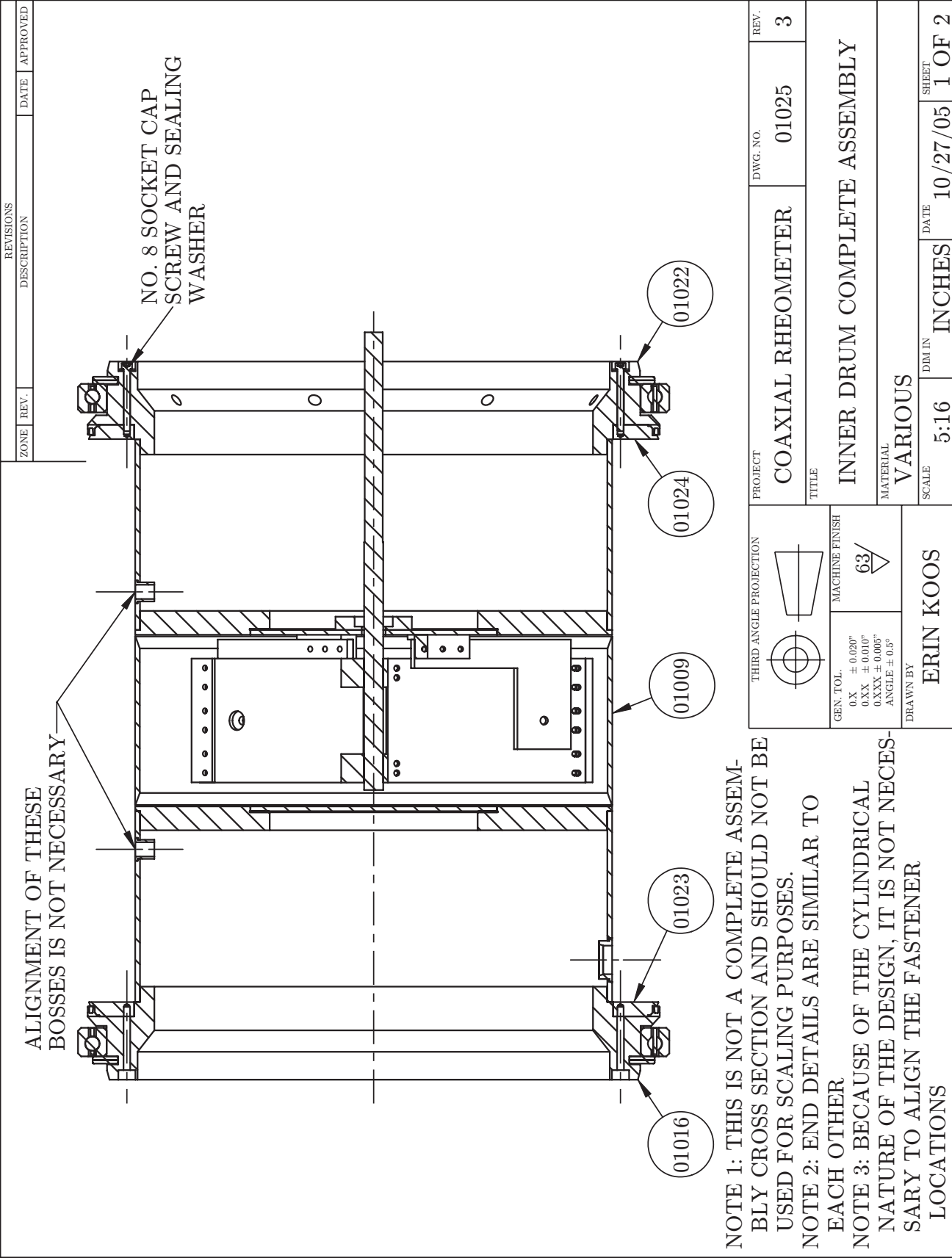


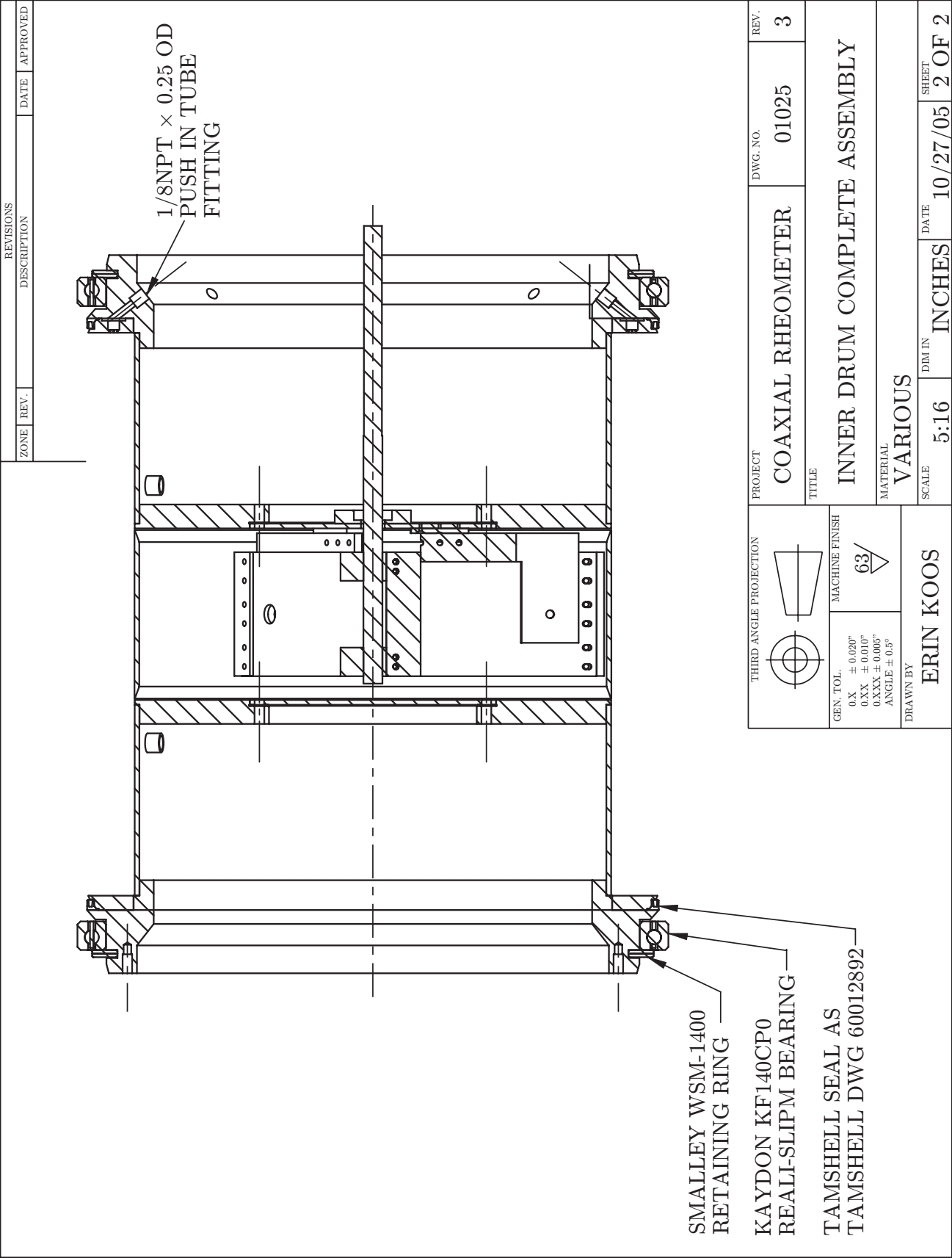




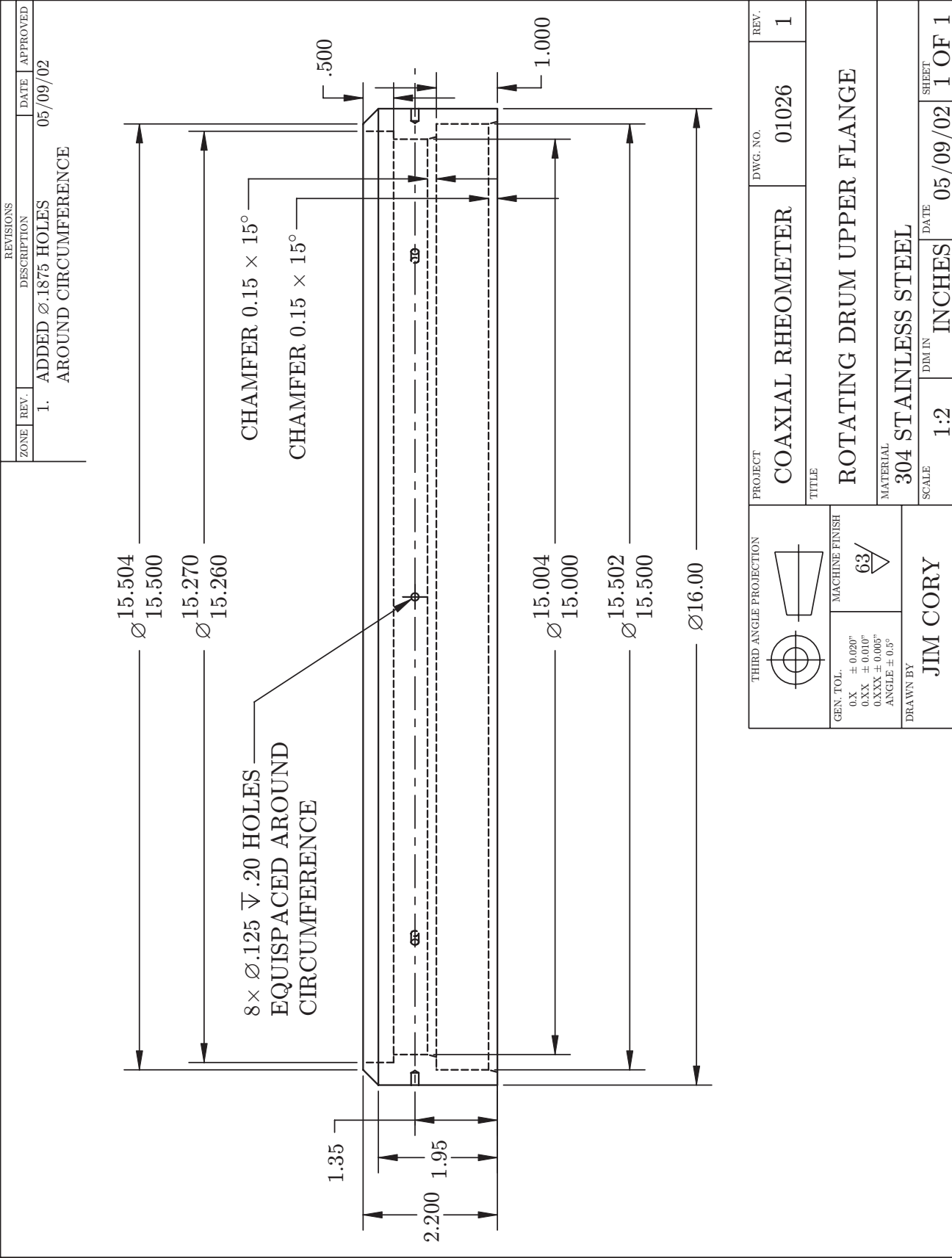


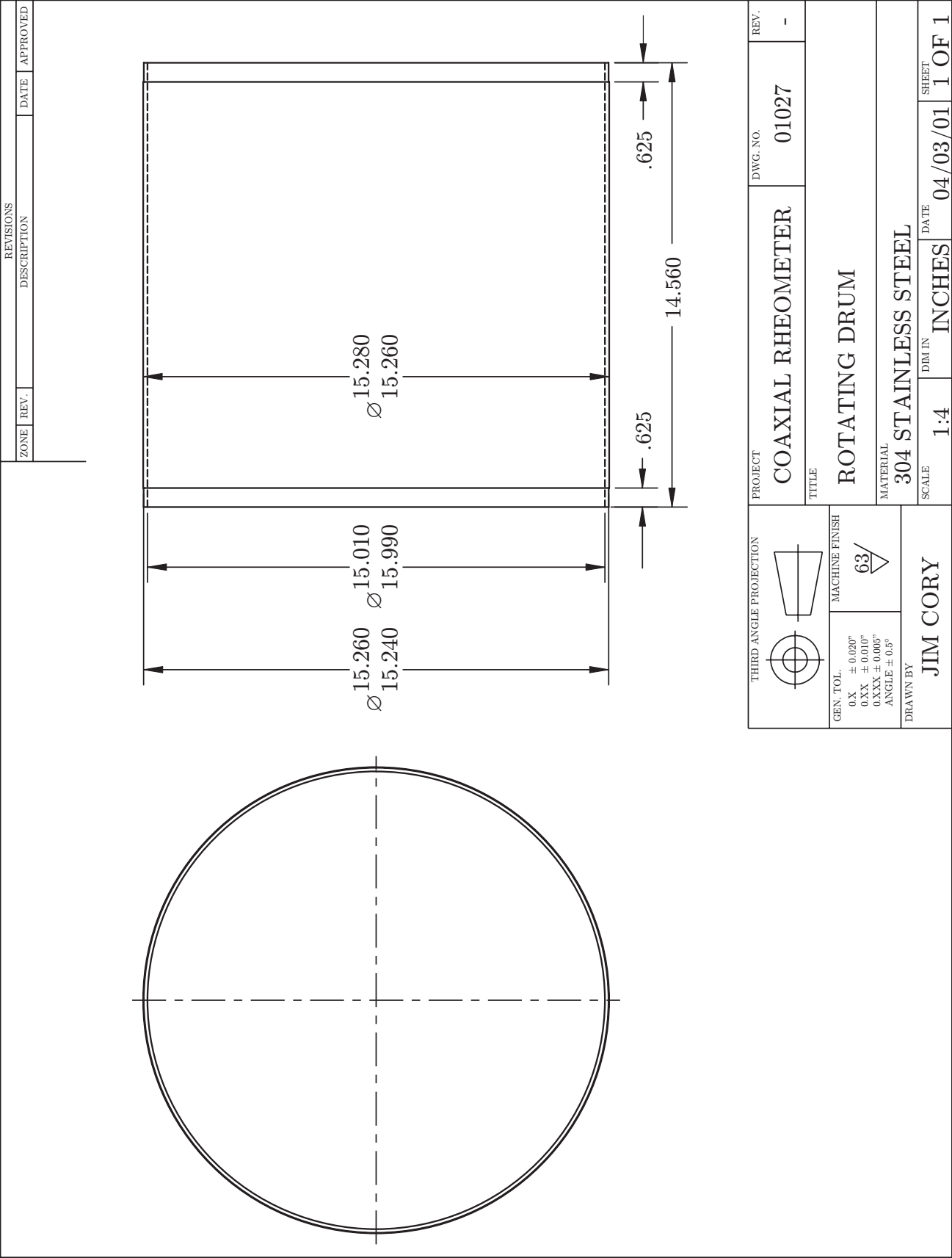


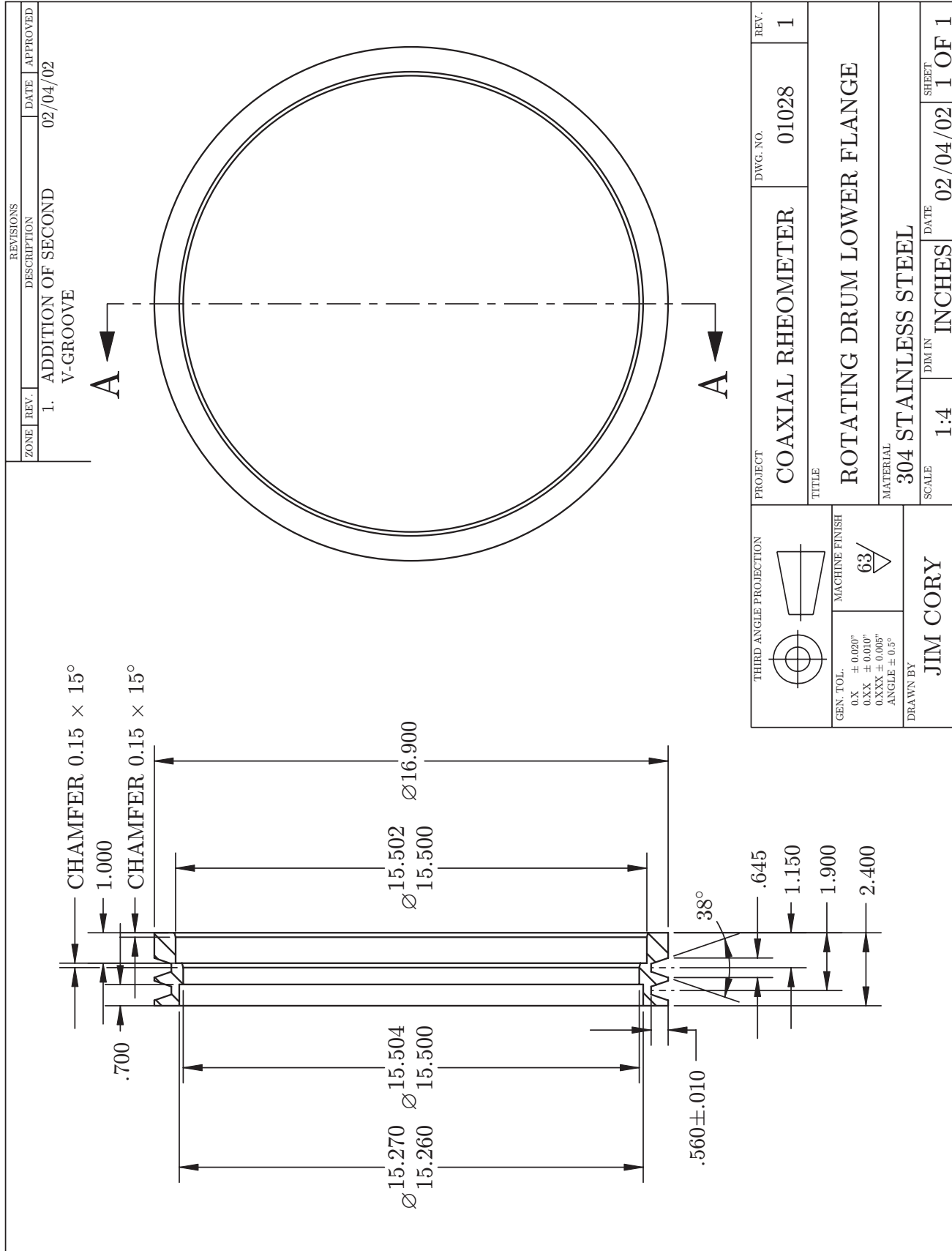


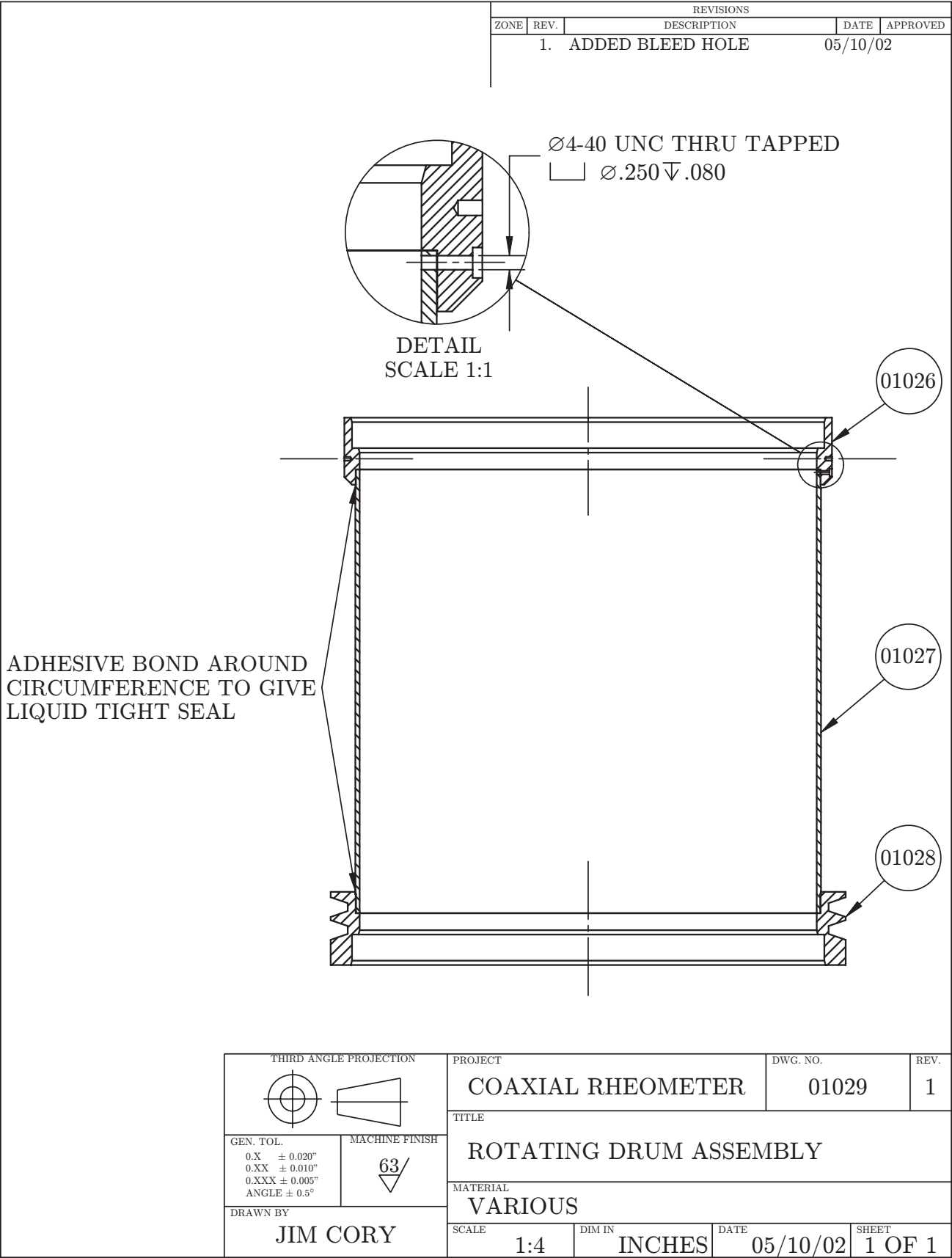






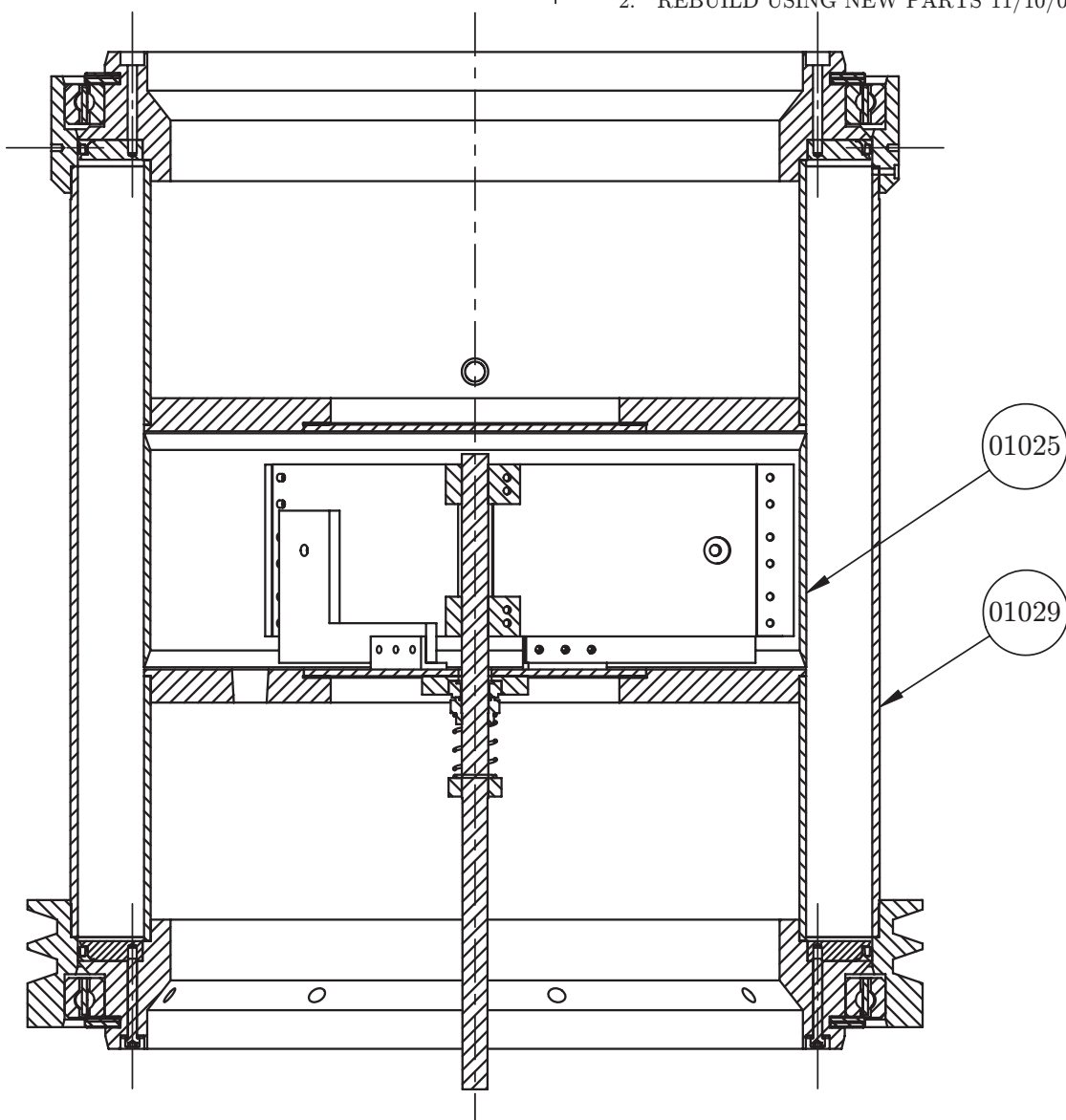






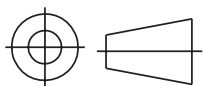

## REVISIONS

ZONE	REV.	DESCRIPTION	DATE	APPROVED
	1.	ADDED FILL PORT BOSS AND DRAIN PORT TAPPING	05/28/02	
	2.	REBUILD USING NEW PARTS	11/10/05	

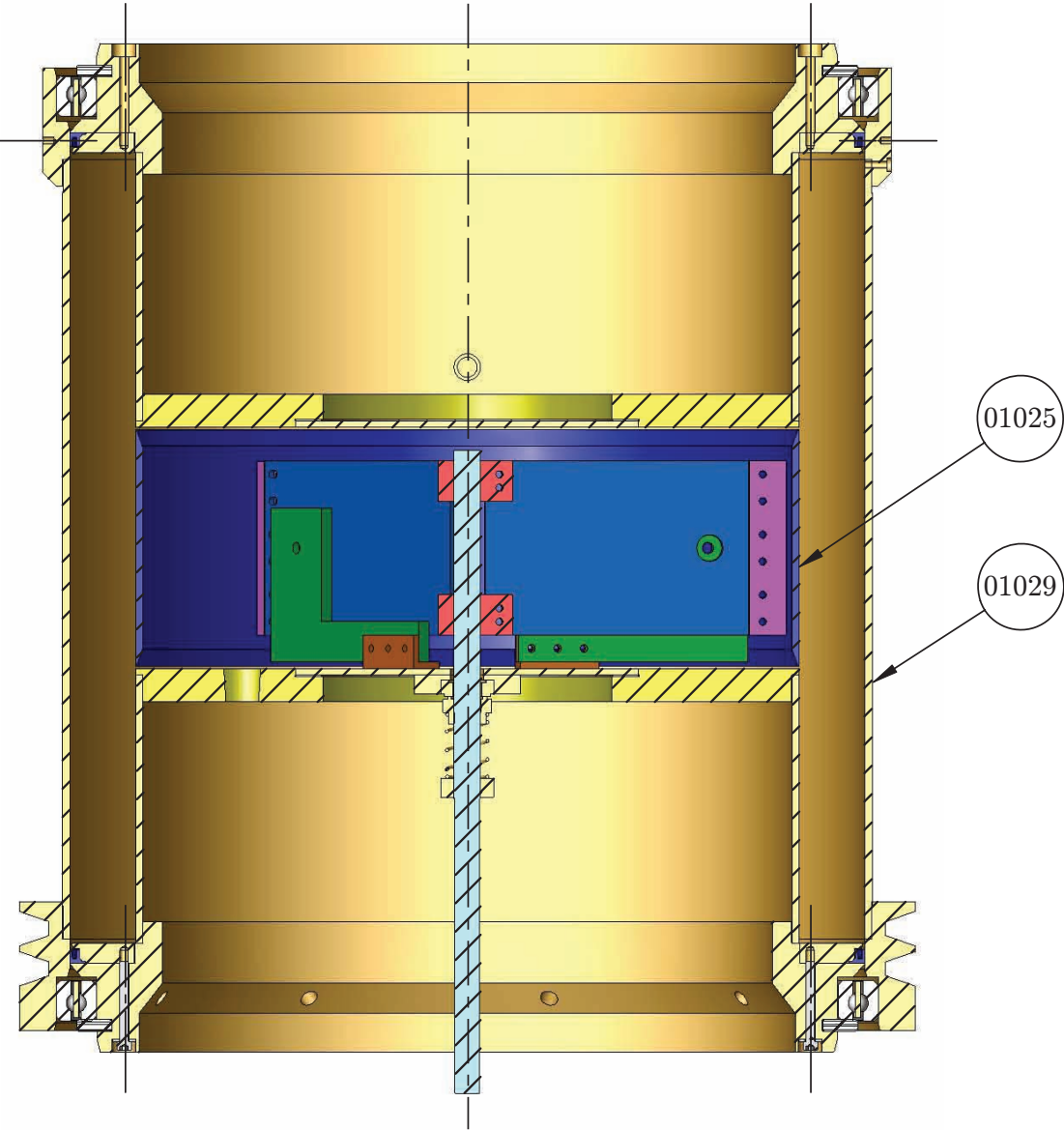


NOTE 1: THIS IS NOT A COMPLETE CROSS-SECTION  
AND SHOULD NOT BE USED FOR SCALING PURPOSES

NOTE 2: FOR AN ASSEMBLY OF THE INNER DRUM  
ALONE, PLEASE SEE DRAWING 01025

THIRD ANGLE PROJECTION		PROJECT	DWG. NO.	REV.
		COAXIAL RHEOMETER	01030	2
GEN. TOL. 0.X $\pm 0.020"$ 0.XX $\pm 0.010"$ 0.XXX $\pm 0.005"$ ANGLE $\pm 0.5^\circ$		TITLE COMPLETE DRUM ASSEMBLY		
MACHINE FINISH 		MATERIAL VARIOUS		
DRAWN BY ERIN KOOS		SCALE 1:3	DIM IN INCHES	DATE 11/10/05
				SHEET 1 OF 2

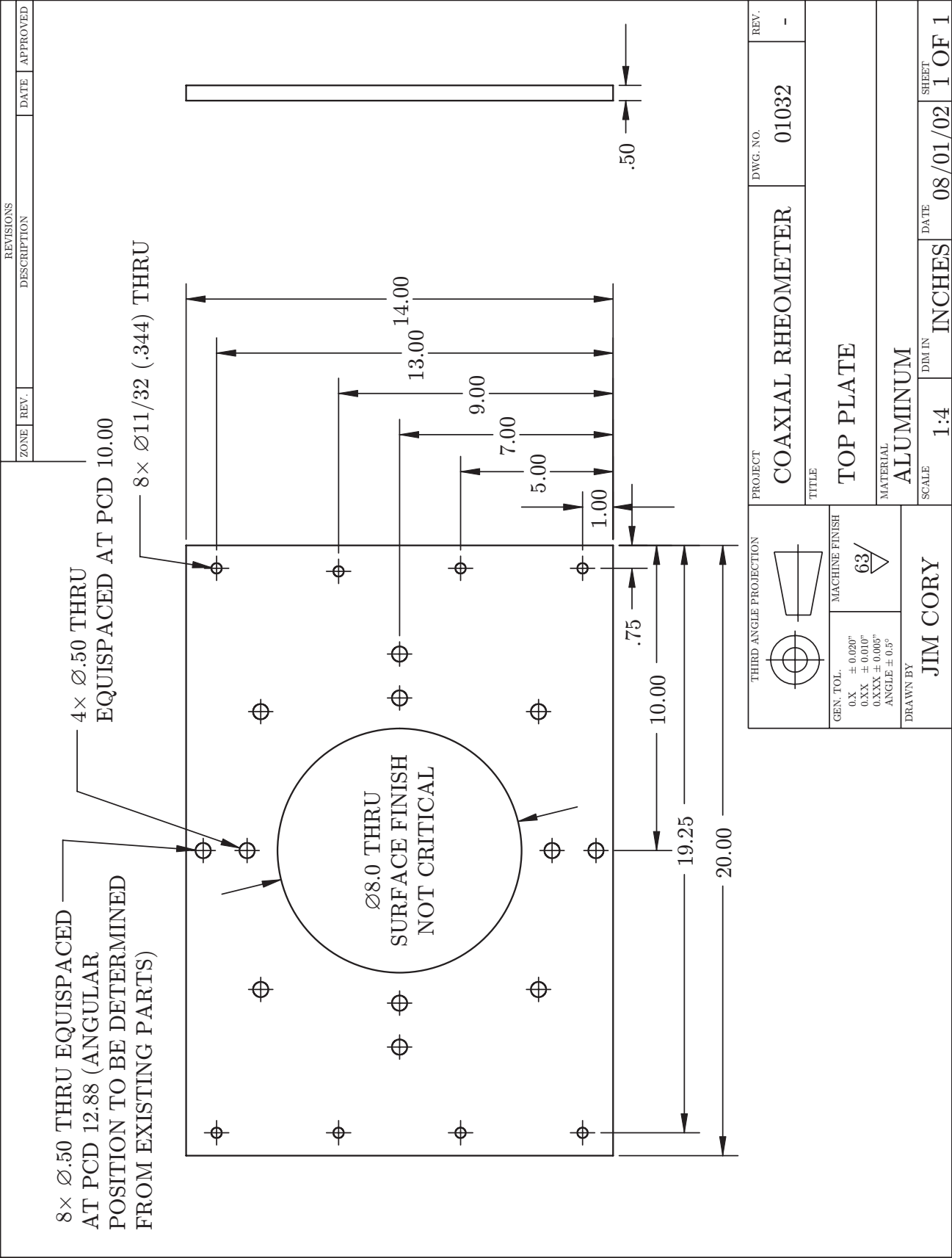
REVISIONS				
ZONE	REV.	DESCRIPTION	DATE	APPROVED
	1.	ADDED FILL PORT BOSS AND DRAIN PORT TAPPING	05/28/02	
	2.	REBUILD USING NEW PARTS	11/10/05	



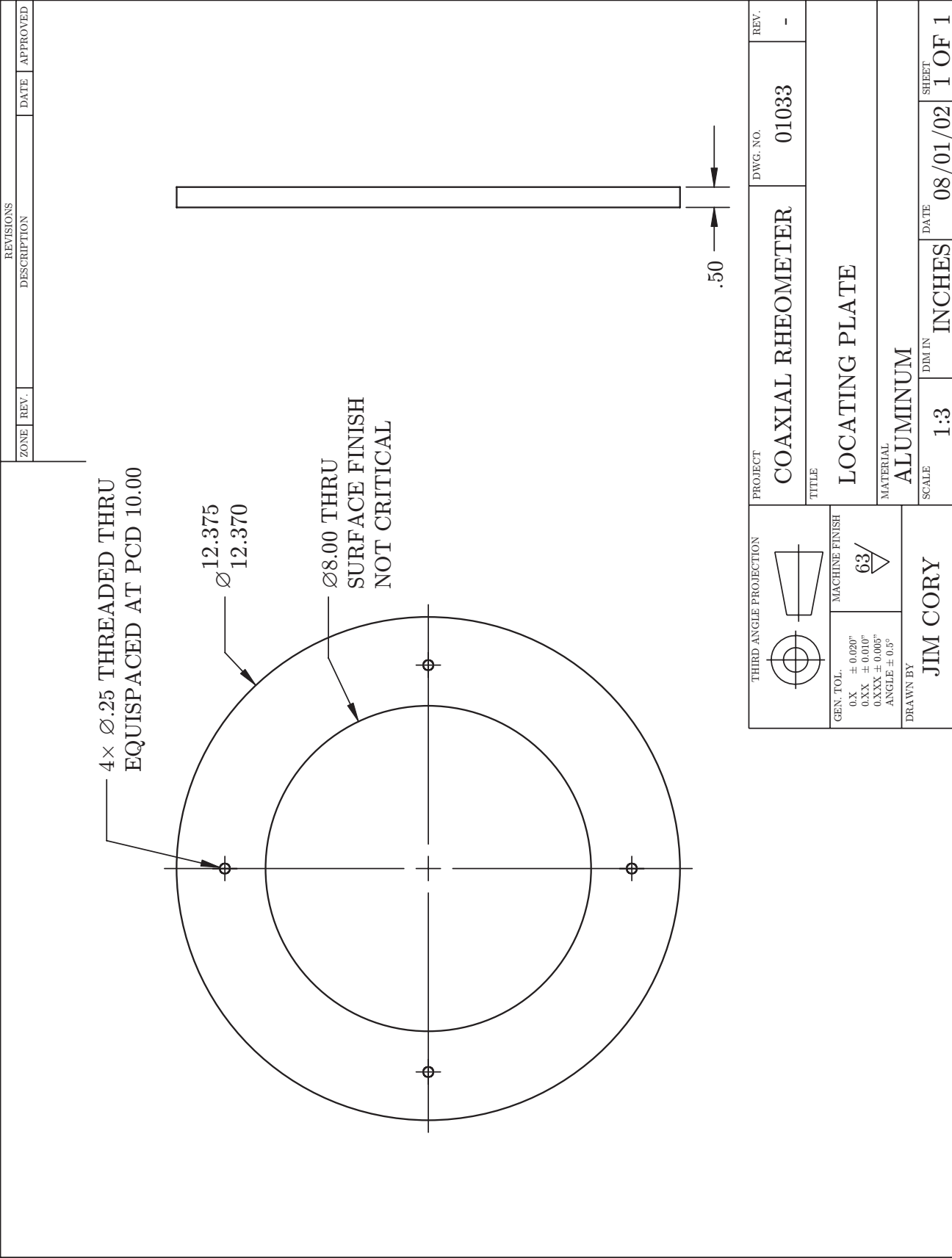
NOTE: THIS IS PURELY AN IMPRESSION OF THE ASSEMBLED  
DEVICE. DO NOT SCALE OR USE AS AN ASSEMBLY GUIDE

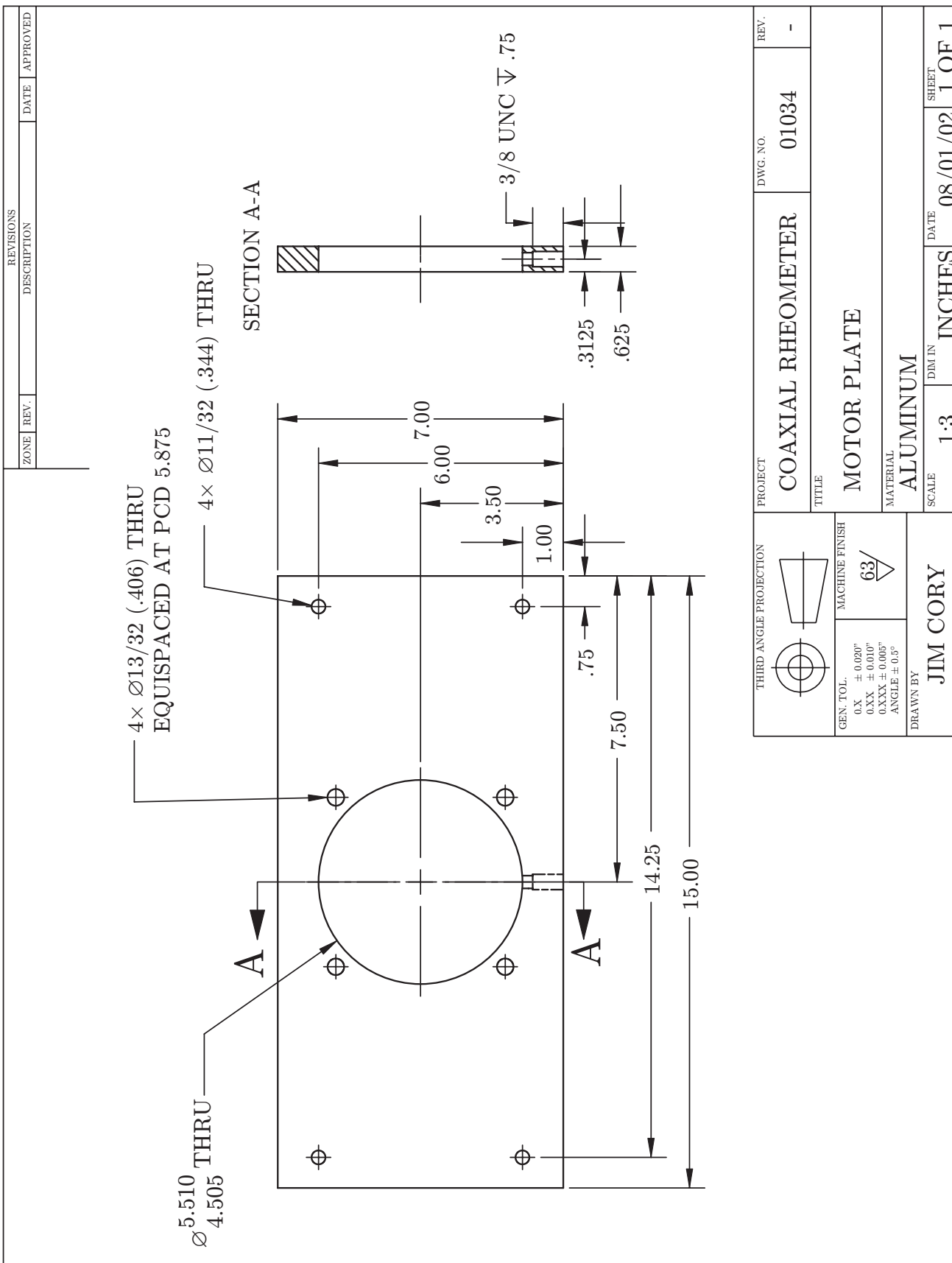
THIRD ANGLE PROJECTION 		PROJECT COAXIAL RHEOMETER	DWG. NO. 01030	REV. 2
GEN. TOL. 0.X ± 0.020" 0.XX ± 0.010" 0.XXX ± 0.005" ANGLE ± 0.5°		TITLE COMPLETE DRUM ASSEMBLY		
MACHINE FINISH 63/		MATERIAL VARIOUS		
DRAWN BY ERIN KOOS		SCALE 1:3	DIM IN INCHES	DATE 11/10/05
				SHEET 2 OF 2

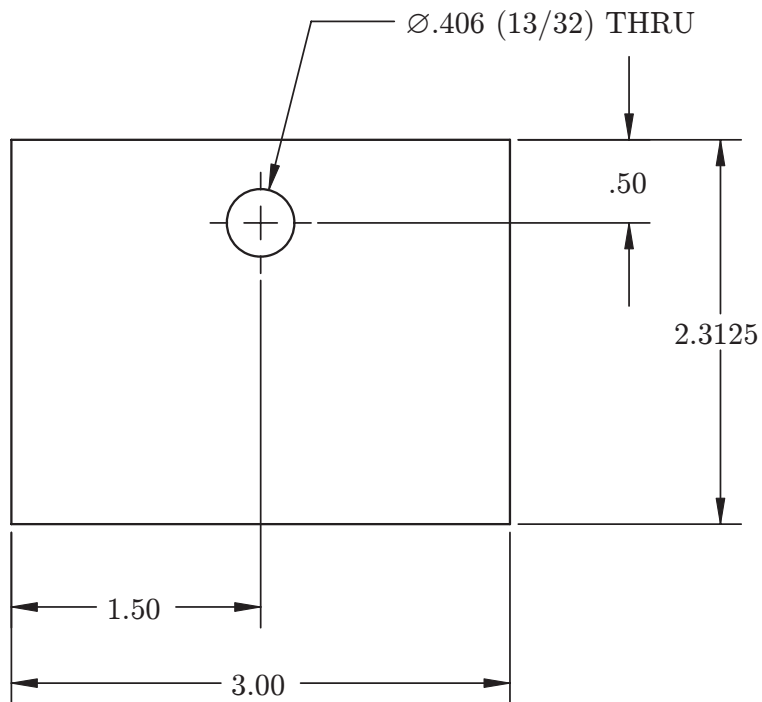
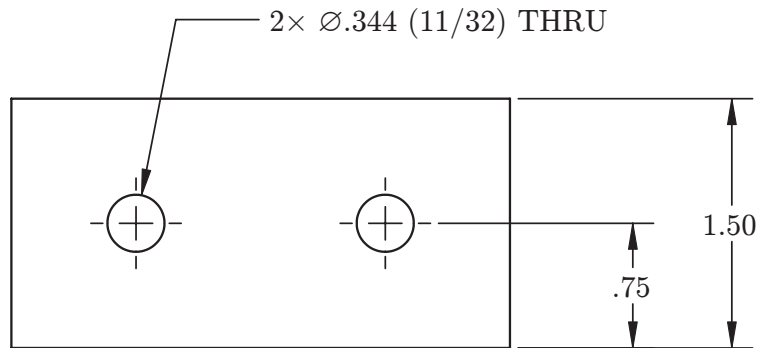




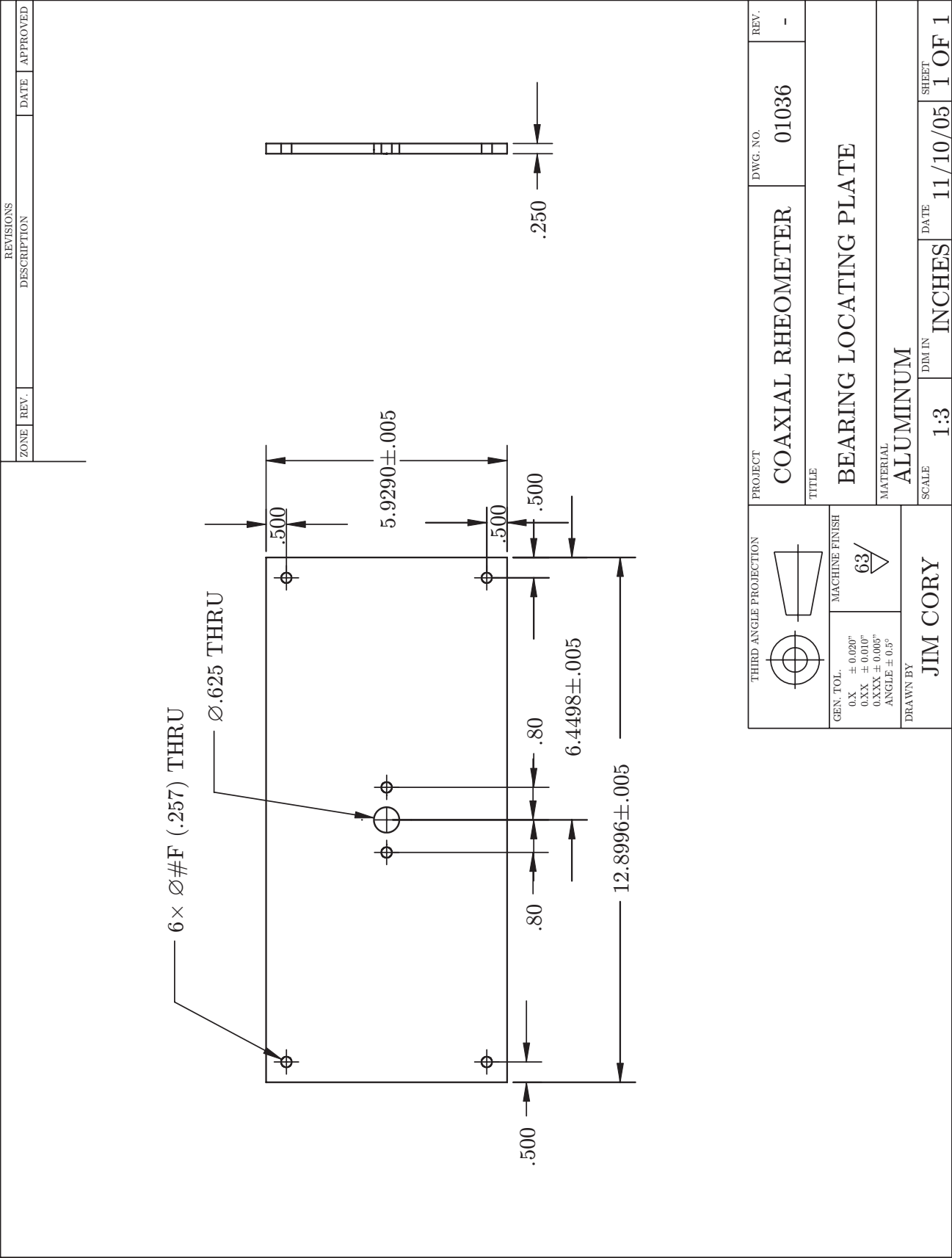


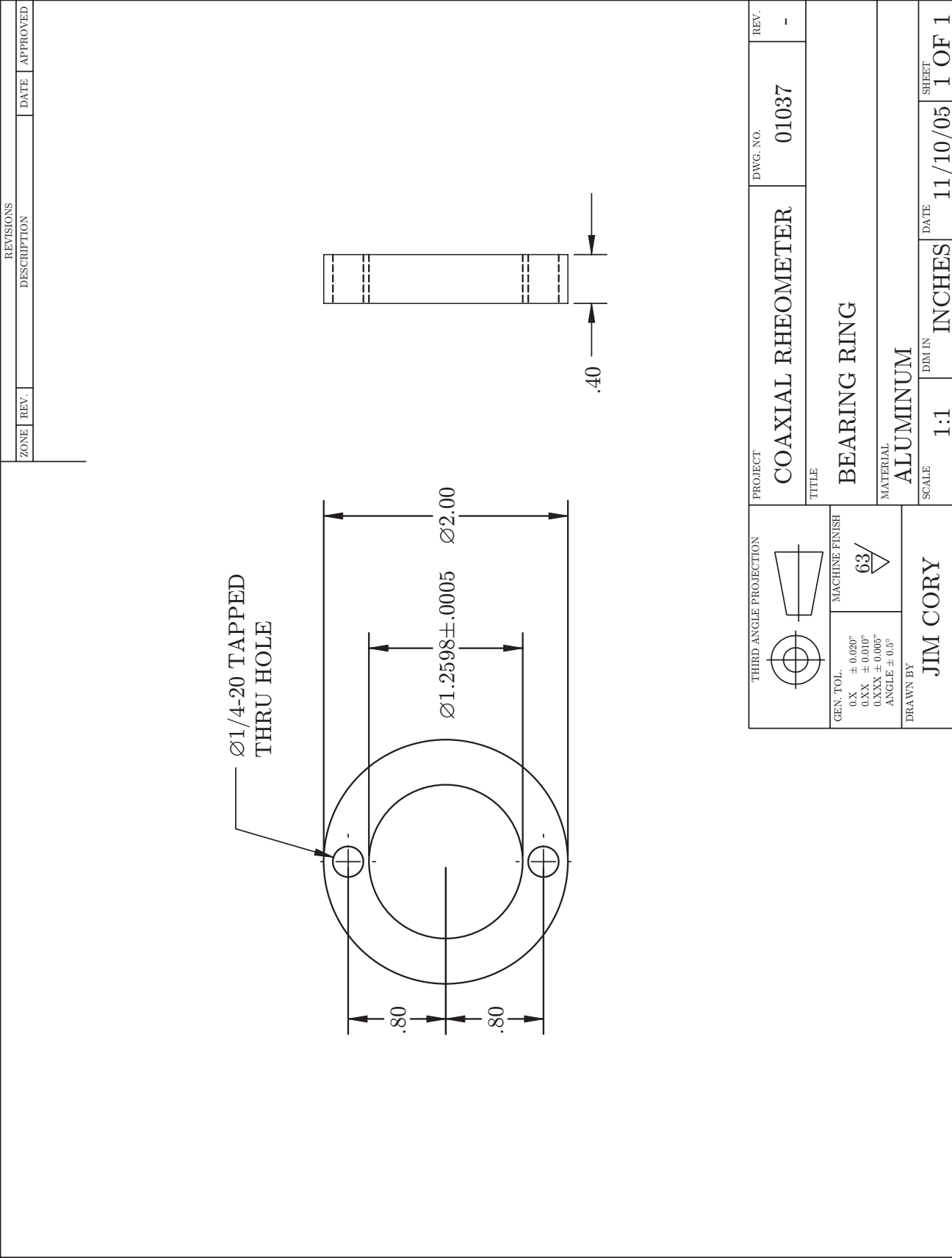


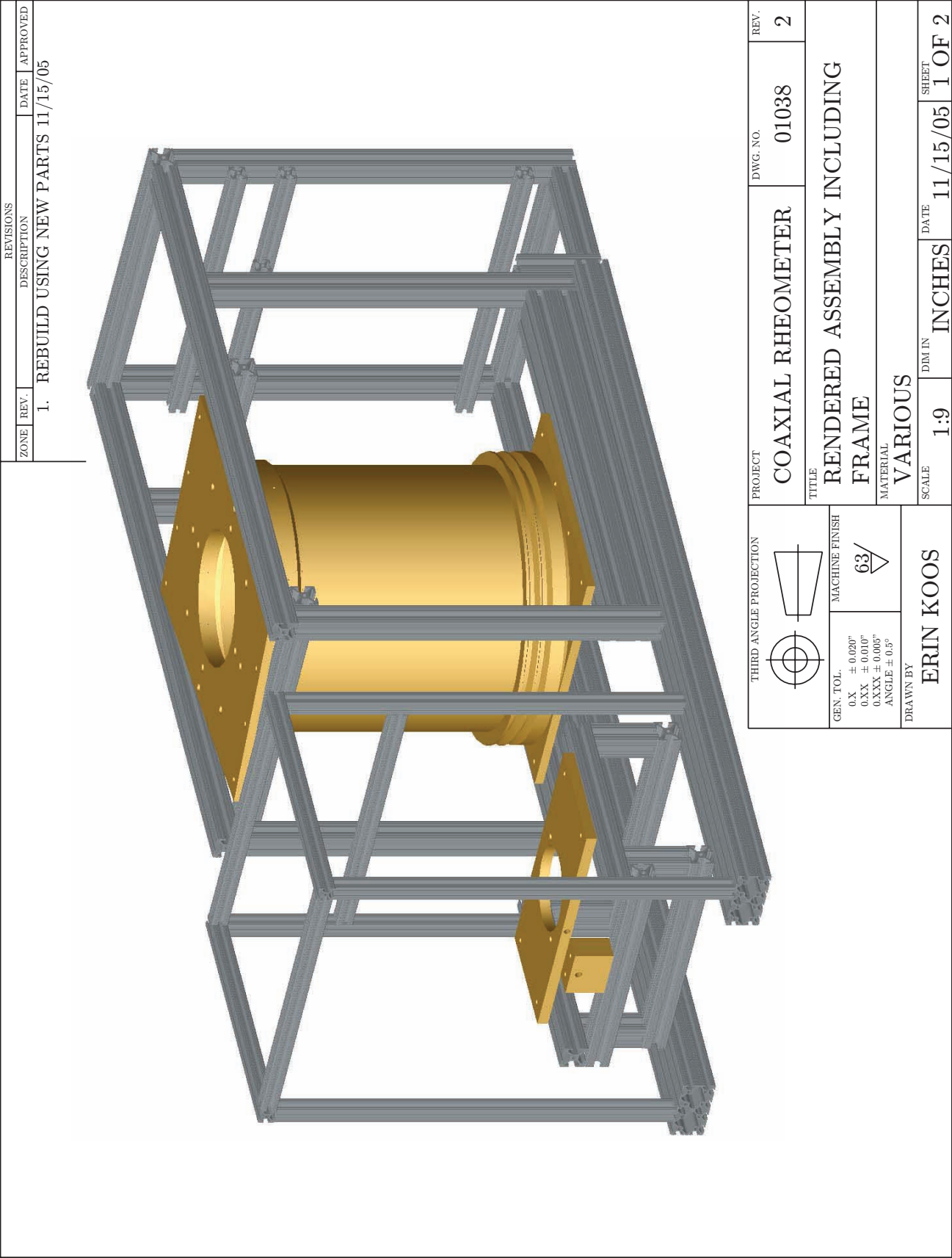


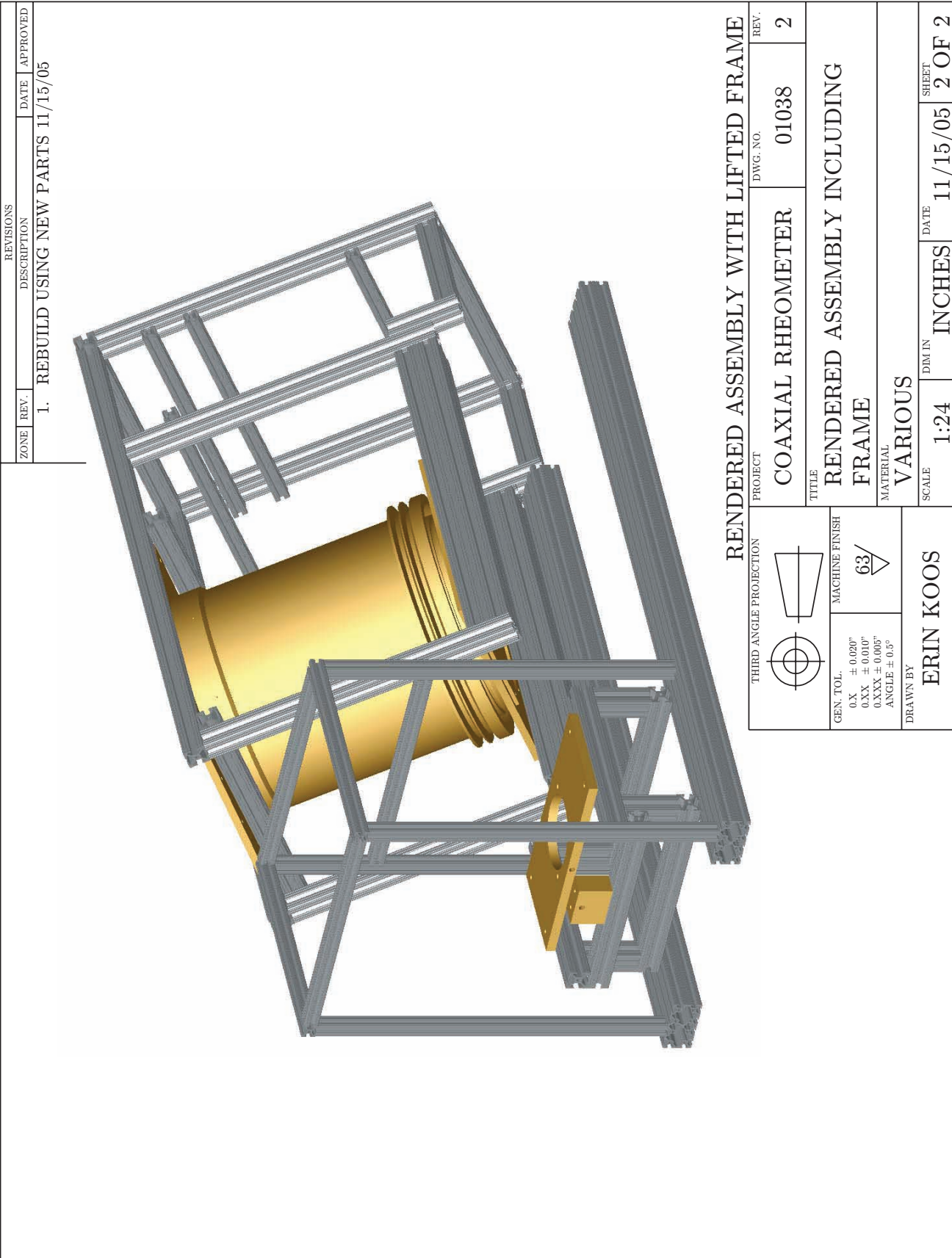


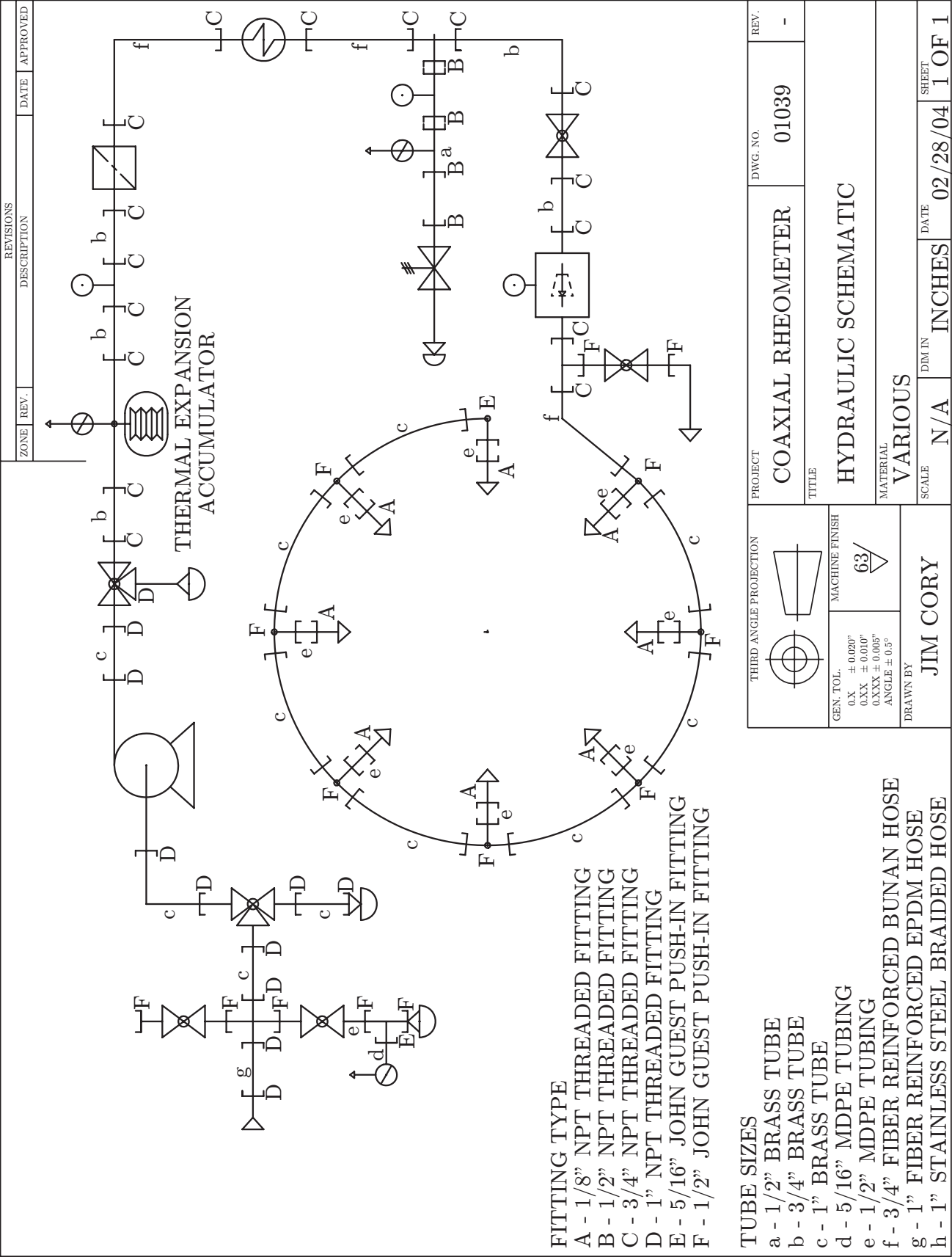
THIRD ANGLE PROJECTION		PROJECT		DWG. NO.		REV.	
		COAXIAL RHEOMETER		01035		-	
GEN. TOL.		TITLE					
0.X ± 0.020" 0.XX ± 0.010" 0.XXX ± 0.005" ANGLE ± 0.5°		MACHINE FINISH		TENSIONER BLOCK			
		63/		MATERIAL			
DRAWN BY		ALUMINUM					
JIM CORY		SCALE		DIM IN		DATE	
		1:1		INCHES		08/01/02	
						SHEET	
						1 OF 1	















# Bibliography

- J. R. ABBOTT, N. TETLOW, A. L. GRAHAM, S. A. ALTABELLI, E. FUKUSHIMA, L. A. MONDY, AND T. S. STEPHENS (1991). Experimental observations of particle migration in concentrated suspensions: Couette flow. *Journal of Rheology* **35** (5), 773–795.
- A. ACRIVOS (1992). The rheology of concentrated suspensions of non-colloidal particles. In *Particulate Two-Phase Flow*, (edited by M. C. ROCO), chapter 5. Boston: Butterworth-Heinemann, 169–189.
- A. ACRIVOS, X. FAN, AND R. MAURI (1994). On the measurements of the relative viscosity of suspensions. *Journal of Rheology* **38** (5), 1285–1296.
- T. ASTE, M. SAADATFAR, A. SAKELLARIOU, AND T. SENDEN (2004). Investigating the geometrical structure of disordered sphere packings. *Physica A* **339**, 16–23.
- T. ASTE, M. SAADATFAR, AND T. SENDEN (2005). Geometrical structure of disordered sphere packings. *Physical Review E* **71** (6), 1302–1317.
- R. A. BAGNOLD (1954). Experiments on a gravity-free dispersion of large solid spheres in a Newtonian fluid under shear. *Proceedings of the Royal Society of London, Series A* **225** (1160), 49–53.
- R. A. BAGNOLD (1956). The flow of cohesionless grains in fluids. *Proceedings of the Royal Society of London, Series A* **249** (946), 235–297.
- R. A. BAGNOLD (1966). The shearing and dilatation of dry sand and the “singing” mechanism. *Proceedings of the Royal Society of London, Series A* **295** (1442), 219–232.
- H. A. BARNES (1995). A review of the slip (wall depletion) of polymer solutions, emulsions and particle suspensions in viscometers: its cause, character, and cure. *Journal of Non-Newtonian Fluid Mechanics* **56** (3), 221–251.
- H. A. BARNES (2000). Measuring the viscosity of large-particle (and flocculated) suspensions – a note on the necessary gap size of rotational viscometers. *Journal of Non-Newtonian Fluid Mechanics* **94** (2–3), 213–217.
- Y. M. BASHIR AND J. D. GODDARD (1991). A novel simulation method for the quasi-static mechanics of granular assemblages. *Journal of Rheology* **35** (5), 849–885.

- G. K. BATCHELOR (1970). The stress system in a suspension of force-free particles. *Journal of Fluid Mechanics* **41**, 545–570.
- G. K. BATCHELOR (1977). The effect of Brownian motion on the bulk stress in a suspension of spherical particles. *Journal of Fluid Mechanics* **83**, 97–117.
- G. K. BATCHELOR AND J. T. GREEN (1972). The determination of the bulk stress in a suspension of spherical particles to order  $c^2$ . *Journal of Fluid Mechanics* **56**, 401–427.
- R. F. BENENATI AND C. B. BROSILOW (1962). Void fraction distribution in beds of spheres. *American Institute of Chemical Engineers Journal* **8** (3), 359–361.
- C. H. BENNETT (1972). Serially deposited amorphous aggregates of hard spheres. *Journal of Applied Physics* **43** (6), 2727–2734.
- J. G. BERRYMAN (1983). Random close packing of hard spheres and disks. *Physical Review A* **27** (2), 1053–1061.
- H. BI AND L. S. FAN (1992). Existence of turbulent regime in gas–solid fluidization. *American Institute of Chemical Engineers Journal* **38** (2), 297–301.
- C. E. BRENNEN (2005). *Fundamentals of Multiphase Flows*. Cambridge University Press.
- R. BUSCALL AND I. J. MCGOWAN (1983). Sedimentation and viscous flow of a weakly flated concentrated dispersion. *Faraday Special Discussions of the Chemical Society* **76**, 277–290.
- R. BUSCALL, I. J. MCGOWAN, AND A. J. MORTON-JONES (1993). The rheology of concentrated dispersions of weakly attracting colloidal particles with and without wall slip. *Journal of Rheology* **37** (4), 621–641.
- R. BUSCALL, I. J. MCGOWAN, AND C. A. MUMME-YOUNG (1990). Rheology of weakly interacting colloidal particles at high concentration. *Faraday Special Discussions of the Chemical Society* **90**, 115–127.
- M. E. CATES, M. D. HAW, AND C. B. HOLMES (2005). Dilatancy, jamming, and the physics of granulation. *Journal of Physics: Condensed Matter* **17** (24), S2517–S2531.
- C. L. CHEN AND C. H. LING (1996). Granular-flow rheology: Role of shear-rate number in transition regime. *Journal of Engineering Mechanics, ASCE* **122** (5), 469–480.
- D. COLES (1965). Transition in circular Couette flow. *Journal of Fluid Mechanics* **21**, 385–424.
- S. L. CONWAY, T. SHINBROT, AND B. J. GLASSER (2004). A Taylor vortex analogy in granular flows. *Nature* **431**, 433–437.
- P. COUSSOT AND C. ANCEY (1999). Rheophysical classification of concentrated suspensions and granular pastes. *Physical Review E* **59** (4), 4445–4457.

- D. J. CUMBERLAND AND R. J. CRAWFORD (1987). *The Packing of Particles*, volume 6 of *Handbook of Powder Technology*. Amsterdam: Elsevier.
- O. CZARNY, E. SERRE, P. BONToux, AND R. M. LUEPTOW (2003). Interaction between Ekman pumping and the centrifugal instability in Taylor–Couette flow. *Physics of Fluids* **15** (2), 467 – 477.
- A. G. DIXON (1988). Correlations for wall and particle shape effects on fixed bed bulk voidage. *Canadian Journal of Chemical Engineering* **66** (5), 705–708.
- H. EGGER AND K. M. MCGRATH (2006). Estimating depletion layer thickness in colloidal systems: correlation with oil-in-water emulsion composition. *Colloids and Surfaces A: Physiochemical Engineering Aspects* **275**, 107–113.
- H. EILERS (1941). The viscosity of emulsions made of highly viscous materials as a function of concentration. *Kolloid-Z* **97**, 313.
- A. EINSTEIN (1906). On the theory of Brownian motion. *Annalen der Physik* **19** (4), 371–381.
- S. ELGHOBASHI (1994). On predicting particle-laden turbulent flows. *Applied Scientific Research* **52** (4), 309–329.
- F. FERRINI, D. ERCOLANI, B. DE CINDIO, L. NICODEMO, L. NICOLAIS, AND S. RANAUDO (1979). Shear viscosity of settling suspensions. *Rheologica Acta* **18** (2), 289–296.
- J. L. FINNEY (1970). Random packings and the structure of simple liquids: I. The geometry of random close packing. *Proceedings of the Royal Society of London, Series A* **319** (1539), 5746–5746.
- N. A. FRANKEL AND A. ACRIVOS (1967). On the viscosity of a concentrated suspension of solid spheres. *Chemical Engineering Science* **22**, 847–853.
- R. A. GORE AND C. T. CROWE (1991). Modulation of turbulence by a dispersed phase. *Journal of Fluids Engineering* **113** (2), 304–307.
- K. GOTOH AND J. L. FINNEY (1974). Statistical geometrical approach to random packing density of equal spheres. *Nature* **252**, 202–205.
- S. A. GULMUS AND U. YILMAZER (2007). Effect of the surface roughness and construction material on wall slip in the flow of concentrated suspensions. *Journal of Applied Polymer Science* **103** (5), 3341–3347.
- D. M. HANES AND D. L. INMAN (1985). Observations of rapidly flowing granular-fluid materials. *Journal of Fluid Mechanics* **150**, 357–380.
- D. P. HAUGHEY AND G. S. G. BEVERIDGE (1966). Local voidage variation in a randomly packed bed of equal-sized spheres. *Chemical Engineering Science* **21** (10), 905–916.

- C. L. HENLEY (1986). Sphere packings and local environments in Penrose tilings. *Physical Review B* **34** (2), 797–816.
- M. L. HUNT, R. ZENIT, C. S. CAMPBELL, AND C. E. BRENNEN (2002). Revisiting the 1954 suspension experiments of R.A. Bagnold. *Journal of Fluid Mechanics* **452**, 1–24.
- G. G. JOSEPH (2003). Collisional dynamics of macroscopic particles in a viscous fluid. Ph.D. thesis, California Institute of Technology.
- G. G. JOSEPH AND M. L. HUNT (2004). Oblique particle-wall collisions in a liquid. *Journal of Fluid Mechanics* **510**, 71–93.
- G. G. JOSEPH, R. ZENIT, M. L. HUNT, AND A. M. ROSENWINKEL (2001). Particle-wall collisions in a viscous fluid. *Journal of Fluid Mechanics* **433**, 329–346.
- R. P. KING (2001). *Introduction to practical fluid flow*. Butterworth-Heinemann.
- J. H. LAZARUS AND I. D. NEILSON (1978). A generalized correlation for friction head losses of settling mixtures in horizontal smooth pipelines. *Hydrotransport 5 Proceedings of the 5th International Conference on Hydraulic Transport of Solids in Pipes* **1**, B1–1 – B1–32.
- E. J. LEFEVRE (1973). Hard-sphere fluid. *Journal of Chemical Physics* **59** (10), 497–493.
- D. LEIGHTON (1985). The shear induced migration of particulates in concentrated suspensions. Ph.D. thesis, Stanford University, Palo Alto, California.
- D. LEIGHTON AND A. ACRIVOS (1987). Measurement of shear-induced self-diffusion in concentrated suspensions of spheres. *Journal of Fluid Mechanics* **177**, 109–131.
- R. J. LINGWOOD (1997). Absolute instability of the Ekman layer and related rotating flows. *Journal of Fluid Mechanics* **331**, 405–428.
- J. P. MATAS, J. F. MORRIS, AND É. GUZZELLI (2003). Transition to turbulence in particulate pipe flow. *Physical Review Letters* **90** (1), 4501–4504.
- A. J. MATHESON (1974). Computation of a random packing of hard spheres. *Journal of Physics C: Solid State Physics* **7**, 2569–2576.
- C. S. O’HERN, S. A. LANGER, A. J. LIU, AND S. R. NAGEL (2002). Random packings of frictionless particles. *Physical Review Letters* **88** (7), 5507–5510.
- G. Y. ONODA AND E. G. LINIGER (1990). Random loose packings of uniform spheres and the dilatancy onset. *Physical Review Letters* **64** (22), 2727–2730.

- S. J. PARTRIDGE (1985). The rheology of cohesive sediments. Ph.D. thesis, University of Bristol.
- P. PHILIPPE AND D. BIDEAU (2001). Numerical model for granular compaction under vertical tapping. *Physical Review E* **63** (5), 1304–1313.
- C. PICART, J. M. PIAU, H. GALLIARD, AND P. CARPENTIER (1978). Human blood shear yield stress and its hematocrit dependence. *Journal of Rheology* **42** (1), 1–12.
- O. POULIQUEN AND N. RENAUT (1996). Onset of granular flows on an inclined rough surface: Dilatancy effects. *Journal de Physique II* **6**, 923–935.
- D. PRASAD AND H. K. KYTÖMAA (1995). Particle stress and viscous compaction during shear of dense suspensions. *International Journal of Multiphase Flow* **21** (5), 775–785.
- O. REYNOLDS (1885). On the dilatancy of media composed of rigid particles in contact, with experimental illustrations. *Philosophical Magazine* **5** (20), 469–481.
- L. H. S. ROBLEE, R. M. BAIRD, AND J. W. TIERNEY (1958). Radial porosity variations in packed beds. *American Institute of Chemical Engineers Journal* **4** (4), 460–464.
- P. W. ROWE (1962). The stress-dilatancy relation for static equilibrium of an assembly of particles in contact. *Proceedings of the Royal Society of London, Series A* **269** (1339), 500–527.
- A. RUIZ-ANGULO (2008). Surface deformation in a liquid environment resulting from single particle collisions. Ph.D. thesis, California Institute of Technology, Pasadena, California.
- A. RUIZ-ANGULO AND M. L. HUNT (2009). Measurements of the coefficient of restitution for particle collisions with ductile surfaces in a liquid. *Granular Matter* (**submitted**).
- R. RUTGERS (1962). Relative viscosity of suspensions of rigid spheres in Newtonian liquids. *Rheologica Acta* **2** (3), 202–210.
- S. B. SAVAGE AND S. MCKEOWN (1983). Shear stresses developed during rapid shear of concentrated suspensions of large spherical particles between concentric cylinders. *Journal of Fluid Mechanics* **127**, 453–472.
- H. SCHLICHTING (1951). *Boundary Layer Theory*. New York: McGraw Hill, 7th edition.
- G. D. SCOTT (1960). Packing of spheres: Packing of equal spheres. *Nature* **188**, 908–909.
- G. D. SCOTT AND D. M. KILGOUR (1969). The density of random close packing of spheres. *Journal of Physics D: Applied Physics* **2** (2), 863–866.
- N. C. SHAPLEY, R. C. ARMSTRONG, AND R. A. BROWN (2002). Laser Doppler velocimetry measurements of particle velocity fluctuations in a concentrated suspension. *Journal of Rheology* **46** (1), 241–272.

- F. SOLTANI AND U. YILMAZER (1998). Slip velocity and slip layer thickness in flow of concentrated suspensions. *Journal of Applied Polymer Science* **70** (3), 515–522.
- J. J. STICKEL AND R. L. POWELL (2005). Fluid mechanics and rheology of dense suspensions. *Annual Review of Fluid Mechanics* **37** (1), 129–149.
- G. I. TAYLOR (1936a). Fluid friction between rotating cylinders, I. Torque measurements. *Proceedings of the Royal Society of London, Series A* **157** (892), 546–564.
- G. I. TAYLOR (1936b). Fluid friction between rotating cylinders, II. Distribution of velocity between concentric cylinders when outer one is rotating and inner one is at rest. *Proceedings of the Royal Society of London, Series A* **157** (892), 565–578.
- S. TORQUATO, T. M. TRUSKETT, AND P. G. DEBENEDETTI (2000). Is random close packing of spheres well defined? *Physical Review Letters* **84** (10), 2064–2067.
- P. B. UMBANHOWAR AND D. I. GOLDMAN (2006). Low density fragile states in cohesive powders. *American Journal of Physics* **74** (8), 720–721.
- W. M. VISSCHER AND M. BOLSTERI (1972). Random packing of equal and unequal spheres in two and three dimensions. *Nature* **239**, 504–507.
- F. WENDT (1933). Turbulente strömungen zwischen zwei rotierenden konaxialen zylindern. *Ingenieur Archiv* **4**, 577–595.
- D. M. WOOD (1991). *Soil Behaviour and Critical State Soil Mechanics*. Cambridge University Press.
- L. V. WOODCOCK (1976). Hard-sphere fluid equation of state. *Journal of the Chemical Society - Faraday Transactions II* **72**, 731–735.
- A. YANG, C. T. MILLER, AND L. D. TURCOLIVER (1996). Simulation of correlated and uncorrelated packing of random size spheres. *Physical Review E* **53** (2), 1516–1524.
- F. L. YANG (2006). Interaction law for a collision between two solid particles in a viscous liquid. Ph.D. thesis, California Institute of Technology.
- F. L. YANG AND M. L. HUNT (2006). Dynamics of particle-particle collisions in a viscous liquid. *Physics of Fluids* **18** (12), 1506–1516.
- U. YILMAZER AND D. M. KALYON (1989). Slip effects in capillary and parallel disk torsional flows of highly filled suspensions. *Journal of Rheology* **33** (8), 1197–1212.
- Y. B. ZELDOVICH (1981). On the friction of fluids between rotating cylinders. *Proceedings of the Royal Society of London, Series A* **374** (1758), 299–312.

- R. ZENIT, M. L. HUNT, AND C. E. BRENNEN (1997). Collision particle pressure measurements in solid-liquid flows. *Journal of Fluid Mechanics* **353**, 261–283.
- R. P. ZOU AND A. B. YU (1995). The packing of spheres in a cylindrical container: the thickness effect. *Chemical Engineering Science* **50** (9), 1504–1507.
- R. P. ZOU AND A. B. YU (1996). Evaluation of the packing characteristics of mono-sized non-spherical particles. *Powder Technology* **88** (1), 71–79.



This thesis was prepared in  $\text{\LaTeX} 2_{\epsilon}$  using the `new_cit_thesis` class file written by Daniel M. Zimmerman.<sup>1</sup> It was typeset directly to Adobe Portable Document Format on a MacBook Pro running Mac OS X using pdf $\text{\TeX}$  as included in Thomas Esser's  $\text{\TeX}$  distribution. The figures were prepared using MATLAB<sup>®</sup> and the schematic diagrams were drawn in Adobe<sup>®</sup> Illustrator<sup>®</sup> CS3.

The the typeface used in the main text is URW Palladio L, an adaptation to Palatino, designed by Hermann Zapf. The monospaced font used to describe MATLAB variables is `Courier`, designed by Howard "Bud" Kettler. The remaining fonts used for mathematical symbols, Greek characters and in figures are from the European Computer Modern font family, designed by Jörg Knappen.<sup>2</sup>

---

<sup>1</sup>`new_cit_thesis.cls` is adapted from the  $\text{\LaTeX} 2_{\epsilon}$  report class and M. Kelsey's `cit_thesis.sty`

<sup>2</sup>an updated version of the Computer Modern font developed by Donald Knuth